



universität
wien

DISSERATATION

Titel der Dissertation
Merging GW with DMFT

Verfasser
Mag. Merzuk Kaltak

angestrebter akademischer Grad
Doktor der Naturwissenschaften (Dr. rer. nat.)

Wien, 2015

Sudienkennzahl lt. Studienblatt: A 791 411
Dissertationsgebiet lt. Studienblatt: Physik
Betreuerin / Betreuer: Univ.-Prof. Dipl.-Ing. Dr. Georg Kresse

Vorwort

Die vorliegende Arbeit besteht aus zwei Teilen. Der erste Teil deckt im wesentlichen Literatur von Vielelektronensystemen in kondensierter Materie ab und fasst alle theoretischen Grundlagen zusammen, die notwendig sind um die GW -Näherung der Schwinger-Dyson-Gleichungen mit der Dynamischen Molekularfeldtheorie (DMFT) zu kombinieren. Die Vereinigung von GW mit DMFT (besprochen in Kapitel 4) ist theoretisch anspruchsvoll und benötigt eine detaillierte Einführung in die diagrammatische Störungstheorie (Kapitel 2 und 3), um eine konsistente Terminologie für das Verständnis des zweiten Teils der vorliegenden Dissertation aufzubauen.

Der zweite Teil der vorliegenden Arbeit beinhaltet zwei Kapitel die aus einer Kollektion von kürzlich publizierten Arbeiten bestehen. Darin werden methodologische Entwicklungen für das Ausführen von praktischen GW +DMFT-Rechnungen vorgestellt beginnend mit einem effizienten Algorithmus für die Berechnung der elektronischen Korrelationsenergie in der Random-Phase-Approximation (RPA) in Kapitel 5. Da die GW -Näherung mit der RPA eng verwandt ist, kann der präsentierte RPA-Algorithmus als der erste Schritt zu einem effizienten GW -Algorithmus betrachtet werden. In Kapitel 6 wird ein vereinfachter GW +DMFT-Zugang vorgestellt. Das beinhaltet die Ableitung einer beschränkten RPA-Methode (CRPA), welche die Berechnung der effektiven Wechselwirkung im korrelierten Unterraum, der durch die DMFT akkurat beschrieben wird, erlaubt. Um die Spektralfunktion von SrVO_3 zu berechnen, werden im letzten Teil die Quasi-Teilchen- GW - mit der DMFT-Näherung kombiniert. Das Resultat dieser Kombination führt zu einer guten Übereinstimmung mit dem Experiment.

Preface

The present thesis is divided into two parts. The first part covers basic textbook knowledge about the electronic problem of condensed matter physics and introduces the theoretical background to merge the GW approximation of the Schwinger-Dyson equations with dynamical mean field theory (DMFT). The combination of GW with DMFT (discussed in chapter 4) is a rather complex topic and the absence of textbooks with a main focus on this subject requires a detailed introduction into diagrammatic perturbation theory (covered by chapter 2 and 3) to build a consistent terminology for the second part of the following thesis.

The second part presents recently developed methods to carry out GW +DMFT calculations from first principles. Emphasize is put on the random phase approximation (RPA) in chapter 5, where a low scaling algorithm for the determination of the RPA correlation energy is discussed. Due to the strong relation between the GW and the random phase approximation, this algorithm should be seen as a first step towards the improvement and acceleration of the commonly applied quasi particle (qp) GW approximation of Kotani and Schilfgaarde. In chapter 6 a simplified GW +DMFT algorithm is presented based on the qp GW approximation including a derivation of a constrained RPA scheme for the *ab initio* determination of effective interaction parameters for DMFT Hamiltonians. The resulting qp GW +DMFT scheme is applied to SrVO₃ finding good agreement with experimentally measured spectral functions.

Contents

I	Theoretical Background	1
1	Introduction: Mean Field Methods	3
1.1	The electronic problem	4
1.2	The Hartree-Fock Approximation	5
1.3	Density Functional Theory	8
1.3.1	Kohn-Sham Equations	10
1.3.2	Approximations to the exchange-correlation kernel	12
1.3.2.1	Local Density Approximation	12
1.3.2.2	Generalized Gradient Approximation	14
2	Quantum Field Theory for Condensed Matter	17
2.1	Second Quantization	18
2.2	Groundstate Energy and Normal Ordering	22
2.3	Particle-Hole Transformation	23
2.4	Feynman Propagator	24
2.4.1	Analytic Properties of non-interacting Green's functions	26
2.5	Interaction Picture and Time Evolution	29
2.6	Interacting Quantum Fields and Gell-Mann and Low Theorem	31
2.7	Imaginary Time and Statistical Physics	34
2.7.1	Finite-Temperature Feynman Propagator	36
2.7.2	Statistical Physics and Imaginary Time	39
3	Many-Body Perturbation Theory	43
3.1	Perturbation Series of the Grand Canonical Potential	43
3.1.1	The Wick Theorem	44

CONTENTS

3.2	Feynman Diagrams	47
3.3	Random Phase Approximation	52
4	Spectral Properties	57
4.1	Schwinger-Dyson Equations	57
4.1.1	Interacting Green's Function and Self-energy	57
4.1.2	Effective Interaction and Polarizability	61
4.1.3	Vertex and Bethe-Salpeter Equation	64
4.2	Hedin Equations and Self-Consistency Limit	68
4.2.1	The <i>GW</i> Approximation in Practice	69
4.3	The Path Integral	73
4.3.1	Path Integral for Quantum Fields	75
4.4	Effective Hamiltonians	77
4.4.1	The Many-Body problem in the Wannier Basis	77
4.5	Local effective Hamiltonians	78
4.5.1	Dynamical Mean Field Theory	83
II	Methodological Developments	87
5	Low Scaling Algorithm for the Random Phase Approximations	89
5.1	Computational Scheme	89
5.2	Imaginary Time and Frequency Grids	90
5.2.1	The Fitting Problem	91
5.2.2	Integral Quadrature Formulas for RPA and Direct MP Energies	93
5.2.3	Non-uniform Cosine Transformation	97
5.2.4	Technical Details	100
5.2.5	Grid Convergence for ZnO and Si	102
5.2.6	Grid Convergence for Al and Nb atom	105
5.2.7	Conclusion	107
5.3	Fast Fourier Transforms within supercells	109
5.4	Forming $G(\tau)G(-\tau)$ in the PAW Basis	113
5.5	Symmetry	117
5.6	Technical details	117

CONTENTS

5.7	Application to Si Defect Energies	118
5.7.1	Bulk properties	118
5.7.2	Time complexity for large supercells	119
5.7.3	Interstitial and vacancy	121
5.7.3.1	Considered structures and k-points sampling	121
5.7.3.2	Energetics of point defects	122
5.7.3.3	Diffusion barrier of interstitial	126
5.7.3.4	Small unit cells	127
5.8	Discussion and Conclusions	127
6	Merging <i>GW</i> with DMFT	131
6.1	Constrained Random Phase Approximation	134
6.1.1	Terminology	134
6.1.2	Correlated Subspaces and Wannier Representation	139
6.1.3	CRPA in the Kubo formalism	141
6.1.3.1	Technical details	146
6.1.4	Computational details	147
6.1.5	Wannier basis	149
6.1.6	Transition metals	151
6.1.6.1	Bare Coulomb interaction	151
6.1.6.2	Fully screened RPA interaction	152
6.1.6.3	Effective Coulomb interaction	154
6.1.7	La_2CuO_4	156
6.2	Unscreening Method for Isolated Target States	158
6.2.1	Implementation Details	159
6.2.2	Application to SrVO_3	159
6.2.3	Comparison with CRPA	160
6.3	Quasi Particle <i>GW</i> +DMFT	162
6.3.1	Comparing qp <i>GW</i> +DMFT and LDA+DMFT for SrVO_3	162
6.3.2	Results	165
6.3.3	Comparison to Photoemission Spectroscopy	168
7	Conclusion	171

CONTENTS

Appendices	175
A From QED to the Many-Body Problem	177
B Non-Interacting Lehman Amplitudes	183
C Functional Integral Identities	185
C.1 Grassmann Algebra	185
C.2 Hubbard-Strotonovich Transformation	187
D Analytic Continuation of Spectral Functions	189
E Interaction Matrices for La_2CuO_4 and the 3d TM series	191
List of Figures	193
List of Tables	199
References	201
Acronyms	209
Glossary	211

Part I

Theoretical Background

1

Introduction: Mean Field Methods

This thesis is dedicated to the many-body problem of condensed matter physics. This problem can be simply stated as finding the solution of the Schrödinger equation of N interacting valence electrons in the presence of an attractive periodic Coulomb potential. The resulting equation is presented in the following section and can be derived from the Lagrangian of quantum electrodynamics, see appendix A.

There are basically two different routes to the electronic problem. On the one side, there are mean-field methods based on the first quantization formalism of quantum physics, such as Hartree-Fock or density functional theory. These methods use a one-electron picture and assume that the many-body wavefunction can be written as product of one-electron wavefunctions. The current first chapter serves, apart from a general introduction to the electronic problem, as an introduction to these mean-field methods.

On the other side, quantum field theory methods, such as GW or dynamical mean field theory, tackle the problem from an alternative point of view. Here the propagator functions of the electrons and the photons are in the center of attention, and one tries to solve a set of three coupled Schwinger-Dyson equations instead. The main route of this thesis follows this approach and is discussed in chapters 2 to 6.

1. INTRODUCTION: MEAN FIELD METHODS

1.1 The electronic problem

We consider N_a non-interacting atomic nuclei in the primitive cell ordered on a periodic lattice forming an external attractive potential

$$\hat{\phi}(\mathbf{r}_l) = -\frac{1}{2} \sum_{i=1}^{N_a} \frac{Z_i}{|\mathbf{r} - \mathbf{R}_i|} \quad (1.1)$$

for an electron located at \mathbf{r}_l . It is assumed that the motion of electrons close to the core is frozen and can be absorbed in the definition of the potential $\hat{\phi}$. Hence, only valence electrons are considered and, furthermore, it is assumed that relativistic effects, such as pair creation or spin-orbit coupling, can be safely disregarded.

The kinetic energy of N of these valence electrons is then described by the non-relativistic term

$$\hat{T} = -\frac{1}{2} \sum_{l=1}^N \Delta_l, \quad (1.2)$$

whereas the interaction between the considered valence electrons is given by the Coulomb term

$$\hat{V}_{ee} = \frac{1}{2} \sum_{l=1}^N \sum_{n \neq l}^N \frac{1}{|\mathbf{r}_n - \mathbf{r}_l|}. \quad (1.3)$$

The last three Eqs. describe the total Hamiltonian

$$\hat{H} = \hat{T} + \sum_{l=1}^N \hat{\phi}(\mathbf{r}_l) + \hat{V}_{ee} \quad (1.4)$$

of the electronic problem one seeks the solution of following many-body Schrödinger equation

$$\hat{H} |\Omega_\mu\rangle = \Omega_\mu |\Omega_\mu\rangle. \quad (1.5)$$

Here, Ω_μ is the eigenenergy of the total wavefunction $|\Omega_\mu\rangle$ with μ being a superindex of quantum numbers describing N interacting electrons at positions $\mathbf{r}_1, \dots, \mathbf{r}_N$

It is well-known that equation (1.5) can be solved analytically for one electron and one proton, *i.e.* the hydrogen atom. In this case, the Schrödinger equation is effectively a two-body problem due to the absence of the electron-electron interaction (1.3). For more than one electron this term is present and a solution cannot be found exactly, so that one has to rely on approximations. In the following, we focus ourselves on the approximate determination of the interacting eigenstates $|\Omega_\mu\rangle$ and their energies Ω_μ .

1.2 The Hartree-Fock Approximation

We consider two different methods to solve Eq. (1.5) approximately, starting with the Hartree-Fock approximation, which goes back to the early 1930s.

1.2 The Hartree-Fock Approximation

One way to find an approximate estimate for the the many-body wavefunction is to assume that Ω_μ can be written in terms of one-electron orbital functions ϕ_α , where α stands for a set of quantum numbers, like angular momentum l_α , magnetic quantum number m_α , energy quantum number n_α and spin polarization σ_α . Furthermore, to take the Pauli principle into account, the wavefunction must vanish if two electrons have the same configuration. This is fulfilled for the Slater determinant $|\Psi_\mu^{(N)}\rangle$, see Ref. 1, defined as

$$\Psi_\mu^{(N)}(\mathbf{r}_1 \cdots \mathbf{r}_N) = [\varepsilon_{(\mu)}]^{\alpha_1 \cdots \alpha_N} \phi_{\alpha_1}(\mathbf{r}_1) \cdots \phi_{\alpha_N}(\mathbf{r}_N), \quad (1.6)$$

where the Levi-Civita symbol can be written as, see Ref. 2,

$$[\varepsilon_{(\mu)}]^{\alpha_1 \cdots \alpha_N} = \frac{1}{\sqrt{N!}} \begin{vmatrix} \delta_{1\alpha_1} & \cdots & \delta_{1\alpha_N} \\ \vdots & \ddots & \vdots \\ \delta_{N\alpha_1} & \cdots & \delta_{N\alpha_N} \end{vmatrix}, \quad \alpha_1, \cdots, \alpha_N \in I_\mu^{(N)} \quad (1.7)$$

and $I_\mu^{(N)}$ is a set of configurations describing the Slater determinant $|\Psi_\mu^{(N)}\rangle$. For instance, in the ground state $|\Psi_0^{(N)}\rangle$, the corresponding index set $I_0^{(N)}$ contains only the indices of the N lowest energy states, whereas higher excited states $|\Psi_{\mu>1}^{(N)}\rangle$ are obtained by replacing occupied indices $\alpha = i$ by unoccupied (or virtual) indices $\alpha = a$. In the following we stick to this notation and use Latin indices starting with i, j, \cdots for occupied, respectively starting with a, b, \cdots for unoccupied states, whereas Greek indices indicate arbitrary states.

For the time being, we consider a non-interacting system of N electrons and assume that the one-electron orbitals ϕ_α are solutions of the one-electron Schrödinger equation

$$\hat{h}_l \phi_\alpha(\mathbf{r}_l) = \epsilon_\alpha \phi_\alpha(\mathbf{r}_l), \quad (1.8)$$

where

$$\hat{h}_l = -\frac{\Delta_l}{2} + \hat{\varphi}(\mathbf{r}_l) \quad (1.9)$$

1. INTRODUCTION: MEAN FIELD METHODS

is the non-interacting Hamiltonian for an electron at \mathbf{r}_l . Furthermore, we assume orthogonality of the orbitals

$$\langle \phi_\alpha | \phi_\beta \rangle = \delta_{\alpha\beta}, \quad (1.10)$$

which can be achieved always using the orthogonalization method of Löwdin, see Ref. 3 for more details. These properties imply the completeness relation

$$1 = \sum_{\mu=0}^{\infty} \left| \Psi_\mu^{(N)} \right\rangle \left\langle \Psi_\mu^{(N)} \right| \quad (1.11)$$

and the fact that the Slater determinants are an eigensystem of the non-interacting many-body Schrödinger equation

$$\underbrace{\hat{H}_0}_{\sum_{i=1}^N \hat{h}_i} \left| \Psi_\mu^{(N)} \right\rangle = \underbrace{E_\mu^{(N)}}_{\sum_{\alpha \in I_\mu^{(N)}} \epsilon_\alpha} \left| \Psi_\mu^{(N)} \right\rangle. \quad (1.12)$$

In traditional Hartree-Fock (HF) theory, one assumes that the Slater determinant ansatz (1.6) is valid also in the presence of an interaction term \hat{V}_{ee} . In fact, one can show that the ansatz

$$\Omega_\mu^{\text{HF}}(\mathbf{r}_1 \cdots \mathbf{r}_N) = [\varepsilon(\mu)]^{\alpha_1 \cdots \alpha_N} \psi_{\alpha_1}(\mathbf{r}_1) \cdots \psi_{\alpha_N}(\mathbf{r}_N), \quad (1.13)$$

satisfies

$$\langle \Omega_\mu^{\text{HF}} | \hat{H} | \Omega_\mu^{\text{HF}} \rangle = \Omega_\mu^{\text{HF}}, \quad (1.14)$$

where Ω_μ^{HF} is the so-called *Hartree-Fock energy* of the Slater determinant $|\Omega_\mu^{\text{HF}}\rangle$. Using the explicit form of the Hamiltonian (1.5) and the ansatz (1.13), the Schrödinger equation (1.14) becomes effectively an one-electron equation

$$\left[\hat{h} + \hat{V}_h - \hat{V}_x \right] |\psi_\alpha\rangle = e_\alpha |\psi_\alpha\rangle \quad (1.15)$$

for the one-electron HF-orbitals $|\psi_\alpha\rangle$ and energies e_α , see Ref. 4. Here, we have introduced the common definition of the *Hartree* potential

$$\hat{V}_h(\mathbf{r}) = \sum_{\beta \in I_\mu} \int d\mathbf{r}' \frac{|\psi_\beta(\mathbf{r}')|^2}{|\mathbf{r}' - \mathbf{r}|} \quad (1.16)$$

and the *exchange* potential

$$\hat{V}_x(\mathbf{r}) |\psi_\alpha\rangle = - \sum_{\beta \in I_\mu} \int d\mathbf{r}' \frac{\psi_\beta^*(\mathbf{r}') \psi_\alpha(\mathbf{r}')}{|\mathbf{r}' - \mathbf{r}|} |\psi_\beta\rangle. \quad (1.17)$$

1.2 The Hartree-Fock Approximation

The Hartree potential is a local quantity and describes the repulsive, classical electrostatic interaction of all electrons, whereas the non-local exchange part can be attractive or repulsive for an electron at \mathbf{r} and is a result of the Pauli principle.

The last two expressions reveal that Eq. (1.15) is a set of N coupled non-linear differential equations for the HF one-electron orbitals $\psi_{\alpha_1}, \dots, \psi_{\alpha_N}$. This set is typically called the HF equations and must be solved self-consistently. Usually one is interested in the groundstate $|\Omega_0^{\text{HF}}\rangle$ only and one starts with a first guess for the one-electron orbitals, for instance the non-interacting solution of Eq. (1.8), *i.e.* the non-interacting groundstate Slater-determinant $|\Psi_0^{(N)}\rangle$. In the first step, one determines the corresponding Hartree and exchange contributions $V_{\text{h}}^{(0)}$ and $V_{\text{x}}^{(0)}$ using the non-interacting one-electron orbitals of $|\Psi_0^{(N)}\rangle$. Using these potentials, the Hartree-Fock equations (1.9) are solved successively, obtaining a new set of solutions $\{e_i^{(1)}, \psi_i^{(1)}\}_{i \in I_0^{(N)}}$, followed by an update of the mean-field potentials obtaining $V_{\text{h}}^{(1)}, V_{\text{x}}^{(1)}$ and so on. The procedure is iterated until a convergence criterion is reached, for instance the variation of the total energy $\sum_{i \in I_0^{(N)}} |e_i^{(k+1)} - e_i^{(k)}| \rightarrow 0$. The final solution of this procedure gives the HF orbitals $\{\psi_i, e_i\}_{i \in I_0^{(N)}}$ and the corresponding HF eigensystem (1.14) for $\mu = 0$. It is important to mention, that due to the non-linearity of the HF equations (1.15), the solution $|\Omega_0^{\text{HF}}\rangle$ is non-unique. This means that, in general, there might be more than one set of orbitals $\{\psi_i, e_i\}_{i \in I_0^{(N)}}$ giving the same groundstate Hartree-Fock energy Ω_0^{HF} .¹

This energy is in general larger than the true groundstate energy Ω_0 of the system. The remaining piece is called the electronic correlation energy $E_c^{(N)}$ and is defined as

$$E_c^{(N)} = \Omega_0^{\text{HF}} - \Omega_0^{(N)}. \quad (1.18)$$

This part is in general unknown and its accurate determination is the true demanding part of condensed matter physics and quantum chemistry. The reason for this is, that the true interacting groundstate $|\Omega_0\rangle$ cannot be described by a single Slater determinant $|\Omega_0^{\text{HF}}\rangle$, as it is done in the Hartree-Fock approximation. It is fairly obvious that the complete many electron Hilbert space is spanned by all Slater determinants $|\Omega_{\mu}^{\text{HF}}\rangle$. Thus, the true groundstate wavefunction $|\Omega_0\rangle$ must be a linear combination of all possible HF Slater determinants

$$|\Omega_0\rangle = \sum_{\mu=1}^{\infty} t_{\mu}^{(0)} |\Omega_{\mu}^{\text{HF}}\rangle, \quad t_{\mu}^{(0)} \in \mathbb{C} \quad (1.19)$$

¹However, degeneracies are seldom in practice. More often, one might get 'stuck' in local minima.

1. INTRODUCTION: MEAN FIELD METHODS

This implies that $|\Omega_0\rangle$ contains also contributions of excited Slater-determinants and thus also originally unoccupied one-electron states $|\psi_a\rangle$.

The expansion coefficients $t_\mu^{(0)}$ can be determined with the so-called configuration interaction (CI) method. In small molecules, it is sufficient to restrict the considered basis functions $|\Omega_\mu^{\text{HF}}\rangle$ to singly, doubly or triply excited determinants, *i.e.* where one, two respectively three occupied states in $|\Omega_0^{\text{HF}}\rangle$ are replaced by one (singles), two (doubles) respectively three (triples) excited states. However, the drawback of CI is the large computation cost of the method scaling exponentially with the system size N and that it is not size consistent if truncated at finite order, see Ref. 5. This is problematic for solids, because the correlation energy converges to zero, if the CI expansion (1.19) truncated and the system size is increased.

A computationally cheaper, but in principle exact method, is density functional theory and is discussed in the following section.

1.3 Density Functional Theory

Density functional theory (DFT) relies on two theorems, found by Hohenberg and Kohn published in [6] in the 1960s and are formulated as follows.

Theorem 1.3.1 (Hohenberg-Kohn I) *There is exactly one functional $\mathcal{F} : \mathcal{C}^\infty(\mathbb{R}^3) \rightarrow \mathbb{R}$, $\rho'(\mathbf{r}) \mapsto \mathcal{F}[\rho'(\mathbf{r})]$ with $\varphi = \mathcal{F}[\rho(\mathbf{r})] + \alpha$, $\alpha \in \mathbb{R}$, where $\rho(\mathbf{r}) = \langle \Omega_0 | \mathbf{r} \rangle \langle \mathbf{r} | \Omega_0 \rangle$ is the groundstate density of the interacting Hamiltonian $\hat{H} = \hat{T} + \sum_{i=1}^N \hat{\varphi}(\mathbf{r}_i) + \hat{V}_{\text{ee}}$.*

Proof The proof for this theorem is indirect. We assume that two external potentials φ and φ' with corresponding Hamiltonians \hat{H} and \hat{H}' have the same ground state energy, but differ by a non-constant term. Assume $|\Omega_0\rangle$ and $|\Omega'_0\rangle$ are the corresponding groundstate wavefunctions of \hat{H} and \hat{H}' . Since $\hat{H} \neq \hat{H}' \Rightarrow |\Omega_0\rangle \neq |\Omega'_0\rangle$ but $\langle \Omega_0 | \mathbf{r} \rangle \langle \mathbf{r} | \Omega_0 \rangle = \rho(\mathbf{r}) = \langle \Omega'_0 | \mathbf{r} \rangle \langle \mathbf{r} | \Omega'_0 \rangle$. It follows for the groundstate energies, that $\Omega_0 = \langle \Omega_0 | \hat{H} | \Omega_0 \rangle < \langle \Omega'_0 | \hat{H} | \Omega'_0 \rangle = \Omega'_0$. Strict inequality holds only if the groundstate is non-degenerate, however, it is not mandatory to assume this, see Ref. 7 for more details.

1.3 Density Functional Theory

Furthermore, from rewriting

$$\begin{aligned}
\langle \Omega'_0 | \hat{H} | \Omega'_0 \rangle &= \Omega'_0 + \langle \Omega'_0 | \hat{H} - \hat{H}' | \Omega'_0 \rangle \\
&= \Omega'_0 + \langle \Omega'_0 | \hat{\varphi} - \hat{\varphi}' | \Omega'_0 \rangle \\
&= \Omega'_0 + \int d\mathbf{r} [\varphi(\mathbf{r}) - \varphi'(\mathbf{r})] \rho(\mathbf{r}) \\
\Rightarrow \Omega_0 &< \Omega'_0 + \int d\mathbf{r} [\varphi(\mathbf{r}) - \varphi'(\mathbf{r})] \rho(\mathbf{r}).
\end{aligned}$$

Analogously, we obtain

$$\Omega'_0 < \Omega_0 + \int d\mathbf{r} [\varphi'(\mathbf{r}) - \varphi(\mathbf{r})] \rho(\mathbf{r})$$

and adding both inequalities yields the contradiction

$$\Omega_0 + \Omega'_0 < \Omega'_0 + \Omega_0.$$

Thus two different potentials φ, φ' yielding the same groundstate density ρ do not exist, as assumed above. Therefore ρ is uniquely defined by the external potential φ .

Theorem 1.3.2 (Hohenberg-Kohn II) *There is exactly one functional $\mathcal{E} : \mathcal{C}^\infty(\mathbb{R}^3) \rightarrow \mathbb{R}, \rho'(\mathbf{r}) \mapsto \mathcal{E}[\rho'(\mathbf{r})]$, where $\Omega_0 = \mathcal{E}[\rho(\mathbf{r})]$ is the groundstate energy and the groundstate density $\rho(\mathbf{r}) = \langle \Omega_0 | \mathbf{r} \rangle \langle \mathbf{r} | \Omega_0 \rangle$ satisfies $\left. \frac{\delta \mathcal{E}[\rho]}{\delta \rho'} \right|_{\rho'=\rho} = 0$.*

Proof From theorem 1.3.1 follows, that the groundstate density ρ determines φ . Since φ determines the full Hamiltonian \hat{H} , the corresponding wavefunction $|\Omega_0[\rho]\rangle$ depends on the density. Therefore the energy functional $\mathcal{E}_{\text{HK}} : \mathcal{C}^\infty(\mathbb{R}^3) \rightarrow \mathbb{R}$ defined as

$$\mathcal{E}_{\text{HK}}[\rho'] = \langle \Omega_0[\rho'] | \hat{T} + \hat{V}_{\text{ee}} | \Omega_0[\rho'] \rangle + \int d\mathbf{r} \varphi(\mathbf{r}) \rho'(\mathbf{r}), \quad \rho' \in \mathcal{C}^\infty(\mathbb{R}^3) \quad (1.20)$$

satisfies

$$\mathcal{E}_{\text{HK}}[\rho'] = \Omega_0, \quad (1.21)$$

where Ω_0 is the groundstate energy of the interacting groundstate electron density $\rho(\mathbf{r})$. From this equation it also follows, that

$$\mathcal{E}_{\text{HK}}[\rho'] > \Omega_0, \quad \forall \rho' \neq \rho.$$

Hence ρ is the global minimum of the functional $\mathcal{E}_{\text{HK}}[\rho']$ and the theorem is proven.

1. INTRODUCTION: MEAN FIELD METHODS

These two theorems provide the mathematical basis for density functional theory. They guarantee the existence of an universal energy functional. Its minimum yields the interacting groundstate density. For this purpose one needs the explicit form of the energy functional (1.20), which we want discuss in the following. One usually subdivides the electron-electron interaction functional into a Hartree term \mathcal{E}_h and a so-called exchange-correlation part \mathcal{E}_{xc}

$$\langle \Omega_0[\rho] | \hat{V}_{ee} | \Omega_0[\rho] \rangle = \mathcal{E}_h[\rho] + \mathcal{E}_{xc}[\rho]. \quad (1.22)$$

The Hartree term is exactly known from Hartree-Fock theory [compare to Eq. (1.16)]

$$\mathcal{E}_h[\rho] = \frac{1}{2} \int d\mathbf{r}' d\mathbf{r} \frac{\rho(\mathbf{r}')\rho(\mathbf{r})}{|\mathbf{r} - \mathbf{r}'|} \quad (1.23)$$

and describes the classical electrostatic energy.

The second part \mathcal{E}_{xc} contains two contributions

$$\mathcal{E}_{xc}[\rho] = \mathcal{E}_x[\rho] + \mathcal{E}_c[\rho]. \quad (1.24)$$

The Fock-exchange functional $\mathcal{E}_x[\rho]$, corresponding to the potential (1.17), is well-known from Hartree-Fock theory and can be determined exactly. However, in practice one usually approximates this part together with the remaining contribution, the unknown correlation functional $\mathcal{E}_c[\rho]$, that describes all electronic interactions beyond the Hartree-Fock approximation.

The big success of density functional theory relies on the fact that the complicated electronic interaction (1.22) is separated into three terms of decreasing importance, where the Hartree energy is the largest and the correlation energy the smallest contribution. This allows for approximations to the exchange-correlation functional and we discuss two of them in section 1.3.2.

1.3.1 Kohn-Sham Equations

The Hohenberg-Kohn theorems presented in the previous section particularly useful as they stand, since \mathcal{E}_c is entirely unknown. Furthermore, they do not tell us how the functional of the kinetic energy, by far the largest contribution to the total energy, looks

1.3 Density Functional Theory

like. The problem hereby is that the kinetic functional $\mathcal{T}[\rho]$, is related to the Laplacian of the many-body wavefunction $|\Omega_0\rangle$

$$T = \left\langle \Omega_0 \left| -\frac{1}{2} \sum_{i=1}^N \Delta_i \right| \Omega_0 \right\rangle \quad (1.25)$$

rather than its density ρ . Kohn and Sham assumed the existence of a non-interacting system of electrons with the same density as the interacting system, see Ref. 8. In the following we call this system, the Kohn-Sham (KS) system and write $\{\tilde{\phi}_i, \tilde{\epsilon}_i\}$ for the one-electron orbitals and energies. Using the occupancies \tilde{f}_i , the KS ansatz is

$$\rho(\mathbf{r}) = \sum_{i=1}^{\infty} \tilde{f}_i \left| \tilde{\phi}_i(\mathbf{r}) \right|^2, \quad (1.26)$$

where the ground state density ρ integrates to the total number of electrons

$$\int d\mathbf{r} \rho(\mathbf{r}) = \sum_{i=1}^{\infty} \tilde{f}_i = N. \quad (1.27)$$

The exact groundstate wavefunction of the KS system is therefore explicitly known and is given by the Slater determinant of the Kohn-Sham orbitals $\tilde{\phi}_i$. Consequently the kinetic functional of the non-interacting system can be written as

$$\mathcal{T}_{\text{KS}}[\rho] = -\frac{1}{2} \sum_{i=1}^{\infty} \tilde{f}_i \left\langle \tilde{\phi}_i \left| \Delta \right| \tilde{\phi}_i \right\rangle. \quad (1.28)$$

Inserting this expression and Eq. (1.26) into the Hohenberg-Kohn functional (1.20), we end up with the Kohn-Sham energy functional

$$\mathcal{E}_{\text{KS}}[\tilde{\rho}] = \mathcal{T}_{\text{KS}}[\tilde{\rho}] + \mathcal{E}_{\text{h}}[\tilde{\rho}] + \int d\mathbf{r} \tilde{\rho}(\mathbf{r}) \varphi(\mathbf{r}) + \mathcal{E}_{\text{xc}}[\tilde{\rho}], \quad \tilde{\rho} \in \mathcal{C}^{\infty}(\mathbb{R}^3). \quad (1.29)$$

This functional can be varied w.r.t. the density, under the constraint (1.27), *i.e.*

$$\frac{\delta}{\delta \tilde{\rho}(\mathbf{r})} \left[\mathcal{E}_{\text{KS}}[\tilde{\rho}] - \lambda \left(\int d\mathbf{r} \tilde{\rho}(\mathbf{r}) - N \right) \right] = 0, \quad \lambda \in \mathbb{R}. \quad (1.30)$$

Here λ is a Lagrangian multiplier and a priori unknown. By using the chain rule for the functional derivative

$$\frac{\delta}{\delta \tilde{\rho}(\mathbf{r})} = \left(\frac{\delta \tilde{\rho}(\mathbf{r})}{\delta \tilde{\phi}_j^*(\mathbf{r})} \right)^{-1} \frac{\delta}{\delta \tilde{\phi}_j^*(\mathbf{r})} \quad (1.31)$$

1. INTRODUCTION: MEAN FIELD METHODS

the factor λ can be identified with the KS energy $\tilde{\epsilon}_j$ of the orbital $\tilde{\phi}_j$ and we obtain

$$\tilde{f}_j \tilde{\phi}_j(\mathbf{r}) \left\{ \left[-\frac{1}{2} \Delta + \varphi(\mathbf{r}) + \int d\mathbf{r}' \frac{\tilde{\rho}(\mathbf{r}')}{|\mathbf{r} - \mathbf{r}'|} \right] \tilde{\phi}_j(\mathbf{r}) + \frac{\delta \mathcal{E}_{\text{xc}}[\tilde{\rho}]}{\delta \tilde{\phi}_j^*(\mathbf{r})} \right\} = \tilde{f}_j \tilde{\phi}_j(\mathbf{r}) \tilde{\epsilon}_j \tilde{\phi}_j(\mathbf{r}) \quad (1.32)$$

for Eq. (1.30). Dividing Eq. (1.32) by $\tilde{f}_j \tilde{\phi}_j(\mathbf{r})$ yields the Kohn-Sham equations

$$\left[-\frac{1}{2} \Delta + \varphi(\mathbf{r}) + \int d\mathbf{r}' \frac{\tilde{\rho}(\mathbf{r}')}{|\mathbf{r} - \mathbf{r}'|} + \frac{\delta \mathcal{E}_{\text{xc}}[\tilde{\rho}]}{\delta \tilde{\rho}(\mathbf{r})} \right] \tilde{\phi}_j(\mathbf{r}) = \tilde{\epsilon}_j \tilde{\phi}_j(\mathbf{r}). \quad (1.33)$$

This is a set of one-electron Schrödinger equations for a system of N non-interacting electrons. Because the density $\tilde{\rho}$ depends on the orbitals, the solution $\{\tilde{\epsilon}_j, \tilde{\phi}_j\}$ appears on both sides of these equations and therefore has to be solved self-consistently, similar to Hartree-Fock theory.

Before we discuss approximations to the exchange-correlation functional \mathcal{E}_{xc} , we make some remarks on the physical meaning of the KS equations. It is important to recall that the KS orbitals are constructed, such that the non-interacting density (1.26) coincides with the ground-state density of the interacting system. Their physical meaning is questionable and still a debate in the solid state community, only the energy differences $\tilde{\epsilon}_a - \tilde{\epsilon}_j$, can be considered as well-defined approximations for excitation energies.[9] Nevertheless it is common to consider the Kohn-Sham eigensystem $\{\tilde{\phi}_i, \tilde{\epsilon}_i\}$, because, undoubtedly, it provides a good basis set to study more enhanced methods.

1.3.2 Approximations to the exchange-correlation kernel

In order to solve the Kohn-Sham equations (1.33) in practice, one has to approximate the exchange-correlation functional \mathcal{E}_{xc} . Today, various functionals are known. Here we mention only the two most important ones, on which most of the functionals rely on. This is the local density approximation (LDA) and the generalized gradient approximation (GGA). For a comprehensive review of different density functionals the reader is referred to Ref. 4.

1.3.2.1 Local Density Approximation

The local density approximation of \mathcal{E}_{xc} was proposed by Kohn and Sham in their seminal paper and relies on ideas used in Thomas-Fermi theory of the homogeneous electronic gas, see Ref. 8. They assumed that the energy density of a general system can be

1.3 Density Functional Theory

approximated locally by the density of the homogenous electron gas (HEG), referred as $\varepsilon_{xc}^{\text{HEG}}$ in the following. This gives rise to the following ansatz of the LDA

$$\varepsilon_{xc}^{\text{LDA}}[\rho(\mathbf{r})] = \int d\mathbf{r} \rho(\mathbf{r}) \varepsilon_{xc}^{\text{HEG}}[\rho(\mathbf{r})]. \quad (1.34)$$

It is customary to separate the energy density into an exchange and correlation term[10]

$$\varepsilon_{xc}^{\text{HEG}} = \varepsilon_x^{\text{HEG}} + \varepsilon_c^{\text{HEG}} \quad (1.35)$$

and to use the result of Dirac for the former, derived in Ref. 11

$$\varepsilon_x^{\text{HEG}} = -\frac{3}{4} \left(\frac{3\rho(\mathbf{r})}{\pi} \right)^{\frac{1}{3}}. \quad (1.36)$$

The general expression for the correlation part $\varepsilon_c^{\text{HEG}}$ is unknown, except for the high and low density limit.

The high density limit can be obtained using diagrammatic techniques and the so-called random phase approximation (RPA), discussed in chapter 3 in more detail, and reads (in units of eV)

$$\varepsilon_c^{\text{RPA}} = 0.846 \ln r_s - 1.306 + \mathcal{O}(r_s), \quad r_s = \frac{1}{a_0} \left(\frac{3}{4\pi\rho} \right)^{\frac{1}{3}}. \quad (1.37)$$

Here $a_0 = \hbar^2/me^2$ is the Bohr radius (= 1 in atomic units) and ρ is the electron density or the inverse volume per electron, so that the Wigner-Seitz radius r_s measures roughly the average distance between electrons in a HEG. The result (1.37) can be obtained by an infinite summation of specific diagrammatic contributions following Gell-Mann and Brueckner in Ref. 12 and is valid for $r_s \approx 0$.

In the low density limit $r_s \gg 1$ the kinetic energy of the electrons vanishes as r_s^{-2} and the remaining positive charge distribution, which goes with r_s^{-1} , forces the electrons to form a stable lattice. This was shown first by Wigner, see Ref. 13, who proved that in general the low-density limit can be expanded in terms of $r_s^{-\frac{1}{2}}$ as

$$\varepsilon_c^{\text{LOW}} = \frac{g_0}{r_s} + \frac{g_1}{r_s^{\frac{3}{2}}} + \frac{g_2}{r_s^2} + \mathcal{O}(r_s^{-\frac{5}{2}}), \quad g_0, g_1, g_2 \in \mathbb{R}. \quad (1.38)$$

Here g_0, g_1 and g_2 are constants and depend on the considered lattice of the low density limit. For a collection of different limits, *i.e.* lattices, the interested reader is referred to Refs. 14, 15, 16.

1. INTRODUCTION: MEAN FIELD METHODS

In the intermediate regime $0 \ll r_s \ll \infty$ only numerical estimates of $\varepsilon_c^{\text{HEG}}$ are known and were first computed by Ceperley and Alder by means of quantum Monte Carlo simulations, see Ref. 17. These results have been used by Vosko, Wilk and Nusair in order to find an analytic expression for the correlation energy density, which interpolates the high (1.37) and low density limit (1.38). The resulting expression assumes the form[18]

$$\varepsilon_c^{\text{HEG}}(r_s) = \frac{A}{2} \left\{ \ln \frac{x^2}{X(x)} + \frac{2b}{\sqrt{4c-b^2}} \arctan \frac{\sqrt{4c-b^2}}{2x+b} - \frac{bx_0}{X(x_0)} \left[\ln \frac{(x-x_0)^2}{X(x)} + \frac{2(b+2x_0)}{\sqrt{4c-b^2}} \arctan \frac{\sqrt{4c-b^2}}{2x+b} \right] \right\} \quad (1.39)$$

with the auxiliary functions

$$x = \sqrt{r_s} \quad \text{and} \quad X(x) = x^2 + bx + c \quad (1.40)$$

and the constants $A = 0.062$, $x_0 = -0.409$, $b = 13.072$, $c = 42.720$ for the paramagnetic case. For the spin-polarized case the interested reader is referred to Ref. 10.

Today the LDA is still used, especially for many uniform systems, like bulk metals, some semiconductors or ionic crystals. Nevertheless, LDA is far from being perfect and often fails if inhomogenities play an important role in the considered system. This gives rise to a further approximation of the exchange-correlation functional.

1.3.2.2 Generalized Gradient Approximation

Real systems are typically far away from the HEG picture and contain typically inhomogenities, which LDA neglects completely. One way to describe these inhomogenities is to consider a more general expression than the LDA ansatz (1.34) and to take also the gradient of the electronic density $\nabla\rho$ into account.

However, a naive decomposition of the exchange-correlation functional in terms of the density and its derivatives fails. The reason is due to the fact that the corresponding series is not monotonically decreasing and expansions in terms of the density gradient $\nabla\rho$ have to be performed very carefully, as discussed in Ref. 4. This gives rise to the so-called GGA and in the past thirty years many different GGAs have been developed. Here we mention only the Perdew-Burke-Ernzerhof (PBE) functional, which is widely used in the community. A good summary of alternative GGAs can be found in Ref. 4.

1.3 Density Functional Theory

The PBE functional separates the exchange-correlation functional \mathcal{E}_{xc} into a correlation and an exchange part analogously to the LDA. However, the exchange part is given by

$$\mathcal{E}_x^{\text{PBE}}[\rho] = \int d\mathbf{r} \varepsilon_x^{\text{HEG}}(r_s) F_x(s) \quad (1.41)$$

and includes the dimensionless gradient

$$s = \frac{|\nabla\rho(\mathbf{r})|}{2k_{\text{F}}(\mathbf{r})\rho(\mathbf{r})} \quad (1.42)$$

with the local Fermi vector

$$k_{\text{F}}(\mathbf{r}) = [3\pi^2\rho(\mathbf{r})]^{1/3}. \quad (1.43)$$

An appropriate function F_x was suggested by Perdew Burke and Ernzerhof by imposing four conditions on the exchange functional (1.41). These conditions are found in Ref. 19 and are fulfilled for the following expression

$$F_x(s) = 1 + \frac{\kappa\mu s^2}{\kappa + \mu s^2} \quad (1.44)$$

with $\kappa = 0.804$ and $\mu = 0.2195$.

For the correlation part the PBE ansatz reads

$$\mathcal{E}_c^{\text{PBE}}[\rho] = \int d\mathbf{r} \rho(\mathbf{r}) [\varepsilon_c^{\text{HEG}}(r_s) + H(r_s, t)] \quad (1.45)$$

with the function H given by

$$H(r_s, t) = \gamma \ln \left(1 + \frac{\beta t^2}{\gamma} \frac{1 + t^2 A(r_s)}{1 + t^2 A(r_s) + t^4 |A(r_s)|^2} \right). \quad (1.46)$$

Here the dimensionless gradient $t = |\nabla\rho|/(2k_{\text{TF}}\rho)$ depends on the Thomas-Fermi screening wavevector

$$k_{\text{TF}} = \sqrt{r_s} \left(\frac{16}{3\pi^2} \right)^{1/3}, \quad (1.47)$$

rather than the Fermi vector and the auxiliary function A is

$$A(r_s) = \frac{\beta}{\gamma} \left[\exp \left(-\frac{\varepsilon_c^{\text{HEG}}(r_s)}{\gamma} \right) + 1 \right]^{-1} \quad (1.48)$$

with the dimensionless constants $\beta = 0.0667$, $\gamma = 0.0311$. Spin-polarized expressions are found in Ref. 19, whereas optimized parameters for solids are found in Ref. 20. In this work we exclusively use the latter functional.

1. INTRODUCTION: MEAN FIELD METHODS

DFT provides access only to the groundstate density and the corresponding energy and there is no denying that LDA and GGA is far from being perfect. These approximations often fail for systems, where effects of excited states play an important role and cannot be neglected. A way to describe these systems within DFT is to use Hybrid or Meta hybrid functionals, where the exchange-correlation potential is constructed by using the exact form of the Hartree-Fock exchange energy (1.17) in combination with an attenuated Coulomb kernel. These methods often introduce additional parameters, which are fitted to the experiment, so that the true *ab-initio* spirit of DFT is lost, see Refs. 4, 7 for an overview.

An alternative approach, being more versatile, is discussed in the next chapter and uses methods from high-energy physics.

2

Quantum Field Theory for Condensed Matter

Quantum field theory (QFT) was developed during the 1930s and 1940s in order to understand the physics of highly relativistic electrons interacting with each other. The underlying equation is the Dirac equation and soon it became clear that a consistent interpretation of this equation is possible only in terms of a many-particle theory, where the one-particle picture has to be disregarded. The resulting theory is called quantum electrodynamics (QED) and is by far the most successful theory we have, in the sense that the Landé factor of the electron is verified experimentally with an accuracy of 10^{-11} . [21]

The big success of QED relies mostly on its robust formulation in terms of quantized fields (describing electrons and photons), propagators (describing their motion) and the concept of renormalization of charge. The latter allows for the perturbative treatment of interacting systems in terms of a diagrammatic language and was mainly pushed forward by Schwinger, Feynman, Tomonaga and Dyson in the 1940s. The achievements of QED were soon recognized by the condensed matter community and physicists started using the same concepts successfully for the description of liquids, crystals and other non-relativistic systems. Here, the pioneers of the 1950s, such as Pines, Hubbard, Salam, Galitskii and Migdal, have to be mentioned followed by Hedin, Baym, Kadanoff and others, see Ref. 22 for a good overview of these early years.

The aim of this chapter is to give an introductory summary covering the basic concepts of QFT found in these years. This includes the quantization of the free Schrödinger

2. QUANTUM FIELD THEORY FOR CONDENSED MATTER

field, discussed in section 2.1, the introduction of the free Feynman propagator in section 2.4 and the corresponding interacting field theory, presented in section 2.6. We end this chapter with the imaginary time formalism in section 2.7.1 to bridge the gap to statistical physics.

2.1 Second Quantization

In appendix A we recall the Lagrangian field theory of QED and derive from the Dirac equation the non-relativistic Schrödinger field equation using very basic concepts. The final field Hamiltonian

$$H = H_0(t) + V(t) \quad (2.1)$$

is actually time-independent, see Eq. (A.6), and contains a non-interacting term

$$H_0(t) = \int d^3\mathbf{r} \psi^*(\mathbf{r}, t) \left(-\frac{1}{2}\Delta + q\varphi(\mathbf{r}) \right) \psi(\mathbf{r}, t) \quad (2.2)$$

and an interacting part

$$V(t) = \frac{q^2}{2} \int d^3\mathbf{r} d^3\mathbf{r}' \frac{\psi^*(\mathbf{r}, t)\psi(\mathbf{r}, t)\psi^*(\mathbf{r}', t)\psi(\mathbf{r}', t)}{|\mathbf{r} - \mathbf{r}'|}. \quad (2.3)$$

In the following the quantization of the free field theory described by the free Hamiltonian (2.2) is discussed. Using the equation of motion (A.14) one ends up with the free Schrödinger equation

$$i\frac{\partial\psi_s(\mathbf{r}, t)}{\partial t} = \hat{h}\psi_s(\mathbf{r}, t) \quad (2.4)$$

for the Schrödinger field ψ_s with the one-electron Hamiltonian \hat{h} given in Eq. (1.9). To avoid confusion, the Schrödinger picture is indicated with the subscript s in the following.

As a first step, one solves the Schrödinger equation (2.4) for the static case for one particle

$$\hat{h}\phi_\alpha(\mathbf{r}) = \epsilon_\alpha\phi_\alpha(\mathbf{r}), \quad (2.5)$$

obtaining the eigensystem $\{\epsilon_\alpha, \phi_\alpha\}$, where α is a set of quantum numbers characterizing the solution ϕ_α . It is assumed that the one-electron orbitals are orthonormalized w.r.t. the scalar product

$$\langle \phi_\alpha | \phi_\beta \rangle = \int d^3\mathbf{r} \phi_\alpha^*(\mathbf{r})\phi_\beta(\mathbf{r}) = \delta_{\alpha\beta}, \quad (2.6)$$

2.1 Second Quantization

so that also

$$\sum_{\alpha} \phi_{\alpha}^{*}(\mathbf{r}) \phi_{\alpha}(\mathbf{r}) = (2\pi)^3 \delta(\mathbf{r} - \mathbf{r}') \quad (2.7)$$

holds.¹ This allows to decompose the static solutions $\psi(\mathbf{r}) = \psi_s(\mathbf{r}, 0)$ of Eq. (2.4) into field modes

$$\psi(\mathbf{r}) = \sum_{\alpha} c_{\alpha} \phi_{\alpha}(\mathbf{r}), \quad c_{\alpha} \in \mathbb{C}. \quad (2.8)$$

The time-dependent solution of the Schrödinger picture is obtained from

$$\psi_s(\mathbf{r}, t) = e^{-i\hat{H}t} \psi(\mathbf{r}). \quad (2.9)$$

In order to treat electrons and holes on the same footing, as it is done in relativistic QFT, we allow the one-particle energies ϵ_{α} of Eq. (2.5) to take positive and negative values. In the following we will use the same notation as in section 1.2, where indices a, b indicate quantum numbers with energy $\epsilon_a > 0$, indices i, j describe states with negative energy $\epsilon_i < 0$, whereas ϵ_{α} denote arbitrary energies.

With this notation the fields $\psi_s(\mathbf{r}, t)$ and $\psi_s^{*}(\mathbf{r}, t)$ can be decomposed in positive and negative energy modes [see Ref. 23, 24]

$$\psi_s(\mathbf{r}, t) = \sum_a a_a \phi_a(\mathbf{r}) e^{-i\epsilon_a t} + \sum_i b_i^{*} \phi_i(\mathbf{r}) e^{i\epsilon_i t} \quad (2.10)$$

$$\psi_s^{*}(\mathbf{r}, t) = \sum_i b_i \phi_i^{*}(\mathbf{r}) e^{-i\epsilon_i t} + \sum_a a_a^{*} \phi_a^{*}(\mathbf{r}) e^{i\epsilon_a t}, \quad a_a, b_i \in \mathbb{C}. \quad (2.11)$$

These representations emphasize the Feynman-Stückelberg interpretation of QFT, where $\psi_s(\mathbf{r}, t)$ describes simultaneously particles with positive energies ϵ_a moving forward in time and antiparticles with negative energies ϵ_i moving backward in time. This interpretation, although originally proposed for the Dirac and the Klein-Gordon equation, see Ref. 25, is a consequence of the charge-parity-time inversion (CPT) theorem and also valid for non-relativistic theories.² The exponential factors, highlighting the particle (positive energy) and anti-particle (negative energy) contributions to the field, appear explicitly only in the Schrödinger picture.

However, it is advantageous to perform the second quantization in the Heisenberg picture, where the corresponding field $\psi(\mathbf{r})$ is time-independent and coincide with the

¹ If this is not the case one replaces $\phi_{\alpha}(\mathbf{r}) \rightarrow \frac{\phi_{\alpha}(\mathbf{r})}{\sqrt{\langle \phi_{\alpha} | \phi_{\alpha} \rangle}}$.

²Feynman and Stückelberg proposed this interpretation to understand the Klein-Paradox[26], where in the one-particle picture the tunneling of a particle is more probable with increasing potential barriers.

2. QUANTUM FIELD THEORY FOR CONDENSED MATTER

Schrödinger picture $\psi_s(\mathbf{r}, t)$ at $t = 0$. In the forthcoming, we therefore use only the field decompositions at zero time

$$\psi(\mathbf{r}) = \sum_a a_a \phi_a(\mathbf{r}) + \sum_i b_i^* \phi_i(\mathbf{r}) \quad (2.12)$$

$$\psi^*(\mathbf{r}) = \sum_i b_i \phi_i^*(\mathbf{r}) + \sum_a a_a^* \phi_a^*(\mathbf{r}) \quad (2.13)$$

with their inverse transformations

$$a_a = \int d^3\mathbf{r} \phi_a^*(\mathbf{r}) \psi(\mathbf{r}), \quad b_i = \int d^3\mathbf{r} \phi_i^*(\mathbf{r}) \psi(\mathbf{r}) \quad (2.14)$$

$$a_a^* = \int d^3\mathbf{r} \phi_a(\mathbf{r}) \psi^*(\mathbf{r}), \quad b_i^* = \int d^3\mathbf{r} \phi_i(\mathbf{r}) \psi^*(\mathbf{r}). \quad (2.15)$$

Under second quantization one understands the promotion of the expansion coefficients a_a, b_i, a_a^*, b_i^* to operators, $\hat{a}_a, \hat{b}_i, \hat{a}_a^\dagger, \hat{b}_i^\dagger$. These operators act on states $|\phi_1, \phi_2, \dots\rangle$ in the Fock space \mathbb{F} defined as the direct sum

$$\mathbb{F} = \bigoplus_{N=1}^{\infty} \wedge^N \mathbb{H} \quad (2.16)$$

of antisymmetrized many-particle Hilbert spaces[27]

$$\wedge^N \mathbb{H} = \text{span} \left\{ \left| \Psi_\mu^{(N)} \right\rangle \right\}_{\mu \in I_\mu^{(N)}}. \quad (2.17)$$

Here $\left| \Psi_\mu^{(N)} \right\rangle$ is a specific Slater-determinant of N particles and was defined in Eq. (1.6). Considered as an ordinary vector space, the Fock space \mathbb{F} contains a null element. This element is called the vacuum state $|0\rangle$ and is defined as[23]

$$\hat{a}_a |0\rangle = \hat{b}_i |0\rangle = 0, \quad \forall a, i. \quad (2.18)$$

The operators \hat{a}_a, \hat{b}_i are called annihilation operators and annihilate electrons ($\epsilon_a > 0$) and holes ($\epsilon_i < 0$) respectively. In contrast, the creation operators $\hat{a}_a^\dagger, \hat{b}_i^\dagger$ create electrons $|\phi_a\rangle$ and holes $|\phi_i\rangle$ from the vacuum $|0\rangle$

$$\hat{a}_a^\dagger |0\rangle = |\phi_a\rangle, \quad \hat{b}_i^\dagger |0\rangle = |\phi_i\rangle. \quad (2.19)$$

General N particle states can be created via

$$\left| \Omega^{(N)} \right\rangle = \sum_{k=1}^{\infty} \sum_{l=1}^{\infty} \left(\hat{a}_{b_k}^\dagger \right)^{n_k} \left(\hat{b}_{i_l}^\dagger \right)^{n_l} |0\rangle, \quad n_k, n_l \in \mathbb{N}, \quad (2.20)$$

2.1 Second Quantization

with $\sum_{k=1}^{\infty} n_k + \sum_{l=1}^{\infty} n_l = N$. This includes the non-interacting Slater determinants $|\Psi_{\mu}^{(N)}\rangle$ by choosing the occupancies n_k and n_l in agreement with the index sets $I_{\mu}^{(N)}$.

One postulates the canonical anticommutation rules

$$\{\hat{a}_a, \hat{a}_b^{\dagger}\} = \delta_{ab} \quad \{\hat{b}_i, \hat{b}_j^{\dagger}\} = \delta_{ij} \quad (2.21)$$

$$\{\hat{a}_a, \hat{b}_i^{\dagger}\} = 0 \quad \{\hat{b}_i, \hat{a}_a^{\dagger}\} = 0 \quad (2.22)$$

with the anticommutator given by

$$\{\hat{A}, \hat{B}\} = \hat{A}\hat{B} + \hat{B}\hat{A}. \quad (2.23)$$

From these relations follows that the occupation number n_i of a state $|\phi_i\rangle$ is either 1 or 0. Furthermore, exchanging two states

$$|\phi_i\phi_j\rangle = \hat{b}_i^{\dagger}\hat{b}_j^{\dagger}|0\rangle = -\hat{b}_j^{\dagger}\hat{b}_i^{\dagger}|0\rangle = -|\phi_j\phi_i\rangle, \quad i \neq j, \quad (2.24)$$

introduces a minus sign. Similar arguments hold for unoccupied states, implying that Fock states containing two one-particle states with identical quantum numbers are zero. This is the essence of the Pauli principle and guarantees that the particles described by the creation and annihilation operators, introduced above, obey the Fermi-Dirac statistics.[28]

Promoting the Fourier modes a_a and b_i to operators implies the promotion of the field $\psi(\mathbf{r})$ to an field operator $\hat{\psi}(\mathbf{r})$. This field operator acts onto arbitrary N particle states $|\Omega^{(N)}\rangle$, obtained from Eq. (2.20) by removing a particle located at \mathbf{r} and yielding an $N - 1$ particle state $|\hat{\psi}(\mathbf{r})\Omega^{(N)}\rangle$. For instance, the action onto the non-interacting Slater determinants $|\Psi_{\mu}^{(N)}\rangle$ can be written in position space as[29]

$$\langle \mathbf{r}_2, \dots, \mathbf{r}_N | \hat{\psi}(\mathbf{r})\Psi_{\mu}^{(N)} \rangle = \sqrt{N} \int d\mathbf{r}_1 \delta(\mathbf{r} - \mathbf{r}_1) \Psi_{\mu}^{(N)}(\mathbf{r}_1, \dots, \mathbf{r}_N) \quad (2.25)$$

and reveals, that the field operator $\hat{\psi}$ acts similar to the annihilation operators \hat{a}_a and \hat{b}_i . In fact, the field operator and its conjugate satisfy

$$\{\hat{\psi}(\mathbf{r}), \hat{\psi}^{\dagger}(\mathbf{r}')\} = i\delta(\mathbf{r} - \mathbf{r}'), \quad (2.26)$$

which can be shown straightforwardly using the anticommutation rules (2.21).

2. QUANTUM FIELD THEORY FOR CONDENSED MATTER

2.2 Groundstate Energy and Normal Ordering

Within the second quantization formalism, one is able to express the non-interacting field Hamiltonian (2.2), in terms of creation and annihilation operators. Inserting the field representations (2.12)-(2.15) into the field Hamiltonian (2.2) and using the one-particle eigenvalue Eq. (2.5) with Eq. (2.9) gives

$$\begin{aligned}
 \hat{H}_0(t) &= \sum_{ia} e^{-i(\epsilon_i + \epsilon_a)t} \epsilon_a \hat{b}_i \hat{a}_a \langle \phi_i | \phi_a \rangle + \sum_{ab} e^{i(\epsilon_a - \epsilon_b)t} \epsilon_b \hat{a}_a^\dagger \hat{a}_b \langle \phi_a | \phi_b \rangle \\
 &+ \sum_{ij} e^{-i(\epsilon_i - \epsilon_j)t} \epsilon_j \hat{b}_i \hat{b}_j^\dagger \langle \phi_i | \phi_j \rangle + \sum_{ij} e^{i(\epsilon_a + \epsilon_j)t} \epsilon_j \hat{a}_a \hat{b}_j^\dagger \langle \phi_a | \phi_j \rangle \\
 &= \sum_a \epsilon_a \hat{a}_a^\dagger \hat{a}_a + \sum_i \epsilon_i \underbrace{\hat{b}_i \hat{b}_i^\dagger}_{1 - \hat{b}_i^\dagger \hat{b}_i} = \sum_a \epsilon_a \hat{a}_a^\dagger \hat{a}_a - \sum_i \epsilon_i \hat{b}_i^\dagger \hat{b}_i + \sum_i \epsilon_i, \quad (2.27)
 \end{aligned}$$

where in the last step the anticommutation relation (2.21) was used.

This expression shows that \hat{H}_0 is indeed time-independent and consistent with the Schrödinger picture, but has a major deficiency. Due to the presence of the last term one can reach arbitrary low energies by multiple actions of \hat{H}_0 on the vacuum $|0\rangle$ yielding ultimately an unstable theory. Fortunately, in physical experiments only energy differences are measurable, and since the last term in Eq. (2.27) is just a constant one may replace the naive expression above by the difference $\hat{H}_0 - \sum_i \epsilon_i$.

The same effect can be achieved in a more elegant way, by introducing the normal ordering operator $:\cdot:$. This operator, replaces a product of creation and annihilation operators by the ordered product, where all annihilation operators are to the right of the creation operators. For instance

$$:\hat{b}_i \hat{b}_j^\dagger := -\hat{b}_j^\dagger \hat{b}_i, \quad (2.28)$$

where the minus sign comes from the fact that the r.h.s. follows from an odd number of interchanges of operators from the l.h.s. Consequently, one obtains for the normal ordered Hamiltonian in the vacuum state

$$\langle 0 | : \hat{H}_0 : | 0 \rangle = \sum_a \epsilon_a \langle 0 | \hat{a}_a^\dagger \hat{a}_a | 0 \rangle - \sum_i \epsilon_i \langle 0 | \hat{b}_i^\dagger \hat{b}_i | 0 \rangle = 0. \quad (2.29)$$

This expression is well defined and represents the energy operator, but for a constant shift. We shall, henceforth, use only normal-ordered Hamiltonians. However, in order to keep notation simple the normal-ordering symbol $:\cdot:$ is suppressed in the forthcoming.

2.3 Particle-Hole Transformation

Instead of decomposing $\hat{\psi}$ into positive and negative field modes (2.12)-(2.13), one may decompose the fields $\hat{\psi}, \hat{\psi}^\dagger$ into

$$\hat{\psi}(\mathbf{r}) = \sum_{\alpha} \hat{c}_{\alpha} \phi_{\alpha}(\mathbf{r}) \quad (2.30)$$

$$\hat{\psi}^\dagger(\mathbf{r}) = \sum_{\alpha} \hat{c}_{\alpha}^\dagger \phi_{\alpha}(\mathbf{r}) \quad (2.31)$$

and relate the operators $\hat{c}_{\alpha}, \hat{c}_{\alpha}^\dagger$ to the creation and annihilation operators $\hat{a}_a^\dagger, \hat{b}_i^\dagger, \hat{a}_a, \hat{b}_i$ by a Bogoliubov transformation of the form[30]

$$\hat{c}_{\alpha} = \sum_a \Theta(\epsilon_{\alpha}) \delta_{\alpha a} \hat{a}_a + \sum_i \Theta(-\epsilon_{\alpha}) \delta_{\alpha i} \hat{b}_i^\dagger. \quad (2.32)$$

Here Θ is the step function. This transformation on the other hand implies the anti-commutation rules

$$\left\{ \hat{c}_{\alpha}^\dagger, \hat{c}_{\beta} \right\} = \delta_{\alpha\beta} \quad \text{and} \quad \left\{ \hat{c}_{\alpha}, \hat{c}_{\beta} \right\} = 0, \quad (2.33)$$

which follow easily from (2.21).

However, the corresponding vacuum $|\tilde{0}\rangle$, defined by $\hat{c}_{\alpha} |\tilde{0}\rangle = 0$, differs from $|0\rangle$, since

$$\hat{c}_{\alpha} |0\rangle = 0 + \sum_i \Theta(-\epsilon_{\alpha}) \delta_{\alpha i} |\phi_i\rangle = \Theta(-\epsilon_{\alpha}) |\phi_{\alpha}\rangle \neq 0. \quad (2.34)$$

Hence repeated action of occupied annihilation operators on the vacuum yields

$$\prod_{k=1}^N c_{\alpha_k} |0\rangle = \Theta(-\epsilon_{\alpha_1}) \cdots \Theta(-\epsilon_{\alpha_N}) |\phi_{\alpha_1}, \cdots, \phi_{\alpha_N}\rangle = |\Psi_0^{(N)}\rangle, \quad (2.35)$$

where $|\Psi_0^{(N)}\rangle$ is the non-interacting groundstate of N electrons given in Eq. (1.6).

On the other hand,

$$\hat{a}_b |\Psi_0^{(N)}\rangle = 0 = \langle \Psi_0^{(N)} | \hat{a}_b^\dagger, \quad \forall \epsilon_b > 0 \quad (2.36)$$

holds, so that the Fock-vector $|\Psi_0^{(N)}\rangle$ can be seen as a *redefined* vacuum state and is therefore often named *Fermi vacuum*, see Ref. 31. The Fermi vacuum $|\Psi_0^{(N)}\rangle$ is the state containing no electrons above, respectively no holes below the Fermi level $\mu = 0$. This requires a *redefinition* of the hole operators \hat{b}_i by postulating

$$\hat{b}_i |\Psi_0^{(N)}\rangle = 0 = \langle \Psi_0^{(N)} | \hat{b}_i^\dagger, \quad \forall \epsilon_i < 0, \quad (2.37)$$

2. QUANTUM FIELD THEORY FOR CONDENSED MATTER

in order to be consistent with the terminology introduced in section 2.1.¹

To exploit both properties, Eq. (2.36) and Eq. (2.37), in real space, it is convenient to perform the particle-hole transformations by splitting the fields (2.12) and (2.13) into a particle and hole part

$$\hat{\psi}(\mathbf{r}) = \hat{\psi}_{>}(\mathbf{r}) + \hat{\psi}_{<}^{\dagger}(\mathbf{r}) \quad (2.38)$$

$$\hat{\psi}^{\dagger}(\mathbf{r}) = \hat{\psi}_{>}^{\dagger}(\mathbf{r}) + \hat{\psi}_{<}(\mathbf{r}) \quad (2.39)$$

Here, the electron and hole field operators are given by

$$\hat{\psi}_{>}(\mathbf{r}) = \sum_{\alpha} \Theta(\epsilon_{\alpha}) \phi_{\alpha}(\mathbf{r}) \hat{c}_{\alpha} = \sum_a \phi_a(\mathbf{r}) \hat{a}_a \quad (2.40)$$

$$\hat{\psi}_{<}(\mathbf{r}) = \sum_{\alpha} \Theta(-\epsilon_{\alpha}) \phi_{\alpha}^*(\mathbf{r}) \hat{c}_{\alpha}^{\dagger} = \sum_i \phi_i^*(\mathbf{r}) \hat{b}_i, \quad (2.41)$$

where $\hat{\psi}_{>}^{\dagger}$ ($\hat{\psi}_{>}$) creates (annihilates) electrons above, whereas $\hat{\psi}_{<}^{\dagger}$ ($\hat{\psi}_{<}$) creates (annihilates) holes below the Fermi level $\mu = 0$.

Consequently,

$$\hat{\psi}_{>}(\mathbf{r}) \left| \Psi_0^{(N)} \right\rangle = 0 = \left\langle \Psi_0^{(N)} \left| \hat{\psi}_{>}^{\dagger}(\mathbf{r}) \right. \right. \quad (2.42)$$

$$\hat{\psi}_{<}(\mathbf{r}) \left| \Psi_0^{(N)} \right\rangle = 0 = \left\langle \Psi_0^{(N)} \left| \hat{\psi}_{<}^{\dagger}(\mathbf{r}) \right. \right. \quad (2.43)$$

holds, which turn out to be useful properties for perturbation theory, in particular for the Wick's theorem, see Refs. 31, 32. We discuss this in more detail in chapter 3.

2.4 Feynman Propagator

We apply the developed formalism of the previous sections, in order to evaluate the non-interacting Feynman propagator[33, 34]

$$G^0(\mathbf{r}', \mathbf{r}, t) = -i\Theta(t) \left\langle \Psi_0^{(N)} \left| \hat{\psi}(\mathbf{r}, t) \hat{\psi}^{\dagger}(\mathbf{r}') \right| \Psi_0^{(N)} \right\rangle + i\Theta(-t) \left\langle \Psi_0^{(N)} \left| \hat{\psi}^{\dagger}(\mathbf{r}') \hat{\psi}(\mathbf{r}, t) \right| \Psi_0^{(N)} \right\rangle, \quad (2.44)$$

where $\hat{\psi}(\mathbf{r}, t)$ indicates the Heisenberg notation

$$\hat{\psi}(\mathbf{r}, t) = e^{i\hat{H}_0 t} \hat{\psi}(\mathbf{r}) e^{-i\hat{H}_0 t}. \quad (2.45)$$

¹We emphasize that for the redefined operators $\hat{b}_i |0\rangle \neq 0$ holds, because they annihilate holes w.r.t. the Fermi vacuum $\left| \Psi_0^{(N)} \right\rangle$ rather than the true vacuum $|0\rangle$.

2.4 Feynman Propagator

The propagator is an important function in many-body perturbation theory and we discuss it in more detail in the following.

The first term on the r.h.s. of Eq. (2.44) describes the undisturbed propagation of an electron with positive energy forward in time from the spacetime point $(\mathbf{r}', 0)$ to (\mathbf{r}, t) , whereas the second term describes the propagation of the corresponding hole with negative energy from (\mathbf{r}, t) to $(\mathbf{r}', 0)$. This becomes evident, when inserting the electron-hole transformations (2.38), (2.39) in Eq. (2.44) and using the Fermi vacuum identities (2.42) and (2.43) resulting in

$$G^0(\mathbf{r}', \mathbf{r}, t) = \Theta(t)G_{>}^0(\mathbf{r}', \mathbf{r}, t) - \Theta(-t)G_{<}^0(\mathbf{r}', \mathbf{r}, t). \quad (2.46)$$

with the *greater* and *lesser* functions defined as

$$G_{>}^0(\mathbf{r}', \mathbf{r}, t) = -i \langle \Psi_0^{(N)} | \hat{\psi}_{>}(\mathbf{r}, t) \hat{\psi}_{>}^\dagger(\mathbf{r}') | \Psi_0^{(N)} \rangle \quad (2.47)$$

$$G_{<}^0(\mathbf{r}', \mathbf{r}, t) = -i \langle \Psi_0^{(N)} | \hat{\psi}_{<}(\mathbf{r}') \hat{\psi}_{<}^\dagger(\mathbf{r}, t) | \Psi_0^{(N)} \rangle \quad (2.48)$$

For the time being, we concentrate ourselves on the lesser part. Inserting the completeness relation of all Slater-determinants (1.11) for N' particles into Eq. (2.48) and using the eigenvalue equation 1.12 yields

$$G_{<}^0(\mathbf{r}', \mathbf{r}, t) = -i \sum_{\nu=0}^{\infty} e^{-i(E_0^{(N)} - E_\nu^{(N')})t} \langle \Psi_0^{(N)} | \hat{\psi}_{<}(\mathbf{r}') | \Psi_\nu^{(N')} \rangle \langle \Psi_\nu^{(N')} | \hat{\psi}_{<}^\dagger(\mathbf{r}) | \Psi_0^{(N)} \rangle. \quad (2.49)$$

When the field operator $\hat{\psi}_{<}^\dagger(\mathbf{r})$ acts on $|\Psi_0^{(N)}\rangle$ it creates a hole at \mathbf{r} , *i.e.* removes an occupied state from $|\Psi_0^{(N)}\rangle$ and yields effectively an $N - 1$ singly excited Slater-determinant. Thus, only for $N' = N - 1$ and singly excited Slater-determinants $|\Psi_\nu^{(N-1)}\rangle$ the expression above is non-zero. The matrix elements on the r.h.s. of Eq. (2.49) are called *Lehmann amplitudes* and are expressible in terms of one-particle orbitals $\phi_\beta(\mathbf{r})\phi_\beta^*(\mathbf{r}')$, see appendix (B). For N non-interacting electrons, considered here, the exponent in Eq. (2.49) may be rewritten in terms of occupied one-particle energies[35]

$$E_0^{(N)} - E_\nu^{(N-1)} = \epsilon_\beta < 0. \quad (2.50)$$

Consequently, the lesser part contains only occupied states with energies $\epsilon_j < 0$ and reads

$$G_{<}^0(\mathbf{r}', \mathbf{r}, t) = -i \sum_j e^{-i\epsilon_j t} \phi_j(\mathbf{r}) \phi_j^*(\mathbf{r}'), \quad \epsilon_j < 0. \quad (2.51)$$

2. QUANTUM FIELD THEORY FOR CONDENSED MATTER

Analogously, the greater part contains only unoccupied states with positive energies

$$G_{>}^0(\mathbf{r}', \mathbf{r}, t) = i \sum_a e^{-i\epsilon_a t} \phi_a(\mathbf{r}) \phi_a^*(\mathbf{r}'), \quad \epsilon_a > 0 \quad (2.52)$$

so that the Feynman propagator (2.44) assumes the orbital form

$$G^0(\mathbf{r}', \mathbf{r}, t) = -i \sum_{\beta} \phi_{\beta}(\mathbf{r}) \phi_{\beta}^*(\mathbf{r}') e^{-i\epsilon_{\beta} t} [\Theta(t)\Theta(\epsilon_{\beta}) - \Theta(-t)\Theta(-\epsilon_{\beta})]. \quad (2.53)$$

We emphasize that for non-vanishing Fermi energy $\mu \neq 0$ the correct representation is

$$G^0(\mathbf{r}', \mathbf{r}, t) = -i \sum_{\beta} \phi_{\beta}(\mathbf{r}) \phi_{\beta}^*(\mathbf{r}') e^{-i(\epsilon_{\beta} - \mu)t} [\Theta(t)\Theta(\epsilon_{\beta} - \mu) - \Theta(-t)\Theta(\mu - \epsilon_{\beta})]. \quad (2.54)$$

The Feynman propagator is also often called Green's function (of the non-interacting system). The reason for this name is examined in the following section.

2.4.1 Analytic Properties of non-interacting Green's functions

To investigate the analytic behavior of the Feynman propagator, one notes that G^0 is the inverse of the free Schrödinger equation (2.4)

$$\left(i \frac{\partial}{\partial t} - \hat{h}_0(\mathbf{r}) \right) G^0(\mathbf{r}', \mathbf{r}, t - t') = \delta(t - t') \delta(\mathbf{r} - \mathbf{r}') \quad (2.55)$$

and satisfies the boundary conditions

$$G^0(\mathbf{r}', \mathbf{r}, t) \approx -ie^{-i\epsilon_a t}, \quad t > 0, \epsilon_a > 0 \quad (2.56)$$

$$G^0(\mathbf{r}', \mathbf{r}, t) \approx +ie^{-i\epsilon_i t}, \quad t < 0, \epsilon_i < 0. \quad (2.57)$$

This follows trivially from the identity

$$\frac{d\Theta(t)}{dt} = \delta(t), \quad (2.58)$$

Eq. (2.53) and the one-electron eigenvalue equation (2.5). The propagator is therefore also named non-interacting Green's function in analogy to the theory of partial differential equations. We examine the Green's function and its analytic properties in more detail in the following.

From the mathematical point of view, G^0 should be seen as a special boundary value of a distribution f , see for instance Refs. 36, 37. This distribution is found from the principal solution of the Fourier representation of the equation (2.55)

$$\left[\omega - \hat{h}_0(\mathbf{r}) \right] f(\mathbf{r}', \mathbf{r}, \omega) = 1 \quad (2.59)$$

2.4 Feynman Propagator

and reads

$$f(\mathbf{r}', \mathbf{r}, \omega) = \sum_{\alpha} \frac{\phi_{\alpha}(\mathbf{r})\phi_{\alpha}^*(\mathbf{r}')}{\omega - \epsilon_{\alpha}}. \quad (2.60)$$

Allowing for complex arguments $\omega \rightarrow z$ yields a multivalued function on the real axis. The reason for this is, that one can always add terms of the form

$$\lambda_{\alpha}\delta(z - \epsilon_{\alpha})\phi_{\alpha}(\mathbf{r})\phi_{\alpha}^*(\mathbf{r}'), \quad \lambda_{\alpha} \in \mathbb{C} \quad (2.61)$$

to Eq. (2.60), because they result in zeros when inserted in Eq. (2.59), due to the identity $z\delta(z) = 0$. Thus the most general solution of Eq. 2.59 is

$$f(\mathbf{r}', \mathbf{r}, z) = \sum_{\alpha} \phi_{\alpha}(\mathbf{r})\phi_{\alpha}^*(\mathbf{r}') \left[\mathcal{P} \frac{1}{z - \epsilon_{\alpha}} + \lambda_{\alpha}\delta(\epsilon_{\alpha} - z) \right], \quad \lambda_{\alpha}, \in \mathbb{C} \quad (2.62)$$

where the \mathcal{P} symbol indicates that the corresponding term in the inverse Fourier transformation

$$f(\mathbf{r}', \mathbf{r}, t) = \int \frac{dz}{2\pi} f(\mathbf{r}', \mathbf{r}, z) e^{-izt} \quad (2.63)$$

is treated as principle value integral. This integral can be evaluated straightforwardly and reads

$$f(\mathbf{r}', \mathbf{r}, t) = \sum_{\alpha} \phi_{\alpha}(\mathbf{r})\phi_{\alpha}^*(\mathbf{r}') \left[\frac{i}{2} e^{-i\epsilon_{\alpha}t} \text{sgn}(-t) + \frac{\lambda_{\alpha}}{2\pi} e^{-i\epsilon_{\alpha}t} \right]. \quad (2.64)$$

To satisfy the boundary conditions (2.56) and (2.57) for instance, the complex constants λ_{α} must read

$$\lambda_{\alpha} = \Theta(-\epsilon_{\alpha})i\pi - \Theta(\epsilon_{\alpha})i\pi, \quad (2.65)$$

whereas different boundary conditions, yield different coefficients.

One can include all possible boundary conditions in the following contour integral

$$f(\mathbf{r}', \mathbf{r}, t) = \oint_{\mathcal{C}} \frac{dz}{2\pi} e^{-izt} \sum_{\alpha} \frac{\phi_{\alpha}(\mathbf{r})\phi_{\alpha}^*(\mathbf{r}')}{z - \epsilon_{\alpha}} \quad (2.66)$$

by choosing the contour of integration \mathcal{C} appropriately, see Ref. 36. Specifically, the Feynman boundary conditions (2.56), (2.57) are fulfilled, for the contour shown in Fig. 2.1.

Representation (2.66) shows, that the general solution of the differential equation (including the special one in Eq. (2.59)) has a branch cut along the real axis, where different Riemannian sheets of the function $f(\mathbf{r}', \mathbf{r}, z)$ are glued together. Thereby each sheet corresponds to specific boundary values imposed on the general solution. Crossing

2. QUANTUM FIELD THEORY FOR CONDENSED MATTER

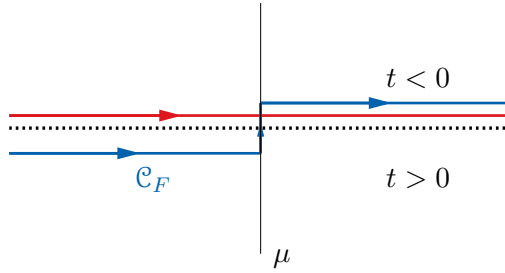


Figure 2.1: Complex frequency plane for $f(z)$ defined in (2.66) with branch cut (dashed line). Blue line: Feynman contour \mathcal{C}_F for the complex frequency plane. Red line: Contour for the retarded propagator (2.67). Contours are closed for negative (positive) times and occupied (unoccupied) energies $\epsilon_\mu < 0$ in upper (lower) half-plane.

the branch cut means changing the branch of the function f and therefore using different boundary conditions. This gives rise to different choices for the integration contour in Eq. (2.66) to reach different branches of the function f . For instance, the physically relevant *retarded* solution

$$G^0_{\mathbf{r}}(\mathbf{r}', \mathbf{r}, t) = -i\Theta(t) \left\langle \Psi_0^{(N)} \left| \left\{ \hat{\psi}(\mathbf{r}t), \hat{\psi}^\dagger(\mathbf{r}') \right\} \right| \Psi_0^{(N)} \right\rangle \quad (2.67)$$

can be obtained with the red contour in Fig. 2.1, whereas the time-ordered solution, *i.e.* the Feynman propagator G^0 is obtained with the blue contour.

In practice, the chosen contour is indicated by adding an infinitesimal η in the denominators of $f(\mathbf{r}', \mathbf{r}, z)$ and it is understood that the limit $\eta \rightarrow 0$ is taken after the Fourier transformation into time domain (2.63) is performed. For example for the Feynman propagator the correct prescription is

$$G^0(\mathbf{r}', \mathbf{r}, z) = \sum_{\alpha} \frac{\phi_{\alpha}(\mathbf{r})\phi_{\alpha}^*(\mathbf{r}')}{z - \epsilon_{\alpha} - i\eta\text{sgn}(\epsilon_{\alpha})}, \quad (2.68)$$

whereas for the retarded propagator one writes

$$G^0_{\mathbf{r}}(\mathbf{r}', \mathbf{r}, z) = \sum_{\alpha} \frac{\phi_{\alpha}(\mathbf{r})\phi_{\alpha}^*(\mathbf{r}')}{z - \epsilon_{\alpha} - i\eta}. \quad (2.69)$$

These representations are known as *Lehman representations* and are useful to indicate the considered branch of the distribution $f(\mathbf{r}', \mathbf{r}, z)$. We emphasize that the positions of the poles of the retarded, the Feynman and all other propagators are located always along the real line at $z = \epsilon_{\alpha}$, because the infinitesimal η in the denominators (2.68) and

2.5 Interaction Picture and Time Evolution

(2.69) contains only the information about the chosen contour and is not 'shifting' the poles away.

So far we have considered the second quantization for the non-interacting field theory only. In order to extend this formalism to interacting quantum fields we introduce the convenient interaction picture in the following section.

2.5 Interaction Picture and Time Evolution

The second quantization of the free field theory induces (together with the normal-ordering prescription from section 2.2) following representation for the Coulomb operator defined in Eq. (2.3)

$$\hat{V} = \frac{q^2}{2} \int d^3\mathbf{r} d^3\mathbf{r}' \frac{\hat{\psi}^\dagger(\mathbf{r}) \hat{\psi}^\dagger(\mathbf{r}') \hat{\psi}(\mathbf{r}') \hat{\psi}(\mathbf{r})}{|\mathbf{r} - \mathbf{r}'|} \quad (2.70)$$

and the full Hamiltonian (2.1) in second quantization formalism reads

$$\hat{H} = \hat{H}_0 + \hat{V}. \quad (2.71)$$

In order to study interacting quantum fields, especially their time evolution, it is convenient to work in the interaction picture. We summarize the basic concepts of this picture, going back to Dirac, in the following.

One makes the observation that the coupling constant q of the electromagnetic interaction appears quadratically in the interaction part \hat{V} of the many-body Hamiltonian (2.70) and linearly in the non-interacting part \hat{H}_0 . Therefore, one often considers the interaction \hat{V} as a perturbation to the non-interacting system and separates the time-dependence of the non-interacting part (described by \hat{H}_0) from the Schrödinger eigenstates $|\Omega_\mu^{(s)}\rangle$.

For this purpose the state vector $|\Omega_\mu(t)\rangle$ in the interaction picture is defined by

$$|\Omega_\mu(t)\rangle = e^{i\hat{H}_0 t} |\Omega_\mu^{(s)}(t)\rangle \quad (2.72)$$

with $|\Omega_\mu^{(s)}(t)\rangle$ satisfying the Schrödinger equation

$$i \frac{\partial}{\partial t} |\Omega_\mu^{(s)}(t)\rangle = \hat{H} |\Omega_\mu^{(s)}(t)\rangle = [\hat{H}_0 + \hat{V}] |\Omega_\mu^{(s)}(t)\rangle. \quad (2.73)$$

2. QUANTUM FIELD THEORY FOR CONDENSED MATTER

Differentiating Eq. (2.72) w.r.t. time and comparing with the time-dependent Schrödinger equation (2.73) one obtains[34]

$$i \frac{\partial |\Omega_\mu(t)\rangle}{\partial t} = \underbrace{e^{i\hat{H}_0 t} \hat{V} e^{-i\hat{H}_0 t}}_{=\hat{V}(t)} |\Omega_\mu(t)\rangle \quad (2.74)$$

and concludes, that in the interaction picture both, the states as well as the operators depend on the time.

Next, one seeks the time-evolution operator \hat{S} defined implicitly via

$$|\Omega_\mu(t)\rangle = \hat{S}(t, t_0) |\Omega_\mu(t_0)\rangle. \quad (2.75)$$

The operator in question can be found quickly, by rewriting Eq. (2.72) into

$$|\Omega_\mu(t)\rangle = e^{i\hat{H}_0 t} \underbrace{|\Omega_\mu^{(s)}(t)\rangle}_{e^{i\hat{H}(t-t_0)} \underbrace{|\Omega_\mu^{(s)}(t_0)\rangle}_{e^{-i\hat{H}_0 t_0} |\Omega_\mu(t_0)\rangle}} \quad (2.76)$$

and comparing with Eq. (2.75) yields the explicit form of the evolution operator

$$\hat{S}(t, t_0) = e^{i\hat{H}_0 t} e^{-i\hat{H}(t-t_0)} e^{-i\hat{H}_0 t_0}. \quad (2.77)$$

One emphasizes that \hat{V} and \hat{H}_0 do not commute, so that the correct order of the operators \hat{H} and \hat{H}_0 in Eq. (2.77) must be taken care of.

The time-evolution operator \hat{S} satisfies the group properties[34]

$$\hat{S}(t, t) = 1 \quad (2.78)$$

$$\hat{S}(t, t_0) = \hat{S}(t, t_1) \hat{S}(t_1, t_0) \quad (2.79)$$

$$\hat{S}^\dagger(t, t_0) = \hat{S}^{-1}(t, t_0) \quad (2.80)$$

and the differential equation

$$i \frac{\partial \hat{S}(t, t_0)}{\partial t} = \hat{V}(t) \hat{S}(t, t_0). \quad (2.81)$$

The latter follows from Eq. (2.75) and (2.74) and can be integrated to yield

$$\hat{S}(t, t_0) = 1 - i \int_{t_0}^t dt_1 \hat{V}(t_1) \hat{S}(t_1, t_0). \quad (2.82)$$

2.6 Interacting Quantum Fields and Gell-Mann and Low Theorem

This is a Fredholm equation of the second kind and has as unique solution in terms of the Liouville-Neumann series[38]

$$\hat{S}(t, t_0) = 1 + \sum_{n=1}^{\infty} (-i)^n \hat{I}_n(t, t_0) \quad (2.83)$$

$$\hat{I}_n(t, t_0) = \int_{t_0}^t dt_1 \hat{V}(t_1) \int_{t_0}^{t_1} dt_2 \hat{V}(t_2) \cdots \int_{t_0}^{t_{n-1}} dt_n \hat{V}(t_n). \quad (2.84)$$

In practice one rewrites the resolvent \hat{I}_n in terms of the time-ordering operator \hat{T} , defined by[39]

$$\hat{T} [\hat{\mathcal{O}}_1(t_1) \cdots \hat{\mathcal{O}}_n(t_n)] = \sum_{\sigma \in S^n} \text{sgn}(\sigma) \prod_{l=1}^{n-1} \Theta [t_{\sigma(l+1)} - t_{\sigma(l)}] \hat{\mathcal{O}}_{\sigma(l)}(t_{\sigma(l)}) \hat{\mathcal{O}}_{\sigma(n)}(t_{\sigma(n)}) \quad (2.85)$$

with $\text{sgn}(\sigma) = 1$ for bosonic operators, such as \hat{V} , whereas for fermionic operators, like $\hat{\psi}$, $\text{sgn}(\sigma) = 1$ for even and $\text{sgn}(\sigma) = -1$ for odd permutations σ of the permutation group S^n . Consequently, one obtains[34]

$$\hat{I}_n(t, t_0) = \frac{1}{n!} \int_{t_0}^t dt_1 dt_2 \cdots dt_n \hat{T} [\hat{V}(t_1) \hat{V}(t_2) \cdots \hat{V}(t_n)] \quad (2.86)$$

and in combination with Eq. (2.83), the evolution operator assumes the form

$$\hat{S}(t, t_0) = \hat{T} e^{-i \int_{t_0}^t dt \hat{V}(t)}. \quad (2.87)$$

We will use this operator in the next section to relate interacting to non-interacting eigenstates of the the Hamiltonian.

2.6 Interacting Quantum Fields and Gell-Mann and Low Theorem

Basically one knows everything about the non-interacting system, described by \hat{H}_0 , including groundstate energy and the corresponding one-particle eigensystem $\left\{ \left| \Psi_{\mu}^{(N)} \right\rangle, E_{\mu}^{(N)} \right\}$, see section 2.1. In contrast, the more interesting eigensystem $\left\{ \left| \Omega_{\mu}^{(N)} \right\rangle, \Omega_{\mu}^{(N)} \right\}$ in the presence of the interaction \hat{V} is unknown (we drop the superscript (N) for the time being to keep the notation simple). In this section we follow Gell-Mann and Low in order

2. QUANTUM FIELD THEORY FOR CONDENSED MATTER

to develop the mathematical framework to represent the eigenstates of the interacting theory in terms of the non-interacting eigensystem.[40]

One replaces the coupling constant q in the interaction term

$$\hat{V}(t) = \frac{q^2}{2} e^{i\hat{H}_0 t} \int d^3\mathbf{r} d^3\mathbf{r}' \frac{\hat{\psi}^\dagger(\mathbf{r}) \hat{\psi}^\dagger(\mathbf{r}') \hat{\psi}(\mathbf{r}') \hat{\psi}(\mathbf{r})}{|\mathbf{r} - \mathbf{r}'|} e^{-i\hat{H}_0 t}. \quad (2.88)$$

by a time-dependent charge

$$q \rightarrow q(t) = qe^{-\eta t^2}, \quad \eta \rightarrow 0 \quad (2.89)$$

and denotes the corresponding interaction term by $\hat{V}_\eta(t)$. Let us consider following set of problems

$$\left[\hat{H}_0 + \hat{V}_\eta(t) \right] |\Omega_\mu^\eta(t)\rangle = \Omega_\mu^\eta(t) |\Omega_\mu^\eta(t)\rangle, \quad (2.90)$$

with the properties

$$|\Omega_\mu^\eta(\pm\infty)\rangle = |\Psi_\mu\rangle \quad \text{and} \quad \Omega_\mu(\pm\infty) = E_\mu \quad (2.91)$$

$$|\Omega_\mu^\eta(0)\rangle = |\Omega_\mu\rangle \quad \text{and} \quad \Omega_\mu(0) = \Omega_\mu \quad (2.92)$$

This means that the system for $t \rightarrow \pm\infty$ is described by the known eigenstates of the non-interacting Hamiltonian \hat{H}_0 , whereas for $t = 0$ (where the interaction is at its full strength) the solution of Eq. (2.90) is the unknown interacting eigensystem.

Consider the time evolution operator $\hat{S}_\eta(t, t_0)$ satisfying the analogue of Eq. (2.81)

$$i \frac{\partial \hat{S}_\eta(t, t_0)}{\partial t} = \hat{V}_\eta(t) \hat{S}_\eta(t, t_0) \quad (2.93)$$

and implying

$$|\Omega_0^\eta\rangle = \hat{S}_\eta(0, \pm\infty) |\Psi_0\rangle. \quad (2.94)$$

This relation is mathematically well-defined for $\eta > 0$, provided the time evolution operator \hat{S}_η satisfies the boundary condition $\hat{S}_\eta(t_0, t_0) = 1$.¹ However, in the interesting limit $\eta \rightarrow 0$, the expression above is ill-defined, and one considers the limit

$$\frac{|\Omega_0\rangle}{\langle \Psi_0 | \Omega_0 \rangle} = \lim_{\eta \rightarrow 0} \frac{\hat{S}_\eta(0, \pm\infty) |\Psi_0\rangle}{\langle \Psi_0 | \hat{S}_\eta(0, \pm\infty) |\Psi_0\rangle} \quad (2.95)$$

instead.[34, 40] The Gell-Mann and Low theorem can be formulated as follows.

¹The Liouville-Neumann series (2.83) is well-defined for all times, see Ref. 38, so this is fulfilled.

2.6 Interacting Quantum Fields and Gell-Mann and Low Theorem

Theorem 2.6.1 (Gell-Mann and Low) *If the limit, defined in Eq.(2.95), exists to infinite order in perturbation theory and the non-interacting groundstate $|\Psi_0\rangle$ is not degenerate, it is an eigenvector of the interacting many-body Hamiltonian $\hat{H}_0 + \hat{V}$.*

The proof of this theorem can be found in Refs. 34, 40, 41 and will not be repeated here. In contrast we rather emphasize that 2.6.1 does not imply that $|\Omega_0\rangle$ is necessarily the interacting groundstate. In addition, non-degeneracy of the non-interacting groundstate $|\Psi_0\rangle$ is demanded.¹ In this thesis, however, we assume adiabaticity of the non-interacting eigenstates, as well as non-degeneracy of $|\Psi_0\rangle$, so that $|\Omega_0\rangle$ in Eq. (2.95) is the interacting groundstate.

This implies that the state vectors

$$\frac{|\Omega_\mu\rangle}{\langle\Psi_\mu|\Omega_\mu\rangle} = \frac{\hat{S}(0, -\infty)|\Psi_\mu\rangle}{\langle\Psi_\mu|\Omega_\mu\rangle} \quad (2.96)$$

are eigenvectors of the interacting many-body Hamiltonian

$$\hat{H} \frac{|\Omega_\mu\rangle}{\langle\Psi_\mu|\Omega_\mu\rangle} = \Omega_\mu \frac{|\Omega_\mu\rangle}{\langle\Psi_\mu|\Omega_\mu\rangle} \quad (2.97)$$

with ordered energies $\Omega_0 < \Omega_1 < \Omega_2 \dots$. In general the states $|\Omega_\mu\rangle$ differ from $|\Omega_\mu\rangle / \langle\Psi_\mu|\Omega_\mu\rangle$ by a phase, see Ref. 34, however it is convenient (and sufficient) to assume the normalization condition

$$\langle\Omega_\mu| \left(\frac{|\Omega_\mu\rangle}{\langle\Psi_\mu|\Omega_\mu\rangle} \right) = 1 \quad (2.98)$$

Together with Eq. (2.97) this implies for the interacting energy eigenstates

$$\Omega_\mu = \frac{\langle\Omega_\mu|\hat{H}|\Omega_\mu\rangle}{\langle\Omega_\mu|\Omega_\mu\rangle}. \quad (2.99)$$

a representation in terms of non-interacting eigenstates

$$\Omega_\mu = \frac{\langle\Psi_\mu|\hat{S}(\infty, 0)\hat{H}\hat{S}(0, -\infty)|\Psi_\mu\rangle}{\langle\Psi_\mu|\hat{S}(\infty, -\infty)|\Psi_\mu\rangle}. \quad (2.100)$$

It is possible to exchange the evolution operator $\hat{S}(\infty, 0)$ with the Hamiltonian in the numerator, see Ref. 34, such that one obtains

$$\Omega_\mu = \frac{\langle\Psi_\mu|\hat{H}\hat{S}(\infty, -\infty)|\Psi_\mu\rangle}{\langle\Psi_\mu|\hat{S}(\infty, -\infty)|\Psi_\mu\rangle}. \quad (2.101)$$

¹In fact, recent calculations for a 2×2 dimensional toy model with a degenerate groundstate demonstrate the breakdown of the Gell-Mann and Low theorem.[42]

2. QUANTUM FIELD THEORY FOR CONDENSED MATTER

Expanding the time-evolution operators in the nominator and denominator provides the starting point for a perturbative approximation of the interacting groundstate energy at zero temperature in terms of the non-interacting system.

Considered from a statistical point of view, however, Eq. (2.101) looks similar to the ensemble average of the Hamiltonian, where the density operator is replaced by $S(\infty, -\infty)$. In the following section we consider this expression in imaginary time to make this connection manifest.

2.7 Imaginary Time and Statistical Physics

It is possible to establish an intriguing relationship between the inverse temperature $\beta = T^{-1}$ and the imaginary time τ of a system. To see this, one generalizes the adiabatic charge function Eq. (2.89), to a meromorphic function

$$q(z) = qe^{-\eta|z|^2} \quad (2.102)$$

and allows for complex times z in the time evolution. Then the integration over the real axis in the time-evolution operator \hat{S} may be written as

$$-i \int_{-\infty}^{\infty} dt \hat{V}_\eta(t) = -i \int_{\mathcal{C}_+} dz \hat{V}_\eta(z), \quad (2.103)$$

where z is the complex time and the complex path $t \in \mathcal{C}_+$ is the positive real line depicted in Fig. 2.2. The index η indicates a finite infinitesimal. Closing the contour as shown in the same figure, the overall integral vanishes

$$\oint_{\mathcal{C}} dz \hat{V}_\eta(z) = 0, \quad (2.104)$$

as well as the integration over the quarter circle paths $\mathcal{C}_{-\infty}, \mathcal{C}_\infty$. Thus, the integral over the real line might be rewritten as an integral over the imaginary time axis

$$-i \int_{\mathcal{C}_+} dz \hat{V}_\eta(z) = i \int_{\mathcal{C}_i} dz \hat{V}_\eta(z) = (-i)^2 \lim_{\beta \rightarrow \infty} \int_{-\frac{\beta}{2}}^{\frac{\beta}{2}} d\tau \hat{V}_\eta(i\tau) = - \lim_{\beta \rightarrow \infty} \int_{-\frac{\beta}{2}}^{\frac{\beta}{2}} d\tau \hat{V}_\eta(-i\tau). \quad (2.105)$$

In the next step one shifts the imaginary time integration by $\tau \rightarrow \tau + \frac{\beta}{2}$ to the interval

2.7 Imaginary Time and Statistical Physics

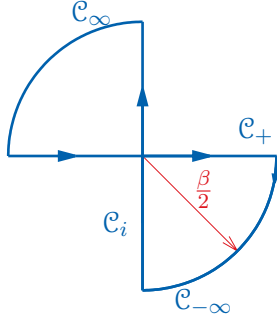


Figure 2.2: Complex contour for the Wick rotation from real time t to imaginary time τ .

$0 \leq \tau \leq \beta$ and perform the limit $\eta \rightarrow 0$ to obtain

$$-\lim_{\beta \rightarrow \infty} \lim_{\eta \rightarrow 0} \int_{-\frac{\beta}{2}}^{\frac{\beta}{2}} d\tau \hat{V}_\eta(-i\tau) = -\lim_{\beta \rightarrow \infty} \int_0^\beta d\tau e^{-\hat{H}_0 \frac{\beta}{2}} \hat{V}(-i\tau) e^{\hat{H}_0 \frac{\beta}{2}}, \quad (2.106)$$

where

$$\hat{V}(-i\tau) = e^{\hat{H}_0 \tau} \hat{V} e^{-\hat{H}_0 \tau}. \quad (2.107)$$

With slight abuse of notation, we suppress the $-i$ factor in the following and write simply $\hat{V}(\tau)$ for $\hat{V}(-i\tau)$ and other analytically continued observables and functions. Analogously, other operators and functions are analytically continued to the imaginary time axis and the time-ordering symbol \hat{T} orders operators along the imaginary time axis τ in the same way as it does for real times t . Furthermore, the exponential factors $e^{\hat{H}_0 \frac{\beta}{2}}, e^{-\hat{H}_0 \frac{\beta}{2}}$ in Eq. (2.106) cancel each other due to time ordering

$$\hat{T} e^{-\lim_{\beta \rightarrow \infty} \int_0^\beta d\tau e^{-\hat{H}_0 \frac{\beta}{2}} \hat{V}(\tau) e^{\hat{H}_0 \frac{\beta}{2}}} = \hat{T} e^{-\lim_{\beta \rightarrow \infty} \int_0^\beta d\tau \hat{V}(\tau)} \quad (2.108)$$

and are disregarded from now on.

The analytic continuation of the time integration path is an important step in combining statistical physics with QFT and was proposed first by Wick in Ref. 43. Before we discuss this connection in detail we consider the analytically continued Feynman propagator G^0 . The replacement $t \rightarrow -i\tau$ in the zero-temperature Green's function of the non-interacting system (2.53) yields

$$G^0(\mathbf{r}', \mathbf{r}, \tau) = -\sum_{\beta} \phi_{\beta}(\mathbf{r}) \phi_{\beta}^*(\mathbf{r}') e^{-\epsilon_{\beta} \tau} [\Theta(\tau) \Theta(\epsilon_{\beta}) - \Theta(-\tau) \Theta(-\epsilon_{\beta})]. \quad (2.109)$$

2. QUANTUM FIELD THEORY FOR CONDENSED MATTER

Thus, in contrast to real time, the Feynman propagator is a decaying and non-oscillating function in imaginary time τ . This is a favorable property for practical calculations allowing for accurate representations of G^0 on coarse imaginary time grids. We exploit this property in chapter 5 extensively.

2.7.1 Finite-Temperature Feynman Propagator

To bridge the gap to statistical physics we follow Ref. 44 and introduce the density matrix of N non-interacting electrons

$$\hat{\rho}_0 = \frac{e^{-\beta\hat{H}_0}}{Z_0(\beta)}, \quad Z_0(\beta) = \sum_{\mu=0}^{\infty} \langle \Psi_{\mu} | e^{-\beta\hat{H}_0} | \Psi_{\mu} \rangle. \quad (2.110)$$

with the zero-temperature limit $\beta \rightarrow \infty$ given by

$$\lim_{\beta \rightarrow \infty} \hat{\rho}_0 = |\Psi_0\rangle \langle \Psi_0|. \quad (2.111)$$

For further reference the notation $\langle \cdot \rangle_{\beta}$ is introduced to indicate ensemble averages w.r.t. the non-interacting system

$$\langle \hat{O}(\tau) \rangle_{\beta} = \sum_{\mu=0}^{\infty} \langle \Psi_{\mu} | \hat{\rho}_0 \hat{O}(\tau) | \Psi_{\mu} \rangle = \text{Tr} \left\{ \hat{\rho}_0 \hat{O}(\tau) \right\} \quad (2.112)$$

for an operator \hat{O} . Then (2.109) is the zero-temperature limit $\beta \rightarrow \infty$ of the non-interacting finite-temperature Green's function

$$G^0(\mathbf{r}', \mathbf{r}, \tau) = - \left\langle \hat{T} \hat{\psi}(\mathbf{r}, \tau) \hat{\psi}^{\dagger}(\mathbf{r}', 0) \right\rangle_{\beta}. \quad (2.113)$$

We use the same symbol G^0 for both, the zero and finite-temperature Green's function, because the former can always be recovered from the latter by taking the limit $\beta \rightarrow \infty$.

Considering the finite-temperature case has the advantage of exploiting the property, see Ref. 30, 45,

$$G^0(\mathbf{r}', \mathbf{r}, \tau + \beta) = -G^0(\mathbf{r}', \mathbf{r}, \tau), \quad (2.114)$$

2.7 Imaginary Time and Statistical Physics

which follows from the antiperiodicity of the trace¹

$$\begin{aligned}
\left\langle \hat{\psi}(\mathbf{r}, \tau + \beta) \hat{\psi}^\dagger(\mathbf{r}') \right\rangle_\beta &= \frac{1}{Z_0(\beta)} \text{Tr} \left\{ e^{-\beta \hat{H}_0} e^{(\beta + \tau) \hat{H}_0} \hat{\psi}(\mathbf{r}) e^{-(\beta + \tau) \hat{H}_0} \hat{\psi}^\dagger(\mathbf{r}') \right\} \\
&= \frac{1}{Z_0(\beta)} \text{Tr} \left\{ e^{\tau \hat{H}_0} \hat{\psi}(\mathbf{r}) e^{-\tau \hat{H}_0} e^{-\beta \hat{H}_0} \hat{\psi}^\dagger(\mathbf{r}') \right\} \\
&= \frac{1}{Z_0(\beta)} \text{Tr} \left\{ e^{-\beta \hat{H}_0} \hat{\psi}^\dagger(\mathbf{r}') e^{\tau \hat{H}_0} \hat{\psi}(\mathbf{r}) e^{-\tau \hat{H}_0} \right\} \\
&= \left\langle \hat{\psi}^\dagger(\mathbf{r}') \hat{\psi}(\mathbf{r}, \tau) \right\rangle_\beta = - \left\langle \hat{T} \hat{\psi}(\mathbf{r}, \tau) \hat{\psi}^\dagger(\mathbf{r}') \right\rangle_\beta, \quad \tau < 0.
\end{aligned} \tag{2.115}$$

It can be shown, see Ref. 45, that the orbital representation of the finite temperature Green's function is given by

$$G^0(\mathbf{r}', \mathbf{r}, \tau) = - \sum_\alpha \phi_\alpha(\mathbf{r}) \phi_\alpha^*(\mathbf{r}') e^{-\epsilon_\alpha \tau} [\Theta(\tau)(1 - f_\beta(\epsilon_\alpha)) - \Theta(-\tau)f_\beta(\epsilon_\alpha)], \tag{2.116}$$

where f_β is the Fermi occupancy function

$$f_\beta(\epsilon) = \frac{1}{e^{\beta\epsilon} + 1}. \tag{2.117}$$

The convergence of the finite-temperature Green's function G^0 is guaranteed only for the interval $-\beta \leq \tau \leq \beta$. One, therefore, continues $G^0(\tau)$ antiperiodically onto the complete real line, so that the function can be decomposed into a Fourier series

$$G^0(\mathbf{r}', \mathbf{r}, \tau) = \frac{1}{\beta} \sum_{n=-\infty}^{\infty} e^{-i\omega_n \tau} G^0(\mathbf{r}', \mathbf{r}, i\frac{\pi n}{\beta}), \tag{2.118}$$

with coefficients

$$G^0(\mathbf{r}', \mathbf{r}, i\frac{\pi n}{\beta}) = \frac{1}{2} \int_{-\beta}^{\beta} d\tau e^{i\frac{\pi n}{\beta} \tau} G^0(\mathbf{r}', \mathbf{r}, \tau), \quad n \in \mathbb{Z} \tag{2.119}$$

In the zero-temperature limit $\beta \rightarrow \infty$, the Fourier spectrum becomes continuous $i\frac{\pi n}{\beta} \rightarrow i\omega$ and take arbitrary values on the imaginary frequency axis $i\omega$. Consequently, in agreement with Fourier analysis, the series representation (2.118) becomes a Fourier integral

$$G^0(\mathbf{r}', \mathbf{r}, \tau) = \frac{1}{2\pi} \int_{-\infty}^{\infty} d\omega e^{-i\omega \tau} G^0(\mathbf{r}', \mathbf{r}, i\omega), \quad \beta \rightarrow \infty. \tag{2.120}$$

¹The same follows for $\tau > 0$.

2. QUANTUM FIELD THEORY FOR CONDENSED MATTER

We emphasize that on the imaginary frequency axis the Green's function is well-behaved, due to

$$G^0(\mathbf{r}', \mathbf{r}, i\omega) = \sum_{\alpha} \frac{\phi_{\alpha}(\mathbf{r})\phi_{\alpha}^*(\mathbf{r}')}{i\omega - \epsilon_{\alpha}}, \quad (2.121)$$

and no branch cut is crossed when approaching $\omega \rightarrow \epsilon_{\alpha}$ as in the case for real frequencies, see section 2.4.1. Hence, the imaginary frequency integration in Eq. (2.120) can be carried out straightforwardly and a deformation of the integration contour, as in (2.68), is not necessary.

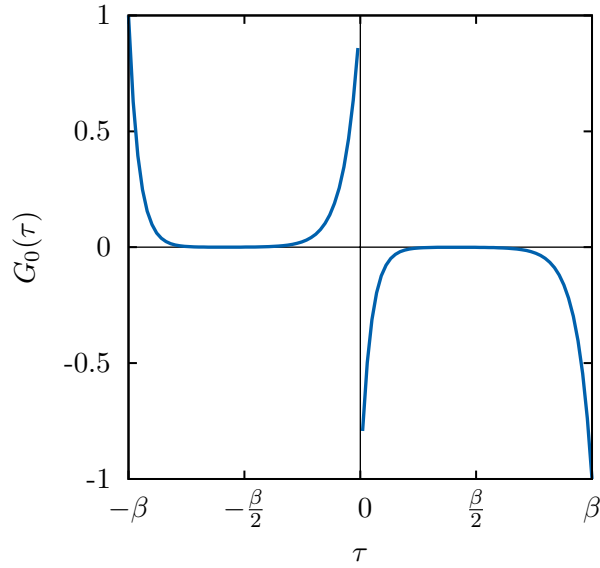


Figure 2.3: Typical imaginary time-dependence of the non-interacting propagator G^0 illustrating the anti-periodicity property (2.114). Here a two-state model with one occupied state with energy $\epsilon_1 = -1.5$ eV and an unoccupied state with energy $\epsilon_2 = 2.3$ eV for a inverse temperature of $\beta = 10$ eV $^{-1}$ is shown.

For finite temperatures, however, it is sufficient to restrict the imaginary time interval either to $0 \leq \tau \leq \beta$ or to $-\frac{\beta}{2} \leq \tau \leq \frac{\beta}{2}$, as shown in Fig. 2.3. In this work we exclusively use the former interval $0 \leq \tau \leq \beta$, where the representations (2.118) and (2.119) read

$$G^0(\mathbf{r}', \mathbf{r}, \tau) = \frac{1}{\beta} \sum_{n=-\infty}^{\infty} e^{-i\omega_n \tau} G^0(\mathbf{r}', \mathbf{r}, i\omega_n) \quad (2.122)$$

$$G^0(\mathbf{r}', \mathbf{r}, i\omega_n) = \int_0^{\beta} d\tau e^{i\omega_n \tau} G^0(\mathbf{r}', \mathbf{r}, \tau), \quad n \in \mathbb{Z} \quad (2.123)$$

2.7 Imaginary Time and Statistical Physics

and the discrete Fourier spectrum $i\omega_n$ is restricted to the *fermionic Matsubara frequencies*

$$\omega_n = \frac{(2n-1)\pi}{\beta}, \quad n \in \mathbb{Z}. \quad (2.124)$$

This follows from Eqs. (2.118) and (2.119) by shifting the integration variable on the interval $[-\beta, 0]$ in Eq. (2.119) to $\tau \rightarrow \tau + \beta$ and using property (2.114), see Ref. 45.

2.7.2 Statistical Physics and Imaginary Time

One introduces the interacting partition function $Z(\beta)$ and the corresponding density operator $\hat{\rho}$ of the system

$$Z(\beta) = \text{Tr} \left\{ e^{-\beta\hat{H}} \right\}, \quad \hat{\rho} = \frac{\exp(-\beta\hat{H})}{Z(\beta)} \quad (2.125)$$

where the trace is evaluated w.r.t. the interacting eigenstates $|\Omega_\mu\rangle$. This partition function can be used to compute the ensemble average $\text{Tr} \left\{ \rho \hat{O}_H(\tau) \right\}$ of an arbitrary Heisenberg-operator

$$\hat{O}_H(\tau) = e^{\beta\hat{H}} \hat{O} e^{-\beta\hat{H}}. \quad (2.126)$$

With the help of the Gell-Mann and Low theorem and the property

$$e^{-\beta\hat{H}} = e^{-\beta\hat{H}_0} \underbrace{\hat{S}(-i\beta, 0)}_{=\hat{S}(\beta)} = Z_0(\beta) \hat{\rho}_0 \hat{S}(\beta), \quad (2.127)$$

see Refs. 45, 46,¹ the trace w.r.t. interacting eigenstates $|\Omega_\mu\rangle$ can be rewritten into a trace w.r.t. to the non-interacting eigenstates $|\Psi_\mu^{(N)}\rangle$. For instance, the partition function $Z(\beta)$ can be expressed as

$$Z(\beta) = Z_0(\beta) \text{Tr} \left\{ \hat{\rho}_0(\beta) \hat{S}(\beta) \right\} = Z_0(\beta) \left\langle \hat{S}(\beta) \right\rangle_\beta \quad (2.128)$$

to separate the grand partition function into

$$Z(\beta) = Z_0(\beta) Z_v(\beta) \quad (2.129)$$

with the interacting part $Z_v(\beta)$ given by

$$Z_v(\beta) = \left\langle \hat{S}(\beta) \right\rangle_\beta. \quad (2.130)$$

¹ Eq. (2.127) follows from analytic continuation of (2.77) using $t \rightarrow -i\beta$.

2. QUANTUM FIELD THEORY FOR CONDENSED MATTER

Alternatively, the grand canonical potential Φ of the system can be written as

$$\Phi = -\frac{1}{\beta} \ln Z(\beta) = -\frac{1}{\beta} [\ln Z_0(\beta) + \ln Z_v(\beta)] = \Phi_0 + \Phi_v \quad (2.131)$$

or the internal energy E of the system can be computed via

$$E = -\frac{\partial}{\partial \beta} \ln Z(\beta) = -\frac{\partial}{\partial \beta} [\ln Z_0(\beta) + \ln Z_v(\beta)] = \langle \hat{H}_0 \rangle_\beta + \frac{Z_0(\beta)}{Z_v(\beta)} \langle \hat{S}(\beta) \hat{V} \rangle_\beta. \quad (2.132)$$

In particular, one obtains for the zero-temperature limit $\beta \rightarrow \infty$, a representation of the interacting groundstate energy

$$\Omega_0 = \lim_{\beta \rightarrow \infty} E = \underbrace{\langle \Psi_0 | \hat{H}_0 | \Psi_0 \rangle}_{E_0} + \frac{\langle \Psi_0 | \hat{T} e^{-\int_0^\infty d\tau \hat{V}(\tau)} \hat{V} | \Psi_0 \rangle}{\langle \Psi_0 | \hat{T} e^{-\int_0^\infty d\tau \hat{V}(\tau)} | \Psi_0 \rangle}. \quad (2.133)$$

It is interesting to compare this expression with the Gell-Mann and Low expression for the interacting eigenenergies (2.101). It is not difficult to show, see [44, 46], that in general thermal averages of Heisenberg-operators (2.126) can be expressed as

$$\text{Tr} \left\{ \rho \hat{O}_H(\tau) \right\} = \sum_{\mu=0}^{\infty} \langle \Omega_\mu | \hat{\rho} \hat{O}_H(\tau) | \Omega_\mu \rangle = \frac{\langle \hat{S}(\beta) \hat{T} \hat{O}(\tau) \rangle_\beta}{\langle \hat{S}(\beta) \rangle_\beta}. \quad (2.134)$$

In general, all observables are expressible in terms of field and conjugate field operators $\hat{\psi}, \hat{\psi}^\dagger$.¹ Therefore, it is convenient to introduce the generating functional of QFT, following Refs. 39, 47,

$$\mathcal{W}[j, j^*] = \ln \left\{ \left\langle \hat{S}(\beta) \hat{T} e^{-\int_0^\beta d\tau \int d\mathbf{r} (j^\dagger(\mathbf{r}, \tau) \hat{\psi}(\mathbf{r}, \tau) + \hat{\psi}(\mathbf{r}, \tau) j^*(\mathbf{r}, \tau))} \right\rangle_\beta \right\} \quad (2.135)$$

from which arbitrary expectation values of the interacting system can be calculated as functional derivatives w.r.t. source fields j, j^* . Specifically, the interacting finite-temperature propagator G , discussed in detail in chapter 4.1.1, can be written as

$$G(\mathbf{r}', \mathbf{r}, \tau) = \sum_{\mu=0}^{\infty} \langle \Omega_\mu | \hat{\rho} \hat{T} \hat{\psi}_H(\mathbf{r}, \tau) \psi_H^\dagger(\mathbf{r}') | \Omega_\mu \rangle \quad (2.136)$$

$$= - \frac{\delta^2 \mathcal{W}[j, j^*]}{\delta j^*(\mathbf{r}') \delta j(\mathbf{r}, \tau)} \Big|_{j, j^*=0} \quad (2.137)$$

$$= - \frac{\langle \hat{S}(\beta) \hat{T} \hat{\psi}(\mathbf{r}, \tau) \psi^\dagger(\mathbf{r}') \rangle_\beta}{\langle \hat{S}(\beta) \rangle_\beta}. \quad (2.138)$$

¹Similarly in classical Hamiltonian mechanics, every observable is expressible in terms of conjugate variables q, p .

2.7 Imaginary Time and Statistical Physics

All expressions so far are exact. However, in practice one has to evaluate the interacting expectation values (2.134) perturbatively. For this purpose the diagrammatic method is introduced in the following section.

2. QUANTUM FIELD THEORY FOR CONDENSED MATTER

3

Many-Body Perturbation Theory

3.1 Perturbation Series of the Grand Canonical Potential

Due to the complex structure of Eq. (2.128) it is hopeless to evaluate the grand canonical potential Φ with Eq. (2.131) exactly. The same holds true for the zero-temperature case¹

$$\Omega_0 = \lim_{\beta \rightarrow \infty} \Phi, \quad (3.1)$$

so that one has to rely on approximations. Fortunately, the expressions for the partition function and canonical potential, presented in the previous section, provide a good starting point.

For this purpose one expands the exponential in the interacting partition function $Z_v(\beta)$, defined in Eq. (2.130), into a series

$$Z_v(\beta) = \left\langle \hat{S}(\beta) \right\rangle_{\beta} = \left\langle \hat{T} e^{-\int_0^{\beta} d\tau \hat{V}(\tau)} \right\rangle_{\beta} \quad (3.2)$$

allows for a perturbative treatment of the interacting degrees of freedom. In particular,

¹This identity holds true, due to our convention $\mu = 0$.

3. MANY-BODY PERTURBATION THEORY

the zeroth, first and second order terms read

$$Z_v^{(0)} = \langle 1 \rangle_\beta = 1 \quad (3.3)$$

$$Z_v^{(1)} = - \int_0^\beta d\tau \langle \hat{T} \hat{V}(\tau) \rangle_\beta \quad (3.4)$$

$$Z_v^{(2)} = \frac{1}{2} \int_0^\beta d\tau_1 d\tau_2 \langle \hat{T} \hat{V}(\tau_1) \hat{V}(\tau_2) \rangle_\beta \quad (3.5)$$

and the n order term is

$$Z_v^{(n)} = \frac{(-1)^n}{n!} \int_0^\beta d\tau_1 \cdots d\tau_n \langle \hat{T} \hat{V}(\tau_1) \cdots \hat{V}(\tau_n) \rangle_\beta \quad (3.6)$$

Inserting this expansion into Eq. (2.131) one obtains an approximative formula for the interacting part Φ_v of the grand canonical potential

$$\Phi_v = -\frac{1}{\beta} \ln Z_v(\beta) = -\frac{1}{\beta} \ln \left(1 + Z_v^{(1)} + Z_v^{(2)} \cdots \right). \quad (3.7)$$

In summary, the perturbation series of the grand canonical potential reduces to the evaluation of time-ordered matrix elements of products of Coulomb operators \hat{V} . In the following section, we discuss the evaluation of these expectation values in detail.

3.1.1 The Wick Theorem

The Coulomb operator can be written in terms of two-particle integrals

$$V^{\alpha\beta\gamma\delta} = q^2 \int d\mathbf{r} d\mathbf{r}' \frac{\phi_\alpha^*(\mathbf{r}) \phi_\beta^*(\mathbf{r}') \phi_\gamma(\mathbf{r}') \phi_\delta(\mathbf{r})}{|\mathbf{r} - \mathbf{r}'|} = \langle \phi_\alpha, \phi_\beta | \hat{V} | \phi_\delta, \phi_\gamma \rangle, \quad (3.8)$$

and the creation and annihilation operators

$$\hat{V}(\tau) = \frac{1}{2} V^{\alpha\beta\gamma\delta} \hat{c}_\alpha^\dagger(\tau) \hat{c}_\beta^\dagger(\tau) \hat{c}_\gamma(\tau) \hat{c}_\delta(\tau). \quad (3.9)$$

This follows from the normal-ordered operator (2.70) and the transformation rules (2.30) and (2.31). As in the last expression we adopt the Einstein summation convention in the following. Within this convention, the first order term of the partition function (3.4) is

$$Z_v^{(1)} = - \int_0^\beta d\tau \langle \hat{T} \hat{V}(\tau) \rangle_\beta = -\frac{1}{2} V^{\alpha\beta\gamma\delta} \int_0^\beta d\tau \langle \hat{T} \hat{c}_\alpha^\dagger(\tau) \hat{c}_\beta^\dagger(\tau) \hat{c}_\gamma(\tau) \hat{c}_\delta(\tau) \rangle_\beta. \quad (3.10)$$

3.1 Perturbation Series of the Grand Canonical Potential

Suppressing the imaginary time dependence τ_i for the operators $\hat{c}_{\alpha_i}^\dagger, \dots, \hat{c}_{\delta_i}$ for the time being, the n^{th} order term (3.6) of the partition function reads

$$Z_v^{(n)}(\beta) = \frac{(-1)^n}{n!} \frac{V^{\alpha_1 \beta_1 \gamma_1 \delta_1} \dots V^{\alpha_n \beta_n \gamma_n \delta_n}}{2^n} \int_0^\beta d\tau_1 \dots d\tau_n \left\langle \hat{T} \hat{c}_{\alpha_1}^\dagger \dots \hat{c}_{\delta_n} \right\rangle_\beta. \quad (3.11)$$

Let us consider the zero-temperature limit $\beta \rightarrow \infty$ of this expression for a moment. In this limit the ensemble operator $\hat{\rho}_0$ reduces to the groundstate projector (2.111) and

$$\left\langle \hat{T} \hat{c}_{\alpha_1}^\dagger \dots \hat{c}_{\delta_n} \right\rangle_\infty = \langle \Psi_0 | \hat{T} \hat{c}_{\alpha_1}^\dagger \dots \hat{c}_{\delta_n} | \Psi_0 \rangle, \quad 0 < \tau_1, \dots, \tau_n < \infty \quad (3.12)$$

holds. To evaluate the r.h.s. one needs the Wick theorem, which uses the contraction of two operators. This contraction is defined as

$$\overline{\hat{O}(\tau_1) \hat{O}(\tau_2)} = \hat{T} \hat{O}(\tau_1) \hat{O}(\tau_2) - : \hat{O}(\tau_1) \hat{O}(\tau_2) :, \quad (3.13)$$

where the normal ordering operator $: \cdot :$ was introduced in Eq. (2.28). Specifically, for the contraction of an annihilation and creation operator one obtains when applied to the groundstate

$$\begin{aligned} \langle \Psi_0 | \overline{\hat{c}_\alpha(\tau_1) \hat{c}_\beta^\dagger(\tau_2)} | \Psi_0 \rangle &= \langle \Psi_0 | \hat{T} \hat{c}_\alpha(\tau_1) \hat{c}_\beta^\dagger(\tau_2) - : \hat{c}_\alpha(\tau_1) \hat{c}_\beta^\dagger(\tau_2) : | \Psi_0 \rangle \\ &= \underbrace{\langle \Psi_0 | \hat{T} \hat{c}_\alpha(\tau_1) \hat{c}_\beta^\dagger(\tau_2) | \Psi_0 \rangle}_{=-G_{\beta\alpha}^0(\tau_1 - \tau_2)} - 0, \end{aligned} \quad (3.14)$$

since the normal ordered product vanishes when acting on the Fermi vacuum, see Eqs. (2.36) and (2.37). Here the object on the r.h.s. of Eq. (3.14) is the well-known non-interacting Feynman propagator G^0 in the one-particle basis

$$G_{\beta\alpha}^0(\tau_1 - \tau_2) = \int d^3\mathbf{r} d^3\mathbf{r}' \phi_\alpha(\mathbf{r}') G^0(\mathbf{r}', \mathbf{r}, \tau_1 - \tau_2) \phi_\beta^*(\mathbf{r}), \quad (3.15)$$

where it is diagonal

$$G_{\alpha\beta}^0(\tau) = -\delta_{\alpha\beta} e^{-\epsilon_\alpha \tau} [\Theta(\tau) \Theta(\epsilon_\alpha) - \Theta(-\tau) \Theta(-\epsilon_\alpha)] \equiv \delta_{\alpha\beta} G_\alpha^0(\tau). \quad (3.16)$$

With this definitions the Wick theorem can be formulated in the following way, see Refs. 34, 46.

3. MANY-BODY PERTURBATION THEORY

Theorem 3.1.1 (Wick Theorem) *A time-ordered product of operators $\hat{O}_i = \hat{O}(t_i)$ in the interaction picture, can be decomposed into a normal-ordered sum of all possible contractions, i.e.*

$$\begin{aligned} \hat{T}(\hat{O}_1 \hat{O}_2 \cdots \hat{O}_n) &= : \overbrace{\hat{O}_1 \hat{O}_2 \hat{O}_3 \cdots \hat{O}_n} : + : \overbrace{\hat{O}_1 \hat{O}_2 \hat{O}_3} \overbrace{\hat{O}_4 \cdots \hat{O}_n} : \\ &+ : \overbrace{\hat{O}_1 \hat{O}_2 \hat{O}_3 \hat{O}_4 \cdots \hat{O}_n} : + \cdots \end{aligned} \quad (3.17)$$

The proof of this statement can be found in every good book about QFT, for instance Refs. 34, 46, and will not be given here.

The Wick theorem is a powerful utility when applied to the r.h.s. of Eq. (3.12). On the one side, only contractions between creation and annihilation operators remain, due to the orthogonality of the Slater determinants

$$\langle \Psi_\mu^{(N)} | \Psi_\nu^{(M)} \rangle = \delta_{NM} \delta_{\mu\nu}. \quad (3.18)$$

On the other side, only fully contracted terms survive, because terms like

$$: \overbrace{\hat{c}_\alpha^\dagger \hat{c}_\beta^\dagger \hat{c}_\gamma \hat{c}_\delta} := - : \hat{c}_\alpha^\dagger \hat{c}_\gamma \hat{c}_\beta^\dagger \hat{c}_\delta := - \overbrace{\hat{c}_\alpha^\dagger \hat{c}_\gamma} : \hat{c}_\beta^\dagger \hat{c}_\delta : \quad (3.19)$$

vanish when evaluated for the groundstate

$$\langle \Psi_0 | - \overbrace{\hat{c}_\alpha^\dagger \hat{c}_\gamma} : \hat{c}_\beta^\dagger \hat{c}_\delta : | \Psi_0 \rangle = 0. \quad (3.20)$$

Evidently, all orders of the interacting energy Ω_0 at zero-temperature in Eq. (3.1) are expressible in terms of the non-interacting Green's function G_α^0 and the Coulomb matrix elements $V_{\alpha\beta\gamma\delta}$.

This conclusion relies on the Fermi vacuum properties (2.36) and (2.37), implying Eq. (3.14), and is not valid a priori for finite-temperatures $\beta < \infty$. This is due to the presence of excited Slater determinants $|\Psi_\mu^{(N)}\rangle$ in the thermal averages $\langle \cdots \rangle_\beta$. However, one can show that all normal-ordered thermal averages $\langle : \hat{c}_\alpha \hat{c}_\beta^\dagger : \rangle_\beta$ vanish in the thermodynamic limit, see Ref. 46, and consequently Eq. (3.14) is ultimately valid also for finite β .

Equipped with this knowledge, we evaluate the first two orders of the partition function $Z_v(\beta)$ given in Eqs. (3.3)-(3.5) in the next section using the diagrammatic method.

3.2 Feynman Diagrams

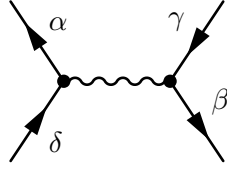


Figure 3.1: Labeled diagram for the interaction matrix element $G_\alpha^0 G_\beta^0 V^{\alpha\beta\gamma\delta} G_\gamma^0 G_\delta^0$.

3.2 Feynman Diagrams

We start with the first order term $Z_v^{(1)}$ given in Eq. (3.4). Using the Wick theorem 3.17 and suppressing the τ -dependence in the notation, the corresponding interaction matrix elements (3.10) can be written as

$$\left\langle \hat{T} \hat{c}_\alpha^\dagger \hat{c}_\beta^\dagger \hat{c}_\gamma \hat{c}_\delta \right\rangle_\beta = - \underbrace{\left\langle \hat{T} \hat{c}_\gamma \hat{c}_\alpha^\dagger \right\rangle_\beta}_{-G_{\alpha\gamma}^0(0)} \underbrace{\left\langle \hat{T} \hat{c}_\delta \hat{c}_\beta^\dagger \right\rangle_\beta}_{-G_{\beta\delta}^0(0)} + \underbrace{\left\langle \hat{T} \hat{c}_\delta \hat{c}_\alpha^\dagger \right\rangle_\beta}_{-G_{\alpha\delta}^0(0)} \underbrace{\left\langle \hat{T} \hat{c}_\beta \hat{c}_\gamma^\dagger \right\rangle_\beta}_{-G_{\beta\gamma}^0(0)}. \quad (3.21)$$

Hence the first order term of the partition function reads

$$Z_v^{(1)} = -\frac{\beta}{2} \left(G_\alpha^0(0) G_\beta^0(0) V^{\alpha\beta\alpha\beta} - G_\alpha^0(0) G_\beta^0(0) V^{\alpha\beta\beta\alpha} \right). \quad (3.22)$$

Here, we note that the quantity $G_\alpha^0(0)$ is always evaluated as $\lim_{\tau \nearrow 0} G_\alpha^0(\tau)$ and corresponds to the density matrix.

It is convenient to visualize specific contractions, including those above, with the help of diagrams, originally proposed by Feynman to evaluate matrix elements in QED, see Ref. 48. This method is adopted as follows. Green's functions G_α^0 are represented by directed lines $\xrightarrow{\alpha}$ and interaction matrix elements $V^{\alpha\beta\gamma\delta}$ by wiggly lines \sim . Particle lines attach to interaction lines at vertices, represented by dots \bullet , as shown in Fig. 3.1. Typically, the horizontal direction represents time, whereas the vertical direction stands for spatial coordinates. However, as one shall see in a moment, only the topology of the diagrams is important, so that in the end it does not matter whether the diagrams are drawn vertically or horizontally.

Using these prescriptions the two terms in Eq. (3.22) can be visualized as shown in Fig. 3.2 and are called Hartree and Fock diagrams. These names come from the facts that, the two terms in Eq. (3.22) assume the form of the Fock-exchange $\langle \phi_\alpha \phi_\beta | |\mathbf{r} - \mathbf{r}'|^{-1} | \phi_\beta \phi_\alpha \rangle$ and the Hartree energy $\langle \phi_\alpha \phi_\beta | |\mathbf{r} - \mathbf{r}'|^{-1} | \phi_\alpha \phi_\beta \rangle$ [compare to section 1.1].

To gain more insight, one proceeds with the evaluation of higher order terms of the partition function, however, this must be done carefully. The naive application of the

3. MANY-BODY PERTURBATION THEORY

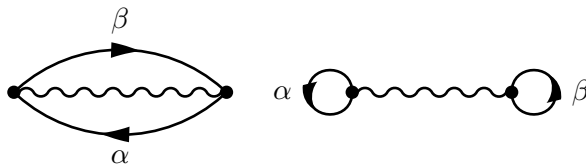


Figure 3.2: Hartree (right) and Fock diagram (left).

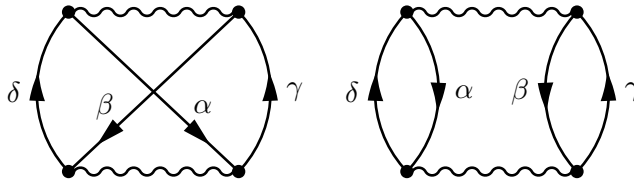


Figure 3.3: Ladder (left) and bubble (right) contraction as labeled diagrams.

Wick theorem to each term of the perturbation series (3.11) is problematic, since the number of non-zero contractions increases exponentially with order n . For instance in second order, there are 24 non-trivial contributions, two of them are shown in Fig. 3.3. For $n = 3$ one has $6 \times 5 \times 4 \times 3 \times 2 = 720$ possible contributions and in general for order n there are in total $(2n)!$ labeled diagrams, see Ref. 32, 39. To deal with this large number of different contractions we follow Negele and Orland and consider two different symmetries.

On the one side, one can exploit the symmetry of the interaction matrix elements

$$V^{\alpha\beta\gamma\delta} = V^{\beta\alpha\delta\gamma}, \quad (3.23)$$

which follows from the change of the spatial integration variable in Eq. (3.8). This property implies that two labeled diagrams are equivalent, if the exchange of two incoming and outgoing particle lines at one vertex yields topologically the same diagram. In total there are 2^n possible exchanges for a diagram with n interaction lines. On the other side, one obtains the same contribution if two permutations $\sigma, \sigma' \in S^n$ of the time integration variables $\tau_{\sigma(1)}, \dots, \tau_{\sigma(n)}$ and $\tau_{\sigma'(1)}, \dots, \tau_{\sigma'(n)}$ yield the same diagram. For n interactions this yields $n!$ possible permutations. In the following, these symmetries are considered from a more general point of view to deduce a simple summation rule for diagrams.

A general transformation θ from one diagram γ to another diagram $\theta\gamma = \gamma'$ is a combination of (3.23) and permutations in $\tau_1 \dots \tau_n$. The set of all possible transformations θ yields a group Γ and has $2^n n!$ elements in total. We call two transformations $\theta, \theta' \in \Gamma$ equivalent $\theta \simeq \theta'$, if they transform topologically into the same graph, that is

3.2 Feynman Diagrams

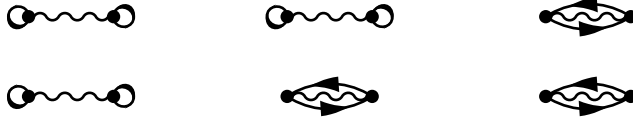


Figure 3.4: Disconnected unlabeled diagrams in second order. The symmetry factors (from left to right) are 8, 4 and 8.

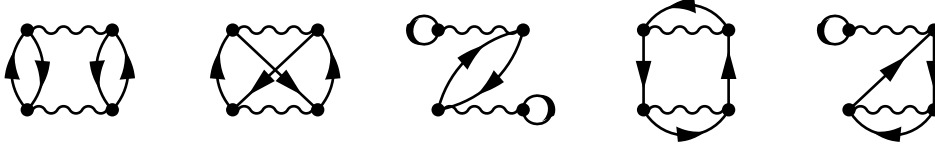


Figure 3.5: Second order irreducible, connected diagrams. With symmetry factors 4, 4, 2, 2, 1 (from left to right).

$\theta\gamma$, $\theta'\gamma$ and γ yield the same contribution to the partition function $Z(\beta)$. This defines equivalence classes H_γ , and S_γ denotes the number of elements in H_γ , i.e. the number of topologically equivalent diagrams contained in H_γ . Because H_γ is a subgroup of Γ , S_γ must be a divisor of $2^n n!$ and $2^n n! / S_\gamma \in \mathbb{N}$. Then the diagram γ appears $2^n n! / S_\gamma$ times for order n , resulting in an effective $1/S_\gamma$ symmetry factor in the partition function $Z(\beta)$ for the equivalence class of γ . The diagram γ defining the equivalence class H_γ is called *irreducible* and is represented by an *unlabeled* diagram, where the indices $\alpha, \beta \dots$ of the wiggly and particle lines are suppressed.

In practice, one, therefore, translates only the irreducible diagrams for a given order into integrals and multiplies the result by the corresponding symmetry factor $1/S_\gamma$. As an consistency check, one may use the following sum rule, valid for each order

$$\sum_{\gamma} \frac{1}{S_\gamma} = \frac{(2n)!}{n!2^n} = (2n-1)(2n-3)(2n-5)\dots = (2n-1)!!, \quad (3.24)$$

where the sum on the r.h.s. is over all irreducible (topologically equivalent) diagrams for order n .

As an example we show in Figs. 3.5 and 3.4 all irreducible graphs for the second order with the corresponding symmetry factors. For instance the symmetry property of Eq. (3.23) yields $2 \times 2 = 4$ identical contributions for the first diagram in Fig. 3.4 and for each contribution there are only 2 possible rearrangements of the integration variables τ_1, τ_2 yielding topologically the same diagram, so that in total a symmetry

3. MANY-BODY PERTURBATION THEORY

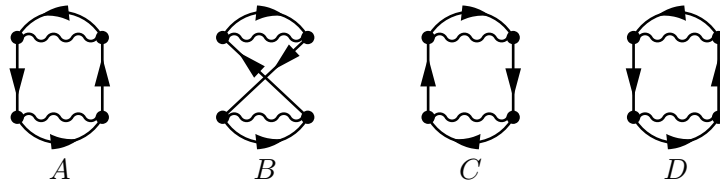


Figure 3.6: Illustration of the symmetry factor of diagram A . Diagram B is obtained from A using Eq. (3.23) for the upper interaction line, whereas diagram C follows from B using the same identity for the lower one and diagram D is obtained from C after exchanging $\tau_1 \leftrightarrow \tau_2$. Only diagram A and D belong to the same equivalence class with symmetry factor $S_\gamma = 2$, because they are topologically the same directed graph.

factor of $S_\gamma = 2^3 = 8$ is obtained. The fourth diagram in Fig. 3.5 has a symmetry factor of $S_\gamma = 2$, because there is only one symmetry operation giving the same result: The exchange of both horizontal vertices (using Eq. (3.23)) combined with a change of the integration variables $\tau_1 \leftrightarrow \tau_2$. This symmetry operation is illustrated in Fig. 3.6. Analogously, the symmetry factors of other diagrams are obtained, see Ref. 39 for a comprehensive discussion. In summary, the 24 labeled diagrams for $n = 2$ can be grouped into 8 equivalence classes H_γ and the sum over all inverse symmetry factors $1/S_\gamma$, see caption of Figs. 3.5 and 3.4, yields 3 and satisfies Eq. (3.24).

One can reduce the relevant number of diagrams even further using the so-called *linked cluster theorem*. This theorem was published by Goldstone in Ref. 49 and proved for the groundstate energy at zero temperature. However, it can be shown that a similar theorem holds for finite temperatures, see Ref. 46. Here we present the linked cluster theorem as formulated by Abrikosov *et al.*

Theorem 3.2.1 (Linked Cluster Theorem) *The perturbation series of $\ln Z_\beta$ contains only connected diagrams.*

Diagrams as in Fig. 3.4, which separate into smaller order subdiagrams, are called *disconnected*, whereas those in Fig. 3.5, are named *connected*. Hence, only connected, topologically distinct contractions need to be determined for the perturbative analysis of the grand canonical potential Φ .

We summarize the results of this section by formulating following Feynman rules for the diagrammatic expansion of the grand canonical potential. Similar rules for the Fourier domain can be found elsewhere, see for instance Refs. 34, 39, 46, and are not discussed here.

3.2 Feynman Diagrams

Feynman rules in one-particle basis

- f1 Draw all connected, topologically distinct diagrams for each order n .
- f2 Assign an imaginary time τ and an one-particle index α to each particle line and include the factor $G_\alpha^0(\tau)$.
- f3 For each interaction line include the factor $V^{\alpha\beta\gamma\delta}$.
- f4 Multiply the result by the factor $\frac{(-1)^n(-1)^l}{S_\gamma}$, where l is the number of closed particle loops and S_γ the symmetry factor of the graph.¹
- f5 Integrate over imaginary times in $[0, \beta]$ and sum over all one-particle indices.

In analogy to the one-particle basis, similar Feynman rules can be formulated in position space and imaginary time.

Feynman rules for spacetime domain

- F1 Draw all connected, topologically distinct diagrams for each order n .
- F2 Assign a spacetime point $x = (\mathbf{r}, \tau)$ to each vertex.
- F3 For each wiggly line starting at $x' = (\mathbf{r}', \tau')$ and ending in $x = (\mathbf{r}, \tau)$ assign a factor $\frac{\delta(\tau - \tau')}{|\mathbf{r} - \mathbf{r}'|}$. Analogously, assign a factor $G^0(\mathbf{r}', \mathbf{r}, \tau - \tau')$ to each particle line originating in x' and ending in x .
- F4 Multiply the result by the factor $\frac{(-1)^n(-1)^l}{S_\gamma}$, where l is the number of closed particle loops and S_γ the symmetry factor of the graph.
- F5 Integrate over spacetime points x in the domain $[0, \beta] \times C$, where C is the unit cell.

Both sets of rules hold for the zero-temperature case as well, with the difference that finite-temperature propagators are replaced by their zero-temperature limit and integration is performed over $[0, \infty)$.

Nevertheless, the number of distinct, irreducible and connected diagrams becomes huge and intractable with increasing order. Even worse, often diagrams, such as the

¹The reason for the loop contribution can be found in Ref. 39.

3. MANY-BODY PERTURBATION THEORY

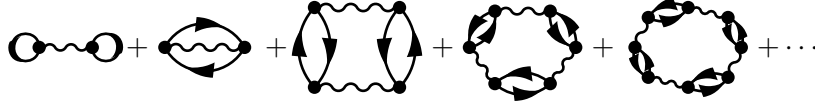


Figure 3.7: Random Phase Approximation for the grand canonical potential.

bubble graphs in Fig. 3.3 diverge for each order in perturbation theory for prototypical systems such as the HEG, see Ref. 33. However, Gell-Mann and Brueckner showed that evaluating the infinite sum of all bubble diagrams yields a finite result, see Ref. 12.

This technique, that is summation over all orders of specific equivalence classes, is the true power of the diagrammatic method. In the following the rules F1-F5 are applied to the subset of all bubble graphs and an approximation for the interacting grand canonical potential is obtained.

3.3 Random Phase Approximation

Restricting the perturbation series of the grand-canonical potential to the subset of all bubble diagrams, see Fig. 3.7, one obtains the so-called random phase approximation (RPA). The RPA is widely used in condensed matter physics today, due to two reasons. First, the RPA yields accurate estimates for the grand canonical potential Φ , respectively the interacting groundstate energy Ω_0 , and becomes exact for the HEG in the asymptotic limit $r_s \approx 0$ yielding an energy density given by Eq. (1.37). Second, the RPA can be calculated with a decent computational effort. The latter is due to its simple expression, which is derived in the following with the methods learned from the previous section.

As a first step, one observes, that the symmetry factor S_γ for each diagram beyond the first order is twice the number of cyclic permutations of $\tau_{\sigma(1)} \cdots \tau_{\sigma(n)}$, so simply $2n$. [39] Second, it is useful to work with the independent-particle polarizability χ^0 , defined by

$$\chi^0(\mathbf{r}', \mathbf{r}, \tau - \tau') = (-1) \times \begin{array}{c} x' \\ \bullet \end{array} \begin{array}{c} \curvearrowright \\ \curvearrowleft \end{array} \begin{array}{c} \bullet \\ x \end{array} = -G^0(\mathbf{r}', \mathbf{r}, \tau - \tau')G^0(\mathbf{r}, \mathbf{r}', \tau' - \tau). \quad (3.25)$$

With this definition and the Feynman rules F1-F5 from previous section, the second

3.3 Random Phase Approximation

and third order diagram can be written as

$$\Phi^{(2)} = -\frac{1}{\beta} \frac{(-1)^2(-1)^2}{4} \int_0^\beta d\tau_1 d\tau_2 \text{Tr} \left[\frac{\chi^0(\mathbf{r}_2, \mathbf{r}_1, \tau_2 - \tau_1) \chi^0(\mathbf{r}_4, \mathbf{r}_3, \tau_1 - \tau_2)}{|\mathbf{r}_1 - \mathbf{r}_4| |\mathbf{r}_2 - \mathbf{r}_3|} \right] \quad (3.26)$$

$$\begin{aligned} \Phi^{(3)} &= -\frac{1}{\beta} \frac{(-1)^3(-1)^3}{6} \int_0^\beta d\tau_1 d\tau_2 d\tau_3 \\ &\times \text{Tr} \left[\frac{\chi^0(\mathbf{r}_2, \mathbf{r}_1, \tau_2 - \tau_1) \chi^0(\mathbf{r}_4, \mathbf{r}_3, \tau_4 - \tau_2) \chi^0(\mathbf{r}_5, \mathbf{r}_6, \tau_4 - \tau_1)}{|\mathbf{r}_1 - \mathbf{r}_6| |\mathbf{r}_2 - \mathbf{r}_3| |\mathbf{r}_4 - \mathbf{r}_5|} \right]. \end{aligned} \quad (3.27)$$

Here Tr indicates spatial integration over all coordinates $\mathbf{r}_1, \mathbf{r}_2, \dots$. Higher order terms contain higher order convolutions in imaginary time.

These expressions can be further simplified by exploiting the periodic property

$$\chi^0(\mathbf{r}', \mathbf{r}, \tau + \beta) = \chi^0(\mathbf{r}', \mathbf{r}, \tau), \quad (3.28)$$

which follows from the antiperiodicity of the non-interacting propagator (2.114) and is illustrated in Fig. 3.8 using the same model for G^0 as in Fig. 2.3. This allows to decompose the independent-particle polarizability χ^0 into a Fourier series

$$\chi^0(\mathbf{r}', \mathbf{r}, \tau) = \frac{1}{\beta} \sum_{m=-\infty}^{\infty} e^{-i\nu_m \tau} \chi^0(\mathbf{r}', \mathbf{r}, i\nu_m) \quad (3.29)$$

with coefficients

$$\chi^0(\mathbf{r}', \mathbf{r}, i\nu_m) = \int_0^\beta d\tau e^{i\nu_m \tau} \chi^0(\mathbf{r}', \mathbf{r}, \tau), \quad m \in \mathbb{Z}. \quad (3.30)$$

Here, the *bosonic Matsubara frequencies*

$$\nu_n = \frac{2m\pi}{\beta}, \quad m \in \mathbb{Z} \quad (3.31)$$

are used in Eqs. (3.29) and (3.30) rather than their fermionic counterparts ω_n . Inserting Eq. (3.29) into Eq. (3.26) and using the completeness relation

$$\int d\tau e^{-i\tau(\nu_m - \nu_{m'})} = \beta \delta_{mm'}, \quad (3.32)$$

the imaginary-time integrals in Eq. (3.26) reduce to a simple Matsubara sum

$$\Phi^{(2)} = -\frac{1}{4\beta} \sum_{n=-\infty}^{\infty} \underbrace{\text{Tr} \left[\frac{\chi^0(\mathbf{r}_2, \mathbf{r}_1, i\nu_n) \chi^0(\mathbf{r}_4, \mathbf{r}_3, i\nu_n)}{|\mathbf{r}_1 - \mathbf{r}_4| |\mathbf{r}_2 - \mathbf{r}_3|} \right]}_{\text{Tr}[\chi^0(i\nu_n)V]^2}. \quad (3.33)$$

3. MANY-BODY PERTURBATION THEORY

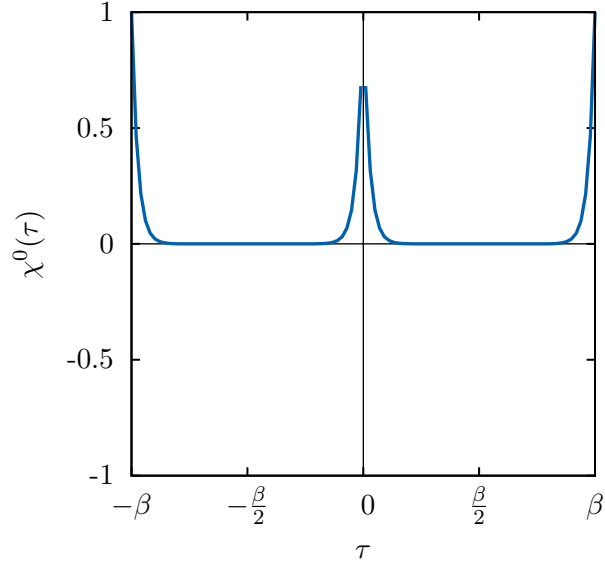


Figure 3.8: Typical imaginary time-dependence of the independent-particle polarizability χ^0 illustrating the periodic property (3.28). Here a two-state model with one occupied state with energy $\epsilon_1 = -1.5$ eV and an unoccupied state with energy $\epsilon_2 = 2.3$ eV for a inverse temperature of $\beta = 10$ eV $^{-1}$ is shown.

The same holds true for arbitrary order

$$\Phi^{(n)} = -\frac{(-1)^{2n}}{2\beta} \sum_{m=-\infty}^{\infty} \frac{\text{Tr} [\chi^0(i\nu_m)V]^n}{n}. \quad (3.34)$$

Finally, using the power series of the logarithm

$$\ln(1-x) = -\sum_{n=1}^{\infty} \frac{x^n}{n}, \quad (3.35)$$

one obtains for the sum of all bubble diagrams

$$\Phi_c^{\text{RPA}} = \frac{1}{2\beta} \sum_{m=-\infty}^{\infty} \text{Tr} \{ \ln [1 - \chi^0(i\nu_m)V] + \chi^0(i\nu_m)V \}. \quad (3.36)$$

Specifically, for the zero-temperature limit $\beta \rightarrow \infty$, this yields E_c^{RPA} , the correlation energy of the RPA

$$E_c^{\text{RPA}} = \frac{1}{4\pi} \int_{-\infty}^{\infty} d\nu \text{Tr} \{ \ln [1 - \chi^0(i\nu)V] + \chi^0(i\nu)V \}, \quad (3.37)$$

3.3 Random Phase Approximation

with the zero-temperature polarizability on the imaginary frequency axis having the form

$$\lim_{\beta \rightarrow \infty} \chi^0(\mathbf{r}', \mathbf{r}, i\nu) = \sum_{ia} \phi_i(\mathbf{r}') \phi_i^*(\mathbf{r}) \phi_a(\mathbf{r}) \phi_a^*(\mathbf{r}') \frac{2\xi_{ai}}{\xi_{ai}^2 + \nu^2}, \quad \xi_{ai} = \epsilon_a - \epsilon_i > 0. \quad (3.38)$$

Here i indicates an occupied and a an unoccupied one-particle index, see section 1.2. The last expression follows straightforwardly from the general contraction formula (3.25), the orbital representation of the Feynman propagator (2.109) and an additional Fourier transformation to Matsubara space. Expression (3.37) follows also from the so-called adiabatic connection fluctuation dissipation theorem (ACFDT), so that Eq. (3.37) is sometimes called the ACFDT formula. The reader is referred to Ref. 50 for more details.

In practical calculations, one determines the Fourier representation $\chi_{\mathbf{q}}^0(\mathbf{g}, \mathbf{g}', i\nu)$ of Eq. 3.38 and calculates the RPA correlation energy as

$$E_c^{\text{RPA}} = \frac{1}{4\pi} \sum_{k=1}^n \gamma_k \frac{1}{N_{\mathbf{q}}} \sum_{\mathbf{g}\mathbf{g}'\mathbf{q}} \left\{ [\ln(1 - \chi^0 V)]_{\mathbf{q}}(\mathbf{g}, \mathbf{g}', i\nu_k) + \chi_{\mathbf{q}}^0(\mathbf{g}, \mathbf{g}', i\nu_k) V_{\mathbf{q}}(\mathbf{g}, \mathbf{g}') \right\}, \quad (3.39)$$

where \mathbf{g}, \mathbf{g}' represent reciprocal lattice vectors, \mathbf{q} a point in the first Brillouin zone, $\{\gamma_k, \nu_k\}_{k=1}^n$ a frequency integral quadrature and

$$V_{\mathbf{q}}(\mathbf{g}, \mathbf{g}') = \frac{\delta_{\mathbf{g}\mathbf{g}'}}{|\mathbf{q} + \mathbf{g}|^2} \quad (3.40)$$

the Coulomb potential in reciprocal space. It is common to calculate the Fourier representation $\chi_{\mathbf{q}}^0(\mathbf{g}, \mathbf{g}', i\nu_k)$ directly from the Adler and Wiser formula[51, 52]

$$\chi_{\mathbf{q}}^0(\mathbf{g}, \mathbf{g}', i\nu) = \frac{1}{N_{\mathbf{k}}} \sum_{nn'\mathbf{k}} \frac{2\xi_{\mathbf{a}\mathbf{i}}}{\xi_{\mathbf{a}\mathbf{i}}^2 + \nu^2} \langle \phi_{\mathbf{i}} | e^{i(\mathbf{g}+\mathbf{q})\mathbf{r}} | \phi_{\mathbf{a}} \rangle \langle \phi_{\mathbf{a}} | e^{-i(\mathbf{g}'+\mathbf{q})\mathbf{r}'} | \phi_{\mathbf{i}} \rangle, \quad (3.41)$$

with $\mathbf{i} = (n, \mathbf{k})$ denoting the occupied and $\mathbf{a} = (n', \mathbf{k} + \mathbf{q})$ the unoccupied Bloch index. This approach is widely used in the community, although the unfavorable scaling of Eq. 3.41 (roughly with $\mathcal{O}(N^4)$) bears an obstacle to compute RPA energies for large systems.

In principle, one is able to evaluate χ^0 with $\mathcal{O}(N^3)$ scaling using the imaginary time Green's functions $G^0(\mathbf{r}, \mathbf{r}', \tau)$ and equation (3.25). This approach was discussed by Rojas *et al.*[53] and was recently implemented for molecules by Foerster *et al.*[54] and by Moussa[55], but a cubic-scaling RPA algorithm for periodic systems has not been implemented. In chapter 5 we develop an efficient zero-temperature RPA algorithm,

3. MANY-BODY PERTURBATION THEORY

based on the considerations from this section and apply the method to calculate Si-defect energies for large unit cells.

So far only the grand potential, respectively total energies have been considered. In the following chapter we discuss how to determine spectral properties of many-body systems using a set of coupled equations.

4

Spectral Properties

In chapter 3 a diagrammatic perturbation series for the interacting grand canonical potential was derived, respectively the correlation energy at zero-temperature. This chapter is dedicated to spectral properties, which can be described by the interacting propagator G as the solution of the *Schwinger-Dyson equations*. To solve these equations approximately, in the following two complementary approaches are considered, known as the *GW* [see section 4.2.1] and the *dynamical mean field approximation* [see section 4.5.1].

4.1 Schwinger-Dyson Equations

In this section the diagrammatic technique is extended in order to find a set of self-consistent equations, that describes the spectral properties of the system in terms of three quantities, the propagator G , the effective interaction W and the vertex function Γ . The resulting three equations are known as Schwinger-Dyson equations and are discussed in sections 4.1.1, 4.1.2 and 4.1.3 separately. Fairly heuristic arguments are used to derive these equations, since the only purpose of this section is to give the basic idea of this approach. The reader is referred to the literature for a mathematically rigorous derivation.[44, 56, 57]

4.1.1 Interacting Green's Function and Self-energy

We start with the interacting Feynman propagator G . This function describes the propagation of an interacting electron (respectively hole) from one spacetime point to another

4.1 Schwinger-Dyson Equations

where we have introduced the abbreviation $\int dx = \int d^3\mathbf{r} \int_0^\beta d\tau$ for convenience. Analogously, higher order, for instance the second order terms shown in Fig. 4.1, can be translated to integrals. Looking at this figure (or Eqs. (4.3), (4.4)), one clearly sees that



Figure 4.1: Second order contributions to the interacting Feynman propagator.

all diagrams have an incoming and an outgoing non-interacting Green's function 'leg'. The infinite number of terms between the incoming and outgoing Green's function defines the *self-energy* $\tilde{\Sigma}$, so that the interacting Green's function satisfies the equation[34]

$$G(x', x) = G^0(x', x) + \int dx_1 \int dx_2 G^0(x', x_1) \tilde{\Sigma}(x_1, x_2) G^0(x_2, x), \quad x = (\mathbf{r}, \tau) \quad (4.5)$$

The two-point quantity

$$\boxed{\tilde{\Sigma}} = \text{diagram 1} + \text{diagram 2} + \text{diagram 3} + \text{diagram 4} + \dots \quad (4.6)$$

contains repeated insets of diagrams (third and fourth diagram) and is therefore called the *reducible* self-energy. These terms separate into *irreducible* self-energy diagrams, if by cutting and removing a particle line, two disconnected self-energy diagrams are obtained. For instance the third diagram in Eq. (4.6) contains two diagrams of the first term, whereas the fourth term contains the first and second diagram connected by a propagator G^0 .

One takes advantage of this fact and defines the *irreducible* self-energy Σ , containing only irreducible diagrams. With this, we obtain the first Schwinger-Dyson equation[33, 58]

$$G(x', x) = G^0(x', x) + \int dx_1 \int dx_2 G^0(x', x_1) \Sigma(x_1, x_2) G(x_2, x), \quad (4.7)$$

which reads diagrammatically

$$\text{diagram} = \text{diagram} + \text{diagram} \boxed{\Sigma} \text{diagram} \quad (4.8)$$

4. SPECTRAL PROPERTIES

where the irreducible self-energy Σ is given by

$$\boxed{\Sigma} = \text{diagram 1} + \text{diagram 2} + \text{diagram 3} + \text{diagram 4} + \dots \quad (4.9)$$

and we used thick particle lines in Eq. (4.8) to indicate interacting Green's functions G . We emphasize that Σ and $\tilde{\Sigma}$ obey a Dyson equation of the type

$$\Sigma(x', x) = \tilde{\Sigma}(x', x) + \int dx_1 \int dx_2 \tilde{\Sigma}(x', x_1) G^0(x_1, x_2) \Sigma(x_2, x), \quad (4.10)$$

which follows trivially from comparison of Eqs. (4.5) and (4.7).[34]

The first term in the irreducible self-energy (4.9)

$$\Sigma^{(1)}(x', x) = -\delta(x - x') \int dx_3 \frac{\delta(\tau_3 - \tau')}{|\mathbf{r}_3 - \mathbf{r}'|} G^0(x_3, x_3) \quad (4.11)$$

is the time-independent Hartree term and is often absorbed in the non-interacting Green's function yielding the Hartree-dressed Green's function $G^{(1)}$, indicated by a double line in the following. The latter is obtained from the truncation of (4.9) after the first term and solving the corresponding Dyson equation[33]

$$\text{double line} = \text{single line} + \text{single line with loop} \quad (4.12)$$

The Dyson equation for the full Green's function, then reads

$$G(x', x) = G^{(1)}(x', x) + \int dx_1 dx_2 G^{(1)}(x', x_1) \Sigma^{(>1)}(x_1, x_2) G(x_2, x) \quad (4.13)$$

respectively

$$\text{double line} = \text{double line} + \text{double line with } \boxed{\Sigma^{(>1)}} \quad (4.14)$$

with $\Sigma^{(>1)}$ being the exchange-correlation part $\Sigma - \Sigma^{(1)}$ of the irreducible self-energy[56]

$$\boxed{\Sigma^{(>1)}} = \text{diagram 1} + \text{diagram 2} + \text{diagram 3} + \dots \quad (4.15)$$

We note, that the exchange-correlation part $\Sigma^{(>1)}$ is expressed in terms of the Hartree Green's function $G^{(1)}$ rather than the non-interacting propagator G^0 . This procedure above is, however, not restricted necessarily to the Hartree term. Instead, one can include

4.1 Schwinger-Dyson Equations

more terms in the irreducible self-energy and solve the corresponding Dyson equation for the interacting Green's function.

The general procedure is called *renormalization* and describes the inclusion of irreducible (for instance the first n) self-energy terms in the *skeleton* ('non-interacting' Green's function G^0). The resulting Green's function $G^{(n)}$ is called *dressed propagator* and describes physically the propagation of a renormalized *quasi-electron* (or quasi-hole). These quasi-particles can be seen as bare electrons (holes) surrounded by a cloud of particles with heavier effective mass than their undressed counterparts. Due to the latter, it can be expected that quasi-particles interact via an *effective interaction* W . This interaction, also named *screened interaction*, is usually weaker than the bare interaction V , so that one can expect that a perturbation series for the self-energy in terms of W converges faster than Eq. (4.15). [33] As we shall see in a moment, the effective interaction can be obtained by a similar renormalization procedure for the Coulomb interaction V .

4.1.2 Effective Interaction and Polarizability

The instantaneous Coulomb interaction

$$V(x, x') = \frac{\delta(\tau - \tau')}{|\mathbf{r} - \mathbf{r}'|}, \quad x = (\mathbf{r}, \tau) \quad (4.16)$$

can be seen as the $(0, 0)$ component of the undressed electromagnetic Feynman-propagator

$$D_{\mu\nu}^0(x, x') = - \left\langle \hat{T} \hat{A}_\mu(x) \hat{A}_\nu(x') \right\rangle_\beta \quad (4.17)$$

in the Coulomb gauge, where \hat{A}^μ is the field operator of the electromagnetic field. For more information we refer the reader to Refs. 59, 60. Dyson showed (see Ref. 58), that the corresponding interacting propagator $D_{\mu\nu}$ satisfies an equation of the same kind as the Dyson equation for the Green's function (4.7). However, we are mostly interested in the $(0, 0)$ components of this equation and write $W(x, x') = D_{00}(x, x')$ for the dressed and $V(x, x') = \frac{\delta(\tau - \tau')}{|\mathbf{r} - \mathbf{r}'|} = D_{00}^0(x, x')$ for the bare propagator. Furthermore, we do not assume that any spatial components of the bare and dressed photon-propagator mix with the time components, so that W is a functional of V and G only.

4. SPECTRAL PROPERTIES

With these assumptions and the considerations from the previous section Eq. (4.5), the following ansatz is obvious

$$W(x', x) = V(x', x) + \int dx_1 \int dx_2 V(x', x_1) \tilde{\chi}(x_1, x_2) V(x_2, x) \quad (4.18)$$

Here $\tilde{\chi}$ is called the *reducible polarizability* and was introduced by Hubbard in Ref. 32. It describes all possible polarization effects between two interaction lines, like for instance the bubble polarization  appearing in the second term of the self-energy (4.15). An explicit expression of $\tilde{\chi}$ in terms of the density operator is given in section 4.2, here we indicate only the diagrammatic expansion

$$\tilde{\chi} = \text{bubble} + \text{bubble} \text{---} \text{bubble} + \text{bubble} \text{---} \text{bubble} \text{---} \text{bubble} + \dots \quad (4.19)$$

Comparing to (4.6), one sees that $\tilde{\chi}$ plays the same role for the screened interaction W as the self-energy $\tilde{\Sigma}$ for the Green's function G . Thus, the validity of the analogue of Eq. (4.10) can be assumed for the reducible polarizability

$$\tilde{\chi}(x', x) = \chi(x', x) + \int dx_1 \int dx_2 \chi(x', x_1) V(x_1, x_2) \tilde{\chi}(x_2, x), \quad (4.20)$$

in terms of the *irreducible polarizability* χ . In analogy to the irreducible self-energy, the irreducible polarizability χ is defined by those subsets of the polarizability χ , that can not be separated into more polarizability diagrams by cutting and removing a Coulomb line V . For instance, the first and third diagram in Eq. (4.19) are irreducible, whereas the second diagram is reducible.[33, 34]

Diagrams representing the expansion of χ were given first by Hedin in Ref. 56 and are shown below

$$\chi = \text{bubble} + \text{bubble} \text{---} \text{bubble} + \text{bubble} \text{---} \text{bubble} \text{---} \text{bubble} + \text{bubble} \text{---} \text{bubble} \text{---} \text{bubble} \text{---} \text{bubble} + \dots \quad (4.21)$$

In analogy to the first Schwinger-Dyson equation (4.7), the second Schwinger-Dyson equation for the screened interaction reads[56]

$$W(x', x) = V(x', x) + \int dx_1 \int dx_2 V(x', x_1) \chi(x_1, x_2) W(x_2, x). \quad (4.22)$$

If  indicates W in diagrams, the last expression translates to

$$\text{wavy line} = \text{wavy line} + \text{wavy line} \text{---} \text{bubble} \text{---} \text{wavy line} \quad (4.23)$$

4.1 Schwinger-Dyson Equations

The introduction of the irreducible polarizability χ has two main advantages. First, χ contains lesser terms than the reducible polarizability $\tilde{\chi}$. Second, and more important, it allows for a partial renormalization of the bare interaction V , *i.e.* an approximative determination of the screened interaction W . [56]

One important approximation is obtained by truncating the series (4.21) after the first term, that is approximating the independent particle polarizability by [34]

$$\chi(x', x) \approx \chi^{(1)}(x', x) = -G^{(n)}(x', x)G^{(n)}(x, x'). \quad (4.24)$$

Here the superscript n stands either for non-interacting, Hartree Green's function $G^{(1)}$ or any other dressed propagator. The RPA-type approximation (4.24) gives rise to the screened interaction in the RPA

$$W^{(1)}(x', x) = V(x', x) + \int dx_1 \int dx_2 V(x', x_1) \chi^{(1)}(x_1, x_2) W^{(1)}(x_2, x) \quad (4.25)$$

translating to diagrams as



$$\text{wavy line} = \text{wavy line} + \text{wavy line} \text{ with bubble} \quad (4.26)$$

The advantage of using dressed propagators $G^{(n)}$, respectively screened interactions $W^{(n)}$ instead of skeleton propagators G^0 and bare interactions V becomes evident already for the first order approximations of Eq. (4.15) and Eq. (4.19). For instance, inserting the RPA interaction $W^{(1)}$ of Eq. (4.26) for the bare interaction line in the first term of the self-energy (4.15) generates a whole class of skeleton diagrams



$$\text{self-energy} = \text{skeleton 1} + \text{skeleton 2} + \text{skeleton 3} + \dots \quad (4.27)$$

Higher order terms of the self-energy are then given by



$$\boxed{\Sigma^{(>1)}} = \text{diagram 1} + \text{diagram 2} + \text{diagram 3} + \dots \quad (4.28)$$

where we indicated only one of six different third order terms, see Ref. 56.

Similarly, more terms in the irreducible polarizability can be taken into account giving rise to other, more accurate, partially screened interactions $W^{(n)}$. Specifically for $W^{(1)}$, the RPA interaction of (4.26), the screening Eq. (4.22) reads

$$W(x', x) = W^{(1)}(x', x) + \int dx_1 \int dx_2 W^{(1)}(x', x_1) \chi^{(>1)}(x_1, x_2) W(x_2, x). \quad (4.29)$$

4. SPECTRAL PROPERTIES

or

$$\text{---} = \text{---} + \text{---} \circlearrowleft \chi^{(>1)} \text{---}, \quad (4.30)$$

where $\chi^{(>1)} = \chi - \chi^{(1)}$ and reads in diagrams

$$\text{---} \circlearrowleft \chi^{(>1)} \text{---} = \text{---} \circlearrowleft \text{---} \text{---} + \dots \quad (4.31)$$

So far we have discussed the renormalization of the Green's function and the interaction, which are summarized algebraically by Eq. (4.13) and Eq. (4.29), respectively in terms of diagrams by Eq. (4.14) and Eq. (4.30). Thereby the dressed Green's function $G^{(n)}$ is determined by the irreducible self-energy $\Sigma^{(>n)}$, whereas the dressed interaction $W^{(n)}$ is determined by the irreducible polarizability $\chi^{(>n)}$. For both irreducible quantities only the first few diagrammatic contribution has been given in Eqs. (4.28) and (4.31). However, algebraic expressions for $\Sigma^{(>1)}$ and $\chi^{(>1)}$ are desirable for practical calculations. These expressions can be obtained in terms of the irreducible vertex Γ , which we consider in the following section.

4.1.3 Vertex and Bethe-Salpeter Equation

To keep the notation simple, we use the conventional abbreviation $1 = x_1 = (\mathbf{r}_1, \tau_1)$ in the following.[56]

First, we consider the irreducible polarizability χ given in Eq. (4.21) and try to write it in a closed form. For this purpose we consider the vertex in diagrams more closely and generalize its properties to a general vertex Γ . The aim is to find a Dyson equation for the generalized vertex and to apply the concept of renormalization, known from the previous sections.

The vertex, in general, is a function $\Gamma(1; 2, 3)$ connecting one interaction line at 1 with one incoming and one outgoing particle line at 2, respectively 3. For the bare vertex Γ^0 , represented by \bullet in diagrams, this function is given by

$$\Gamma^0(1; 2, 3) = \delta(1, 2)\delta(2, 3) \quad (4.32)$$

with

$$\delta(1, 2) = \delta(x_1 - x_2) = \delta(\tau_1 - \tau_2)\delta(\mathbf{r}_1 - \mathbf{r}_2). \quad (4.33)$$

To find higher order terms of Γ , represented by \blacktriangleleft in diagrams, we assume that the bare propagator G^0 is dressed by the Hartree term and the bare interaction V is dressed by the

4.1 Schwinger-Dyson Equations

RPA polarizability $\chi^{(1)}$ and choose the following ansatz for the irreducible polarizability

$$\chi = \text{bubble diagram} = \text{bubble diagram with shaded triangle} \quad (4.34)$$

This relation reads explicitly in terms of integrals

$$\chi(1, 2) = - \int d(1')d(2')\Gamma(1; 1', 2')G^{(1)}(2, 1')G^{(1)}(2', 2). \quad (4.35)$$

The idea is to compare the r.h.s. of Eq. (4.34) with the diagrammatic expansion of χ from Eq. (4.21), respectively Eq. (4.31), to determine the vertex function Γ . This is straight forward for the first terms and we identify them as

$$\text{shaded triangle} = \bullet + \text{triangle with wavy line} + \text{triangle with two wavy lines} + \text{triangle with three wavy lines} + \text{triangle with four wavy lines} + \dots \quad (4.36)$$

Next, we focus on the diagrammatic expansion of the irreducible self-energy Σ . Looking at the diagrammatic expansion (4.28) it seems that the first three terms can be summarized in following diagram

$$\boxed{\Sigma^{(>1)}} = \text{triangle with wavy line and shaded triangle} \quad (4.37)$$

This relationship can be written explicitly as

$$\Sigma^{(>1)}(1, 2) = \int d(1')d(2')G^{(1)}(1', 2)W^{(1)}(2', 2)\Gamma(2'; 1, 1') \quad (4.38)$$

and was proven by Hedin in the 1960s.[56]

With Eqs. (4.38) and Eqs. (4.35) the irreducible self-energy and polarizability in the Schwinger-Dyson equations for the Green's function (4.7) respectively for the screened interaction (4.22) can be eliminated, leaving only three unknown quantities G , W and Γ . What remains is to find the equation for the irreducible vertex function.

For this reason one takes a close look at the diagrammatic series Eq. (4.36) and 'open' the left vertex in each graph on the r.h.s. introducing the four-point irreducible vertex $\Gamma(1, 2; 3, 4)$ function. This quantity is indicated by

$$\Gamma(1, 2; 3, 4) = \text{shaded square with vertices 1, 2, 3, 4} \quad (4.39)$$

4. SPECTRAL PROPERTIES

in diagrams in the following and satisfies

$$\Gamma(1, 1; 3, 4) = \Gamma(1; 3, 4) = \begin{array}{c} 3 \\ \diagup \text{---} \text{---} \text{---} \diagdown \\ \text{---} \text{---} \text{---} \\ \diagdown \text{---} \text{---} \text{---} \diagup \\ 4 \end{array} \quad (4.40)$$

so that 2, 3 are incoming and 1, 4 are outgoing legs in Eq. (4.39). Similarly \square indicates the bare four-vertex function

$$\Gamma^0(1, 2; 3, 4) = \delta(1, 3)\delta(2, 4), \quad (4.41)$$

as a generalization of the three-point quantity of Eq. (4.32).

Then the diagrammatic series (4.36) can be redrawn in a closed Schwinger-Dyson form[44]

$$\begin{array}{c} \text{---} \text{---} \text{---} \\ \text{---} \text{---} \text{---} \end{array} = \begin{array}{c} \text{---} \text{---} \text{---} \\ \text{---} \text{---} \text{---} \end{array} + \begin{array}{c} \text{---} \text{---} \text{---} \text{---} \text{---} \text{---} \\ \text{---} \text{---} \text{---} \text{---} \text{---} \text{---} \end{array} \quad (4.42)$$

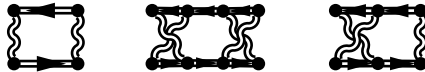
translating to integrals as

$$\begin{aligned} \Gamma(1, 2; 3, 4) &= \Gamma^0(1, 2; 3, 4) + \int d(1') \cdots d(6') \\ &\times \Gamma^0(1, 2; 3', 4') I(3', 4'; 5', 6') G^{(1)}(1', 5') G^{(1)}(6', 2') \Gamma(1', 2'; 3, 4). \end{aligned} \quad (4.43)$$

This equation is also known as the Bethe-Salpeter equation,[56, 61] where IGG is the kernel of the equation. This kernel is the analogue of the Σ and χ for the Dyson equations of the Green's function (4.7) and the effective potential (4.22). The four-point object I is called *irreducible scattering amplitude* and describes all necessary interactions between particles and holes.[34, 44] To avoid double counting of diagrammatic contributions, the amplitude contains only terms, irreducible in the particle-hole channel. That is, diagrams of I do not separate into smaller order diagrams when 'cutting' vertically through a particle and a hole line. For instance the following scattering diagrams are irreducible



and the following are reducible in the particle hole channel



4.1 Schwinger-Dyson Equations

An explicit expression for the scattering amplitude can be obtained from

$$I^{(n)}(1, 2; 3, 4) = \frac{\delta\Sigma^{(n)}(1, 2)}{\delta G^{(n-1)}(4, 3)} \quad (4.44)$$

for each order in perturbation theory.[62]

The three Schwinger-Dyson equations (4.43), (4.7) and (4.22) provide an alternative view on a system of interacting electrons and allow for higher order approximations beyond the HF or DFT method.[24, 34, 63] Here the approximation degree is determined by the number of diagrams considered in the scattering amplitude I . For a comprehensive overview of different approximations the reader is referred to Ref. 57.

4. SPECTRAL PROPERTIES

4.2 Hedin Equations and Self-Consistency Limit

The three Schwinger-Dyson equations (4.43), (4.7), (4.22) and the equations for the self-energy (4.38) and polarizability (4.35) are known as *Hedin equations* among condensed matter physicists.[56, 62, 64] The reason for this is mainly due to practical calculations, where one has to solve the set of equations for Γ , χ , W , Σ and G self-consistently by means of the scheme depicted in Fig. 4.2. This figure illustrates the iterative algorithm to solve the Hedin equations

$$\Sigma^{(n)} = G^{(n-1)}W^{(n-1)}\Gamma^{(n-1)} \quad (4.45)$$

$$G^{(n)} = G^{(n-1)} + G^{(n-1)}\Sigma^{(n)}G^{(n)} \quad (4.46)$$

$$I^{(n)} = \frac{\delta\Sigma^{(n)}}{\delta G^{(n-1)}} \quad (4.47)$$

$$\Gamma^{(n)} = \Gamma^{(n-1)} + \Gamma^{(n-1)}I^{(n)}G^{(n)}G^{(n)}\Gamma^{(n)} \quad (4.48)$$

$$\chi^{(n)} = -G^{(n)}G^{(n)}\Gamma^{(n)} \quad (4.49)$$

$$W^{(n)} = W^{(n-1)} + W^{(n-1)}\chi^{(n)}W^{(n)} \quad (4.50)$$

with $W^{(0)} = V$ using following prescription[62]

Hedin Algorithm

- H1 Calculate the self-energy $\Sigma^{(n)}$ with Eq. (4.45).
- H2 Solve Eq. (4.46) for the dressed propagator $G^{(n)}$.
- H3 Determine scattering amplitude from Eq. (4.47) (skip this step for $n = 1$).
- H4 Solve Eq. (4.48) for the dressed vertex $\Gamma^{(n)}$.
- H5 Compute the polarizability $\chi^{(n)}$ with Eq. (4.49).
- H6 Solve Eq. (4.50) for the dressed interaction $W^{(n)}$.
- H7 Iterate H1-H6 until convergence is found.

Each iteration n of H1-H6 dresses the propagator $G^{(n)}$, interaction $W^{(n)}$ and vertex function $\Gamma^{(n)}$ with more and more irreducible diagrams, so that in the self-consistency limit $n \rightarrow \infty$ the iterative procedure converges to

$$G^{(n)} \rightarrow G, \quad W^{(n)} \rightarrow W, \quad \Gamma^{(n)} \rightarrow \Gamma, \quad \chi^{(n)} \rightarrow \chi, \quad \Sigma^{(n)} \rightarrow \Sigma, \quad n \rightarrow \infty. \quad (4.51)$$

4.2 Hedin Equations and Self-Consistency Limit

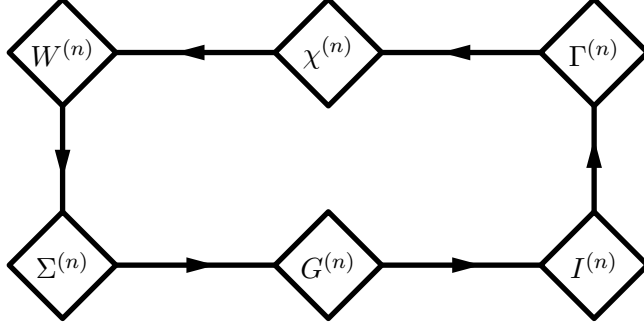


Figure 4.2: Hedin scheme for the self-consistent solution of Eqs. (4.45)-(4.50).

In practice, one is hardly able to calculate the vertex function for $n = 2$ for realistic systems, due to the increasing computational cost, see Ref. 62. Therefore, the self-consistency circle is stopped after Eq. (4.46) for $n = 2$, where the self-energy assumes the form

$$\Sigma^{(2)}(x', x) = G^{(1)}(x', x)W^{(1)}(x', x). \quad (4.52)$$

The corresponding diagram is shown in Eq. (4.27) and due to the form of the diagram, this approximation is known as the GW approximation (GWA). It turns out that the GWA is often sufficiently accurate to calculate spectral properties, band gaps and other system specific quantities for a wide range of materials.[56, 62, 65, 66, 67, 68] In the following we discuss the GWA in more detail.

4.2.1 The GW Approximation in Practice

Typically finite-temperature effects are neglected in GW calculations, so that we consider the zero-temperature limit of Eq. (4.51) and Eq. (4.52) in the following. To understand how the GWA is used in practice, we consider the Lehman representation of the zero-temperature Green's function in real time

$$G(\mathbf{r}, \mathbf{r}', t) = -i \left\langle \Omega_0^{(N)} \left| \hat{T} \hat{\psi}_H(\mathbf{r}t) \hat{\psi}_H^\dagger(\mathbf{r}') \right| \Omega_0^{(N)} \right\rangle, \quad (4.53)$$

where the subscript H indicates the Heisenberg time-evolution and $\left| \Omega_0^{(N)} \right\rangle$ the interacting groundstate of N electrons. This representation can be obtained analogously to the non-interacting propagator, discussed in section 2.4, and reads

$$G(\mathbf{r}', \mathbf{r}, \omega) = \sum_{\nu=0}^{\infty} \frac{I_{\nu}^+(\mathbf{r}', \mathbf{r})}{\omega - \omega_{\nu} + i\eta} + \frac{I_{\nu}^-(\mathbf{r}', \mathbf{r})}{\omega + \omega_{\nu} - i\eta}, \quad (4.54)$$

4. SPECTRAL PROPERTIES

with the interacting Lehman amplitudes

$$I_\nu^+(\mathbf{r}', \mathbf{r}) = \Theta(\omega_\nu) \langle \Omega_0^{(N)} | \hat{\psi}(\mathbf{r}) | \Omega_\nu^{(N+1)} \rangle \langle \Omega_\nu^{(N+1)} | \hat{\psi}^\dagger(\mathbf{r}') | \Omega_0^{(N)} \rangle \quad (4.55)$$

$$I_\nu^-(\mathbf{r}', \mathbf{r}) = \Theta(-\omega_\nu) \langle \Omega_0^{(N)} | \hat{\psi}^\dagger(\mathbf{r}') | \Omega_\nu^{(N-1)} \rangle \langle \Omega_\nu^{(N-1)} | \hat{\psi}(\mathbf{r}) | \Omega_0^{(N)} \rangle. \quad (4.56)$$

and excitation energies given by[35]

$$\omega_\nu = \begin{cases} \Omega_\nu^{(N-1)} - \Omega_0^{(N)}, & \omega_\nu < 0 \\ \Omega_\nu^{(N+1)} - \Omega_0^{(N)}, & \omega_\nu > 0 \end{cases}. \quad (4.57)$$

It is convenient to introduce the spectral densities

$$A^\pm(\mathbf{r}', \mathbf{r}, \omega) = \sum_{\nu=0}^{\infty} I_\nu^\pm(\mathbf{r}', \mathbf{r}) \delta(\omega \mp \omega_\nu) \quad (4.58)$$

and to rewrite Eq. (4.54) into

$$G(\mathbf{r}', \mathbf{r}, \omega) = \int_{-\infty}^{\infty} d\omega' \left[\frac{A^+(\mathbf{r}', \mathbf{r}, \omega')}{\omega - \omega' + i\eta} + \frac{A^-(\mathbf{r}', \mathbf{r}, \omega')}{\omega - \omega' - i\eta} \right], \quad (4.59)$$

Then the first term of the Lehman representation (4.59) describes the effect of adding an electron at \mathbf{r}' to a system of N interacting electrons in the groundstate and removing an electron at \mathbf{r} , whereas the second term describes the inverse propagation for a hole. The same equation shows that the poles of the interacting propagator are all located along the real axis, so that G has a similar analytic behavior as the non-interacting propagator G^0 . In contrast to G^0 , the Lehman amplitudes cannot be written in terms of one-electron orbitals $\tilde{\phi}_\nu$, *i.e.*

$$I_\nu^+(\mathbf{r}', \mathbf{r}) \neq \tilde{\phi}_\nu(\mathbf{r}) \tilde{\phi}_\nu^*(\mathbf{r}') \neq I_\nu^-(\mathbf{r}', \mathbf{r}). \quad (4.60)$$

This is because in general the interacting groundstate $|\Omega_0^{(N)}\rangle$ is not exactly a single Slater-determinant of the orbitals $\tilde{\phi}_\nu$, but rather a linear combination of all possible determinants, see end of section 1.2. However, often the interacting groundstate of many systems can be approximated sufficiently accurate by one single Slater-determinant. For these systems the GWA, as discuss below, is a good approximation.

The first calculations in the GWA have been done by Hybertsen and Louie for semi-conductors in the 1980s by solving the eigenvalue problem[64]

$$\langle \tilde{\phi}_\mu | \hat{h}_0 + \hat{V}_h + \hat{\Sigma}^{(2)}(\tilde{\epsilon}_\nu) | \tilde{\phi}_\nu \rangle = \tilde{\epsilon}_\nu \langle \tilde{\phi}_\mu | \tilde{\phi}_\nu \rangle \quad (4.61)$$

4.2 Hedin Equations and Self-Consistency Limit

for the quasi particle (qp) one-particle eigensystem $\left\{ \left| \tilde{\phi}_\nu \right\rangle, \tilde{\epsilon}_\nu \right\}$. Here \hat{h}_0 is the one-electron Hamiltonian (2.4), \hat{V}_h the operator of the Hartree energy (1.16) and $\hat{\Sigma}^{(2)}$ the self-energy operator in the GW approximation with spacetime representation given in Eq. (4.52). Since the eigensystem of Eq. (4.61) is unknown a priori, Hybertsen and Louie evaluated the operators $\hat{h}_0, \hat{V}_h, \hat{\Sigma}^{(2)}$ w.r.t. to a DFT one-orbital basis set $\{\phi_\nu, \epsilon_\nu\}$. Furthermore, they linearized the self-energy w.r.t. to the KS energies ϵ_ν

$$\hat{\Sigma}^{(2)}(\tilde{\epsilon}_\nu) = \hat{\Sigma}^{(2)}(\epsilon_\nu) + \underbrace{\frac{d\hat{\Sigma}^{(2)}(\omega)}{d\omega}}_{=\hat{\Sigma}'^{(2)}(\epsilon_\nu)} \Big|_{\omega=\epsilon_\nu} (\tilde{\epsilon}_\nu - \epsilon_\nu) + \mathcal{O}((\tilde{\epsilon}_\nu - \epsilon_\nu)^2), \quad (4.62)$$

and observed that off-diagonal matrix elements of Eq. (4.61) are negligibly small compared to the diagonal ones, so that they effectively solved

$$\left\langle \phi_\nu \left| \hat{h}_0 + \hat{V}_h + \hat{\Sigma}^{(2)}(\epsilon_\nu) - \epsilon_\nu \hat{\Sigma}'^{(2)}(\epsilon_\nu) \right| \phi_\nu \right\rangle = \tilde{\epsilon}_\nu Z_\nu^{-1} \quad (4.63)$$

for the quasi-particle energies $\tilde{\epsilon}_\nu$. Here the renormalization factor

$$Z_\nu = \frac{1}{\left\langle \phi_\nu \left| 1 - \hat{\Sigma}'^{(2)}(\epsilon_\nu) \right| \phi_\nu \right\rangle} \quad (4.64)$$

typically increases the band gap of the KS system.

It turns out that this scheme, today known as G_0W_0 approximation, yields often very good band gap estimates of semiconductors, see Ref. 64. A success of the G_0W_0 approach motivated researchers to improve the scheme and allow for self-consistent GW (scGW) calculations. Specifically, the self-consistent scheme of Kotani and Schilfgaard, respectively the slightly reformulated approach of Shishkin *et al.* should be mentioned at this point, see Refs. 67, 68. In the latter, the eigenvalue equation

$$\left[\hat{h}_0 + \hat{V}_h + \hat{\Sigma}^{(2)}(\epsilon_\nu^{(n)}) - \epsilon_\nu^{(n)} \hat{\Sigma}'^{(2)}(\epsilon_\nu^{(n)}) \right] \left| \phi_\nu^{(n+1)} \right\rangle = \epsilon_\nu^{(n+1)} \left[1 - \hat{\Sigma}'^{(2)}(\epsilon_\nu^{(n)}) \right] \left| \phi_\nu^{(n+1)} \right\rangle \quad (4.65)$$

is solved iteratively for the one-electron orbitals $\phi_\nu^{(n)}$ and quasi-particle energies $\epsilon_\nu^{(n)}$ until convergence is found. The advantage of this approach is that the resulting self-consistent solution $\{\tilde{\phi}_\nu, \tilde{\epsilon}_\nu\}$ is independent from the initial KS basis $\{\phi_\nu, \epsilon_\nu\}$. This approach is advantageous for other many-body calculations, where the KS basis does not provide a good starting point.

4. SPECTRAL PROPERTIES

Typically, GW implementations have an $\mathcal{O}(N^4)$ scaling and, thus, are limited to rather small systems, see Ref. 67, 68. The bottleneck for these implementations is the computation of the independent-particle polarizability (4.24) for which the Adler and Wiser expression of Eq. (3.41) is employed, as for conventional RPA algorithms. The computational cost of this step can be reduced to $\mathcal{O}(N^3)$ provided Hedin's equations on the imaginary time respectively imaginary frequency axis are used. This approach is known as the space-time GW approach and was proposed first by Rojas *et al.* in Ref. 53 and further developed by Steinbeck *et al.* in Ref. 69 and Ren *et al.* in Ref. 70. All these GW approaches, however, face the same storage problem as discussed in section 5.2 for the RPA algorithm. As a consequence, conventional space-time GW codes avoid solving the Dyson equation for the propagator (4.46) by assuming implicitly the non-interacting orbital form of Eq. (2.109) for the propagator in all computation steps.

Using the imaginary time and frequency grids, presented in chapter 5, the storage problem can be solved and a true $\mathcal{O}(N^3)$ scaling GW algorithm can be implemented. This approach has the advantage that the Dyson equation for the propagator can be solved self-consistently on the GWA level. The corresponding algorithm is currently investigated and will be presented in a future work.

Nevertheless, the GWA often breaks down for systems with partially filled narrow bands, for instance transition metal oxides. For these systems an alternative view on the many-body problem is helpful. For this purpose we introduce the path integral concept in the following.

4.3 The Path Integral

The path integral (PI) was introduced by Dirac in the 1930s and extensively developed by Feynman in the 1940s and is a powerful tool for QFT. It connects the classical principle of least action, known from Hamiltonian mechanics, with quantum mechanics and statistical mechanics. The interested reader is referred to Ref. 71, 72 for a historical overview, respectively more details about the PI. Here we introduce only the basic concepts of the PI following closely Negele and Orland, see Ref. 39.

We consider a single particle described by the wavefunction ψ and the Hamiltonian

$$\hat{h}(\hat{\mathbf{r}}, \hat{\mathbf{p}}) = \frac{\hat{\mathbf{p}}^2}{2} + \hat{\varphi}(\hat{\mathbf{r}}), \quad (4.66)$$

where $\hat{\mathbf{r}}$ denotes the position and $\hat{\mathbf{p}}$ the momentum operator. In the Schrödinger picture the imaginary time evolution of the corresponding wavefunction ψ_s from $\tau = 0$ to $\tau = \beta$ is given by

$$\psi_s(\mathbf{r}, \beta) = \int d\mathbf{r}' \langle \mathbf{r} | e^{-\beta \hat{h}(\mathbf{r}', \hat{\mathbf{p}})} | \mathbf{r}' \rangle \psi(\mathbf{r}'). \quad (4.67)$$

We slice the time path from 0 to β into M equidistant pieces according to

$$\delta\tau = \frac{\beta}{M}, \quad \tau_i = i\delta\tau, \quad i = 0, \dots, M \quad (4.68)$$

and introduce the notation

$$\mathbf{r}_i = \mathbf{r}(\tau_i), \quad \mathbf{r}_0 = \mathbf{r}', \quad \mathbf{r}_M = \mathbf{r} \quad (4.69)$$

with the eigenvalue equation for the position operator

$$\hat{\mathbf{r}} | \mathbf{r}_i \rangle = \mathbf{r}_i | \mathbf{r}_i \rangle \quad (4.70)$$

Applying this subdivision to Eq. (4.67) and inserting the closure relation

$$1 = \int d\mathbf{r}_i | \mathbf{r}_i \rangle \langle \mathbf{r}_i |, \quad (4.71)$$

one ends up with

$$\psi_s(\mathbf{r}, \beta) = \int \prod_{i=0}^M d\mathbf{r}_i \langle \mathbf{r} | e^{-\delta\tau \hat{h}(\mathbf{r}_{M-1}, \hat{\mathbf{p}})} | \mathbf{r}_{M-1} \rangle \cdots \langle \mathbf{r}_1 | e^{-\delta\tau \hat{h}(\mathbf{r}_0, \hat{\mathbf{p}})} | \mathbf{r}' \rangle \psi(\mathbf{r}') \quad (4.72)$$

4. SPECTRAL PROPERTIES

Any expectation value on the r.h.s. can be rewritten as follows

$$\begin{aligned} \langle \mathbf{r}_{i+1} | e^{-\delta\tau \hat{h}(\mathbf{r}_i, \hat{\mathbf{p}})} | \mathbf{r}_i \rangle &= \underbrace{\langle \mathbf{r}_{i+1} | \mathbf{r}_i \rangle}_{\delta(\mathbf{r}_{i+1} - \mathbf{r}_i)} e^{-\delta\tau h(\mathbf{r}_i, \mathbf{p}_i)} \\ &= \int \frac{d^3 \mathbf{p}_i}{(2\pi)^3} e^{\delta\tau \left(\mathbf{p}_i \frac{\mathbf{r}_{i+1} - \mathbf{r}_i}{-i\delta\tau} - h(\mathbf{r}_i, \mathbf{p}_i) \right)}, \end{aligned} \quad (4.73)$$

where in the first step we used the real-space representation $\mathbf{p}_i = -i\nabla_i$ and the integral representation for the Dirac delta distribution.

Defining the limits $\dot{\mathbf{r}}(\tau_i) = \lim_{\delta\tau \rightarrow 0} \frac{\mathbf{r}_{i+1} - \mathbf{r}_i}{-i\delta\tau}$, the abbreviation $\int_\tau = \int_0^\beta d\tau$ and the PI measure

$$\mathcal{D}[\mathbf{r}(t), \mathbf{p}(t)] = \lim_{M \rightarrow \infty} \prod_{i=0}^M \frac{d^3 \mathbf{r}_i d^3 \mathbf{p}_i}{(2\pi)^3}, \quad (4.74)$$

one obtains for Eq. (4.72) in the limit $M \rightarrow \infty$

$$\psi_s(\mathbf{r}, \beta) = \int_{\mathbf{r}(0)=\mathbf{r}'}^{\mathbf{r}(\beta)=\mathbf{r}} \mathcal{D}[\mathbf{r}(t), \mathbf{p}(t)] e^{\int_\tau [\mathbf{p}(\tau) \dot{\mathbf{r}}(\tau) - \hat{h}(\mathbf{r}(\tau), \mathbf{p}(\tau))]} \psi(\mathbf{r}). \quad (4.75)$$

This expression 4.75 is known as the Hamiltonian form of the path integral.[39, 47] If the Gaussian integral formula (C.2) is used to carry out the integration over momenta \mathbf{p}_i , one ends up with the corresponding Lagrangian form[39]

$$\psi_s(\mathbf{r}, \beta) = \int_{\mathbf{r}(0)=\mathbf{r}'}^{\mathbf{r}(\beta)=\mathbf{r}} \mathcal{D}[\mathbf{r}(t)] e^{\mathcal{S}_{\text{class}}[\mathbf{r}(\tau), \dot{\mathbf{r}}(\tau)]} \psi(\mathbf{r}), \quad (4.76)$$

where the classical action

$$\mathcal{S}_{\text{class}}[\mathbf{r}(\tau), \dot{\mathbf{r}}(\tau)] = \int_\tau \left\{ \frac{\dot{\mathbf{r}}^2(\tau)}{2} - \varphi[\mathbf{r}(\tau)] \right\} \quad (4.77)$$

appears in the exponent of Eq. (4.76).

The last two expressions are intriguing, since they show that the propagation of a quantum particle from state $\psi_s(\mathbf{r}', 0)$ to $\psi_s(\mathbf{r}, \beta)$ is determined by the sum over all classical paths between the spacetime points $(\mathbf{r}', 0)$ and (\mathbf{r}, β) . Furthermore, the path integral allows to bridge the gap to statistical physics, since the partition function of the system can be written elegantly as

$$z(\beta) = \int d^3 \mathbf{r} \langle \mathbf{r} | e^{-\beta \hat{h}} | \mathbf{r} \rangle = \int_{\mathbf{r}(0)=\mathbf{r}(\beta)} \mathcal{D}[\mathbf{r}(\tau), \mathbf{p}(\tau)] e^{\int_\tau [\mathbf{p}(\tau) \dot{\mathbf{r}}(\tau) - h(\mathbf{r}(\tau), \mathbf{p}(\tau))]} \quad (4.78)$$

4.3 The Path Integral

Here, we emphasize that only periodic paths $\mathbf{r}(0) = \mathbf{r}(\beta)$ in the phase space contribute to $z(\beta)$.

One can show, see Ref. 39, that the path integral carries the time-ordering symbol \hat{T} intrinsically in its definition, so that thermal expectation values of time-ordered observables $\mathcal{O}(\hat{\mathbf{r}}(\tau))$ are given by

$$\frac{\text{Tr} \left\{ \hat{T} \mathcal{O}_1(\hat{\mathbf{r}}, \tau_1) \mathcal{O}_2(\hat{\mathbf{r}}, \tau_2) e^{-\beta \hat{h}} \right\}}{\text{Tr} \left\{ e^{-\beta \hat{h}} \right\}} = \frac{\int \mathcal{D}[\mathbf{r}(\tau)] \mathcal{O}_1(\mathbf{r}(\tau_1)) \mathcal{O}_2(\mathbf{r}(\tau_2)) e^{S[\mathbf{r}(\tau), \dot{\mathbf{r}}(\tau)]}}{\int \mathcal{D}[\mathbf{r}(\tau)] e^{S[\mathbf{r}(\tau), \dot{\mathbf{r}}(\tau)]}} \quad (4.79)$$

Here the trace on the l.h.s. indicates a sum over the position eigenstates.

4.3.1 Path Integral for Quantum Fields

So far we have considered a single particle. In the following, we concentrate ourselves to quantum fields, starting with bosonic fields $\hat{\phi}$, which satisfy the canonical commutation relations

$$\left[\hat{\phi}^\dagger(\mathbf{r}, \tau), \hat{\phi}(\mathbf{r}', \tau) \right] = i\delta(\mathbf{r} - \mathbf{r}'). \quad (4.80)$$

In this case, the path integral (4.75) is generalized straightforwardly by applying the rules of first quantization

$$\mathbf{p}(\tau) \rightarrow i\phi^*(\tau), \quad \mathbf{r}(\tau) \rightarrow \phi(\tau), \quad \dot{\mathbf{r}} = \frac{\partial \mathbf{r}}{\partial t} \rightarrow i \frac{\partial \phi}{\partial \tau} \quad (4.81)$$

in Eq. (4.75) obtaining the grand canonical partition function of bosonic QFT[39]

$$Z_b(\beta) = \int_{\phi(0)=\phi(\beta)} \mathcal{D}[\phi(\tau), \phi^*(\tau)] e^{-\int_\tau [\phi^*(\tau) (\frac{\partial}{\partial \tau}) \phi(\tau) + H(\phi^*(\tau), \phi(\tau))]} \quad (4.82)$$

Here $H(\phi(\tau), \phi^*(\tau))$ is the corresponding Hamiltonian of the considered bosonic QFT and the notation $\phi(\tau) = \int d^3\mathbf{r} \phi(\mathbf{r}, \tau)$ is used.

However, we are interested in the fermionic case, where the electronic field operators $\hat{\psi}, \hat{\psi}^\dagger$, satisfy anticommutation rules (2.26) rather than Eq. (4.80). As a consequence, the fermionic analogue of (4.82) has to be defined, such that the antiperiodicity of the trace, see Eq. 2.115, is taken into account. This is achieved by introducing Grassmann fields $\psi(\tau), \psi^*(\tau)$ with antiperiodic boundary conditions $\psi(0) = -\psi(\beta)$. A short introduction of the Grassmann algebra is given in appendix C.1 and more details can be found in Refs. 39, 47.

4. SPECTRAL PROPERTIES

Within this algebra the electronic path integral assumes the same form as for bosons, with the difference that the PI variables ϕ, ϕ^* are replaced by ψ, ψ^* and reads

$$Z(\beta) = \int_{\psi(0)=-\psi(\beta)} \mathcal{D}[\psi(\tau), \psi^*(\tau)] e^{-\int_{\tau} [\psi^*(\tau)(\frac{\partial}{\partial \tau} + \hat{h})\psi(\tau) + V(\psi^*(\tau), \psi(\tau))]} \quad (4.83)$$

Here, $H = H_0 + V$ was used in combination with the field representation of the non-interacting and interacting Hamiltonians (2.2) and (2.3).

In analogy to chapter 3, the expansion of the factor $e^{-\int_{\tau} V}$ into a series generates the perturbation series of the partition function and the same diagrammatic tools as in chapter 3 can be used within the PI formalism. For this purpose, we introduce the notation

$$\langle\langle \mathcal{O}(\mathbf{r}', \tau') \rangle\rangle_{\beta} = \frac{1}{Z_0(\beta)} \int \mathcal{D}[\psi(\tau), \psi^*(\tau)] \mathcal{O}(\mathbf{r}', \tau') e^{-\int_{\tau} \psi^*(\tau)(\frac{\partial}{\partial \tau} + \hat{h})\psi(\tau)} \quad (4.84)$$

to indicate thermal averaging in terms w.r.t. to the non-interacting system, such that

$$Z(\beta) = \langle\langle e^{-\int_{\tau} V} \rangle\rangle_{\beta} \quad (4.85)$$

holds. This notation should be contrasted to the conventional notation $\langle \cdot \rangle_{\beta}$ defined in Eq. (2.112).

Following the discussion in section 2.7.2, the generating functional $\mathcal{W}[j, j^*]$, defined in Eq. (2.135), can be written in the PI formalism as

$$\mathcal{W}[j, j^*] = \ln \left\{ \langle\langle e^{-\int_{\tau} [V(\tau) + j^*(\tau)\psi(\tau) + \psi^*(\tau)j(\tau)]} \rangle\rangle_{\beta} \right\}. \quad (4.86)$$

Here j, j^* indicate Grassman source fields, which are set to zero after differentiation. For instance the interacting Green's function G reads

$$G(x_1, x_2) = - \frac{\delta^2 \mathcal{W}[j^*, j]}{\delta j(x_1) \delta j^*(x_2)} \Big|_{j^*, j=0}, \quad x_i = (\mathbf{r}_i, \tau_i) \quad (4.87)$$

whereas more general correlation functions can be obtained from

$$G(x_1 \cdots, x_n, x'_1, \cdots, x'_n) = (-1)^n \frac{\delta^{2n} \mathcal{W}[j^*, j]}{\delta j(x_1) \cdots \delta j(x_n) \delta j^*(x'_1) \cdots \delta j^*(x'_n)} \Big|_{j^*, j=0}. \quad (4.88)$$

In the following we use the PI to gain an alternative perspective on the many-body problem in terms of effective Hamiltonians, which describe only a small subset of the full Fock space \mathbb{F} . The corresponding effective Hamiltonian can be obtained after specific degrees freedom of the system are integrated out. For instance integrating out all non-local degrees yields a purely local effective Hamiltonian, which describes only a small set of states localized on specific atoms. This is the topic of the following section. For this purpose it is convenient to consider the many-body Hamiltonian in a localized basis set.

4.4 Effective Hamiltonians

In this section we consider the many-body problem from a localized point of view. Our aim is to derive an effective interaction \mathcal{S}_{eff} , where all degrees of freedom are integrated out, except those at $\mathbf{R} = \mathbf{0}$. For this purpose we closely follow Ayrat *et al.*[73] and use the *cavity method* described in Ref. 74.

4.4.1 The Many-Body problem in the Wannier Basis

As a starting point, we consider a localized basis set $|w_\alpha\rangle$ containing a site index α and a real lattice vector index \mathbf{R}_α by bold Greek indices $\alpha = (\alpha, \mathbf{R}_\alpha)$, *i.e.*

$$\langle \mathbf{r} | w_\alpha \rangle = w_\alpha(\mathbf{r} - \mathbf{R}_\alpha) \quad (4.89)$$

Similarly $\alpha = (\alpha, \mathbf{R}_\alpha = \mathbf{0})$ denotes *local* and $\bar{\alpha} = (\alpha, \mathbf{R}_\alpha \neq \mathbf{0})$ *non-local* states, that is states not centered at $\mathbf{R}_\alpha = \mathbf{0}$. The states $|w_\alpha\rangle$, known as Wannier states and are obtained from the Bloch states $|\phi_{n\mathbf{k}}\rangle$ by an unitary transformation $T_{n\alpha}^{(\mathbf{k})}$ with an additional discrete Fourier transformation[75]

$$|w_\alpha\rangle = \frac{1}{N_{\mathbf{k}}} \sum_{n\mathbf{k}} e^{i\mathbf{k}\mathbf{R}_\alpha} T_{n\alpha}^{(\mathbf{k})} |\phi_{n\mathbf{k}}\rangle. \quad (4.90)$$

Here $N_{\mathbf{k}}$ represents the number of \mathbf{k} -points in the first Brillouin zone. We discuss the construction of Wannier states in section 6.1 in more detail. Here, we only use the fact, that field operators can be decomposed into Wannier states (Einstein summation convention)

$$\hat{\psi}(\mathbf{r}) = w^\alpha(\mathbf{r}) \hat{d}_\alpha, \quad \hat{d}_\alpha = \int d\mathbf{r} w_\alpha^*(\mathbf{r}) \hat{\psi}(\mathbf{r}), \quad (4.91)$$

using the annihilation operator in the Wannier basis

$$\hat{d}_\alpha = \frac{1}{N_{\mathbf{k}}} \sum_{n\mathbf{k}} e^{i\mathbf{k}\mathbf{R}_\alpha} T_{n\alpha}^{(\mathbf{k})} \hat{c}_{n\mathbf{k}}. \quad (4.92)$$

Within this notation and the definitions of the hopping and the Coulomb interaction matrix

$$t_{\alpha\beta} = \langle w_\alpha | \hat{h} | w_\beta \rangle \quad (4.93)$$

$$V_{\alpha\beta\gamma\delta} = \langle w_\alpha, w_\beta | \hat{V} | w_\delta, w_\gamma \rangle, \quad (4.94)$$

4. SPECTRAL PROPERTIES

the normal-ordered many-body Hamiltonian \hat{H} in the interaction picture reads

$$\hat{H}(\tau) = t^{\alpha\beta} \hat{d}_{\alpha}^{\dagger}(\tau) \hat{d}_{\beta}(\tau) + \frac{1}{2} V^{\alpha\beta\gamma\delta} \hat{d}_{\alpha}^{\dagger}(\tau) \hat{d}_{\beta}^{\dagger}(\tau) \hat{d}_{\gamma}(\tau) \hat{d}_{\delta}(\tau). \quad (4.95)$$

In the following we assume that the Wannier states are sufficiently localized in real space, such that

$$V_{\alpha\beta\gamma\delta} \propto \delta(\mathbf{R}_{\alpha} - \mathbf{R}_{\delta}) \delta(\mathbf{R}_{\beta} - \mathbf{R}_{\gamma}) \quad (4.96)$$

is a reasonable approximation.

It is convenient to use the anticommutation rules¹

$$\left\{ \hat{d}_{\alpha}^{\dagger}, \hat{d}_{\beta} \right\} = \delta_{\alpha\beta}, \quad (4.97)$$

to rewrite the Wannier Hamiltonian (4.95) into the density form

$$\hat{H}(\tau) = k^{\alpha\beta} \hat{n}_{\alpha\beta}(\tau) + \frac{1}{2} V^{\alpha\beta\gamma\delta} \hat{n}_{\alpha\delta}(\tau) \hat{n}_{\beta\gamma}(\tau) \quad (4.98)$$

by absorbing the exchange term $-\frac{1}{2} V^{\alpha\gamma\beta}$ into the hopping matrix

$$k^{\alpha\beta} = t^{\alpha\beta} - \frac{1}{2} V^{\alpha\gamma\beta} \quad (4.99)$$

and using the number (or density) operator in the Wannier representation

$$\hat{n}_{\alpha\delta} = \hat{d}_{\alpha}^{\dagger} \hat{d}_{\delta}. \quad (4.100)$$

We emphasize, that there is a variety of different rearrangements of the operators in the interaction term. For instance, one can absorb the Hartree term $V^{\alpha\beta}{}_{\beta}{}^{\delta}$ in the hopping matrix instead, see Ref. 39. However, for reasons that will become clear later on and to be compatible with the assumption made in Eq. (4.96), we choose the rearrangement defined in Eqs. (4.98) and (4.99).

4.5 Local effective Hamiltonians

The Wannier representation (4.98) of the Hamiltonian \hat{H} defines a path integral

$$Z(\beta) = \int \mathcal{D}[d, d^*] e^{-S[d, d^*]}, \quad (4.101)$$

¹ This is a consequence from Eq. (4.92) being a unitary transformation and the canonical anticommutation rules Eq. (2.26).

4.5 Local effective Hamiltonians

with antiperiodic Grassmann variables $d_{\alpha}(\tau + \beta) = -d_{\alpha}(\tau)$. Here, the full many-body action $\mathcal{S} = \mathcal{S}_0 + \mathcal{S}_v$ is divided into a non-interacting \mathcal{S}_0 and interacting action \mathcal{S}_v , given by

$$\mathcal{S}_0[d, d^*] = \int_{\tau} d_{\alpha}^*(\tau) [G_x^{-1}(\tau)]^{\alpha\beta} d_{\beta}(\tau) \quad (4.102)$$

$$\mathcal{S}_v[d, d^*] = \frac{1}{2} \int_{\tau} d_{\alpha}^*(\tau) d_{\delta}(\tau) V^{\alpha\beta\gamma\delta} d_{\beta}^*(\tau) d_{\gamma}(\tau). \quad (4.103)$$

For future reference, the exchange Green's function is introduced

$$[G_x^{-1}(\tau)]^{\alpha\beta} = [\delta^{\alpha\beta} \partial_{\tau} - k^{\alpha\beta}] \quad (4.104)$$

in analogy to the non-interacting propagator G^0 , see section 2.4.

To integrate over all non-local Grassman fields $d_{\alpha}^*, d_{\bar{\beta}}$, we use the bosonic variables $n_{\alpha\beta} = d_{\alpha}^* d_{\beta}$ with periodic boundary conditions $n_{\alpha\beta}(\tau + \beta) = n_{\alpha\beta}(\tau)$. The latter property allows for a Hubbard-Stratonovich transformation of the kind (C.15) to decouple the interaction term $e^{-\mathcal{S}_v}$ in Eq. (4.101), to obtain

$$Z(\beta) \propto \int \mathcal{D}[d, d^*, \phi] e^{-\mathcal{S}[d, d^*, \phi]} \quad (4.105)$$

with

$$\begin{aligned} \mathcal{S}[d, d^*, \phi] &= \int_{\tau} d_{\alpha}^*(\tau) [G_x^{-1}(\tau)]^{\alpha\beta} d_{\beta}(\tau) \\ &+ \frac{1}{2} \int_{\tau} \phi_{\alpha\delta}(\tau) [V^{-1}]^{\alpha\beta\gamma\delta} \phi_{\beta\gamma}(\tau) + i \int_{\tau} \phi_{\alpha\beta}(\tau) n^{\alpha\beta}(\tau). \end{aligned} \quad (4.106)$$

using the auxiliary real-valued bosonic fields $\phi_{\alpha\beta}(\tau)$. [76]

In the next step, one splits this action into three parts, a local

$$\begin{aligned} \mathcal{S}_{\text{loc}}[d, d^*, \phi] &= \int_{\tau} d_{\alpha}^*(\tau) [G_x^{-1}(\tau)]^{\alpha\beta} d_{\beta}(\tau) \\ &+ \frac{1}{2} \int_{\tau} \phi_{\alpha\delta}(\tau) [V^{-1}]^{\alpha\beta\gamma\delta} \phi_{\beta\gamma}(\tau) + i \int_{\tau} \phi_{\alpha\beta}(\tau) n^{\alpha\beta}(\tau), \end{aligned} \quad (4.107)$$

a non-local

$$\begin{aligned} \mathcal{S}_{\text{nloc}}[d, d^*, \phi] &= \int_{\tau} d_{\bar{\alpha}}^*(\tau) [G_x^{-1}(\tau)]^{\bar{\alpha}\bar{\beta}} d_{\bar{\beta}}(\tau) \\ &+ \frac{1}{2} \int_{\tau} \phi_{\bar{\alpha}\bar{\delta}}(\tau) [V^{-1}]^{\bar{\alpha}\bar{\beta}\bar{\gamma}\bar{\delta}} \phi_{\bar{\beta}\bar{\gamma}}(\tau) + i \int_{\tau} \phi_{\bar{\alpha}\bar{\beta}}(\tau) n^{\bar{\alpha}\bar{\beta}}(\tau), \end{aligned} \quad (4.108)$$

4. SPECTRAL PROPERTIES

and a mixed term

$$\begin{aligned} \mathcal{S}_{\text{mix}}[d, d^*, \phi] &= - \int_{\tau} t^{\alpha\bar{\beta}} \left[d_{\alpha}^*(\tau) d_{\bar{\beta}}(\tau) + d_{\bar{\beta}}^*(\tau) d_{\alpha}(\tau) \right] \\ &\quad + \int_{\tau} \phi_{\alpha\delta}(\tau) [V^{-1}]^{\alpha\bar{\beta}\bar{\gamma}\delta} \phi_{\bar{\beta}\bar{\gamma}}(\tau) \end{aligned} \quad (4.109)$$

by appropriately restricting the summation over Wannier states α into local $\bar{\alpha} = (\alpha, \mathbf{R}_{\alpha} \neq \mathbf{0})$ and non-local states $\alpha = (\alpha, \mathbf{R}_{\alpha} = \mathbf{0})$ respectively. In arriving at Eqs. (4.107)-(4.109) Eq. (4.96) was used, which implies both, $k^{\alpha\bar{\beta}} = t^{\alpha\bar{\beta}}$ and $\phi_{\bar{\beta}\bar{\gamma}} n^{\bar{\beta}\bar{\gamma}} = 0$, and reveals the reason of the rearrangement in the Hamiltonian (4.98). Furthermore, the last term of Eq. (4.109) was obtained using the relation

$$\frac{1}{2} \phi_{\alpha\delta}(\tau) \left([V^{-1}]^{\alpha\bar{\beta}\bar{\gamma}\delta} + \underbrace{[V^{-1}]^{\bar{\beta}\alpha\delta\bar{\gamma}}}_{[V^{-1}]^{\alpha\bar{\beta}\bar{\gamma}\delta}} \right) \phi_{\bar{\beta}\bar{\gamma}}(\tau) = \phi_{\alpha\delta}(\tau) [V^{-1}]^{\alpha\bar{\beta}\bar{\gamma}\delta} \phi_{\bar{\beta}\bar{\gamma}}(\tau). \quad (4.110)$$

Now the auxiliary fermionic and bosonic field variables

$$\eta_{\bar{\beta}}(\tau) = t_{\alpha\bar{\beta}} d^{\alpha}(\tau) \quad (4.111)$$

$$\zeta^{\bar{\beta}\bar{\gamma}}(\tau) = \phi_{\alpha\delta}(\tau) [V^{-1}]^{\alpha\bar{\beta}\bar{\gamma}\delta} \quad (4.112)$$

are introduced and the mixed term (4.109) is rewritten into

$$\begin{aligned} \mathcal{S}_{\text{mix}}[d, d^*, \phi, \eta^*, \eta, \zeta] &= - \int_{\tau} \left[\eta_{\bar{\beta}}^*(\tau) d^{\bar{\beta}}(\tau) + d_{\bar{\beta}}^*(\tau) \eta^{\bar{\beta}}(\tau) \right] \\ &\quad + \int_{\tau} \zeta^{\bar{\beta}\bar{\gamma}}(\tau) \phi_{\bar{\beta}\bar{\gamma}}(\tau). \end{aligned} \quad (4.113)$$

This expression reveals, that \mathcal{S}_{mix} contains all fermionic and bosonic source fields for a system with a cavity at $\mathbf{R} = \mathbf{0}$. Hence, in analogy to Eq. (4.88) and Eq. (4.86) the corresponding generating functional $\overline{\mathcal{W}}[\eta^*, \eta, \zeta]$ for all connected fermionic and bosonic Green's functions of the system (with a cavity) is given by

$$\overline{\mathcal{W}}[\eta^*, \eta, \zeta] = \ln \int \mathcal{D}[d^*, d, \phi] \Big|_{\mathbf{R} \neq \mathbf{0}} e^{-\mathcal{S}_{\text{nlloc}}[d^*, d, \phi] - \mathcal{S}_{\text{mix}}[d^*, d, \phi, \eta^*, \eta, \zeta]} \quad (4.114)$$

and the corresponding interacting correlation functions are obtained as derivatives

$$\overline{G}_{\bar{\alpha}_1 \dots \bar{\beta}_n}(\tau_1, \dots, \tau'_n) = (-1)^n \frac{\delta^{2n} \overline{\mathcal{W}}[\eta^*, \eta, 0]}{\delta \eta_{\bar{\alpha}_1}^*(\tau_1) \dots \delta \eta_{\bar{\alpha}_n}^*(\tau'_n) \delta \eta_{\bar{\beta}_n}(\tau'_n) \dots \delta \eta_{\bar{\beta}_1}(\tau_1)} \Big|_{\eta, \eta^* = 0} \quad (4.115)$$

$$\overline{W}_{\bar{\alpha}_1 \dots \bar{\beta}_n}(\tau_1, \dots, \tau'_n) = \frac{1}{2^n} \frac{\delta^{2n} \overline{\mathcal{W}}[0, 0, \zeta]}{\delta \zeta_{\bar{\alpha}_1 \bar{\delta}_1}(\tau_1) \dots \delta \zeta_{\bar{\alpha}_n \bar{\delta}_n}(\tau'_n) \delta \zeta_{\bar{\beta}_n \bar{\gamma}_n}(\tau'_n) \dots \delta \zeta_{\bar{\beta}_1 \bar{\gamma}_1}(\tau_1)} \Big|_{\zeta = 0} \quad (4.116)$$

4.5 Local effective Hamiltonians

We emphasize that \bar{G} and \bar{W} is the propagator, respectively the effective interaction, of a system with removed primitive cell at $\mathbf{R} = \mathbf{0}$. Alternatively, one obtains \bar{G} and \bar{W} via the PIs

$$\bar{G}_{\bar{\alpha}_1 \dots \bar{\beta}_n}(\tau_1, \dots, \tau'_n) = \frac{\int \mathcal{D}[d^*, d] |_{\mathbf{R} \neq \mathbf{0}} d_{\bar{\alpha}_1}(\tau_1) \dots d_{\bar{\beta}_n}^*(\tau'_n) e^{-\mathcal{S}_{\text{nlloc}} - \mathcal{S}_{\text{mix}}}}{\int \mathcal{D}[d^*, d] |_{\mathbf{R} \neq \mathbf{0}} e^{-\mathcal{S}_{\text{nlloc}} - \mathcal{S}_{\text{mix}}}} \quad (4.117)$$

$$\bar{W}_{\bar{\alpha}_1 \dots \bar{\beta}_n}(\tau_1, \dots, \tau'_n) = \frac{1}{2^n} \frac{\int \mathcal{D}[\phi] |_{\mathbf{R} \neq \mathbf{0}} \phi_{\bar{\alpha}_1 \bar{\delta}_1}(\tau_1) \dots \phi_{\bar{\beta}_n \bar{\gamma}_n}(\tau'_n) e^{-\mathcal{S}_{\text{nlloc}} - \mathcal{S}_{\text{mix}}}}{\int \mathcal{D}[\phi] |_{\mathbf{R} \neq \mathbf{0}} e^{-\mathcal{S}_{\text{nlloc}} - \mathcal{S}_{\text{mix}}}} \quad (4.118)$$

These correlation functions must not be confused with the correlation functions G, W of the full system.[74]

On the one side, Eqs. (4.115) and (4.116) imply an explicit expression for the cavity functional (4.114) in terms of correlation functions

$$\begin{aligned} \bar{W}[\eta, \eta^*, \zeta] &= \sum_{n=1}^{\infty} (-1)^n \int_{\tau_1} \dots \int_{\tau'_n} \eta_{\bar{\alpha}_1}^*(\tau_1) \dots \bar{G}^{\bar{\alpha}_1, \dots, \bar{\beta}_n}(\tau_1, \dots, \tau'_n) \eta_{\bar{\beta}_1}(\tau'_1) \dots \\ &+ \sum_{n=1}^{\infty} \frac{1}{2^n} \int_{\tau_1} \dots \int_{\tau'_n} \zeta_{\bar{\alpha}_1 \bar{\delta}_1}(\tau_1) \dots \bar{W}^{\bar{\alpha}_1 \bar{\beta}_1, \dots, \bar{\gamma}_n \bar{\delta}_n}(\tau_1, \dots, \tau'_n) \zeta_{\bar{\beta}_1 \bar{\gamma}_1}(\tau'_1) \dots \end{aligned} \quad (4.119)$$

On the other side, Eqs. (4.111), (4.112) show that $\bar{W}[\eta, \eta^*, \zeta]$ depends only on local variables d_α, d_β^* and $\phi_{\alpha\beta}$, so that the integration over all non-local states in the partition function (4.105) can be carried out and yields an factor $e^{\bar{W}[\eta, \eta^*, \zeta]}$ in the same path integral.

The resulting expression has only local terms, so that the partition function of the complete system reads

$$Z(\beta) \propto \int \mathcal{D}[d, d^*, \phi] |_{\mathbf{R}=\mathbf{0}} e^{-\mathcal{S}_{\text{eff}}[d, d^*, \phi, \eta, \eta^*, \zeta]} \quad (4.120)$$

and contains the effective *local* action \mathcal{S}_{eff} , we are looking for

$$\mathcal{S}_{\text{eff}}[d, d^*, \phi, \eta, \eta^*, \zeta] = \mathcal{S}_{\text{loc}}[d, d^*, \phi] - \bar{W}[\eta, \eta^*, \zeta]. \quad (4.121)$$

Finally the ϕ -integration can be evaluated with the inverse Hubbard-Stratonovich transformation (C.15) and one obtains for the partition function

$$Z(\beta) = \int \mathcal{D}[d, d^*] |_{\mathbf{R}=\mathbf{0}} e^{-\mathcal{S}_{\text{eff}}[d, d^*]}. \quad (4.122)$$

4. SPECTRAL PROPERTIES

Here the effective action

$$\begin{aligned} \mathcal{S}_{\text{eff}}[d, d^*] &= \int_{\tau_1} \int_{\tau'_1} d_\alpha^*(\tau_1) [\mathcal{G}^{-1}]^{\alpha\beta}(\tau_1 - \tau'_1) d_\beta(\tau'_1) \\ &+ \frac{1}{2} \int_{\tau_1} \int_{\tau'_1} n_{\alpha\delta}(\tau_1) \mathcal{U}^{\alpha\beta\gamma\delta}(\tau_1 - \tau'_1) n_{\beta\gamma}(\tau'_1) \end{aligned} \quad (4.123)$$

contains the correlation functions

$$\begin{aligned} [\mathcal{G}^{-1}]^{\alpha\beta}(\tau_1 - \tau'_1) &= [G_{\mathbf{x}}^{-1}(\tau_1 - \tau'_1)]^{\alpha\beta} \\ &- t^{\alpha\bar{\mu}_1} [\bar{G}_{\bar{\mu}_1\bar{\nu}_1}(\tau_1 - \tau'_1) + \dots] t^{\beta\bar{\nu}_1} \end{aligned} \quad (4.124)$$

$$\begin{aligned} [\mathcal{U}^{-1}]_{\alpha\beta\gamma\delta}(\tau_1 - \tau'_1) &= [V^{-1}]^{\alpha\beta\gamma\delta} \delta(\tau_1 - \tau'_1) \\ &- [V^{-1}]_{\alpha\bar{\mu}_1\bar{\nu}_1\delta} [\bar{W}^{\bar{\mu}_1\bar{\beta}_1\bar{\gamma}_1\bar{\nu}_1}(\tau_1 - \tau'_1) + \dots] [V^{-1}]_{\bar{\beta}_1\bar{\beta}_1\bar{\gamma}_1\bar{\gamma}_1} \end{aligned} \quad (4.125)$$

where the dots indicate terms of Eq. (4.119) with $n > 1$.

Expression (4.123) has the form of an impurity model, where the impurity cell is located at $\mathbf{R} = \mathbf{0}$ and interacts with an effective, surrounding medium. This medium is described by the cavity correlation functions \bar{G} and \bar{W} , appearing on the r.h.s. of Eqs. (4.124) and (4.125). These cavity functions correct the local exchange Green's function $G_{\mathbf{x}}^{\alpha\beta}$ and the local bare Coulomb interaction $V_{\alpha\beta\gamma\delta}$ of the lattice, yielding the non-interacting *impurity propagator* $\mathcal{G}_{\alpha\beta}(\tau)$, respectively the bare *impurity* interaction $\mathcal{U}_{\alpha\beta\gamma\delta}(\tau)$. The latter describes the interaction between impurity states, whereas the former can be seen as an undressed propagation from site β to site α . The corresponding dressed propagation, *i.e.* the interacting Green's function of the impurity can be obtained as a path integral

$$[G_{\text{imp}}]_{\alpha\beta}(\tau) = \langle\langle d_\alpha(\tau) d_\beta^* \rangle\rangle = - \frac{\int \mathcal{D}[d, d^*] |_{\mathbf{R}=\mathbf{0}} d_\alpha(\tau) d_\beta^* e^{-\mathcal{S}_{\text{eff}}[d, d^*]}}{\int \mathcal{D}[d, d^*] |_{\mathbf{R}=\mathbf{0}} e^{-\mathcal{S}_{\text{eff}}[d, d^*]}}. \quad (4.126)$$

We emphasize that $[G_{\text{imp}}]_{\alpha\beta}$ is both, the interacting Green's function of the impurity model (4.123), as well as the interacting Feynman propagator $G_{\alpha\beta}$ of the full many-body Hamiltonian (4.98) restricted to the unit cell $\mathbf{R} = \mathbf{0}$. Similar arguments hold for the dressed impurity interaction W_{imp} and W , see Ref. 73, so that, we deduce effective Dyson equations for the impurity model (4.123)

$$G_{\alpha\beta}(i\omega_n) = \mathcal{G}_{\alpha\beta}(i\omega_n) + \mathcal{G}_{\alpha\gamma}(i\omega_n) \Sigma_{\text{imp}}^{\gamma\delta}(i\omega_n) G_{\delta\beta}(i\omega_n) \quad (4.127)$$

$$W_{\alpha\beta\gamma\delta}(i\nu_n) = \mathcal{U}_{\alpha\beta\gamma\delta}(i\nu_n) + \mathcal{U}_{\alpha\mu\nu\delta}(i\nu_n) \chi_{\text{imp}}^{\nu\mu\rho\sigma}(i\nu_n) W_{\rho\beta\gamma\sigma}(i\nu_n). \quad (4.128)$$

4.5 Local effective Hamiltonians

Here Σ_{imp} is the effective, irreducible self-energy and χ_{imp} the corresponding bosonic counterpart (irreducible polarizability) of the impurity model. Since the former is a fermionic and the latter a bosonic quantity, ω_n represents fermionic and ν_n bosonic Matsubara frequencies.[73] The fermionic and bosonic self-energies Σ_{imp} and χ_{imp} differ from the lattice self-energies Σ and χ , because the non-interacting fermionic and bosonic propagators \mathcal{G} and \mathcal{U} of the impurity model differ from G^0 , respectively V [see (4.124), (4.125)].

However, one can show that in the limit of infinite dimensions $d \rightarrow \infty$, the self-energies of the impurity coincide with the local self-energies of the full many-body Hamiltonian \hat{H}

$$\lim_{d \rightarrow \infty} [\Sigma_{\text{imp}}]_{\alpha\beta} = \Sigma_{\alpha\beta} \quad (4.129)$$

$$\lim_{d \rightarrow \infty} [\chi_{\text{imp}}]_{\alpha\beta\gamma\delta} = \chi_{\alpha\beta\gamma\delta}. \quad (4.130)$$

The first limit is the starting point of dynamical mean field theory (DMFT), whereas the inclusion of the second limit is used in extended DMFT (eDMFT). In the following we concentrate ourselves on DMFT, more about eDMFT can be found in Ref. 73.

4.5.1 Dynamical Mean Field Theory

We consider standard DMFT in this section, which is traditionally formulated for the Hubbard model. Within this model the hopping matrix $t^{\alpha\beta}$ is restricted to nearest neighbors, which we indicate by the symbol $t^{\langle\alpha\beta\rangle}$ in the following. Originally, the Hubbard model takes only static interactions between opposite spins on the same site into account, see Ref. 77. However, we allow for additional interactions and consider the following model

$$\hat{H}_{\text{mod}} = t^{\langle\alpha\beta\rangle} \hat{d}_{\alpha}^{\dagger} \hat{d}_{\beta} + \frac{1}{2} V^{\alpha\beta\beta\alpha} \hat{n}_{\alpha\alpha} \hat{n}_{\beta\beta}, \quad (4.131)$$

where the interactions are restricted to the unit cell.

Despite of its simplicity, it turns out that the Hubbard model has a rich phase diagram and describes a vast number of physical phenomena, including Mott-Hubbard transitions, the Kondo effect and many kinds of magnetism, see Ref. 78 for an introduction with selected results. These phenomena stem mostly from partially filled narrow bands around the Fermi surface, which demand an accurate description of correlation effects beyond

4. SPECTRAL PROPERTIES

the mean-field (DFT or HF) or even the GWA level. Therefore, one characterizes these systems as *strongly correlated* and often tries to describe them by applying a model of the Hubbard form (4.131).

However, the attempt to solve (4.131) (or similar models) for $d = 3$ dimensions often fails, due to the high dimension of the corresponding Hilbert space. In fact, today only for $d = 1$ and one single Wannier state the Hubbard model can be solved analytically, see Refs. 79, 80. Metzner and Vollhardt tackled this problem not from the low-dimensional, but from the high-dimensional limit, see Ref. 81. They considered the Hubbard model for $d \rightarrow \infty$ dimensions and showed that a non-trivial limit of Eq. (4.131) is obtained if the hopping amplitude is scaled simultaneously according to

$$t_{\alpha\beta} \rightarrow \frac{1}{\sqrt{z_d}} \tilde{t}_{\alpha\beta}, \quad (4.132)$$

where $z_d \in \mathcal{O}(d)$ is the coordination number of the lattice in d dimensions and $\tilde{t}_{\alpha\beta}$ finite for $d \rightarrow \infty$.¹ In the case of our model, defined in Eq. (4.131), the second term has to be scaled as well

$$V^{\alpha\beta\beta\gamma} \rightarrow \frac{1}{z_d} \tilde{V}^{\alpha\beta\beta\gamma} \quad (4.133)$$

(with finite \tilde{V}) to yield a non-trivial limit for $d \rightarrow \infty$, see Ref. 82.

Simple power counting arguments can be used, see Ref. 82, to show that only the first term in the $[\cdot]$ -brackets of Eqs. (4.124) and (4.125) survive for $d \rightarrow \infty$. Consequently, the effective action \mathcal{S}_{eff} of Eq. (4.123) for the model (4.131) in the limit $d \rightarrow \infty$ assumes the form

$$\begin{aligned} \mathcal{S}_{\infty}[d, d^*] &= \lim_{d \rightarrow \infty} \mathcal{S}_{\text{eff}}[d, d^*] \\ &= - \int_{\tau} \left[\int_{\tau'} d_{\alpha}^*(\tau) [\mathcal{G}^{-1}]^{\alpha\beta} (\tau - \tau') d_{\beta}(\tau') + \frac{1}{2} n_{\alpha\delta}(\tau) \mathcal{U}^{\alpha\beta\gamma\delta} n_{\alpha\delta}(\tau) \right] \end{aligned} \quad (4.134)$$

with the Weiss field (4.124) given by

$$[\mathcal{G}^{-1}]^{\alpha\beta} (\tau - \tau') = \delta(\tau - \tau') \delta^{\alpha\beta} \partial_{\tau} - t^{\alpha\bar{\mu}} \overline{G}_{\bar{\mu}\bar{\nu}}(\tau - \tau') t^{\beta\bar{\nu}}, \quad (4.135)$$

This result follows from $t^{\langle\alpha\beta\rangle} = 0$ and the fact that the Hubbard model (4.131) already has the density form of (4.98).

¹ This scaling relation follows from the fact that the density of states for $V = 0$ and $d \rightarrow \infty$ is finite, see Ref. 81.

4.5 Local effective Hamiltonians

This expression simplifies on the Matsubara axis $i\omega_n$,

$$[\mathcal{G}^{-1}]^{\alpha\beta}(i\omega_n) = \delta^{\alpha\beta}i\omega_n - t^{\alpha\bar{\mu}} \bar{G}_{\bar{\mu}\bar{\nu}}(i\omega_n)t^{\beta\bar{\nu}} \quad (4.136)$$

Furthermore, using simple power counting arguments, see Ref. 74, the cavity Green's function can be related to the local lattice propagator G via

$$\bar{G}_{\bar{\mu}\bar{\nu}} = G_{\bar{\mu}\bar{\nu}}(i\omega_n) - G_{\bar{\mu}\gamma}(i\omega_n) [G^{-1}(i\omega_n)]^{\gamma\delta} G_{\delta\bar{\nu}}(i\omega_n), \quad (4.137)$$

which finally results after rewriting Eq. (4.136), see Ref. 73, in

$$[\mathcal{G}^{-1}(i\omega_n)]_{\alpha\beta} = [G^{-1}(i\omega_n)]_{\alpha\beta} + \Sigma_{\alpha\beta}(i\omega_n). \quad (4.138)$$

This expression reveals the connection between a fictitious impurity model located at $\mathbf{R} = \mathbf{0}$ (and determined by \mathcal{G} and \mathcal{U}) and the Hubbard model determined by the renormalized Feynman propagator G and its self-energy Σ . This relationship is exact only in the limit of infinite dimensions. However, it turns out that the identification of the interacting Green's function of the impurity with the local interacting Green's function of the lattice is an excellent approximation for strongly correlated systems in finite dimensions, like $d = 3$. [81] Therefore, Eq. (4.138) is exploited in practice to solve the Hubbard model in finite dimensions by determining the Weiss field \mathcal{G} in Eq. (4.138) self-consistently. This can be done using following algorithm

DMFT Algorithm

- D1 Start with some initial guess for the Weiss field \mathcal{G} and choose a fixed impurity interaction \mathcal{U} .
- D2 Compute the impurity propagator G_{imp} with Eq. (4.126) for the action (4.134) and extract its self-energy with $\Sigma_{\text{imp}} = \mathcal{G}^{-1} - G_{\text{imp}}^{-1}$. This self-energy approximates the local self-energy of the Hubbard model.
- D3 Compute the interacting propagator G of the lattice with $G^{-1} = \Sigma + G_0^{-1}$, where G_0 is the non-interacting Green's function of the Hubbard model.
- D4 The resulting propagator of D3 is used to determine a new estimate for the Weiss field via $\mathcal{G}^{-1} = \Sigma_{\text{imp}} + G^{-1}$.
- D5 Iterate D2-D4 until $|\mathcal{G}^{(n+1)} - \mathcal{G}^{(n)}| \rightarrow 0$.

4. SPECTRAL PROPERTIES

This algorithm yields a good estimate for the interacting Green's function of the Hubbard model. However, the Hubbard model cannot describe the physics of real materials in any detail. Heuristically speaking, DMFT describes only local correlation effects and fails in general to capture non-local many-body effects. Realistic approaches, on the other hand, have to take into account both, local and non-local correlations.

For this purpose the LDA+DMFT method was developed, see Ref. 83 for a comprehensive overview. Within LDA+DMFT the interacting Green's function G (used in step D3) is computed from the KS hopping matrix

$$t_{\alpha\beta}^{(\mathbf{k})} = T_{\alpha n}^{(\mathbf{k})} \epsilon_{n\mathbf{k}} T_{\beta n}^{(\mathbf{k})}. \quad (4.139)$$

via

$$[G^{-1}(i\omega_n)]_{\alpha\beta} = \frac{1}{N_{\mathbf{k}}} \sum_{\mathbf{k}} \left[(i\omega_n + \mu) \delta_{\alpha\beta} - t_{\alpha\beta}^{(\mathbf{k})} - \Sigma_{\alpha\beta}(i\omega_n) + (t_{\text{dc}})_{\alpha\beta}^{(\mathbf{k})} \right]. \quad (4.140)$$

Here $\Sigma_{\alpha\beta}(i\omega_n)$ is the local self-energy of the impurity given on the Matsubara axis ω_n , μ the chemical potential and (t_{dc}) the double-counting correction.[84] The last term is present, due to the fact that the LDA (or any other KS) hopping matrix $t_{\alpha\beta}^{(\mathbf{k})}$ contains local correlation terms, which are also included in the local self-energy $\Sigma_{\alpha\beta}(i\omega_n)$. In the ideal case, these terms are described by $(t_{\text{dc}})_{\alpha\beta}^{(\mathbf{k})}$, however, in practice this term is unknown, because of the non-diagrammatic nature of DFT. This issue is known as *double counting problem* and is typically treated by approximating $(t_{\text{dc}})_{\alpha\beta}^{(\mathbf{k})} = \mu_{\text{dc}} \delta_{\alpha\beta}$ and absorbing the term into the chemical potential. More about the (ambiguous) computation of μ_{dc} is found in Refs. 85, 86 and will not be considered here.

In the following, we follow a more promising route, the combination of the GW with the DMFT approximation. The reason for this is that in GW +DMFT, studied first by Biermann *et al.* in their seminal paper [87], both approaches can be formulated in the diagrammatic language. This has the advantage that, on the one side, the double counting terms can be identified in principle unambiguously within GW +DMFT. On the other side, the GW formalism can be used to determine the effective interaction matrix \mathcal{U} of the impurity model (4.134) and is discussed in detail in section 6.1.3.

Part II

Methodological Developments

5

Low Scaling Algorithm for the Random Phase Approximations

The following chapter presents an efficient zero-temperature RPA algorithm, which scales cubically with the number of electrons N in the system. To keep the notation simple in this chapter, we write G instead of G^0 for the non-interacting Green's function, χ for the independent-particle polarizability χ^0 and suppress the imaginary unit i in the frequency arguments of χ . Furthermore, to avoid confusion we use $\hat{\chi}$ to indicate the imaginary time polarizabilities.

The following chapter was published in Refs. 88 and 89.

5.1 Computational Scheme

We have implemented an RPA algorithm for periodic systems at zero-temperature,¹ which is summarized by the flow diagram shown in Fig. 5.1. This figure shows that the ACFDT formula Eq. (3.37) is only the last step in the calculation of the RPA correlation energy E_c^{RPA} . The evaluation of this step was presented in Ref. 90 and will not be discussed in this thesis. Here, we concentrate on the preceding steps, which are technically more demanding. We discuss each step of Fig. 5.1 in detail in reverse order starting with the cosine transformation (CT) of χ from imaginary time to imaginary frequency

¹Finite-temperature effects are not considered here, but can be included easily by using finite-temperature Green's functions.

5. LOW SCALING ALGORITHM FOR THE RANDOM PHASE APPROXIMATIONS

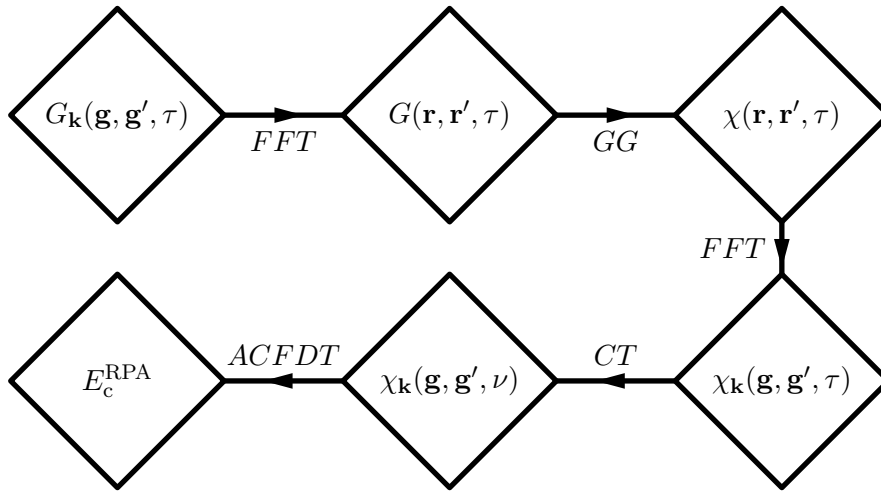


Figure 5.1: Calculation scheme for the RPA correlation energy E_c^{RPA} adopted in this paper. The first and third step is a spatial fast fourier transformation (FFT) described in Sec. 5.3. The second step is the contraction of two Green's functions in the space-time domain (GG) giving the independent-particle polarizability χ (see Sec. 5.4). The cosine transformation (CT) in the fourth step is described in Sec. 5.2.3. The ACFDT is formulated in Eq. (3.37).

in section 5.2. The fast fourier transformation (FFT) of χ from real to reciprocal space is discussed in section 5.3 followed by the contraction step (GG) in section 5.4.

5.2 Imaginary Time and Frequency Grids

The following section was published in Ref. 88.

The fourth step of the RPA algorithm, denoted as CT, is the transformation of the polarizability $\chi_{\mathbf{k}}^0(\mathbf{g}, \mathbf{g}', \tau)$ to the imaginary frequency domain $\chi_{\mathbf{k}}^0(\mathbf{g}, \mathbf{g}', \nu)$. For an accurate discrete Fourier transformation, an equally spaced grid for the time and frequency domain necessitates a few hundred grid points, see Ref. 69. This makes the calculations rather expensive, so that the break even point between the traditional $\mathcal{O}(N^4)$ algorithm and the lower scaling $\mathcal{O}(N^3)$ algorithm is reached only for very large systems. Such large systems are then also difficult to handle, since the storage demands for the polarizability at many frequency points can easily exceed the available memory even on modern large scale computers. This implies that the approach can be applied to large systems only if the number of grid points τ_i, ν_k , which are needed for an accurate representation of the functions $\chi_{\mathbf{k}}^0(\mathbf{g}, \mathbf{g}', \tau)$ and $\chi_{\mathbf{k}}^0(\mathbf{g}, \mathbf{g}', \nu)$, as well as their Fourier transformation, is kept as small as possible.

5.2 Imaginary Time and Frequency Grids

In this section, we first determine tailor-made quadratures for the direct second order Møller-Plesset (MP2) energy in the *imaginary frequency* domain (as opposed to the usual imaginary time domain used in the Laplace-transformed MP2 (LT-MP2) method.[91]). Apart from comparing the Minimax and least square quadratures for the LT-MP2 method, we show that our frequency grid is also able to integrate the RPA correlation energy accurately using ≈ 16 quadrature points. In addition, approximating the Fourier integral of the polarizability by means of a quadrature formula, we find an elegant method to switch from imaginary time to imaginary frequency polarizabilities (and vice versa) without using an interpolation technique or significantly increasing the number of grid points. This allows to evaluate RPA energies with well-controlled approximations (time and frequency grids) with $\mathcal{O}(N^3)$ scaling.

The section is organized as follows. In section 5.2.1 and 5.2.2 we review the necessary mathematical background for tailor-made quadrature formulas. In section 5.2.3, we present a method for the accurate determination of the cosine integral of χ in terms of the imaginary time counterpart $\hat{\chi}$. In section 5.2.5 and 5.2.6 we compare the convergence behavior of the Minimax and least square quadratures for MP2 and RPA calculations. In addition, results for RPA and direct MP2 energies using the non-uniform cosine transformation established in 5.2.3 are given in section 5.2.5 and 5.2.6.

5.2.1 The Fitting Problem

Given a function $f: I = [1, R] \rightarrow \mathbb{R}$ with $R > 1$ and a model function $y: \mathbb{R} \times I \rightarrow \mathbb{R}$, the fitting problem is stated as follows: find the set of coefficients $\boldsymbol{\alpha} = (\alpha_1, \dots, \alpha_n)$, $\boldsymbol{\beta} = (\beta_1, \dots, \beta_n) \in \mathbb{R}^n$ such that the error function

$$\eta(\boldsymbol{\alpha}, \boldsymbol{\beta}, \xi) = f(\xi) - \sum_{i=1}^n \beta_i y(\alpha_i, \xi) \quad (5.1)$$

is minimal with respect to one of the following norms

$$\|\eta\|_2 = \int_1^R d\xi |\eta(\boldsymbol{\alpha}, \boldsymbol{\beta}, \xi)|^2 \quad (5.2)$$

$$\|\eta\|_\infty = \max \{ |\eta(\boldsymbol{\alpha}, \boldsymbol{\beta}, \xi)| \in \mathbb{R} : \xi \in I \}. \quad (5.3)$$

Minimization w.r.t. $\|\cdot\|_2$ gives the least square (LS) coefficients $\boldsymbol{\alpha}^0$ and $\boldsymbol{\beta}^0$. The corresponding fit minimizes the average or *mean error*, but results in an uneven distribution of the error in the interval I , with errors depending on the distribution of the points ξ .

5. LOW SCALING ALGORITHM FOR THE RANDOM PHASE APPROXIMATIONS

A possible way of computing α^0 and β^0 for non-linear fitting problems is the Levenberg-Marquardt algorithm, see Ref. 92, or the variable projection algorithm of Golub and Pereyra.[93] In this work we use exclusively the latter method.

On the other side, minimizing η w.r.t. $\|\cdot\|_\infty$ gives the so called Minimax (MM) solution α^*, β^* .[94] This means that the *maximum error* is minimized and the error is consequently equally distributed inside the interval I . Usually this is desired if the distribution of the ξ points is unknown. Note that throughout this paper we will always use an asterisk, α_i^*, β_i^* , when referring to grids and weights corresponding to Minimax solutions, whereas the conventional least square grids will carry the superscript 0.

Implementations calculating α^*, β^* use typically the Remez algorithm, which relies on Chebyshev's alternation theorem.[95] This theorem states that in the Minimax approximation the error function satisfies

$$\eta(\alpha^*, \beta^*, \xi_j) = (-1)^j \epsilon, \quad \forall j = 1, \dots, 2N + 1, \quad \epsilon > 0 \quad (5.4)$$

where the points ξ_j are the local extrema of η . In total there are $2N + 1$ minima and maxima leading to $2N + 1$ linear independent equations (5.4): $2N$ equations for the coefficients α, β and one for the minimized error extremum ϵ .

Assuming we have a starting guess (say α^0 and β^0) for the coefficients, we can apply the Remez algorithm:

- R1 Find all extrema $\{\xi_j\}_{j=1}^{2N+1}$ of η .
- R2 Solve (5.4) for α, β and ϵ at the determined extrema ξ_j .
- R3 Update coefficients and error α, β and ϵ .
- R4 Iterate R1-R4 until convergence.

The solution of the fitting problem can be used in order to find optimal quadrature formulas for the numerical evaluation of integrals. In the following, we discuss the application for integrals appearing in RPA and MP2.

5.2 Imaginary Time and Frequency Grids

5.2.2 Integral Quadrature Formulas for RPA and Direct MP Energies

We are interested primarily in the numerical evaluation of the RPA correlation energy at zero-temperature given in Eq. (3.37). To keep notation simple we write χ for χ^0 and focus ourselves only on the frequency, respectively the time dependence of the independent particle polarizability. Furthermore the trace symbol in (3.37) will be suppressed in this chapter.

The lowest contribution ($n = 2$) to the RPA is the direct MP2 correlation energy and reads[96, 97]

$$E_c^{(2)} = \frac{1}{8\pi} \int_{-\infty}^{\infty} d\nu \{\chi(\nu)V\}^2. \quad (5.5)$$

Instead of evaluating this integral in the *imaginary frequency* domain, we can insert the Fourier transformation

$$\chi(\nu) = \int_{-\infty}^{\infty} d\tau \hat{\chi}(\tau) e^{i\nu\tau} \quad (5.6)$$

into Eq. (5.5) and use $\int d\nu e^{\pm i\nu(\tau+\tau')} = 2\pi\delta(\tau+\tau')$ in order to obtain the corresponding *imaginary time* representation

$$E_c^{(2)} = \frac{1}{4} \int_{-\infty}^{\infty} d\tau \{\hat{\chi}(\tau)V\}^2. \quad (5.7)$$

This expression is the Laplace transformed direct MP2 energy used by Häser and Almlöf, see Ref. 91 for more details.

In obtaining Eq. (5.7), we used the fact that both representations of the polarizability χ and $\hat{\chi}$ are even functions in their arguments ν , respectively τ as shown in Fig. 3.8. This implies that the Fourier transformation becomes essentially a cosine transformation

$$\chi(\nu) = 2 \int_0^{\infty} d\tau \hat{\chi}(\tau) \cos(\tau\nu) \quad (5.8)$$

$$\hat{\chi}(\tau) = \frac{1}{\pi} \int_0^{\infty} d\nu \chi(\nu) \cos(\tau\nu). \quad (5.9)$$

For the evaluation of the integrals (5.5) and (5.7) only the frequency and time dependence of the polarizability is relevant. The former is given in (3.38). In the following we rewrite this expression into

$$\chi(\nu) = \sum_{\mu} \chi_{\mu} y(\nu, \xi_{\mu}) \quad (5.10)$$

$$\hat{\chi}(\tau) = \sum_{\mu} \chi_{\mu} \hat{y}(\tau, \xi_{\mu}), \quad (5.11)$$

5. LOW SCALING ALGORITHM FOR THE RANDOM PHASE APPROXIMATIONS

where the introduced auxiliary functions

$$y(\nu, \xi) = \frac{2\xi}{\xi^2 + \nu^2} \quad (5.12)$$

$$\hat{y}(\tau, \xi) = e^{-\xi|\tau|} \quad (5.13)$$

describe the frequency, respectively the time dependence. In addition, we have adopted the following notation in Eqs. (5.10) and (5.11):

- μ stands for the compound index (i, a) , where i goes over occupied and a over unoccupied states,
- $\xi_\mu = \epsilon_a - \epsilon_i > 0$ is the transition energy between unoccupied a and occupied states i ,
- and $\chi_\mu = \langle i | e^{i\mathbf{g}\mathbf{r}} | a \rangle \langle a | e^{-i\mathbf{g}'\mathbf{r}'} | i \rangle$, stands for a matrix χ_μ with the dimension given by the number of reciprocal lattice vectors $|\mathbf{g}|^2 \hbar / (2m) \leq E_{\text{cut}}$, compare to Eq. (3.41).

We remind the reader that $\epsilon_{\text{min}} \leq \xi_\mu \leq \epsilon_{\text{max}}$ with ϵ_{min} being the band gap and ϵ_{max} the maximally considered transition energy.

Inserting either expression (5.11) into (5.7), or (5.10) into (5.5), the resulting integrals can be carried out analytically yielding an exact expression for the direct MP2 energy $E_c^{(2)}$ that is often used by quantum chemists:[91, 96, 98]

$$E_c^{(2)} = \frac{1}{2} \sum_{\mu\mu'} \chi_\mu V \chi_{\mu'} V \frac{1}{\xi_\mu + \xi_{\mu'}}. \quad (5.14)$$

Although this expression avoids a frequency respectively time integration, the scaling is not favorable, because it involves a summation over quadruples $(\mu, \mu') = (i, a, i', a')$.

If one evaluates the integrals (5.5) and (5.7) numerically by using an appropriate quadrature

$$E_c^{(2)} \approx \frac{1}{8\pi} \sum_{k=1}^n \gamma_k \{\chi(\nu_k) V\}^2 \quad (5.15)$$

$$E_c^{(2)} \approx \frac{1}{4} \sum_{i=1}^n \sigma_i \{\hat{\chi}(\tau_i) V\}^2, \quad (5.16)$$

one can avoid the computationally expensive summation over pairs (μ, μ') . In order to keep the necessary quadrature points n as small as possible, the error stemming from

5.2 Imaginary Time and Frequency Grids

the discretization of the frequency, respectively time domain, needs to be investigated. For this purpose we subtract Eq. (5.14) from Eq. (5.15) and substitute $\chi(\nu)$ by (5.10) obtaining:

$$\frac{1}{2} \sum_{\mu\mu'} \chi_\mu V \chi_{\mu'} V \left\{ \frac{1}{\xi_\mu + \xi_{\mu'}} - \frac{1}{4\pi} \sum_{k=1}^n \gamma_k y(\nu_k, \xi_\mu) y(\nu_k, \xi_{\mu'}) \right\}. \quad (5.17)$$

The terms in the curly braces can be considered to be the error made when approximating the integral (5.5) by a discrete sum (5.15). This means the error for each pair $(\xi, \xi') \in [\epsilon_{\min}, \epsilon_{\max}] \times [\epsilon_{\min}, \epsilon_{\max}]$ (where (ξ, ξ') are representatives of a pair $(\xi_\mu, \xi_{\mu'})$) is described by the function

$$\mathcal{E}(\boldsymbol{\gamma}, \boldsymbol{\nu}, \xi, \xi') = \frac{1}{\xi + \xi'} - \frac{1}{4\pi} \sum_{k=1}^n \gamma_k y(\nu_k, \xi) y(\nu_k, \xi'). \quad (5.18)$$

Analogously, subtracting Eq. (5.14) from (5.16), one can define an error function $\hat{\mathcal{E}}$ for the time domain, which reads

$$\hat{\mathcal{E}}(\boldsymbol{\sigma}, \boldsymbol{\tau}, \xi + \xi') = \frac{1}{\xi + \xi'} - \frac{1}{2} \sum_{i=1}^n \sigma_i \underbrace{\hat{y}(\tau_i, \xi) \hat{y}(\tau_i, \xi')}_{e^{-(\xi+\xi')\tau_i}}. \quad (5.19)$$

The quadrature $(\boldsymbol{\gamma}, \boldsymbol{\nu})$ (respectively $(\boldsymbol{\sigma}, \boldsymbol{\tau})$) is accurate, if the error \mathcal{E} (respectively $\hat{\mathcal{E}}$) for each pair $(\xi, \xi') \in [\epsilon_{\min}, \epsilon_{\max}] \times [\epsilon_{\min}, \epsilon_{\max}]$ is small. For Eq. (5.19) the error function depends on $\xi + \xi'$ and is consequently one-dimensional. Therefore, one can find the desired quadrature $(\boldsymbol{\sigma}, \boldsymbol{\tau})$ by solving the corresponding fitting problem for $f(\xi + \xi') = (\xi + \xi')^{-1}$ (compare Sec. 5.2.1).[99]

However, the error function in the frequency domain (5.18) depends on two linearly independent variables ξ and ξ' , so that a two-dimensional fitting problem needs to be solved. The corresponding least square solution (*i.e.* minimum of $\|\mathcal{E}\|_2$) can be found relatively easily by means of the Levenberg-Marquardt algorithm, which works for arbitrary dimensions. On the contrary, the Minimax solution is much harder to determine. In fact, a generalization of the Remez algorithm to two (or even higher) dimensions does not exist to our knowledge.

Fortunately, the largest errors of \mathcal{E} are on the diagonal $\xi = \xi'$ as can be seen in Fig. 5.2. Therefore, it is a good approximation to consider the one-dimensional problems

5. LOW SCALING ALGORITHM FOR THE RANDOM PHASE APPROXIMATIONS

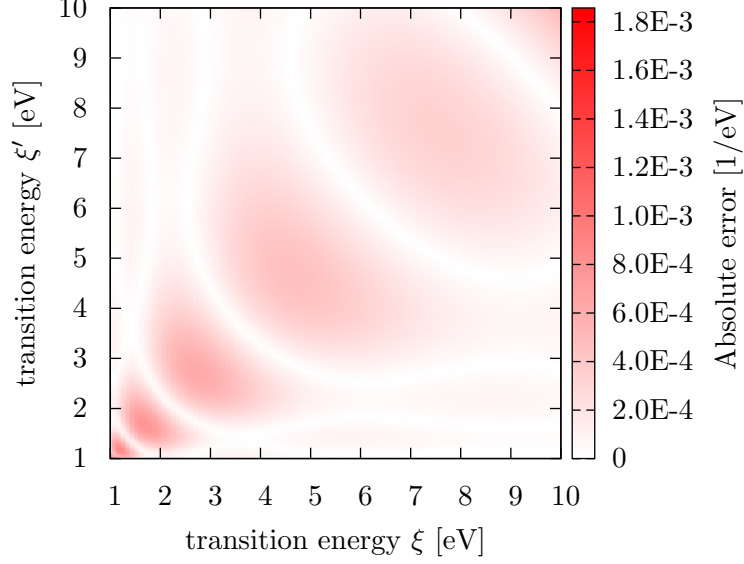


Figure 5.2: Least square error surface $\mathcal{E}(\gamma^0, \nu^0, \xi, \xi')$ measured in $[\text{eV}^{-1}]$ for $\epsilon_{\min} = 1$, $\epsilon_{\max} = 10$ and $n = 3$. The largest errors are located along the diagonal $\xi = \xi'$.

with the following error and model functions:

$$\eta(\gamma, \nu, \xi) = \frac{1}{\xi} - \frac{1}{2\pi} \sum_{k=1}^n \gamma_k y^2(\nu_k, \xi) \quad (5.20)$$

$$\hat{\eta}(\sigma, \tau, \xi) = \frac{1}{\xi} - \sum_{i=1}^n \sigma_i \hat{y}^2(\tau_i, \xi). \quad (5.21)$$

At this point, we note that the scaling relations of the coefficients between the cases $\xi \in [\epsilon_{\min}, \epsilon_{\max}]$ and $\xi \in I = [1, R]$ with $R = \epsilon_{\max}/\epsilon_{\min}$ are trivial (primed coefficients correspond to $\xi \in [1, R]$):

$$\gamma'_k = \epsilon_{\min} \gamma_k, \quad \nu'_k = \epsilon_{\min} \nu_k \quad (5.22)$$

$$\sigma'_i = \sigma_i / 2\epsilon_{\min}, \quad \tau'_i = \tau_i / 2\epsilon_{\min}. \quad (5.23)$$

Hence, we can rely on the considerations of the previous section and minimize η and $\hat{\eta}$ w.r.t. either $\|\cdot\|_2$ or $\|\cdot\|_\infty$. This yields *least square* $(\gamma_k^0, \nu_k^0), (\sigma_i^0, \tau_i^0)$ and *Minimax* $(\gamma_k^*, \nu_k^*), (\sigma_i^*, \tau_i^*)$ quadratures for the frequency and time domain.

5.2 Imaginary Time and Frequency Grids

It is not entirely obvious, which integration method is preferable, but since the exact matrix elements χ_μ as well as the density of the transition energies ξ are not known a priori, a rigorous mathematical analysis suggests that the Minimax grid is superior.[100] If the distribution of the transition energies in the interval $[1, R]$ is taken into account, least square algorithms can become competitive to the Minimax algorithm.[101] In this thesis we have chosen an exponentially decaying distribution of the transition energies centered around $\xi = 1$. This has the advantage of reducing the error for small ξ , *i.e.* the dominating contribution to the polarizability χ . A direct comparison between both methods for the time as well as the frequency domain can be found in section 5.2.5 and 5.2.6.

At the end of previous chapter we showed that the direct MP2 energy $E_c^{(2)}$, with the exact representations (5.5), (5.7) and (5.14), can be seen as the first contribution to the RPA correlation energy E_c^{RPA} defined in Eq. (3.37). Now if $|E_c^{(n)}| < |E_c^{(2)}|$ for $n > 2$, the same must be true for the corresponding errors. In this case, we can expect that the quadrature error of Eq. (3.37) using least square or Minimax coefficients for the frequency domain is of the same order as for Eq. (5.15). Indeed this is shown in section 5.2.5 and 5.2.6.

5.2.3 Non-uniform Cosine Transformation

In this section we consider the duality of a given time and frequency grid for the polarizability. Assume we have given the polarizability $\hat{\chi}$ on a time grid, say τ_i^* . Is it possible to compute the corresponding Fourier transformed polarizability χ at frequency ν_k^* accurately without using an interpolation technique or increasing the number of quadrature points n significantly?

In order to answer this question, we first observe that the Fourier transform in our case reduces to a cosine transformation [cf. Eqs. (5.8) and (5.9)]. Second, we note that in general the Minimax grid points ν_k^*, τ_i^* are non-equally distributed.¹ Thus the vector $\{\chi_k^*\}_{k=1}^n$ cannot be written as a Z-transform of the vector $\{\hat{\chi}_i\}_{i=1}^n$ (as for fast Fourier transforms) and evaluation of the cosine transform in $n \ln(n)$ steps is not straight forward, see Ref. 102 for more details. However, since for our applications the number of grid points is small ($n \leq 20$, cf. Sec. 5.2.5 and 5.2.6), a computational cost of n^2

¹The same holds true for the least square points (ν_k^0, τ_i^0) .

5. LOW SCALING ALGORITHM FOR THE RANDOM PHASE APPROXIMATIONS

is not prohibitive, and we can evaluate the cosine integral directly. Therefore, we may reformulate our problem as follows: we seek a transformation matrix α_{ki} relating the vectors $\hat{\chi}_i, \chi_k$ by

$$\chi_k = \sum_{i=1}^n \alpha_{ki} \hat{\chi}_i, \quad \forall k = 1, \dots, n \quad (5.24)$$

and due to (5.8) we choose the following ansatz for the coefficients

$$\alpha_{ki} = \gamma_{ki} \cos(\nu_k^* \tau_i^*). \quad (5.25)$$

Analogously to section 5.2.2, the coefficients γ_{ki} are determined only by the time and frequency dependence of $\hat{\chi}$ and χ . After inserting expressions for the polarizability in imaginary frequency (5.10) and time (5.11) into (5.24), we end up with the following error function at each frequency point ν_k^* for a specific energy difference $\xi \in [\epsilon_{\min}, \epsilon_{\max}]$:

$$\eta^c(\gamma_k, \xi) = y(\nu_k^*, \xi) - \sum_{i=1}^n \gamma_{ki} \cos(\nu_k^* \tau_i^*) \hat{y}(\tau_i^*, \xi) \quad (5.26)$$

In contrast to section 5.2.1, now only the coefficients γ_{ki} are variational and the abscissas τ_i^* are kept fixed.

On the one hand, we found that η^c has more than $n + 1$ extrema ξ_j . This means that the system of equations (5.4) is over-determined, which implies that the Remez algorithm from 5.2.1 can not be used.

On the other hand, the fitting problem is linear in γ_{ki} . Consequently, we can find the least square solution in a stable way by using the singular value decomposition of the design matrix $D_{ij}^{(k)} = \cos(\nu_k^* \tau_i^*) \hat{y}(\tau_i^*, \xi_j)$. Hence we may use the following *sloppy Remez algorithm*, originally proposed for rational approximations in Ref. 92:

- S1 Choose one frequency point ν_k^* .
- S2 Find all extrema ξ_j of η^c .
- S3 Tabulate the deviations r_j from the median absolute deviation (MAD) r for each ξ_j .
- S4 Solve the over-determined linear system of equations $\eta^c(\gamma_k, \xi_j) + \text{sgn}(r_j)r = 0$ for γ_k in the least-square sense, *i.e.* find the minimum of

$$\|\eta^c(\gamma_k, \xi) + \text{sgn}(r - \xi)r\|_2$$

5.2 Imaginary Time and Frequency Grids

on the discrete set $\xi \in \{\xi_j\}$.

S5 Repeat S1-S4 until convergence is found.

This yields a set of coefficients γ_{ki}^* for $i = 1, \dots, n$ for a specific point ν_k^* .

Alternatively, one can use simply the LS cosine transformation coefficients γ_{ki}^0 obtained from finding the minimum of $\|\eta^c(\gamma_k, \xi)\|_2$ in the minimization interval $[1, R]$. We found that the sloppy MM coefficients γ_{ki}^* tend to increase the error for small transition energies in order to minimize the overall MAD, whereas the LS solution $\|\eta^c(\gamma_k^0, \xi)\|_2$ has typically smaller errors close to $\xi = 1$. The latter comes from the choice of the sampling points (5.28), discussed in the next subsection, and implies that LS cosine coefficients yield effectively more accurate cosine transformations than the MM ones. We, therefore use exclusively the LS solutions γ_{ki}^0 in the forthcoming

The reader may have noticed that the procedure described above is applicable to any, arbitrary frequency point $\nu \in \mathbb{R}$. In principle the set of coefficients $\{\gamma_k^0\}_{k=1}^n$ can be considered to be a vector-valued function $\gamma: \mathbb{R} \rightarrow \mathbb{R}^n$, $\nu \mapsto \gamma(\nu)$ with the property that $\gamma(\nu_k^*) = \gamma_k^0$. Hence, we can actually seek the LS solution $\min \|\eta^c(\nu)\|_2$ and vary the frequency ν continuously. We have done this for various Minimax time grids, *i.e.* for different values of R and n . In all cases, we found that the error $\|\eta^c(\nu)\|_2$ has a frequency dependence as shown in Fig. 5.3. That is, for a time grid τ_i^* , the minima of $\|\eta^c(\nu)\|_2$ are exactly at the Minimax frequency points $\nu = \nu_k^*$.

Conversely, the transformation from the frequency grid to the time grid possesses a similar behavior: for a chosen Minimax frequency grid ν_k^* , the optimal time points of the inverse cosine error function

$$\hat{\eta}^c(\sigma(\tau), \xi) = \hat{y}(\tau, \xi) - \sum_{k=1}^n \sigma_k(\tau) \cos(\nu_k^* \tau) y(\nu_k^*, \xi) \quad (5.27)$$

are exactly at the Minimax time points τ_i^* , as shown in Fig. 5.3 (b). Analogously, if the least square time grid τ_i^0 is chosen, one finds that ν_k^0 are the minima of the function $\min \|\eta^c(\nu)\|_2$, and the converse holds for the back transformation. Therefore we can make the statement that the two grid pairs $\{\nu_k^*\}_{k=1}^n, \{\tau_i^*\}_{i=1}^n$ and $\{\nu_k^0\}_{k=1}^n, \{\tau_i^0\}_{i=1}^n$ are *dual* w.r.t. the cosine transformation. A rigorous mathematical proof is presently, however, not known to us.

5. LOW SCALING ALGORITHM FOR THE RANDOM PHASE APPROXIMATIONS

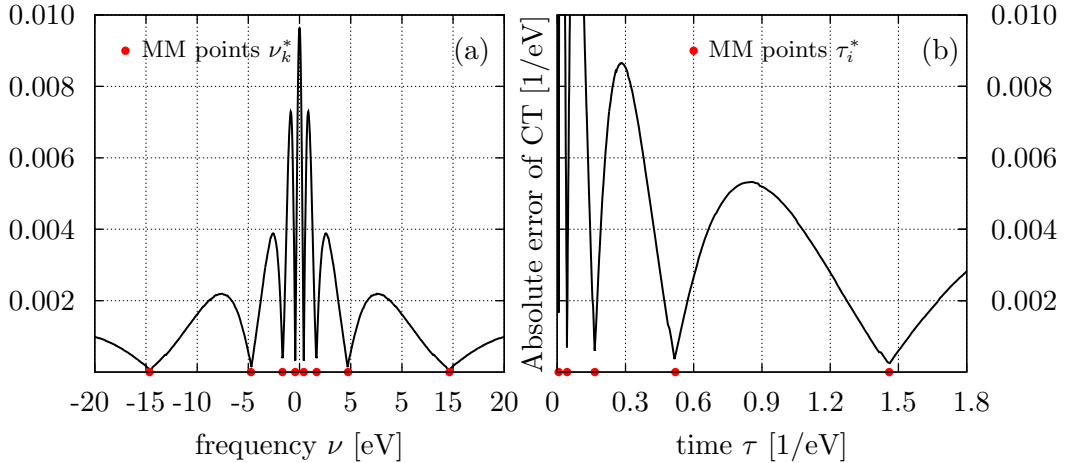


Figure 5.3: (a) Cosine transformation (CT) error $\min \|\eta^c\|_2$ as a function of the frequency ν for a MM time grid $\{\tau_i^*\}_{i=1}^N$ with transition energy ratio $R = 100$ and 5 grid points. (b) transformation error in the time domain $\min \|\hat{\eta}^c\|_2$ for the corresponding MM frequency grid. The error is minimal at the MM points ν_k^* in (a) and τ_i^* in (b) (red dots).

In the following sections, we show the convergence behavior of the Minimax and least square grids for MP2 as well as the RPA correlation energy and investigate the accuracy of the non-uniform cosine transformation.

5.2.4 Technical Details

We have implemented the required code to calculate the least square and Minimax grids for both the imaginary frequency and time domain in VASP.[103, 104]

For the calculation of the least square grid, the nonlinear fitting problem (discussed in section 5.2.1) is solved using the variable projection method presented in Refs. 93 and 105 with uniform starting guesses for $(\gamma^0, \nu^0), (\sigma^0, \tau^0)$. This is done for $R = \epsilon_{\max}/\epsilon_{\min}$. The resulting coefficients are then scaled for the proper interval $[\epsilon_{\min}, \epsilon_{\max}]$ using the relations (5.22). Furthermore, in order to reduce the error for small transition energies (dominating contributions in the polarizability), the minimization interval $[1, R]$ is sampled with points ξ_i corresponding to an exponentially decaying distribution with maximum density towards $\xi = 1$. More precisely, we have chosen the following sampling points

$$\xi_j = e^{\ln R + \cos\left[\frac{2(2M-j)+1}{4M}\pi\right] \ln R}, \quad j = 1, \dots, M \quad (5.28)$$

5.2 Imaginary Time and Frequency Grids

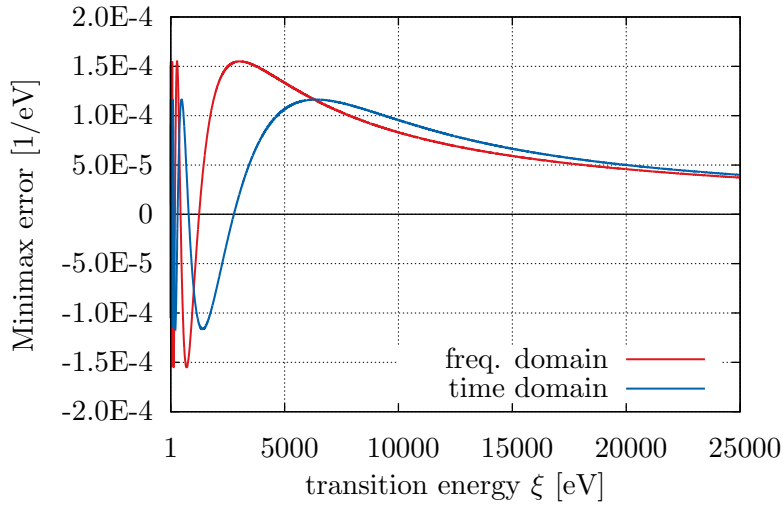


Figure 5.4: Minimax error functions for the time $\hat{\eta}$ (blue line) and frequency η (red line) domain for $R_7 = 28387$ and $n = 7$. Both functions decay strictly for $\xi > R_7$.

where M represents the total number of points.

The LS coefficients are used as starting values for the setup of the corresponding error function. To optimize the error function obtaining Minimax quadratures $(\gamma^*, \nu^*), (\sigma^*, \tau^*)$, we have implemented a Remez algorithm. This algorithm determines the absolute maximum ϵ of η (respectively $\hat{\eta}$) in $[1, R]$ and the ξ_j (set of all local extrema including the boundaries 1 and R in $[1, R]$). In the next step the non-linear set of equations (5.4) is solved using a standard damped Newton-Raphson algorithm. Finally, the procedure is iterated until convergence is reached.

We note that for any given n , an upper bound R_n exists, so that the corresponding error functions $\eta(\xi), \hat{\eta}(\xi)$ decay strictly for all $\xi > R_n$. Fig. 5.4 shows an example of this case. If for a given n , the transition energy ratio R is larger than R_n , the error is minimized in the interval $[1, R_n]$ instead of $[1, R]$, because the total error for both intervals coincide (see Ref. 100 for more details).

The convergence behavior of the cosine transform (5.24) is tested by first calculating the polarizability on an imaginary time grid and then performing the cosine transform. The code first determines the coefficients γ_{ki}^0 by minimizing the error function $\|\eta^c(\gamma_k, \xi)\|_2$ using a singular value decomposition (cf. section 5.2.3). In the next step the polarizability $\hat{\chi}$ is evaluated at the Minimax time grid τ_i^* and the cosine transform is

5. LOW SCALING ALGORITHM FOR THE RANDOM PHASE APPROXIMATIONS

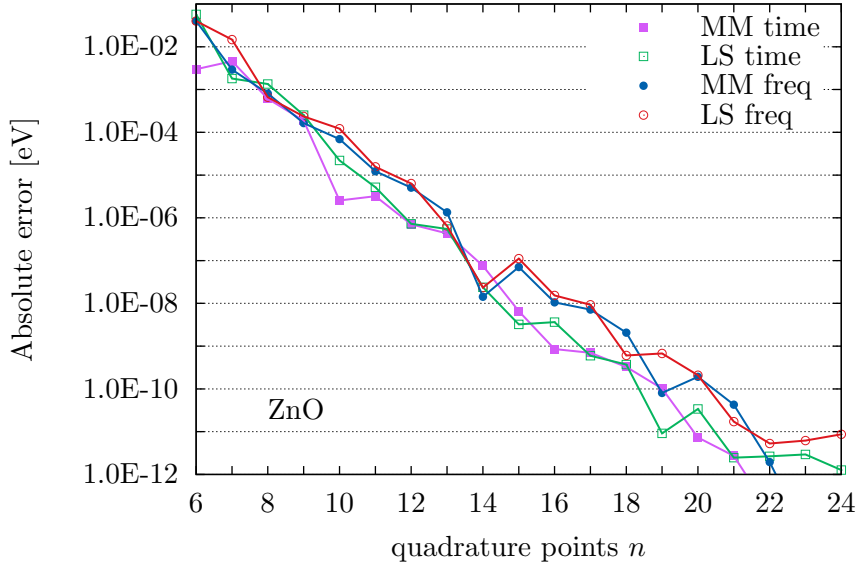


Figure 5.5: Convergence of direct MP2 energy $E_c^{(2)}$ for the least square (LS) and Minimax (MM) quadratures for ZnO.

calculated using Eq. (5.24) with $\alpha_{ki} = \gamma_{ki}^0 \cos(\nu_k^* \tau_i^*)$. In the final step, the RPA correlation energy E_c^{RPA} is calculated with (3.37) using the Minimax quadrature $\{\nu_k^*, \gamma_k^*\}$ for the frequency integral in Eq. (3.37). For the evaluation of $\ln(1 - \chi V)$ the method described in Ref. 90 is applied. The same procedure is tested for the least square quadrature $\{\nu_k^0, \gamma_k^0\}$ as well.

5.2.5 Grid Convergence for ZnO and Si

We have calculated the RPA and direct MP2 energies of zinc-blende ZnO and fcc Si using lattice constants of $a = 4.58 \text{ \AA}$ and $a = 5.43 \text{ \AA}$, respectively. The Brillouin zone was sampled with $4 \times 4 \times 4$ k-points (including the Γ -point) and the sum over \mathbf{g} -vectors and bands in the polarizability were restricted to an energy cutoff of 250 eV and 256 bands respectively.

These two examples are representative of cases, where the number of valence-conduction band pairs is of the order of several millions, so that standard MP2 algorithms are already exceedingly expensive and (at least with our code) hardly doable. However, the single particle gap is sizable in both cases, and does not pose a significant challenge to the numerical quadrature.

5.2 Imaginary Time and Frequency Grids

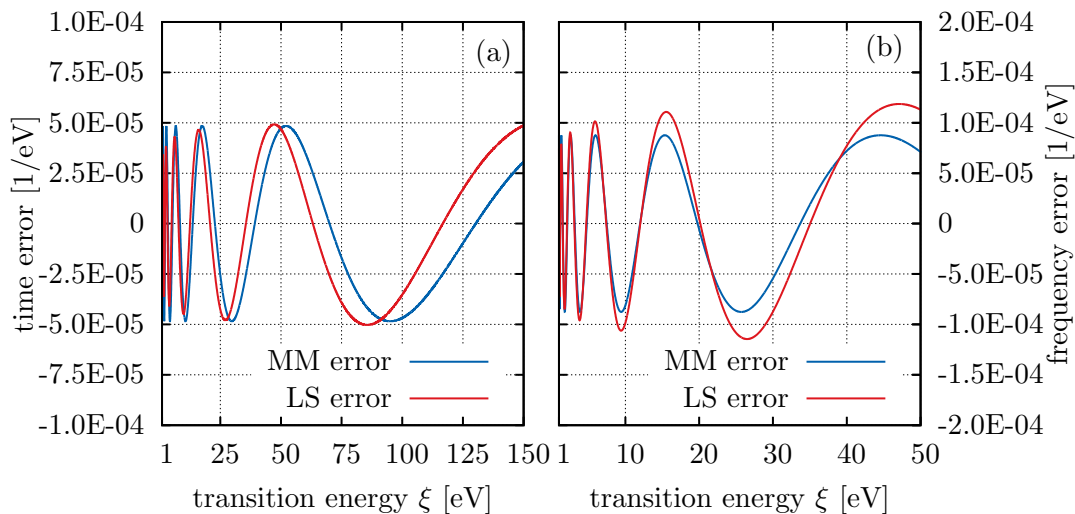


Figure 5.6: Minimax (blue line) and least square error (red line) functions for $R = 500$ and $n = 7$ in the time (a) and frequency domain (b). For small ξ (dominating terms in χ and $\hat{\chi}$) the least square solution is more accurate.

Fig. 5.5 shows the absolute integration error for the direct MP2 energy $E_c^{(2)}$ of ZnO calculated using an imaginary time (squares) and imaginary frequency grid (circles). Here, the polarizabilities were calculated directly on the imaginary time and imaginary frequency axis, respectively (not applying cosine transformations). We found that for both, the least square as well the Minimax grid, the direct MP2 contribution can be evaluated with an accuracy of 1 meV with only 9 quadrature points. Note that these calculations were performed using density functional theory orbitals and one-electron energies (as opposed to the conventionally used Hartree-Fock orbitals). The imaginary time integration converges slightly faster than the frequency integration. This is related to larger errors in the frequency domain as one can see from Fig. 5.6 (a) and (b).

From a direct comparison of the Minimax (MM) with the least square (LS) grid (filled and empty points in Fig. 5.5) one clearly sees that the convergence of the least square grid is competitive with the Minimax quadrature for the direct MP2 energies of ZnO. The situation is similar for the RPA correlation energy shown in Fig. 5.7 (filled and empty circles) and little difference between the MM and LS error for ZnO and Si is observed. Here, and in the MP2 case, μeV accuracy is reached with approximately 13 points using both grids (filled and empty circles in Figs. 5.5 and 5.7). This is mainly due to the fact that we have chosen an exponentially decaying distribution for the transition

5. LOW SCALING ALGORITHM FOR THE RANDOM PHASE APPROXIMATIONS

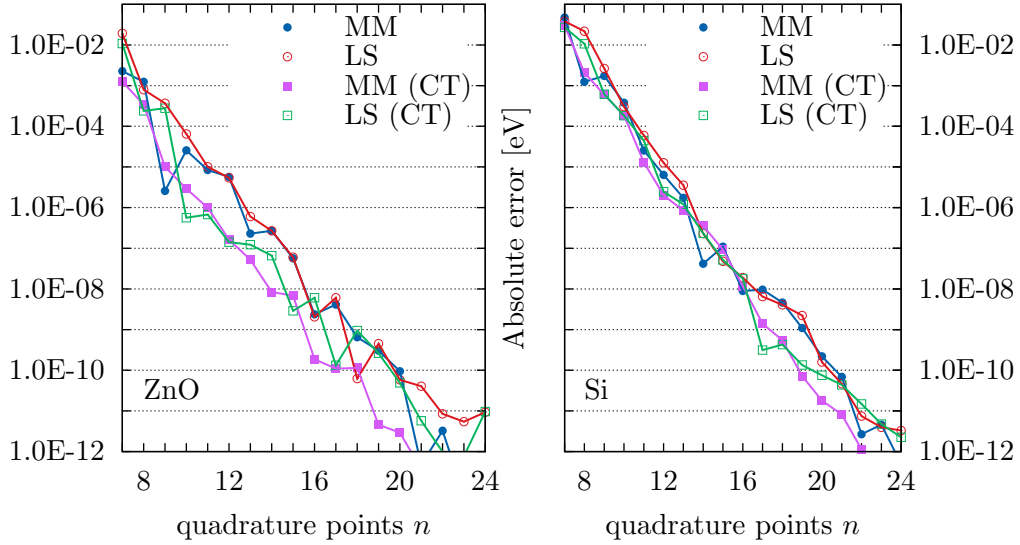


Figure 5.7: Convergence of RPA correlation energy E_c^{RPA} for ZnO and Si w.r.t. the number of grid points n for the LS (red line) and MM (blue line) quadratures. If polarizabilities are determined by cosine transformations (CT) from the time to the frequency axis, larger errors are obtained (purple and green line).

energies ξ , see Eq. (5.28), leading to smaller LS errors for small transition energies and vice versa for large energies. This behavior of the LS solution is depicted by the red lines in Figs. 5.6.

We have also investigated the accuracy of the non-uniform cosine transform described in section 5.2.3. The results for the RPA correlation energy for the Minimax and least square grids are given by the filled and empty squares in Fig. 5.7. One sees clearly that the cosine transformation CT of $\hat{\chi}(\tau_i)$ can be carried out without loss of accuracy, *i.e.* convergence of E_c^{RPA} within 1 meV (1 μeV) is achieved for 9 (12) grid points.¹ This is a remarkable result, since it shows the duality of the MM/LS time and frequency grids. Furthermore, when the polarizability is calculated via a cosine transformation and the ACFDT formula is integrated with the MM weights γ_k^* , both grids show the same convergence. This comes from the aforementioned similarity of the two error functions in both domains as shown in Fig. 5.6.

A final remark is in place here. For Si the 3s and 3p states and for ZnO the Zn-3d

¹The grid convergence is deteriorated using the 'sloppy' MM coefficients γ_{ki}^* and about 30 – 40 % more points for the same accuracy as presented in Figs. 5.7 (a) and (b) are needed, see Ref. 88.

5.2 Imaginary Time and Frequency Grids

and O-2s and O-2p are treated as valence electrons yielding a minimization interval of [1, 525] for the former and [1, 470] for the latter. This results in the good grid convergence shown in Figs. 5.5 and 5.7. In the presence of shallow core electrons the minimization intervals will increase slightly, since the core electrons lie typically 100 to 200 eV lower in the energy than the valence electrons. This will not deteriorate the grid convergence considerably, because the presented integration method converges exponentially with the number of grid points.

5.2.6 Grid Convergence for Al and Nb atom

From the previous discussion, it is clear that the convergence of RPA energies for systems with small gaps is harder to achieve, since a small gap will necessarily increase the width of the interval onto which we map [1,R]. For vanishing or zero gap, the direct MP energies tend to diverge $E_c^{(n)} \rightarrow \infty$, whereas the RPA energy $E_c^{\text{RPA}} = \sum_{n=0}^{\infty} E_c^{(n)}$ usually remains finite.[33] Hence we consider only the RPA correlation energy in this section.

We have studied the convergence of the Minimax grid and the corresponding non-uniform cosine transformation for atomic Al and Nb. Both atoms are characterized by a tiny one-electron gap in density functional theory when the PBE functional is used.[19, 106] For Al, for instance a symmetry broken solution is found where the three (degenerate) p-orbitals split into one occupied and two unoccupied states separated by an energy difference of 80 meV. Analogously, for Nb the one electron Kohn-Sham gap is about 15 meV, so that we can consider both, the Al and Nb atom as particularly challenging model systems for small gap systems. Note that the exact magnitude of the one-electron gap might vary between different implementations and box sizes, but this is irrelevant for the present case, since we only want to demonstrate that reasonably accurate answers can be obtained even in such problematic cases.

The calculations of the RPA correlation energies were done at the Γ -point only in a $7 \times 8 \times 9 \text{ \AA}^3$ cell. An energy cutoff of 250 eV for Al and 286 eV for Nb was chosen. The sum over bands for the polarizability was restricted to 8000 for Al and to 5760 for Nb respectively. The convergence of the Minimax frequency quadrature and the cosine transformation are shown in Fig. 5.8.

One clearly recognizes that the accuracy for the Al and Nb atom is poor compared to ZnO and Si. In order to obtain results with similar accuracy, we need for Al about 30 % more grid points ($n = 12$) as for the semiconductors and for Nb even a denser

5. LOW SCALING ALGORITHM FOR THE RANDOM PHASE APPROXIMATIONS

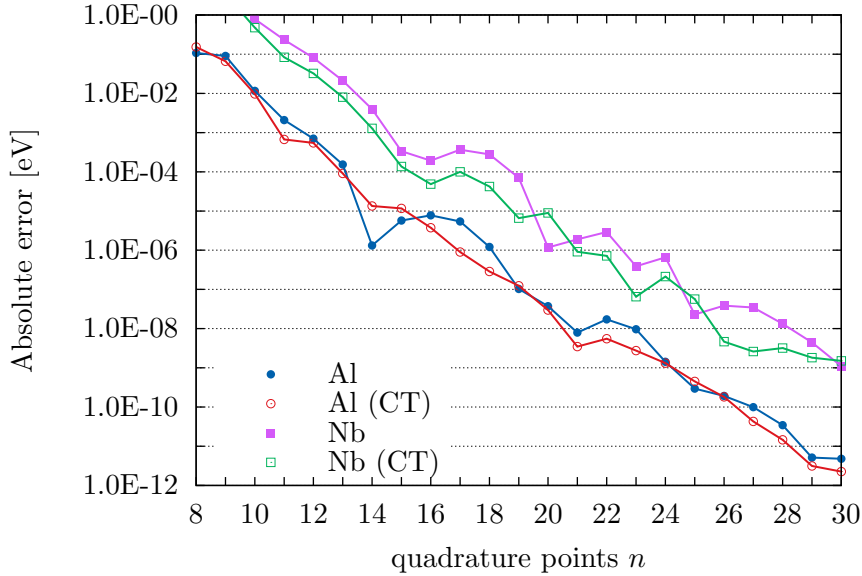


Figure 5.8: Convergence of RPA correlation energy E_c^{RPA} for Al and Nb w.r.t. the number of grid points n for the LS (red line) and MM (blue line) quadratures. If polarizabilities are determined by cosine transformations (CT) from the time to the frequency axis similar errors are obtained (purple and green line).

grid is necessary ($n = 15$). Still at least for Al μeV precision can be reached with about $n \approx 18$ frequency points. The reason for this behavior is the required large minimization interval ($R = 38218$ for Nb and $R = 5390$ for Al) in order to capture also very small energy transitions in the polarizability. This is also indicated by the slightly better convergence of Al due to a smaller value of R compared to Nb.

Although the necessity of dense grids for small gap systems is not surprising, we believe that grids of the order $n \approx 20$ for accurate RPA energies of systems with gaps between 10 and 100 meV are acceptable.

When the response function is calculated first in imaginary time and then cosine transformed, as in the case of the semiconductors, we observe no loss of accuracy. This demonstrates, once again, the strict duality between the non-linear time and frequency grids.

5.2 Imaginary Time and Frequency Grids

5.2.7 Conclusion

In this section, we have discussed the construction of optimized imaginary time and frequency grids for the independent particle polarizability χ and the corresponding cosine transformation. The cosine transformation between imaginary time and imaginary frequency polarizabilities is used in the fourth step of the low-scaling RPA algorithm presented in Fig. 5.1. In section 5.2, we have pointed out, that this algorithm will benefit from optimized imaginary time and frequency grids that keep the number of grid points small.

In order to achieve this goal, we have used non-equally spaced grids based on quadratures for the RPA integral (3.37) and its lowest order contribution, the direct MP2 energy $E_c^{(2)}$. Since the latter can be evaluated efficiently on the imaginary time as well, as the imaginary frequency axis, we have first focused our attention on the MP2 integral representations in imaginary time (5.7) and imaginary frequency (5.5).

The construction of imaginary time quadratures is a well studied problem and appears in Laplace transformed Møller-Plesset perturbation theory. Here we have compared Minimax and weighted least square quadratures, finding that the latter is competitive with the former for the materials considered here (see section 5.2.5).

To evaluate the RPA correlation energy using Eq. (3.37) an imaginary frequency quadrature is needed. In order to obtain accurate frequency grids, we have proceeded analogously to the construction of the time grid, *i.e.* we have minimized the quadrature error of the imaginary frequency representation (5.5) of the direct MP2 energy. In section 5.2.5, we have shown that the resulting frequency quadratures can be used for an accurate frequency integration of the MP2 and RPA energies. For gapped systems, such as ZnO and Si, both quadratures (the Minimax and weighted least square) reach μeV accuracy of $E_c^{(2)}$ and E_c^{RPA} around 13 frequency points (see Figs. 5.7 and 5.5).

Furthermore, in section 5.2.6, we have briefly explained the challenge of determining E_c^{RPA} for small-gap systems. Due to the existence of tiny transition energies in the independent particle polarizability $\chi(i\nu)$ more grid points are necessary for an accurate frequency integration. We have seen that for systems with band gaps of a few 10 meV (atomic Al and Nb), meV accuracy of E_c^{RPA} is only attained around 14 grid points.

The main achievement of the present section is the numerical cosine transformation of the polarizability from the imaginary time to the imaginary frequency axis presented

5. LOW SCALING ALGORITHM FOR THE RANDOM PHASE APPROXIMATIONS

in section 5.2.3. We have approximated the cosine integral (5.8) by a discrete sum and subsequently minimized the corresponding error (5.26). This gives rise to a non-uniform cosine transformation allowing for an accurate switching between imaginary time and frequency polarizabilities without using an interpolation technique or increasing the number of grid points n . Since the computational time, as well as the working memory depend linearly on n , an optimized frequency and time grid helps to reduce the storage and the computational cost of the low scaling RPA algorithm illustrated in Fig. (5.1).

Remarkably, we observe a strict "duality" between the Minimax time and frequency grids: for a given Minimax time grid, errors due to the cosine transform are minimal at the Minimax frequency points, and vice versa. This duality is at first sight maybe somewhat unexpected. For instance, the small frequencies present on the frequency grid imply rapid oscillations as a function of time, and one might then ask, why coarse grids at large imaginary time are sufficient and optimal to represent such oscillations. We have no formal mathematical justification for that observation. However, one should keep in mind that in imaginary time τ a transition, at the energy ξ on the real axis results in an exponentially decaying function $\exp(-\tau\xi)$. The corresponding functions in imaginary frequency ν are decaying rational functions of the form $\xi/(\xi^2 + \nu^2)$. None of these functions are oscillatory: they are smooth and decay towards zero at infinite (imaginary) time and frequency. The spacing of the time and frequency grids are most likely optimal to represent such functions.

We have investigated the convergence of the cosine transform with respect to the number of time and frequency grid points in section 5.2.5. For Si and ZnO, the transformation of $\hat{\chi}(i\tau_i) \rightarrow \chi(i\nu_k)$ and subsequent calculation of the RPA correlation energy can be performed with meV (μeV) accuracy with 10 (14) grid points. An accuracy of about 1 meV for systems with a tiny one electron gap, such as the Al and Nb atom, is reached around 14 grid points, and with 18 grid points, the error approaches about 10 μeV . This should be adequate for most materials and is small compared to errors incurred by the random phase approximation itself. To achieve the same accuracy, the cosine transformation based algorithm requires approximately the same number of time and frequency points, than a direct calculation of the polarizability on the frequency grid.

In the following section we discuss the remaining steps of our RPA algorithm.

5.3 Fast Fourier Transforms within supercells

The remaining part of this chapter was published in [89].

This section is dedicated to the spatial FFTs in step one and three in Fig. 5.1. Using supercells allows to achieve linear scaling with respect to the number of k-points in the contraction step GG [discussed in 5.4]. Before continuing, we review a few basic relations between real and reciprocal space and introduce a concise terminology.

Given a unit cell C , the corresponding first Brillouin zone will be denoted by C^* . We call the set of all translation vectors of the unit cell \mathcal{L}_c , and vice versa, \mathcal{L}_c^* indicates the set of all translation vectors of C^* . The vectors $\mathbf{g} \in \mathcal{L}_c^*$ are the usual reciprocal lattice vectors (large dots in Fig. 5.9). If the unit cell C is replicated \mathcal{N} times along each direction, a supercell S containing \mathcal{N}^3 copies of the original unit cell C is obtained. Then the corresponding Brillouin zone S^* is a subset of C^* . Their origins, the Γ -point, coincide (cf. Fig. 5.9).[7] Analogously to the unit cell, we write \mathcal{L}_s and \mathcal{L}_s^* for the translational vector sets of the supercell S . It follows immediately that[7, 107]

$$\mathcal{L}_c^* \subseteq \mathcal{L}_s^*. \quad (5.29)$$

The reciprocal superlattice vectors \mathbf{G} build a uniform $\mathcal{N} \times \mathcal{N} \times \mathcal{N}$ lattice \mathcal{K}_c^* containing N_k vectors \mathbf{k} in the first Brillouin zone of the original unit cell C^* . These are the k-points (see Fig. 5.9) used to sample the Brillouin zone in the original primitive computational cell. In the following, we will distinguish between reciprocal superlattice vectors $\mathbf{G} \in \mathcal{L}_s^*$ and the k-points $\mathbf{k} \in \mathcal{K}_c^*$.

Quantities, such as the response function χ or the Green's function G are periodic in space

$$G(\mathbf{r} + \mathbf{a}, \mathbf{r}' + \mathbf{a}) = G(\mathbf{r}, \mathbf{r}'), \quad \forall \mathbf{a} \in \mathcal{L}_c. \quad (5.30)$$

This implies that the Fourier representation of G can be written as[108]

$$G(\mathbf{r}, \mathbf{r}') = \frac{1}{N_k} \sum_{\mathbf{k} \in \mathcal{K}_c^*} G_{\mathbf{k}}(\mathbf{r}, \mathbf{r}'), \quad (5.31)$$

where

$$G_{\mathbf{k}}(\mathbf{r}, \mathbf{r}') = \sum_{\mathbf{g}, \mathbf{g}' \in \mathcal{L}_c^*} e^{-i(\mathbf{k}+\mathbf{g})\mathbf{r}} G_{\mathbf{k}}(\mathbf{g}, \mathbf{g}') e^{i(\mathbf{k}+\mathbf{g}')\mathbf{r}'} \quad (5.32)$$

5. LOW SCALING ALGORITHM FOR THE RANDOM PHASE APPROXIMATIONS

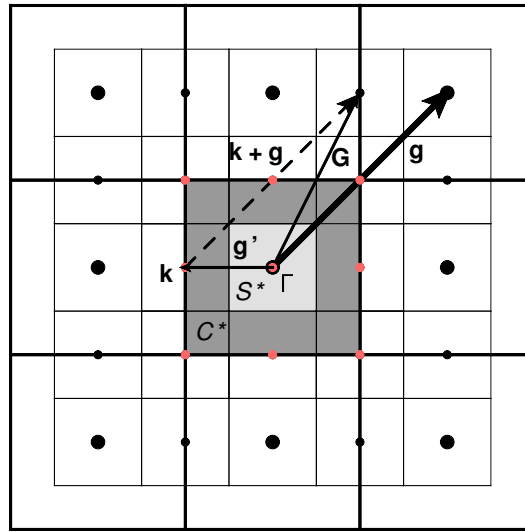


Figure 5.9: Illustration of relation between reciprocal cell C^* (dark gray cell), k-point grid \mathcal{K}_c^* (red dots in dark gray square) and reciprocal supercell S^* (small light gray square) for a two dimensional cubic cell with $S = (2 \times 2)C$. The vector \mathbf{g} is a reciprocal lattice vector of C^* and \mathbf{G} is a reciprocal lattice vector of S^* . The set of all reciprocal lattice vectors \mathcal{L}_c^* is represented by big dots and is a subset of \mathcal{L}_s^* , the set of all reciprocal superlattice vectors (small and big dots). The k-point \mathbf{k} coincides with the reciprocal superlattice vector \mathbf{G}' and every vector $\mathbf{k} + \mathbf{g}$ can be represented by a reciprocal superlattice vector \mathbf{G} .

5.3 Fast Fourier Transforms within supercells

and $N_k = \mathcal{N}^3$ denotes the number of \mathbf{k} -points in the first Brillouin zone of the unit cell. In the last expression the notation

$$G_{\mathbf{k}}(\mathbf{g}, \mathbf{g}') = G(\mathbf{k} + \mathbf{g}, \mathbf{k} + \mathbf{g}'), \quad \forall \mathbf{k} \in \mathcal{K}_c^*, \mathbf{g} \in \mathcal{L}_c^* \quad (5.33)$$

was used, which indicates that for each $\mathbf{k} \in \mathcal{K}_c^*$ a different set of points in the reciprocal space $\mathbf{k} + \mathbf{g}, \mathbf{k} + \mathbf{g}'$ form a matrix $G_{\mathbf{k}}$ with indices $\mathbf{g}, \mathbf{g}' \in \mathcal{L}_c^*$. We note that for each \mathbf{k} , the set $\{\mathbf{k} + \mathbf{g}\}_{\mathbf{g} \in \mathcal{L}_c^*}$ covers a different subset of \mathcal{L}_s^* , so that

$$\mathcal{L}_s^* = \bigcup_{\mathbf{k} \in \mathcal{K}_c^*} \{\mathbf{k} + \mathbf{g}\}_{\mathbf{g} \in \mathcal{L}_c^*} \quad (5.34)$$

holds. This implies that $\mathbf{G} = \mathbf{k} + \mathbf{g}$ is a reciprocal lattice vector of the supercell (dashed vector in Fig. 5.9) and that the Fourier transform (5.31) alternatively can be written as

$$G(\mathbf{r}, \mathbf{r}') = \sum_{\mathbf{G}, \mathbf{G}' \in \mathcal{L}_s^*} e^{-i\mathbf{G}\mathbf{r}} G(\mathbf{G}, \mathbf{G}') e^{i\mathbf{G}'\mathbf{r}'}. \quad (5.35)$$

The notation $G(\mathbf{G}, \mathbf{G}')$ indicates a single huge matrix with indices $\mathbf{G}, \mathbf{G}' \in \mathcal{L}_s^*$. However, one has to keep in mind that this matrix is essentially block diagonal. That is, for two reciprocal lattice vectors $\mathbf{G} = \mathbf{k} + \mathbf{g}$ and $\mathbf{G}' = \mathbf{k}' + \mathbf{g}'$, the matrix reads

$$G(\mathbf{G}, \mathbf{G}') = \delta_{\mathbf{k}\mathbf{k}'} G_{\mathbf{k}}(\mathbf{g}, \mathbf{g}'). \quad (5.36)$$

Therefore, the two representations (5.35) and (5.31) have the same complexity.

In analogy, using inverse arguments for the polarizability, one obtains the two real space Fourier representations

$$\chi_{\mathbf{k}}(\mathbf{g}, \mathbf{g}') = \sum_{\mathbf{r}, \mathbf{r}' \in C} e^{i(\mathbf{k}+\mathbf{g})\mathbf{r}} \chi(\mathbf{r}, \mathbf{r}') e^{-i(\mathbf{k}+\mathbf{g}')\mathbf{r}'} \quad (5.37)$$

$$\chi(\mathbf{G}, \mathbf{G}') = \sum_{\mathbf{R}, \mathbf{R}' \in S} e^{i\mathbf{G}\mathbf{R}} \chi(\mathbf{R}, \mathbf{R}') e^{-i\mathbf{G}'\mathbf{R}'}. \quad (5.38)$$

We summarize the most important result of this subsection so far. The relations (5.31) and (5.35) imply that the Fourier transformation can be evaluated in two different ways. In Eq. (5.31) the Fourier transformation $G_{\mathbf{k}}(\mathbf{g}, \mathbf{g}')$ is a set of $\mathcal{N} \times \mathcal{N} \times \mathcal{N}$ individual matrices "centered" at $\mathbf{k} \in \mathcal{K}_c^*$ with reciprocal lattice vectors of the unit cell $\mathbf{g} \in \mathcal{L}_c^*$. Alternatively, the Green's function (5.35) can be considered to be a single huge block diagonal matrix $G(\mathbf{G}, \mathbf{G}')$ with matrix indices \mathbf{G}, \mathbf{G}' of the reciprocal lattice of the supercell \mathcal{L}_s^* . We note that Steinbeck *et al.* used similar strategies [see Ref. 69], but with

5. LOW SCALING ALGORITHM FOR THE RANDOM PHASE APPROXIMATIONS

one crucial difference: in their work an auxiliary supercell Green's function is defined without the Bloch phase factors $e^{-i\mathbf{k}(\mathbf{r}-\mathbf{r}')}$. Although elegant, we found no way to extend this prescription to the projector augmented wave (PAW) methodology discussed below. The present strategy is equally efficient, but exploits the translational symmetry relations

$$G(\mathbf{r} - \mathbf{a}, \mathbf{r}') = G(\mathbf{r}, \mathbf{r}' + \mathbf{a}) \quad (5.39)$$

$$G(\mathbf{r}, \mathbf{r}') = G^*(\mathbf{r}', \mathbf{r}) \quad (5.40)$$

instead.

These relations follow trivially from the orbital representation of the Green's function (2.109) and imply the symmetry of the matrix $G(\mathbf{R}, \mathbf{R}')$ illustrated in Fig. 5.10 with the irreducible stripe $G(\mathbf{r}, \mathbf{R}')$ depicted by the thick rectangle. This stripe is obtained from the primitive block $G_{\mathbf{k}}(\mathbf{r}, \mathbf{r}')$ using

$$G_{\mathbf{k}}(\mathbf{r}, \mathbf{R}' = \mathbf{r}' + \mathbf{a}) = e^{-i\mathbf{k}\mathbf{a}} G_{\mathbf{k}}(\mathbf{r}, \mathbf{r}') \quad (5.41)$$

with (5.31) and contains all necessary data in order to determine the remaining matrix elements of the super matrix $G(\mathbf{R}, \mathbf{R}')$.

In practice, we exploit these symmetries and evaluate the Fourier transformation of the Green's function in two steps:

$$G(\mathbf{r}, \mathbf{k} + \mathbf{g}') = \sum_{\mathbf{g} \in \mathcal{L}_c^*} G_{\mathbf{k}}(\mathbf{g}, \mathbf{g}') e^{i(\mathbf{k} + \mathbf{g})\mathbf{r}}, \quad (5.42)$$

$$G(\mathbf{r}, \mathbf{R}') = \sum_{\mathbf{G}' \in \mathcal{L}_s^*} e^{-i\mathbf{G}'\mathbf{R}'} G(\mathbf{r}, \mathbf{G}'). \quad (5.43)$$

The first spatial index of the Green's function G is determined by an FFT using the unit cell C , and the second spatial index by an FFT with respect to the supercell S . In the second FFT, \mathbf{G}' is in the union of $\mathbf{k} + \mathbf{g}'$ as specified in Eq. (5.34). Hence, the first spatial index of G is restricted to the unit cell, whereas the second extends over the entire supercell building the irreducible stripe $G(\mathbf{r}, \mathbf{R}')$.

Analogously, the FFT of the RPA polarizability from real space to reciprocal space is determined by

$$\chi(\mathbf{r}, \mathbf{G}') = \sum_{\mathbf{R}' \in S} \chi(\mathbf{r}, \mathbf{R}') e^{i\mathbf{G}'\mathbf{R}'} \quad (5.44)$$

$$\chi_{\mathbf{k}}(\mathbf{g}, \mathbf{g}') = \sum_{\mathbf{r} \in C} e^{-i(\mathbf{k} + \mathbf{g})\mathbf{r}} \chi(\mathbf{r}, \mathbf{k} + \mathbf{g}'). \quad (5.45)$$

5.4 Forming $G(\tau)G(-\tau)$ in the PAW Basis

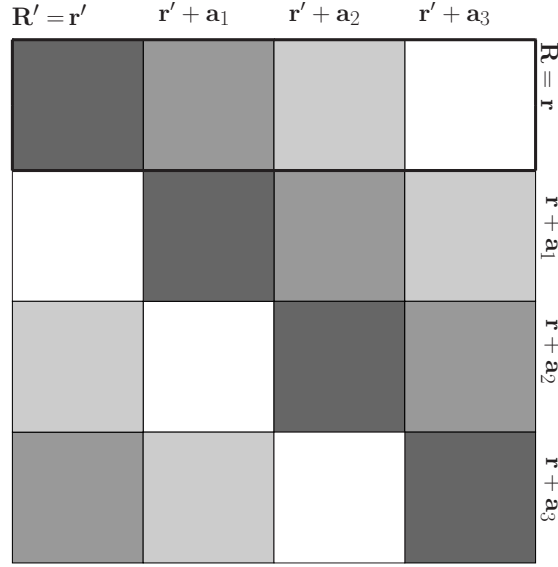


Figure 5.10: Symmetry of the Green's function matrix in real space $G(\mathbf{R}, \mathbf{R}')$ for a $S = (2 \times 2)C$ supercell with the irreducible stripe $G(\mathbf{r}, \mathbf{R}')$ (thick rectangle). Due to Eq. (5.40) the blocks below the diagonal are complex conjugated.

Because of $|\mathcal{L}_s^*| = N_k |\mathcal{L}_c^*| = N_k N_b$ (with N_b being the total number of considered basis vectors \mathbf{g}) the time complexity for all steps (5.42)-(5.45) is of the order

$$\ln(N_b^2 N_k) N_b^2 N_k \approx \ln(N^2 N_k) N^2 N_k, \quad (5.46)$$

i.e. roughly linear in N_k and quadratic in the system size N .

A final remark concerning the first FFT in Fig. 5.1 is in place here. In principle, the FFT step for the Green's functions from reciprocal to real space can be avoided by evaluating the Green's function directly on the real space grid. However, this would require considerably more storage for the Green's function and would increase the compute cost, since the number of real space points is at least twice but often up to 8 times larger than the number of plane wave coefficients.

5.4 Forming $G(\tau)G(-\tau)$ in the PAW Basis

In analogy to the previous section, here and in the following small bold letters indicate vectors of the unit cell, whereas capital letters represent vectors in the super cell.

5. LOW SCALING ALGORITHM FOR THE RANDOM PHASE APPROXIMATIONS

In this section we discuss step two of Fig. 5.1, the contraction of two Green's functions in the space-time domain (3.25) yielding the independent-particle polarizability [53, 69]

$$\chi(\mathbf{r}, \mathbf{R}', \tau) = - \underbrace{G^*(\mathbf{r}, \mathbf{R}', \tau)}_{=G(\mathbf{R}', \mathbf{r}, \tau)} G(\mathbf{r}, \mathbf{R}', -\tau). \quad (5.47)$$

For the PAW basis, this is a rather involved step and requires careful consideration. We start with a short review of the PAW method.

Within the PAW approach, the all-electron orbital ϕ_i is represented by the corresponding pseudo orbital $\tilde{\phi}_i$ via the linear transformation[104, 109]

$$|\phi_i\rangle = |\tilde{\phi}_i\rangle + \sum_{\mu} \left(|\psi_{\mu}\rangle - |\tilde{\psi}_{\mu}\rangle \right) \langle \tilde{p}_{\mu} | \tilde{\phi}_i \rangle. \quad (5.48)$$

Here the second term acts only within the augmentation sphere Ω_R enclosing the atoms. The index $\mu = (\mathbf{R}_{\mu}, n_{\mu}, l_{\mu}, m_{\mu})$ is an abbreviation for the atomic site \mathbf{R}_{μ} , the energy quantum number n_{μ} and angular momentum numbers (l_{μ}, m_{μ}) characterizing the solution ψ_{μ} of the Schrödinger equation for a reference atom. The pseudo counterparts $\tilde{\psi}_{\mu}$ are smooth functions coinciding with ψ_{μ} outside Ω_R . They are dual to the projectors \tilde{p}_{μ} within Ω_R

$$\langle \tilde{p}_{\mu} | \tilde{\psi}_{\nu} \rangle = \delta_{\mu\nu}. \quad (5.49)$$

For further information about the chosen projectors \tilde{p}_{μ} and pseudo partial waves $\tilde{\psi}_{\mu}$ we refer the reader to the literature.[104, 109]

Representing the all-electron orbitals ϕ_i by pseudo orbitals $\tilde{\phi}_i$ using Eq. (5.48), additional contributions to χ appear. These contributions stem from the evaluation of the all-electron matrix elements[104, 110]

$$\langle \phi_i | e^{i(\mathbf{k}+\mathbf{g})\mathbf{r}} | \phi_a \rangle = \langle \tilde{\phi}_i | e^{i(\mathbf{k}+\mathbf{g})\mathbf{r}} | \tilde{\phi}_a \rangle + \sum_{\mu\nu, \mathbf{r} \in C} e^{i(\mathbf{k}+\mathbf{g})\mathbf{r}} \langle \tilde{\phi}_i | \tilde{p}_{\mu} \rangle Q_{\mu\nu}(\mathbf{r}) \langle \tilde{p}_{\mu} | \tilde{\phi}_a \rangle \quad (5.50)$$

and can be identified with the help of Eq. (3.41). Here

$$Q_{\mu\nu}(\mathbf{r}) = \psi_{\mu}^*(\mathbf{r})\psi_{\nu}(\mathbf{r}) - \tilde{\psi}_{\mu}^*(\mathbf{r})\tilde{\psi}_{\nu}(\mathbf{r}) \quad (5.51)$$

describes the difference between the charge density of the pseudo and all electron partial waves. Typically, this function is oscillatory in the augmentation sphere Ω_R , so that in practice further approximations to $Q_{\mu\nu}$ are applied. In the present code, the function is expanded in an orthogonal set of functions, and the rapid spatial oscillations are

5.4 Forming $G(\tau)G(-\tau)$ in the PAW Basis

neglected beyond a certain plane wave energy cutoff. More details about this topic can be found in Refs. 104, 111.

Using Eqs. (5.50) and Fourier transforming the RPA response function (3.41) to real space and imaginary time $i\tau$, the resulting expression for $\chi(\mathbf{r}, \mathbf{R}', \tau)$ contains four terms

$$\chi(\mathbf{r}, \mathbf{R}', \tau) = \sum_{j=1}^4 \chi^{(j)}(\mathbf{r}, \mathbf{R}', \tau). \quad (5.52)$$

Each contribution $\chi^{(j)}$ is characterized as follows: $\chi^{(1)}$ contains a summation of pseudo terms only

$$\chi^{(1)}(\mathbf{r}, \mathbf{R}', \tau) \propto \hat{y}(\tau, \xi_{ia}) \tilde{\phi}_i(\mathbf{r}) \tilde{\phi}_i^*(\mathbf{R}') \tilde{\phi}_a^*(\mathbf{r}) \tilde{\phi}_a(\mathbf{R}') \quad (5.53)$$

and is represented on a plane wave grid. The function \hat{y} was defined in Eq. (5.13) and ξ_{ia} indicates the transition energy and appeared in Eq. (3.38) for the first time. The second $\chi^{(2)}$ and third contribution $\chi^{(3)}$ contain terms from one augmentation sphere

$$\chi^{(2)}(\mathbf{r}, \mathbf{R}', \tau) \propto \hat{y}(\tau, \xi_{ia}) \tilde{\phi}_i(\mathbf{r}) \tilde{\phi}_a^*(\mathbf{r}) \sum_{\alpha\beta} \langle \tilde{\phi}_i | \tilde{p}_\alpha \rangle Q_{\alpha\beta}(\mathbf{R}') \langle \tilde{p}_\beta | \tilde{\phi}_a \rangle \quad (5.54)$$

$$\chi^{(3)}(\mathbf{r}, \mathbf{R}', \tau) \propto \hat{y}(\tau, \xi_{ia}) \tilde{\phi}_i^*(\mathbf{R}') \tilde{\phi}_a(\mathbf{R}') \sum_{\mu\nu} \langle \tilde{\phi}_a | \tilde{p}_\mu \rangle Q_{\mu\nu}(\mathbf{r}) \langle \tilde{p}_\nu | \tilde{\phi}_i \rangle. \quad (5.55)$$

The fourth term contains only augmentation terms

$$\chi^{(4)}(\mathbf{r}, \mathbf{R}', \tau) \propto \hat{y}(\tau, \xi_{ia}) \sum_{\mu\nu\alpha\beta} \langle \tilde{\phi}_a | \tilde{p}_\mu \rangle Q_{\mu\nu}(\mathbf{r}) \langle \tilde{p}_\nu | \tilde{\phi}_i \rangle \langle \tilde{\phi}_i | \tilde{p}_\alpha \rangle Q_{\alpha\beta}(\mathbf{R}') \langle \tilde{p}_\beta | \tilde{\phi}_a \rangle. \quad (5.56)$$

All terms need to be accounted for when computing the RPA polarizability from Green's functions using the contraction formula (5.47). For this purpose, we define the following auxiliary functions

$$G_{\mathbf{k}}^{(1)}(\mathbf{g}, \mathbf{G}', \tau) = \sum_n \langle \tilde{\phi}_{n\mathbf{k}} | \mathbf{g} \rangle \langle \mathbf{G}' | \tilde{\phi}_{n\mathbf{k}} \rangle e^{-\epsilon_{n\mathbf{k}}\tau} \quad (5.57)$$

$$G_{\mathbf{k}}^{(2)}(\mu, \mathbf{G}', \tau) = \sum_n \langle \tilde{\phi}_{n\mathbf{k}} | \tilde{p}_\mu \rangle \langle \mathbf{G}' | \tilde{\phi}_{n\mathbf{k}} \rangle e^{-\epsilon_{n\mathbf{k}}\tau} \quad (5.58)$$

$$G_{\mathbf{k}}^{(3)}(\mathbf{g}, \alpha, \tau) = \sum_n \langle \tilde{\phi}_{n\mathbf{k}} | \mathbf{g} \rangle \langle \tilde{p}_\alpha | \tilde{\phi}_{n\mathbf{k}} \rangle e^{-\epsilon_{n\mathbf{k}}\tau} \quad (5.59)$$

$$G_{\mathbf{k}}^{(4)}(\mu, \alpha, \tau) = \sum_n \langle \tilde{\phi}_{n\mathbf{k}} | \tilde{p}_\mu \rangle \langle \tilde{p}_\alpha | \tilde{\phi}_{n\mathbf{k}} \rangle e^{-\epsilon_{n\mathbf{k}}\tau} \quad (5.60)$$

5. LOW SCALING ALGORITHM FOR THE RANDOM PHASE APPROXIMATIONS

where the notation

$$\langle \tilde{\phi}_{n\mathbf{k}} | \mathbf{g} \rangle = \sum_{\mathbf{r} \in C} \tilde{\phi}_{n\mathbf{k}}^*(\mathbf{r}) e^{i\mathbf{g}\mathbf{r}} \quad (5.61)$$

$$\langle \tilde{\phi}_{n\mathbf{k}} | \mathbf{G} \rangle = \sum_{\mathbf{R}' \in S} \tilde{\phi}_{n\mathbf{k}}^*(\mathbf{R}') e^{i\mathbf{G}\mathbf{R}'} \quad (5.62)$$

was used, the Fermi energy was set to $\mu = 0$ and $\mathbf{G} = \mathbf{k} + \mathbf{g}$ is assumed for Eqs. (5.57)-(5.59). For each function $G^{(j)}$ two representatives $G_{<}^{(j)}, G_{>}^{(j)}$, for occupied and unoccupied states, are stored. They should be seen as lesser and greater parts of the Feynman propagator, see section 2.4 and Eq. (2.46). Lesser Green's functions ($\epsilon_i < 0$) are thereby evaluated on the negative, greater functions ($\epsilon_i > 0$) on the positive time axis τ only. In this way, the resulting Green's functions $G^{(j)}$ are linear combinations of decaying exponentials and bounded in time.

The computational cost for each term $G^{(j)}$ is

$$N_\omega N_k N_b^3 \approx N_\omega N_k N^3, \quad (5.63)$$

where N_ω is the number of imaginary time/frequency points. Using the FFTs (5.42) and (5.43) from the previous section, the real-space Green's functions are contracted as follows:

$$\begin{aligned} \chi(\mathbf{r}, \mathbf{R}', \tau) &= G_{>}^{(1)}(\mathbf{r}, \mathbf{R}', \tau) G_{<}^{*(1)}(\mathbf{r}, \mathbf{R}', -\tau) \\ &+ \sum_{\mu\nu} G_{>}^{(2)}(\mu, \mathbf{R}', \tau) G_{<}^{*(2)}(\nu, \mathbf{R}', -\tau) Q_{\mu\nu}(\mathbf{r}) \\ &+ \sum_{\alpha\beta} G_{>}^{(3)}(\mathbf{r}, \alpha, \tau) G_{<}^{*(3)}(\mathbf{r}, \beta, -\tau) Q_{\alpha\beta}(\mathbf{R}') \\ &+ \sum_{\mu\nu\alpha\beta} G_{>}^{(4)}(\mu, \alpha, \tau) G_{<}^{*(4)}(\nu, \beta, -\tau) Q_{\mu\nu}(\mathbf{r}) Q_{\alpha\beta}(\mathbf{R}'), \quad \tau > 0 \end{aligned} \quad (5.64)$$

Here, the atom positions $\mathbf{R}_\mu, \mathbf{R}_\nu$ are restricted to the unit cell C , whilst $\mathbf{R}_\alpha, \mathbf{R}_\beta$ take values within the supercell S (cf. Sec. 5.3).[69] From $\chi(\mathbf{r}, \mathbf{R}', \tau)$, $\chi_{\mathbf{k}}(\mathbf{g}, \mathbf{g}')$ is finally determined at individual k-points using Eqs. (5.44) and (5.45). After a successive cosine transformation, discussed in the previous section, the correlation energy in the random phase approximation is then determined in the usual manner at each k-point.[90]

Considering the computational time for each step (5.64), (5.63), (5.46) and (5.24) for the evaluation of E_c^{RPA} shows that the present algorithm determines the RPA energy with a computational cost of $\approx N_k N_b^3$. This reduces the time complexity by a factor $\approx N_k N_b$ compared to previous implementations.

5.5 Symmetry

The present code allows to use symmetry partially. For instance, the density functional theory calculations are performed using only the irreducible wedge of the Brillouin zone, and furthermore the RPA correlation energy is only calculated for the irreducible k-points \mathbf{k} using $\chi_{\mathbf{k}}(\mathbf{g}, \mathbf{g}')$ [compare Eq. (5.45)]. The Green's function $G_{\mathbf{k}}(\mathbf{g}, \mathbf{g}')$ could be also constructed in the irreducible wedge, however, presently we first use symmetry to construct the orbitals at all k-points and then construct the Green's function for all k-points in the full Brillouin zone.

Currently we disregard any symmetry, whenever a supercell index \mathbf{G} or \mathbf{R} is involved. This implies that all quadratically scaling steps fail to benefit from symmetry, whereas the cubically scaling steps (except the construction of $G_{\mathbf{k}}(\mathbf{g}, \mathbf{g}')$) exploit symmetry. This seems to be a reasonable compromise between the implementation effort and the compute cost.

5.6 Technical details

In the present work, all calculations were performed with the Vienna Ab initio Simulation Package (VASP) using the projector augmented wave method of Blöchl in the implementation of Kresse and Joubert.[104, 109] The Si potential was constructed to conserve the scattering properties of the atoms well up to about 15 Ry above the vacuum level. This was achieved by using additional projectors above the vacuum level. Core radii of 1.90 a.u. were used. Specifically, the `Si_GW` potential released with `vasp.5.2` was employed.

All plane waves with the kinetic energy E_{cut} lower than 250 eV are used in the DFT calculations, and the DFT calculations are performed using the PBE functional.[19] The exact exchange (EXX)+RPA@PBE calculations are performed at the same plane wave cutoff. When summations over unoccupied Kohn-Sham states are required (virtual orbitals), all orbitals spanned by the basis set are determined by exact diagonalization of the Kohn-Sham Hamiltonian. The correlation energy in the random phase approximation E_c^{RPA} is then calculated as discussed in the previous section.

The response function itself is also expanded in a plane wave basis set. The plane wave cutoff for this basis set is set to 120-166 eV (smaller than the basis set for the

5. LOW SCALING ALGORITHM FOR THE RANDOM PHASE APPROXIMATIONS

orbitals), and the correlation energy is extrapolated to the infinite basis set limit assuming that the basis set error falls off like the inverse of the number of plane waves included in the basis set for the response function.[90] In the VASP code, this requires a single calculation, as the response function is truncated at different cutoffs after calculation at the largest basis set of 166 eV. The extrapolation is performed automatically by the code, requiring a minimum of extra computation time. The structures used for the calculations were determined by relaxing all internal degrees of freedom at the PBE level (keeping the cell shape and volume fixed). In the subsequent RPA calculations, the PBE structures were used, since forces and the stress-tensor are presently not available. Similar strategies are also routinely adopted in diffusion Monte-Carlo simulations and most quantum chemistry, *e.g.* coupled cluster, calculations.

5.7 Application to Si Defect Energies

5.7.1 Bulk properties

With the present PAW potentials the volume per atom is 20.46 \AA^3 and 15.35 \AA^3 for cubic diamond and β -Sn for PBE. As a first test, we calculated the volume per atom for the RPA for these two phases. Using $6 \times 6 \times 6$ k-points and $10 \times 10 \times 10$ k-points for diamond and β -Sn respectively, the predicted atomic volumes are 20.0 \AA^3 and 15.25 \AA^3 , slightly smaller than the PBE volumes. Per atom, the RPA energy difference between the two phases is 380 meV. A similar energy difference of 390 meV using the same PAW potentials was also calculated by Xiao *et al.* in Ref. 112.

This is 100 meV larger than the energy difference predicted by the PBE functional (280 meV). Using diffusion Monte Carlo (DMC) Batista *et al.*, Alfè *et al.* and Henning *et al.* predicted values of 480 ± 50 meV,[113] 475 ± 10 meV,[114] and 424 ± 20 meV,[115] respectively (the latter two values are including core polarization contributions). In this case, the DMC does not seem to be suitable to gauge the quality of the RPA, since the transition pressure from diamond to the β -Sn phase predicted from the DMC data is about 16.5 GPa[113] and 14.0 ± 1.0 GPa,[115] respectively, which is larger than the experimental estimates of 10.3-12.5 GPa.[114] The energy difference predicted by the RPA (380 meV), however, corresponds to a transition pressure of about 13.5 GPa in reasonable agreement with the experimental estimates. The origin of the error of the DMC is not known, but we believe it could be related to the fixed node approximation,

5.7 Application to Si Defect Energies

or insufficient convergence of the sampling of the Brillouin zone for the metallic β -Sn phase.

Including the $2s$ and $2p$ electrons in the valence for the RPA calculations has a negligible effect on the predicted volumes.[116] However, it still lowers the energy difference between the two phases to 340 meV. A similar reduction from core polarization was also predicted in DMC calculations.[114] This lowers the predicted transition pressure to 12 GPa, now in excellent agreement with the experimental estimates. Overall, these results support the quality of the RPA predictions. For a more detailed discussion of RPA results obtained with the same code, for instance inclusion of zero point vibration effects, we refer to Xiao *et al.*[112]

5.7.2 Time complexity for large supercells

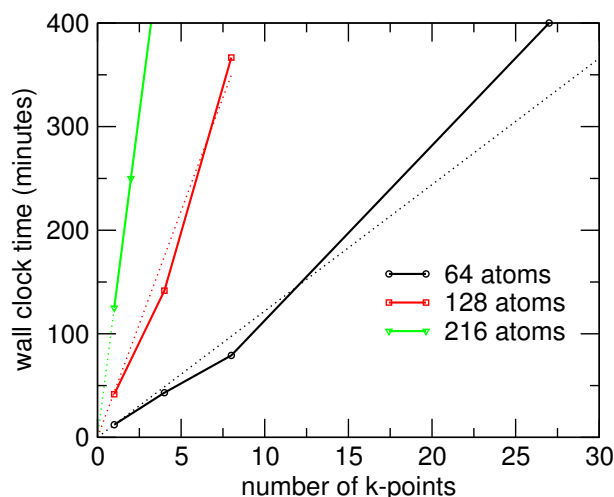


Figure 5.11: Computational time for 64, 128 and 216 atoms as a function of the number of k-points (in the full Brillouin zone). The total (wall clock) time is shown for 64, 128 and 224 cores. The computational demand increases linearly in the number of k-points and cubically in the number of atoms. The deviation from linearity is related to the need to double the number of cores for $3 \times 3 \times 3$ k-points (64 atoms) and $2 \times 2 \times 2$ k-points (128 atoms), and the non perfect scaling with the number of cores. The corresponding reported compute time has been doubled.

The results for the Si self interstitials and Si vacancies will be discussed in the next section. Here we briefly elaborate on the required computation time. The present cal-

5. LOW SCALING ALGORITHM FOR THE RANDOM PHASE APPROXIMATIONS

culations were performed for 64, 128 and 216 atom supercells (and 256 for the vacancy). The RPA corrections were determined for various k-point grids starting with the Γ -point. For the smallest cell, we could perform RPA calculations for up to $3 \times 3 \times 3$ k-points in less than 4 hours on 128 cores, a very modest computational effort. Calculations with more k-points are difficult, since the memory requirements would force us to increase the number of cores, but the parallel efficiency of the present code version is not yet very good making such calculations rather inefficient. The loss of efficiency is already witnessed for $3 \times 3 \times 3$ k-points, where we had to increase the number of cores from 64 to 128, gaining only little speedup from the additional 64 cores (compare Fig. 5.11). This is the reason why the reported computation time for 64 atoms and $3 \times 3 \times 3$ k-points (scaled back to 64 nodes) deviates from the straight line behavior. For 128 atoms we performed Γ -only calculations and calculations using $2 \times 2 \times 2$ k-points. Again calculations using $2 \times 2 \times 2$ k-points required an increase in the number of cores, here from 128 to about 200. A k-point sampling with 4 k-points was also realized by using only every second k-point of the $2 \times 2 \times 2$ grid, corresponding to an fcc sub-grid of the full simple cubic grid. For 216 atoms, the calculations were performed with a single k-point and two and four k-points. The second k-point corresponds to the coordinates $(1/4, 1/4, 1/4) 2\pi/a$ or a bcc sub-grid of a $2 \times 2 \times 2$ mesh.

In order to investigate the scaling with system size in more detail, we performed RPA calculations for 54, 128 and 250 bcc unit cells using the Γ point, see Tab. 5.1. The timings reported in Tab. 5.1 and Fig. 5.11 clearly confirm that the present code scales linear in the number of k-points, and roughly cubically with the number of atoms as discussed at the end of Sec. 5.4.

A few final comments are in place here. First, the reported timings were obtained using a complex code version. At the Γ -point, however, the response function is real valued, which allows to reduce the computational time by a factor two compared to the reported values. The corresponding calculations take 6 minutes for 64 atoms on 64 cores, or about 1 hour for 216 atoms on 224 cores. The scaling is very close to the expected scaling. We can also compare the computational time to our previous code version that scales quadratically with the number of k-points and with the fourth power of the number of atoms. For 64 atoms and the real Γ -point version, the old version required a reasonable 30 minutes (only a factor 5 slower than the new version), however, for 4 k-points the calculations are already a factor 10 slower, and for $3 \times 3 \times 3$ k-points

5.7 Application to Si Defect Energies

we expect the factor to be around 100. Considering common run time constraints on supercomputers, this would make the calculations almost impossible using the previous RPA implementation.[90]

Table 5.1: Timings in minutes for an RPA calculation for different bulk Si bcc cells. The calculations are done for the Γ point only and the number of cores is increased with system size. Since one of the computational steps scales only quadratically with system size, the total scaling is better than cubic.

atoms	cores	time	time \times cores/atoms ³ $\times 10^3$
54	32	14.3	2.91
128	64	83.2	2.54
250	128	299.9	2.45

5.7.3 Interstitial and vacancy

5.7.3.1 Considered structures and k-points sampling

We start with a brief discussion of the various self interstitials. The energetically most stable self-interstitial is the so called dumbbell configuration (X), in which two Si atoms reside at the position originally occupied by a single Si atom. The “dimer” is placed symmetrically in this position and oriented parallel to the [110] direction. The second most favorable position is the hexagonal hollow (H), where the Si interstitial is coordinated to six Si atoms forming a hexagonal ring. In PBE, this position is unstable, and the central Si atom tends to move slightly away from the central position in a direction orthogonal to the hexagonal ring.[117] As for instance done by Rinke *et al.*, we denote this lower symmetry 6 fold coordinated position as C_{3v} (corresponding to the symmetry of this configuration).[118] Somewhat higher in energy than the other interstitial sites is the tetragonal site (T), in which the additional Si atom is coordinated to 4 nearest Si neighbors, so that the local coordination of the interstitial is identical to the other Si atoms. This position is unique insofar that the highest occupied orbital is three fold degenerate (t_2 symmetry) but only occupied by 2 electrons. This would suggest that the position is susceptible to a Jahn-Teller distortion, but at least in PBE and for 64 atoms, a calculation of all vibrational modes does not show any instabilities. Likewise the vacancy (V) is characterized by a three fold degenerate t_2 highest orbital that is

5. LOW SCALING ALGORITHM FOR THE RANDOM PHASE APPROXIMATIONS

also occupied by 2 electrons. This configuration is known to undergo a Jahn-Teller distortion to a D_{2d} symmetry with slow supercell convergence.[119] In PBE, we observe the distortion from the 216 atom cell on, with the distortion fully developed only for a 256 atom cell; *e.g.* the magnitude of the structural distortion is about 25 % smaller in the 216 atom cell than in the 256 atom cell. For the smaller cells, the distortion only occurs if the k-point mesh is chosen artificially coarse (*e.g.* $2 \times 2 \times 2$ for 64 atoms), and we have used such k-point sets to prepare the symmetry reduced Jahn-Teller distorted vacancy (VJT) configuration. The energy difference to the undistorted configuration is, however, small and only of the order of 20 meV and can be safely disregarded for the present purpose.

The DFT calculations were carefully converged. In agreement with other studies we found that $4 \times 4 \times 4$ k-points are usually sufficient for 64 atom cells, and $2 \times 2 \times 2$ k-points for 216 atom cells.[119, 120] The only exception is the metallic T configuration, which in our calculations only converged to meV accuracy using slightly more k-points. The final PBE values reported in Tab. 5.2 were obtained using $8 \times 8 \times 8$, $6 \times 6 \times 6$, $4 \times 4 \times 4$ and $3 \times 3 \times 3$ k-points for 16, 64, 128 and 216 atoms. For the Si vacancy also a 256 atom cell with $3 \times 3 \times 3$ k-points was used. With these settings the values are converged to within a few meV. Except for a constant offset the present PBE values agree well with the values reported by Gao *et al.*[120] It is gratifying that two very different codes can obtain some 10 meV agreement for tiny relative energy differences, when the setups are carefully converged.

5.7.3.2 Energetics of point defects

The results for Si self interstitials and Si vacancies are summarized in Tab. 5.2. The RPA energies were evaluated using 16 frequency points. For 64 atoms, increasing the number of frequency points from 16 to 20 changed the results by less than 0.5 meV supporting the previous claim that few μeV accuracy per atom can be attained (the changes are largest for the defects with very small or even vanishing Kohn-Sham one electron gaps). Here we adopted the strategy to evaluate the difference between RPA+EXX and PBE at various k-point set. This strategy seems to work quite well: even though the PBE energies are wrong by more than 1.2 eV using the Γ -point only (see lines marked X(PBE)), the error in the difference between RPA+EXX and PBE is at most 150 meV at the Γ -point for 64 atoms. First useful corrections to DFT can hence be obtained already with a rather

5.7 Application to Si Defect Energies

Table 5.2: The second, third and fourth columns report the difference between RPA and PBE formation energies for different defect configurations, k-points and supercells, with the k-point set indicated in the first row (all values in eV). The second row in each set reports the k-point convergence of the PBE formation energies. The columns PBE and RPA report the final converged formation energies. The RPA value was calculated by adding the most accurate corrections to the k-point converged PBE values. The range separated range separated RPA (rsRPA) values are from Ref. 121, and the values for Heyd-Scuseria-Ernzerhof (HSE)+van der Waals (vdW) are from Ref. 120.

16 atoms	2^3	3^3	4^3	PBE	RPA	
X(PBE)	2.525	3.481	3.541	3.561		
X	0.824	0.706	0.711	3.561	4.27	
C_{3v}	0.855	0.800	0.745	3.644	4.39	
H	0.830	0.750	0.707	3.740	4.45	
T	0.930	0.882	0.868	3.659	4.53	
V	0.426	0.444	0.446	3.023	3.47	
X→H	0.862	0.809	0.760	3.783	4.54	
64 atom	Γ	2^3	3^3	PBE	RPA	rsRPA
X(PBE)	2.440	3.616	3.611	3.614		
X	0.818	0.659	0.654	3.614	4.27	4.50
C_{3v}	0.849	0.788	0.745	3.651	4.40	
H	0.820	0.753	0.708	3.658	4.37	4.65
T	1.025	1.080	1.046	3.790	4.84	
VJT	0.851	0.813	0.781	3.642	4.42	4.24
X→H	0.789	0.770	0.698	3.924	4.62	4.99
128 atom	Γ	4	2^3	PBE	RPA	
X(PBE)	2.662	3.603	3.571	3.610		
X	0.814	0.670	0.683	3.610	4.29	
C_{3v}	0.843	0.839	0.817	3.647	4.46	
H	0.832	0.775	0.755	3.654	4.41	
T	1.153	1.078	1.112	3.766	4.88	
VJT	0.855	0.795	0.829	3.636	4.47	
216 atom	Γ	2	4	PBE	RPA	vdW+HSE
X(PBE)	3.256	3.341	3.571	3.566		
X	0.724	0.710	0.632	3.566	4.20	4.41
C_{3v}	0.820	0.812	0.743	3.619	4.36	4.40
H	0.789	0.779	0.707	3.626	4.33	
T	1.105	1.144	1.139	3.791	4.93	4.51
VJT	0.789	0.755	0.742	3.646	4.39	4.38
256 atom	Γ	2		PBE	RPA	
VJT(PBE)	3.272	3.518		3.589		
VJT	0.839	0.745		3.589	4.33	

5. LOW SCALING ALGORITHM FOR THE RANDOM PHASE APPROXIMATIONS

coarse sampling. With $2 \times 2 \times 2$ k-points the errors in the RPA correction are below 50 meV, which is most likely acceptable for many purposes. For 128 atoms, the difference between 4 k-points (the fcc grid) and 8 k-points is a rather modest 20 meV. As a general rule of thumb, it seems that the k-point errors in the RPA corrections are about 1/3 of the k-point errors of the PBE energies. This also suggests that 4 and 2 k-points will yield only errors of about 10-20 meV for the calculation of the RPA correction for the 216 and 256 atom cell, respectively.

Considering the Γ -point only, the errors in the DFT energies and the RPA corrections are 300 meV and 100 meV, respectively, for the largest cells (216 and 256 atoms). This confirms the observation of many previous studies that calculations at the Γ -point should be considered with caution. Furthermore, we note that the convergence with the number of atoms of both, the DFT energies and the corrections is not monotonic but shows some residual fluctuations. This might be expected, since the cell shape – simple cubic for 64 and 216 atoms, but fcc for 128 atoms – influences the electronic dispersion, the long range electrostatic, as well as elastic interactions between the defects.[119, 122] For the present case, the k-point converged RPA formation energies vary by at most 100 meV between different super cells.

We start with a comparison with the most accurate theoretical values presently available, DMC data. Our results yield consistently lower formation energies than all DMC calculations, although the agreement with the latest DMC data is overall very good, in particular, for relative energies. Parker *et al.* predicted values of 4.4(1), 5.1(1), and 4.7(1) for X, T and H using DMC,[123] compared to our values of 4.20, 4.93 and 4.33 (largest supercell). We tend to believe that the residual underestimation by 200 meV is an error of the RPA, since the DMC values are so consistently higher in energy.[113, 123, 124] However, one should also keep in mind that most DMC calculations were performed with fairly small 16-atom supercells [113] with extrapolation to the dilute limit based on DFT energies. Likewise the k-point sampling in the DMC calculations was always limited to a single k-point, which might affect the predicted energies. In most DMC calculations, however, many-electron k-point errors due to the discretization of the momentum transfer between two k-points are estimated using the structure factor method, a method we could but have not applied in our RPA calculations.[123, 125] This implies that the k-point errors that we observe in the RPA are not transferable to well

5.7 Application to Si Defect Energies

extrapolated DMC calculations, where many electron k-point errors are expected to be much smaller.

The present formation energies are also very well within the range of experimental values and, furthermore, agree reasonably well with the HSE calculations of Gao *et al.*,[120] and to a lesser extent with the vdW+HSE calculations by the same authors. Specifically, the most stable structure is the dumbbell configuration X, followed by the interstitial in the hexagonal hole H, which is about 100 meV higher in energy, in excellent agreement with HSE calculations. The main discrepancy to the results of Gao is our instability of the tetragonal site.[120] In our calculations, this site is 600 meV above the dumbbell configuration X (in agreement with DMC data). In HSE, the difference is only 300 meV, and in vdW+HSE it is just 100 meV. In vdW-DFT this configuration is lowered compared to HSE by an increase of the polarization at the four nearest neighbor sites in the vdW+HSE calculations. In agreement with this observation, our negative correlation energy is largest for this metallic configuration, almost 2 eV lower than for the other interstitial sites. However, the unfavorable EXX energy of this configuration more than makes up for this increase in the correlation energy. The origin for the unfavorable EXX energy is the “metal” like behavior of this specific configuration with three degenerate partially occupied p orbitals at the Fermi-level: As for any metallic configuration, exact exchange penalizes this configuration, here by more than 2 eV. This is also the reason why this configuration is less favorable in hybrid functionals. We believe that the present seamless approach should give a better description than an introduction of vdW corrections on top of a hybrid functional with an *ad hoc* mixture between exact exchange and semi-local exchange. After all, vdW-DFT is derived from the RPA correlation energy expression considering the interaction between two coupled quantum harmonic oscillators.[126] However, one also needs to concede that the accuracy of the RPA for configurations with symmetry degenerate states at the Fermi-level is certainly not yet fully established and this issue might require further studies. Before continuing, we finally note that the RPA does predict the hexagonal hole to be lower in energy than the symmetry broken C_{3v} configuration. This is consistently observed for all supercell sizes. In this case, RPA clearly does not favor a symmetry broken solution, whereas PBE does.

5. LOW SCALING ALGORITHM FOR THE RANDOM PHASE APPROXIMATIONS

5.7.3.3 Diffusion barrier of interstitial

The final quantity we consider is the diffusion barrier of the interstitial Si atom. In all recent publications, including rsRPA and vdW corrected HSE, it was agreed that the lowest activation barrier for diffusion is encountered for the diffusion of one atom from the dumbbell configuration X to the hexagonal hole H.[120, 121] We first tested this conjecture by performing finite temperature molecular dynamics at 800 K for the 64 atom cell, the PBE functional and a $3 \times 3 \times 3$ k-point mesh. Indeed, Si diffuses fairly rapidly with all diffusion events occurring from the dumbbell configuration X to the hollow site H, followed by a rapid jump from H to another site X'.

In the RPA calculations, the estimated activation enthalpy for interstitial diffusion is 4.62 eV (64 atom cell), in very good agreement with estimates of 4.69 eV,[127] but smaller than the estimates of Bracht *et al.* (4.95 ± 0.03 eV).[128] The diffusion barrier from X to H is calculated to be 350 meV, only slightly larger than the recent value predicted from HSE+vdW (290 meV).[120] Both values are in reasonable, but certainly not great, agreement with the best experimental estimates of 200 meV measured at cryogenic temperatures (from -273 to -150° C).[129] The remaining difference between RPA and HSE+vdW could be related to the fact that we have used PBE geometries throughout this work, whereas Gao *et al.* performed the calculations consistently using geometries determined by HSE+vdW.

Our present estimate for the diffusion barrier differs from the value of 490 meV obtained using rsRPA by Bruneval.[121] Furthermore, whereas the vacancy formation energy of 4.33 eV is identical to rsRPA, our interstitial formation energies are about 200-300 meV lower than those predicted using rsRPA.[121] Since the technical parameters of the calculations of Bruneval are similar to our setups, this is either a consequence of different pseudopotentials or range separation. Although range separation is an approach that allows to reduce the number of occupied orbitals with little impact on accuracy, the results, to some extent, always depend on the range separation parameter, and the optimal choice varies between systems with small lattice constants (large Fermi-vector) and systems with large lattice constants (small Fermi-vector). Also, range separation spoils the basis set extrapolation: For standard RPA the extrapolation with the basis set size of the response function strictly follows a one over basis set size behavior for all systems we have yet considered. This is not the case, when range separation is used,

5.8 Discussion and Conclusions

so that residual errors are difficult to control and estimate. In general, we hence prefer, whenever computable, the standard RPA to an approximate method.

5.7.3.4 Small unit cells

Finally, we would like to comment on the smallest 16 atom unit cell, since most high level DMC calculations are performed for such a small unit cell. Except for the tetragonal site and vacancy, the results are in reasonable agreement with the larger unit cells, both on the level of the PBE, as well as, on the level of the RPA. Furthermore, the calculated energy correction PBE-RPA are accurate to about 50 meV, except again for the vacancy and tetragonal site. We recall that these are the two configurations resulting in partially filled states. Obviously aggregation of such defects reduces their formation energy. This effect is most pronounced and only relevant for the vacancy, which is predicted to be much more stable in the 16 atom unit cell than in the larger unit cells. In fact, our results imply that, configuration entropy disregarded, vacancies should cluster. This is in agreement with Ref. 130, where diffusion of vacancies in Si has been investigated.

5.8 Discussion and Conclusions

In this chapter we have discussed a cubic scaling algorithm for the calculation of the RPA correlation energy and have shown practical applications of the algorithm to supercells containing up to 256 atoms.

The main strategy of the cubic scaling algorithm is to determine the Green's function for positive and negative imaginary time and, concomitantly, occupied and unoccupied states. This step scales like $N_{\text{orbitals}} \times N_b \times N_b$, where N_b specifies the basis set size for the orbitals [see Eq. (5.63)].

The independent particle polarizability is then trivially given by the point wise contraction in real-space of these two Green's functions at any considered time point [cf. Eq. (5.47)]. The contraction is formally only a step scaling like $N_{\text{real}} \times N_{\text{real}}$, where N_{real} is the number of grid points in real space. In practice, this step is fairly involved in the PAW method, so that the computational time of this step is often similar to the calculation of the Green's functions itself [see Eq. (5.64) in Sec. 5.4].

The final step is the Fourier transformation from imaginary time to imaginary frequency. This step is discussed in detail in section 5.2 also elaborating on the issue

5. LOW SCALING ALGORITHM FOR THE RANDOM PHASE APPROXIMATIONS

of optimal time and frequency grids and their duality. We, however, stress here that an accuracy of few $\mu\text{eV}/\text{atom}$ can be attained using about 16 imaginary time and frequency points. After the Fourier transformation to imaginary frequency, the calculations proceed in the same manner as standard RPA calculations, by diagonalization of the polarizability using the plasmon formula for the correlation energy [cf. Eq. (3.37)].

As demonstrated here, calculations for 64 Si atoms and $3 \times 3 \times 3$ k-points can be performed in about 5 hours on 128 cores. About the same time is required for 216 Si atoms and 2 k-points. Because the polarizability is real valued at the Γ -point, the Γ -point only calculations are much cheaper, requiring about 6 minutes for 64 atoms on 64 cores, or one hour for 216 atoms on 224 cores. To put the effort for all the RPA calculations into perspective: the computation time for calculating all occupied and unoccupied orbitals spanned by the basis set using an efficient parallel `scaLAPACK` routine— a prerequisite for RPA calculations—requires about one third to one half of the computational time of the final RPA step. We hope that this high efficiency, makes RPA calculations sufficiently cheap, to perform them routinely a posteriori for any system of interest.

The main physical objective of the present work was a study of the Si interstitial and Si mono-vacancy energies at the level of the RPA. The most stable interstitial defect is the dumbbell configuration with a formation energy of 4.20 eV. The activation energy for diffusion from the dumbbell configuration to the hollow site is predicted to be 350 meV. These values are in reasonable agreement with very recent HSE calculations including semi-empirical van der Waals corrections (dumbbell energy 4.41 eV and migration barrier 290 meV, respectively). The vacancy formation energy is calculated to be 4.38 eV, also in excellent agreement with the HSE+vdW calculations (4.41 eV). We, however, observe that metallic configurations such as the tetragonal interstitial site are significantly higher in energy than predicted with HSE and HSE+vdW, and generally the energy landscape is not as 'washed' out and featureless as in the HSE+vdW prescription. All in all, our result are closer to the straight HSE calculations than the HSE+vdW results, except for the diffusion barrier agreeing well with the HSE+vdW results.

Comparison of the present values with, in principle, highly accurate DMC values is also very gratifying. In general, all predicted interstitial energies are roughly 0.2 eV lower than in DMC. The origin of this small shift might be related to cell size issues in the DMC or an error of the RPA. Finally, we have reported that the RPA yields a very good prediction for the transition pressure between diamond Si and β -Si of about 12

5.8 Discussion and Conclusions

GPa (when $2s$ and $2p$ electrons are included in the valence). Compared to experiment (10-12 GPa), this is slightly better than the best DMC estimates of about 14 GPa. In general, the present work again confirms that the RPA is a promising and quite accurate method to estimate correlation energies. With the present cubically scaling algorithm, defect calculations and the calculation of adsorption energies on surfaces should become a routine task.

5. LOW SCALING ALGORITHM FOR THE RANDOM PHASE APPROXIMATIONS

6

Merging GW with DMFT

In this chapter we discuss how to merge the GW approximation with DMFT. As explained at the end of previous chapter, using the GW method instead of LDA allows, in principle, to avoid a double counting of perturbation terms as well as the determination of the effective interaction matrix \mathcal{U} . The general recipe for GW +DMFT calculations is well known, see Ref. [87], and was derived in section (4.5). In summary the two Dyson equations Eq. (4.127) and (4.128) for the propagator G and screened interaction W need to be solved self-consistently in the limit $d \rightarrow \infty$ with the constraints (4.129) and (4.130). That is, the following (local) equations need to be solved self-consistently for the undressed impurity propagator \mathcal{G} and undressed impurity interaction \mathcal{U}

$$[\mathcal{G}^{-1}(i\omega_n)]_{\alpha\beta} = [G^{-1}(i\omega_n)]_{\alpha\beta} + \Sigma_{\alpha\beta}(i\omega_n) \quad (6.1)$$

$$[\mathcal{U}^{-1}(i\nu_n)]_{\alpha\beta\gamma\delta} = [W^{-1}(i\nu_n)]_{\alpha\beta\gamma\delta} + \chi_{\alpha\beta\gamma\delta}(i\nu_n), \quad (6.2)$$

where G is the dressed propagator, W the screened interaction, Σ and χ the local self-energy and the local polarizability of the considered system, respectively.

Following Ref. [131], a self-consistent GW +DMFT algorithm can be formulated as follows

GW +DMFT Algorithm

GWD1 Obtain the fermionic and bosonic propagators G_{GW} and W_{GW} in the GW approximation as solutions of

$$G_{GW}^{-1} = G_0^{-1} - \Sigma_{GW} \quad (6.3)$$

$$W_{GW}^{-1} = V^{-1} - \chi_{GW} \quad (6.4)$$

6. MERGING GW WITH DMFT

In the first iteration use $\Sigma_{GW} = G_0W$ and $\chi_{GW} = G_0G_0$.

GWD2 Undress local (*i.e.* \mathbf{k} -integrated) contributions of Σ_{GW} and χ_{GW} in the fermionic and bosonic propagators G and W to obtain the undressed impurity correlation functions

$$\mathcal{G}^{-1} = G_{GW}^{-1} + \Sigma_{GW}^{\text{loc}} \quad (6.5)$$

$$\mathcal{U}^{-1} = W_{GW}^{-1} + \chi_{GW}^{\text{loc}} \quad (6.6)$$

GWD3 Compute the dressed impurity propagators G_{imp} and χ_{imp} with the eDMFT action

$$\begin{aligned} \mathcal{S}_\infty[d, d^*] = & - \int_\tau \int_{\tau'} \left[d_\alpha^*(\tau) [\mathcal{G}^{-1}(\tau - \tau')]^{\alpha\beta} d_\beta(\tau') \right. \\ & \left. + \frac{1}{2} n_{\alpha\delta}(\tau) \mathcal{U}^{\alpha\beta\gamma\delta}(\tau - \tau') n_{\alpha\delta}(\tau') \right] \end{aligned} \quad (6.7)$$

using \mathcal{G} and \mathcal{U} from previous step.

GWD4 Extract the fermionic and bosonic impurity self-energies

$$\Sigma_{\text{imp}} = \mathcal{G}^{-1} - G_{\text{imp}}^{-1} \quad (6.8)$$

$$\chi_{\text{imp}} = \mathcal{U}^{-1} - W_{\text{imp}}^{-1} \quad (6.9)$$

GWD5 Replace local contributions in the GW self-energies Σ_{GW} and χ_{GW} by impurity self-energies

$$\Sigma_{GW}^{\text{new}} = \Sigma_{GW} - \Sigma_{GW}^{\text{loc}} + \Sigma^{\text{loc}} \quad (6.10)$$

$$\chi_{GW}^{\text{new}} = \chi_{GW} - \chi_{GW}^{\text{loc}} + \chi^{\text{loc}} \quad (6.11)$$

GWD6 If the convergence criteria $|\Sigma_{GW}^{\text{new}} - \Sigma_{GW}| \rightarrow 0$ and $|\chi_{GW}^{\text{new}} - \chi_{GW}| \rightarrow 0$ are fulfilled the calculation is finished, otherwise go back to GWD1 and solve Eq. (6.3) and (6.4) with updated self-energies.

First GW +DMFT results using this algorithm were presented only recently in Refs. [131], however, only for a single-band Hubbard model. Application of this algorithm to realistic systems is missing so far. This is mainly due to the heavy computational effort of the algorithm, originating in taking the frequency-dependence of the impurity interaction \mathcal{U} into account as well as the frequency-dependence of the GW self-energy.

In this work, we follow an alternative route, based on the following approximations:

- A static impurity interaction

$$U_{\alpha\beta\gamma\delta} = \lim_{\nu \rightarrow 0} \mathcal{U}_{\alpha\beta\gamma\delta}(i\nu) \quad (6.12)$$

is considered and Eq. (6.9) is neglected (DMFT instead of eDMFT).

- The G_0W_0 scheme, as described in section 4.2.1 with the linearized frequency-dependence of Σ_{GW} is used.
- The double counting correction of Eq. (6.5) is treated on the LDA+DMFT level, see Eq. (4.140).
- A single iteration is computed, that is step GWD5 is neglected.

These simplifications reduce the computational cost remarkably, and the resulting algorithm, named $qpGW+DMFT$ in the following, can be applied to realistic systems, see section 6.3.

However, we emphasize that the calculation of the static interaction $U_{\alpha\beta\gamma\delta}$ is still controversially discussed in the literature, especially if states described by the Hubbard Hamiltonian are strongly entangled with the environment. The reason for this is explained in the following section and a general method to compute effective model interactions U from first principles is given.

6. MERGING GW WITH DMFT

6.1 Constrained Random Phase Approximation

The following section was submitted to Physical Review B in June 2015.

6.1.1 Terminology

In this section, we focus our attention on the determination of the effective impurity interaction matrix $U_{\alpha\beta\gamma\delta}$ for the real lattice vector $\mathbf{R} = \mathbf{0}$. This term describes the effective interaction between two electron-hole pairs $(w_\alpha, w_\delta), (w_\beta, w_\gamma)$ and can be written as the expectation value of an effectively screened Coulomb kernel \mathcal{U} via Eq. (6.12). This was first pointed out by Aryasetiawan *et al.*, see Ref. 132, and the method is named constrained random phase approximation (CRPA).

Following Aryasetiawan, we separate the Fockspace into two subspaces

$$\mathbb{F} = \mathbb{D} \oplus \bar{\mathbb{D}}, \quad (6.13)$$

where states within \mathbb{D} are described by the impurity model, *i.e.* on the DMFT level. This space is named *correlated or target subspace* in the following and it is assumed that \mathbb{D} contains only a few strongly localized states $N_{\mathbb{D}}$ around the Fermi level. The complement $\bar{\mathbb{D}}$ is described by the GWA (or alternatively DFT) and contains a large number of (usually delocalized) states.

It is convenient to average over the specific matrix elements of the static interactions $U_{\alpha\beta\gamma\delta}$ and to introduce the so-called *Hubbard-Kanamori* parameters[132]

$$U = \frac{1}{N_{\mathbb{D}}} \sum_{\alpha=1}^{N_{\mathbb{D}}} U_{\alpha\alpha\alpha\alpha} \quad (6.14)$$

$$U' = \frac{1}{N_{\mathbb{D}}(N_{\mathbb{D}} - 1)} \sum_{\alpha \neq \beta=1}^{N_{\mathbb{D}}} U_{\alpha\beta\beta\alpha} \quad (6.15)$$

$$J = \frac{1}{N_{\mathbb{D}}(N_{\mathbb{D}} - 1)} \sum_{\alpha \neq \beta=1}^{N_{\mathbb{D}}} U_{\alpha\beta\alpha\beta}. \quad (6.16)$$

For cubic symmetry, there are in fact only three linearly independent parameters.[133] Additionally, it will be interesting to consider the bare and fully screened Coulomb

6.1 Constrained Random Phase Approximation

interaction averages in the same basis

$$\bar{V} = \frac{1}{N_{\mathbb{D}}} \sum_{\alpha=1}^{N_{\mathbb{D}}} V_{\alpha\alpha\alpha\alpha} \quad (6.17)$$

$$\bar{W} = \frac{1}{N_{\mathbb{D}}} \sum_{\alpha=1}^{N_{\mathbb{D}}} W_{\alpha\alpha\alpha\alpha}. \quad (6.18)$$

The corresponding matrix elements are obtained analogously to (6.12) by replacing the impurity interaction \mathcal{U} with the bare Coulomb kernel $V(\mathbf{r}, \mathbf{r}') = |\mathbf{r} - \mathbf{r}'|^{-1}$ or the solution of the Dyson equation

$$W(i\nu) = V + V\chi(i\nu)W(i\nu). \quad (6.19)$$

Due to the nature of the GW approximation, here χ is the independent particle polarizability χ^0 , describing all polarization effects on the RPA level, see chapter 4 and section 4.2.1 or Refs. 12, 16, 134, 135, 136.

In the CRPA the effective kernel \mathcal{U} is obtained formally from the effective polarizability

$$\chi^r(i\nu) = \chi^0(i\nu) - \chi^d(i\nu) \quad (6.20)$$

and the bare Coulomb interaction V by

$$\mathcal{U}(i\nu) = V + V\chi^r(i\nu)\mathcal{U}(i\nu). \quad (6.21)$$

The effective polarizability χ^r contains all polarization effects, except those within the correlated space \mathbb{D} . These contributions are described by the correlated part χ^d , see Ref. 137. The last expression is consistent with the DMFT limit (6.2), which in our terminology translates into

$$\begin{aligned} W^{-1}(i\nu) &= V^{-1} - \chi^0(i\nu) \\ &= \underbrace{V^{-1} - \chi^r(i\nu)}_{\mathcal{U}^{-1}(i\nu)} - \chi^d(i\nu) \end{aligned} \quad (6.22)$$

This equation may be rewritten into

$$W(i\nu) = \mathcal{U}(i\nu) + \mathcal{U}(i\nu)\chi^d(i\nu)W(i\nu) \quad (6.23)$$

meaning, that in the ideal case χ^d represents only local polarization effects on the RPA level. This case is studied in section (6.2).

6. MERGING GW WITH DMFT

Here we assume that \mathbb{D} contains also non-local states $|w_\alpha\rangle$ with lattice vectors \mathbf{R}_α not necessarily restricted to the unit cell at $\mathbf{R}_\alpha = \mathbf{0}$. This on the other hand implies that the separation (6.13) is trivial in the Bloch domain, only if the correlated space \mathbb{D} forms an isolated set of bands. In this case, it is namely always possible to find a minimal Wannier basis without including itinerant states such as s- or p-states from $\bar{\mathbb{D}}$, see Ref. 138. For these systems, the effective polarizability takes the constrained form of the Adler and Wiser expression (3.41)

$$\chi_{\mathbf{q}}^d(\mathbf{g}, \mathbf{g}', i\nu) = \frac{1}{N_{\mathbf{k}}} \sum_{\mathbf{k}, n, n' \in \mathbb{D}} y(\nu, \xi_{\mathbf{a}\mathbf{i}}) \langle \phi_{\mathbf{i}} | e^{i(\mathbf{g}+\mathbf{q})\mathbf{r}} | \phi_{\mathbf{a}} \rangle \langle \phi_{\mathbf{a}} | e^{-i(\mathbf{g}'+\mathbf{q})\mathbf{r}'} | \phi_{\mathbf{i}} \rangle, \quad (6.24)$$

where $|\phi_{\mathbf{i}=n\mathbf{k}}\rangle$ is an occupied, $|\phi_{\mathbf{a}=n'\mathbf{k}+\mathbf{q}}\rangle$ an unoccupied Bloch state and the function y with the shorthand $\xi_{\mathbf{a}\mathbf{i}} = \epsilon_{\mathbf{a}} - \epsilon_{\mathbf{i}}$ was defined in Eq. (5.12):

$$y(\nu, \xi) = \frac{2\xi}{\xi^2 + \nu^2} \quad (6.25)$$

However, isolated target bands are rare and more often d- and f-states are entangled with other non-correlated s- and/or p-states. Consequently the separation of the subspace \mathbb{D} described by the impurity model in DMFT can be defined unambiguously only in the localized Wannier basis. In general, Wannier states are related to Bloch states by a unitary rotation $T_{n\alpha}^{(\mathbf{k})}$ combined with a discrete Fourier transformation w.r.t. the k-points, see Eq. (4.90) or Ref. 75.

At this point the arbitrariness of the unitary matrices $T_{n\alpha}^{(\mathbf{k})}$ has to be mentioned and was first studied by Kohn in Ref. 75.¹ It was proposed to use the maximally localized Wannier scheme of Marzari and Vanderbilt, see Refs. 140, 141, where a spread functional is minimized yielding maximally localized Wannier functions (MLWFs). However, in practice one often uses the so-called *first guess*, as presented in Ref. 142, for the rotation in Eq.(4.90)

$$T_{n\alpha}^{(\mathbf{k})} = \langle \phi_{n\mathbf{k}} | Y_\alpha \rangle, \quad (6.26)$$

where $|Y_\alpha\rangle$ indicates eigenfunctions of the hydrogen atom. This is due to the fact, that Eq. (6.26) yields Wannier functions resembling atomic orbitals, whereas MLWF often have different symmetry. In this section, we use Wannier functions obtained from (6.26) exclusively and consider MLWF only in section 6.2 and 6.3.

¹ A good review about Wannier functions can be found in Ref. 139.

6.1 Constrained Random Phase Approximation

We emphasize that, in general, the existence of exponentially localized Wannier functions is guaranteed only, if a complete *composite Bloch band*, that is the Bloch bands are isolated and do not cross other bands, is transformed into the Wannier domain.¹ This is the case for instance in SrVO₃ or La₂CuO₄ shown in Fig. 6.9 and Fig. 6.1 respectively. Only in this case equation (4.90) can be seen as a well-defined transformation between the Bloch and Wannier domain. In section 6.1.3 we show that in this context a consistent CRPA framework can be defined, even if the target space \mathbb{D} is smaller than space spanned by the Wannier basis.

If the considered Bloch bands are entangled, *i.e.* no composite Bloch band can be defined, Wannier functions cannot be obtained straightforwardly. For instance this is the case for the 3d transition metal series, investigated in section 6.1.6. For these systems the Wannier states have to be obtained as a projection from Bloch states using an energy window in combination with a disentanglement scheme, for instance the approach of Souza *et al.* [see Ref. 143 for more details]. In principle there are two projections possible. Either one projects the Bloch bands onto a minimal Wannier basis set, which forms the correlated subspace \mathbb{D} , or one includes additional functions in order to reproduce the original Bloch band structure as well as possible.

To our knowledge there are currently two different CRPA schemes, associated with the two Wannier projection schemes:

- (i) Disentangling method introduced in Ref. 144.
- (ii) Weighted method proposed in Refs. 145 and 146.

The disentanglement scheme of Miyake and coworkers projects the Bloch states onto a minimal basis set spanning only the correlated space \mathbb{D} . In the second step, the Hamiltonian of the system is diagonalized separately in \mathbb{D} and the remaining Fock space, so that a disentangled Kohn-Sham eigensystem $\{\tilde{\phi}_{n\mathbf{k}}, \tilde{\epsilon}_{n\mathbf{k}}\}$ for the states around the Fermi level is obtained. If the full polarizability is determined w.r.t. this disentangled eigensystem, giving $\tilde{\chi}$, one can use Eq. (6.24) to remove the correlated polarizability $\tilde{\chi}^d$. The approach seems quite elegant, but suffers from the deficiency, that the minimal basis set (and therefore the effective interactions) depends strongly on the chosen energy window.[147]

¹The interested reader is referred to the excellent article [138] for more details.

6. MERGING GW WITH DMFT

This dependency is weakened in the weighted scheme by including non-correlated delocalized s- and/or p-states in the Wannier projection and using the weighted CRPA formula[145, 146]

$$\chi_{\mathbf{q}}^d(\mathbf{g}, \mathbf{g}', i\nu) = \frac{1}{N_{\mathbf{k}}} \sum_{\mathbf{k}, n, n'} \Upsilon(\nu, \xi_{\mathbf{a}\mathbf{i}}) y(\nu, \xi_{\mathbf{a}\mathbf{i}}) \langle \phi_{\mathbf{i}} | e^{i(\mathbf{g}+\mathbf{q})\mathbf{r}} | \phi_{\mathbf{a}} \rangle \langle \phi_{\mathbf{a}} | e^{-i(\mathbf{g}'+\mathbf{q})\mathbf{r}'} | \phi_{\mathbf{i}} \rangle \quad (6.27)$$

with

$$\Upsilon(\nu, \xi_{\mathbf{a}\mathbf{i}}) = \gamma_{\mathbf{i}, \mathbf{a}} y(\nu, \xi_{\mathbf{a}\mathbf{i}}), \quad \mathbf{i} = n\mathbf{k}, \quad \mathbf{a} = n'\mathbf{k} + \mathbf{q} \quad (6.28)$$

instead. This expression seems reasonable, because the weights

$$\gamma_{\mathbf{i}\mathbf{a}} = \sum_{\alpha \in \mathbb{D}} \left| T_{\alpha n}^{(\mathbf{k})} \right|^2 \sum_{\beta \in \mathbb{D}} \left| T_{\beta n'}^{(\mathbf{k}+\mathbf{q})} \right|^2 \quad (6.29)$$

account for the correlated character of every (occupied-unoccupied) Bloch pair ($\mathbf{i} = n\mathbf{k}, \mathbf{a} = n'\mathbf{k} + \mathbf{q}$). It was claimed that expression (6.27) follows from the general Kubo-Nakano formula for the fluctuation response of the correlated subspace[145]

$$\chi^d(\mathbf{r}, \mathbf{r}', \tau) = \langle \Psi_0 | T [\delta \hat{n}_d(\mathbf{r}, \tau) \delta \hat{n}_d(\mathbf{r}')] | \Psi_0 \rangle, \quad (6.30)$$

where $\delta n_d(\mathbf{r}, \tau)$ is the correlated fluctuation density operator in imaginary time $t = -i\tau$. The latter counts the number of particles in the correlated subspace \mathbb{D} relative to the groundstate and is defined in Eq. (6.45) of following section. We show in section 6.1.3, that this claim is incorrect and that expression (6.30) yields a different result involving the correlated projectors

$$P_{nm}^{(\mathbf{k})} = \sum_{\alpha \in \mathbb{D}} T_{\alpha n}^{*(\mathbf{k})} T_{\alpha m}^{(\mathbf{k})} \quad (6.31)$$

with the correlated Bloch functions

$$|\bar{\phi}_{n\mathbf{k}}\rangle = \sum_m P_{nm}^{(\mathbf{k})} |\phi_{m\mathbf{k}}\rangle \quad (6.32)$$

rather than the probabilities (6.29). The derivation provides the basis for a consistent CRPA framework.

6.1 Constrained Random Phase Approximation

6.1.2 Correlated Subspaces and Wannier Representation

To keep the notation as simple as possible, we use bold Latin indices $\mathbf{n}, \mathbf{m}, \dots$ to indicate Bloch states $\mathbf{n} = (n, \mathbf{k}_n)$ and Greek indices to indicate Wannier states. Here, bold indices $\boldsymbol{\alpha}$ stand for the composite index $(\alpha, \mathbf{R}_\alpha)$, whereas α indicates the site index at $\mathbf{R}_\alpha = \mathbf{0}$. The index s will be used to denote an arbitrary Slater determinant $|\Psi_s\rangle$, defined in Eq.(1.6), with corresponding eigenenergies

$$E_s = \sum_{\mathbf{n} \in I_s} \epsilon_{\mathbf{n}}. \quad (6.33)$$

Each determinant $|\Psi_s\rangle$ contains a specific set of occupied and unoccupied states indicated by the index set I_s . The set $\{|\Psi_s\rangle, E_s\}_{s=1}^\infty$ forms a complete eigenset for the non-interacting many-body Hamiltonian (2.2) and is naturally given in the Bloch domain, see section 1.2. A transformation to the Wannier basis is easily performed by a replacement of $[\varepsilon_{(s)}]$ in Eq. (1.6) by the weighted Levi-Civita tensor

$$[\mathcal{T}_{(s)}]^{\boldsymbol{\alpha}_1 \dots \boldsymbol{\alpha}_N} = [\varepsilon_{(s)}]^{\mathbf{n}_1 \dots \mathbf{n}_N} T_{\mathbf{n}_1}^{\boldsymbol{\alpha}_1} \dots T_{\mathbf{n}_N}^{\boldsymbol{\alpha}_N}. \quad (6.34)$$

Here and in the following we adopt the Einstein convention and use the abbreviation

$$T_{\boldsymbol{\alpha}\mathbf{n}} = e^{i\mathbf{k}_n \mathbf{R}_\alpha} T_{\alpha\mathbf{n}}, \quad (6.35)$$

such that the Wannier-Bloch transformation pair reads

$$|w_{\boldsymbol{\alpha}}\rangle = T_{\boldsymbol{\alpha}}^{\mathbf{n}} |\phi_{\mathbf{n}}\rangle \quad (6.36)$$

$$|\phi_{\mathbf{n}}\rangle = T_{\mathbf{n}}^{*\boldsymbol{\alpha}} |w_{\boldsymbol{\alpha}}\rangle. \quad (6.37)$$

The Fock space of the non-interacting and interacting system is spanned by single, double and higher excited Slater determinants $|\Psi_s\rangle$. For instance singly excited states are obtained by replacing one occupied state $\phi_{\mathbf{i}}$ in the groundstate $|\Psi_0\rangle$ by an unoccupied state $\phi_{\boldsymbol{\alpha}}$ and defining the index set I_s appropriately.

We focus on the field operators $\hat{\psi}(\mathbf{r})$ and its conjugate $\hat{\psi}^\dagger(\mathbf{r})$ for a moment. Convenient representations of the field operators are the Bloch and Wannier representation and their inverses

$$\hat{\psi}(\mathbf{r}) = \phi^{\mathbf{n}}(\mathbf{r}) \hat{c}_{\mathbf{n}}, \quad \hat{c}_{\mathbf{n}} = \int d\mathbf{r} \phi_{\mathbf{n}}^*(\mathbf{r}) \hat{\psi}(\mathbf{r}) \quad (6.38)$$

$$\hat{\psi}(\mathbf{r}) = w^{\boldsymbol{\alpha}}(\mathbf{r}) \hat{d}_{\boldsymbol{\alpha}}, \quad \hat{d}_{\boldsymbol{\alpha}} = \int d\mathbf{r} w_{\boldsymbol{\alpha}}^*(\mathbf{r}) \hat{\psi}(\mathbf{r}). \quad (6.39)$$

6. MERGING GW WITH DMFT

The product of both operators gives the density operator

$$\hat{n}(\mathbf{r}) = \hat{\psi}^\dagger(\mathbf{r})\hat{\psi}(\mathbf{r}), \quad (6.40)$$

which is diagonal in real-space and identified as the number operator. The insertion of Eqs. (6.38) and (6.39) into Eq. (6.40) yields the Bloch and Wannier representations

$$\hat{n}(\mathbf{r}) = \phi^{*\mathbf{n}}(\mathbf{r})\phi^{\mathbf{m}}(\mathbf{r})\hat{c}_{\mathbf{n}}^\dagger\hat{c}_{\mathbf{m}} \quad (6.41)$$

$$\hat{n}(\mathbf{r}) = w^{*\alpha}(\mathbf{r})w^\beta(\mathbf{r})\hat{d}_\alpha^\dagger\hat{d}_\beta. \quad (6.42)$$

The corresponding fluctuation operator $\delta\hat{n}(\mathbf{r})$ is given by

$$\delta\hat{n}(\mathbf{r}) = \hat{n}(\mathbf{r}) - \langle\Psi_0|\hat{n}(\mathbf{r})|\Psi_0\rangle \quad (6.43)$$

and measures the fluctuation of the density w.r.t. the groundstate $|\Psi_0\rangle$, see Ref. 34.

Kubo and Nakano showed that the expectation value of $\delta\hat{n}(\mathbf{r},\tau)\delta\hat{n}(\mathbf{r}')$ in the ground-state describes the density fluctuation at (\mathbf{r},τ) to linear order, which is induced by a density change at $(\mathbf{r}',0)$. This is the essence of linear response theory and it can be shown that

$$\chi^0(\mathbf{r},\mathbf{r}',\tau) = \langle\Psi_0|\hat{T}[\delta\hat{n}(\mathbf{r},\tau)\delta\hat{n}(\mathbf{r}')]|\Psi_0\rangle \quad (6.44)$$

holds, see for instance Ref. 34.

However, we are mainly interested in Eq. (6.30), so that we restrict the sum in Eq. (6.42) to correlated states only, *i.e.* the subspace \mathbb{D} and obtain the correlated density operator

$$\hat{n}_d(\mathbf{r}) = \sum_{\alpha\beta\in\mathbb{D}} w_\alpha^*(\mathbf{r})w_\beta(\mathbf{r})\hat{d}_\alpha^\dagger\hat{d}_\beta. \quad (6.45)$$

Writing $\hat{n}_r(\mathbf{r})$ for the remaining terms in (6.42) induces the simple separation for the full particle number operator

$$\hat{n}(\mathbf{r}) = \hat{n}_d(\mathbf{r}) + \hat{n}_r(\mathbf{r}). \quad (6.46)$$

The fluctuation operator $\delta\hat{n}_d(\mathbf{r})$ measures the density fluctuation in the correlated subspace and is obtained analogously to Eq. (6.45) by

$$\delta\hat{n}_d(\mathbf{r}) = \hat{n}_d(\mathbf{r}) - \langle\Psi_0|\hat{n}_d(\mathbf{r})|\Psi_0\rangle. \quad (6.47)$$

We are now ready to derive an explicit expression for the correlated Kubo response function (6.30).

6.1 Constrained Random Phase Approximation

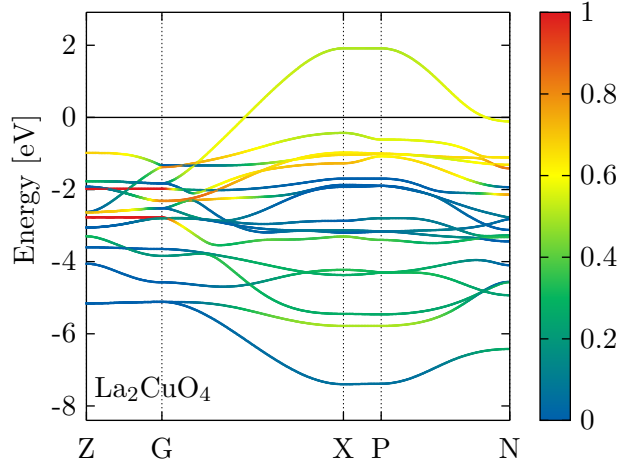


Figure 6.1: Composite band of La_2CuO_4 consisting of 17 Bloch bands. Red bands indicate strong copper d-character, blue bands indicate strong oxygen p-character. The plot was obtained using the Wannier90 library[142]

6.1.3 CRPA in the Kubo formalism

We consider a system with a *composite Bloch band* around the Fermi level. Such a band is defined as a collection of bands, which do not cross other bands, see Ref. 138. However, it is assumed that the Bloch states in the composite band have \mathbf{k} -dependent atomic orbital character. A prototype of such a composite band is the set of 17 Bloch bands in La_2CuO_4 shown in Fig. 6.1. The reason why we restrict our consideration to these systems is, that a composite band guarantees the existence of exponentially decaying Wannier functions, *i.e.* the existence of a bijective map between Bloch and Wannier states (4.90).[138] This is crucial, since we will switch from Wannier to Bloch space in the following whenever convenient. For instance, we seek a reciprocal expression for the correlated polarizability χ^d , similar to Eq. (6.27) or Eq. (6.24). On the other side the correlated subspace \mathbb{D} (d-/f-states) is in general a subspace of the composite band, so that the separation of correlated from non-correlated states is defined in the Wannier space.

We start our derivation by inserting a complete eigenset of the non-interacting many-body system

$$\mathbf{1} = \sum_{s=0}^{\infty} |\Psi_s\rangle \langle \Psi_s| \quad (6.48)$$

into Eq. (6.30) and using Eq. (6.47). Due to the definition of the fluctuation operator

6. MERGING GW WITH DMFT

(6.47) the $s = 0$ contributions drops out and we obtain

$$\begin{aligned} \chi^d(\mathbf{r}, \mathbf{r}', \tau) &= \Theta(+\tau) \sum_{s=1}^{\infty} e^{(E_0 - E_s)\tau} \langle \Psi_0 | \hat{n}_d(\mathbf{r}) | \Psi_s \rangle \langle \Psi_s | \hat{n}_d(\mathbf{r}') | \Psi_0 \rangle \\ &+ \Theta(-\tau) \sum_{s=1}^{\infty} e^{(E_s - E_0)\tau} \langle \Psi_0 | \hat{n}_d(\mathbf{r}') | \Psi_s \rangle \langle \Psi_s | \hat{n}_d(\mathbf{r}) | \Psi_0 \rangle. \end{aligned} \quad (6.49)$$

Here we used the Heisenberg relation $\hat{n}_d(\mathbf{r}, \tau) = e^{\hat{H}_0\tau} \hat{n}_d(\mathbf{r}) e^{-\hat{H}_0\tau}$ and the fact that $|\Psi_s\rangle$ is an eigenvector of the non-interacting Hamiltonian \hat{H}_0 of the complete Fock space \mathbb{F} , defined in Eq. (2.2), with corresponding eigenenergy E_s .

From Eq. (6.49) the desired expression can be obtained in two steps. Both steps are explained in detail in the following.

Step One: Matrix elements in Wannier Representation

Here the matrix elements $\langle \Psi_0 | \hat{n}_d(\mathbf{r}) | \Psi_s \rangle$ of Eq. (6.49) are evaluated. This is achieved by using expression (6.45) for the correlated fluctuation operator in combination with the inverse representation of Eq. (6.39) and yields

$$\langle \Psi_0 | \hat{n}_d(\mathbf{r}) | \Psi_s \rangle = \sum_{\alpha\beta \in \mathbb{D}} w_{\alpha}^*(\mathbf{r}) w_{\beta}(\mathbf{r}) \int d\mathbf{r}_1 d\mathbf{r}_2 w_{\alpha}(\mathbf{r}_1) w_{\beta}^*(\mathbf{r}_2) \langle \Psi_0 | \hat{\psi}^{\dagger}(\mathbf{r}_1) \hat{\psi}(\mathbf{r}_2) | \Psi_s \rangle \quad (6.50)$$

Now we focus on the evaluation of the expectation value on the r.h.s. For a Slater determinant $|\Psi_s\rangle$ the action of the field operator $\psi(\mathbf{r}_2)$ onto the N electron state $\Psi_s(\mathbf{r}'_1, \dots, \mathbf{r}'_N)$ is given by Eq. (2.25), together with the adjoint relation we obtain:

$$\begin{aligned} \langle \Psi_0 | \hat{\psi}^{\dagger}(\mathbf{r}_1) \hat{\psi}(\mathbf{r}_2) | \Psi_s \rangle &= N \int d\mathbf{r}'_2 \dots d\mathbf{r}'_N \Psi_0^*(\mathbf{r}_1, \mathbf{r}'_2, \dots, \mathbf{r}'_N) \Psi_s(\mathbf{r}_2, \mathbf{r}'_2, \dots, \mathbf{r}'_N) \\ &= N \left[\tau_{(0)}^* \right]^{\alpha_1 \alpha_2 \dots \alpha_N} \left[\tau_{(s)} \right]^{\beta_1}_{\alpha_2 \dots \alpha_N} w_{\alpha_1}^*(\mathbf{r}_1) w_{\beta_1}(\mathbf{r}_2) \end{aligned} \quad (6.51)$$

The contraction of the τ tensors in the last line can be evaluated using the identity[47]

$$\left[\varepsilon_{(0)} \right]^{\mathbf{n}_1 \mathbf{n}_2 \dots \mathbf{n}_N} \left[\varepsilon_{(s)} \right]^{\mathbf{m}_1}_{\mathbf{n}_2 \dots \mathbf{n}_N} = \frac{(N-1)!}{N!} \delta_{\mathbf{i}(s)}^{\mathbf{n}_1} \delta_{\mathbf{a}(s)}^{\mathbf{m}_1}, \quad (6.52)$$

where $\mathbf{i}(s)$ is the occupied state (contained in I_0) and is replaced by the unoccupied state $\mathbf{a}(s)$ in the index set I_s , and with Eq. (6.34) obtaining

$$\left[\tau_{(0)}^* \right]^{\alpha_1 \alpha_2 \dots \alpha_N} \left[\tau_{(s)} \right]^{\beta_1}_{\alpha_2 \dots \alpha_N} = \frac{(N-1)!}{N!} T^{*\alpha_1}_{\mathbf{i}(s)} T^{\beta_1}_{\mathbf{a}(s)}. \quad (6.53)$$

6.1 Constrained Random Phase Approximation

Therefore, only singly excited Slater determinants $|\Psi_s\rangle$ contribute to the matrix element (6.50), which may be written as

$$\langle \Psi_0 | \hat{n}_d(\mathbf{r}) | \Psi_s \rangle = \sum_{\alpha\beta \in \mathbb{D}} w_\alpha^*(\mathbf{r}) w_\beta(\mathbf{r}) T^{*\alpha_1}_{i(s)} T^{\beta_1}_{a(s)} \underbrace{\langle w_{\alpha_1} | w_\alpha \rangle}_{\delta_{\alpha_1}^\alpha} \underbrace{\langle w_\beta | w_{\beta_1} \rangle}_{\delta_{\beta_1}^\beta} \quad (6.54)$$

and results in

$$\langle \Psi_0 | \hat{n}_d(\mathbf{r}) | \Psi_s \rangle = \sum_{\alpha\beta \in \mathbb{D}} T^{*\alpha}_{i(s)} w_\alpha^*(\mathbf{r}) w_\beta(\mathbf{r}) T^\beta_{a(s)}. \quad (6.55)$$

Consequently, the Kubo formula (6.49) yields after a Fourier transformation to frequency domain

$$\chi^d(\mathbf{r}, \mathbf{r}', i\nu) = \sum_{\alpha\beta\gamma\delta \in \mathbb{D}} \sum_{s=1}^{\infty} [\Xi_{(s)}(i\nu)]^{\alpha\beta\gamma\delta} w_\alpha^*(\mathbf{r}) w_\beta(\mathbf{r}) w_\gamma^*(\mathbf{r}') w_\delta(\mathbf{r}') \quad (6.56)$$

with the tensor

$$[\Xi_{(s)}(i\nu)]^{\alpha\beta\gamma\delta} = \frac{T^{*\alpha}_{i(s)} T^\beta_{a(s)} T^{*\gamma}_{a(s)} T^\delta_{i(s)}}{E_s - E_0 + i\nu} + \frac{T^{*\alpha}_{a(s)} T^\beta_{i(s)} T^{*\gamma}_{i(s)} T^\delta_{a(s)}}{E_s - E_0 - i\nu} \quad (6.57)$$

The sum over singly excited Slater determinants \sum_s can be rewritten into a double sum of Bloch indices $\mathbf{i} = (n, \mathbf{k})$, $\mathbf{a} = (n', \mathbf{k}')$ using occupancy functions $f_i = f(\epsilon_i)$ as follows

$$\begin{aligned} \sum_{s=1}^{\infty} [\Xi_{(s)}(i\nu)]^{\alpha\beta\gamma\delta} &= \frac{1}{N_{\mathbf{k}}^2} \sum_{nn'\mathbf{k}\mathbf{k}'} f_i (1 - f_a) \\ &\times \left(\frac{T^{*\alpha}_i T^\beta_a T^{*\gamma}_a T^\delta_i}{\epsilon_a - \epsilon_i + i\nu} + \frac{T^{*\alpha}_a T^\beta_i T^{*\gamma}_i T^\delta_a}{\epsilon_a - \epsilon_i - i\nu} \right) \\ &= \frac{1}{N_{\mathbf{k}}^2} \sum_{nn'\mathbf{k}\mathbf{k}'} \frac{f_i (1 - f_a) - f_a (1 - f_i)}{\epsilon_a - \epsilon_i + i\nu} T^{*\alpha}_i T^\beta_a T^{*\gamma}_a T^\delta_i \end{aligned} \quad (6.58)$$

In the second term on the r.h.s. the indices $(\mathbf{i}, \mathbf{a}) \leftrightarrow (\mathbf{a}, \mathbf{i})$ have been swapped. Consequently, Eq. (6.56) can be rewritten into

$$\chi^d(\mathbf{r}, \mathbf{r}', i\nu) = \sum_{\alpha\beta\gamma\delta \in \mathbb{D}} \frac{1}{N_{\mathbf{k}}^2} \sum_{nn'\mathbf{k}\mathbf{k}'} \frac{f_i - f_a}{\epsilon_a - \epsilon_i + i\nu} T^{*\alpha}_i T^\beta_a T^{*\gamma}_a T^\delta_i w_\alpha^*(\mathbf{r}) w_\beta(\mathbf{r}) w_\gamma^*(\mathbf{r}') w_\delta(\mathbf{r}'). \quad (6.59)$$

Before continuing with step two, we make two short remarks: Firstly, Eq. (6.59) is the Wannier representation for the independent particle polarizability (derived by Hanke

6. MERGING *GW* WITH DMFT

and Sham in Refs. 148 and 149), but restricted to the target space \mathbb{D} . Secondly, Eq. (6.59) can be rewritten into¹

$$\chi^d(\mathbf{r}, \mathbf{r}', i\nu) = \sum_{\alpha\beta\gamma\delta \in \mathbb{D}} \frac{1}{N_{\mathbf{k}}^2} \sum_{nn'\mathbf{k}\mathbf{k}'} y(\nu, \xi_{\mathbf{a}\mathbf{i}}) T_{\mathbf{i}}^{*\alpha} T_{\mathbf{a}}^{\beta} T_{\mathbf{a}}^{*\gamma} T_{\mathbf{i}}^{\delta} w_{\alpha}^*(\mathbf{r}) w_{\beta}(\mathbf{r}) w_{\gamma}^*(\mathbf{r}') w_{\delta}(\mathbf{r}'), \quad (6.60)$$

where \mathbf{i} and \mathbf{a} are strictly restricted to occupied and unoccupied Bloch indices respectively. Looking at the Bloch representation (6.24), reveals that χ^d is a contracted four-point propagator and needs to be transformed to the Bloch domain as a four-point rather than a two-point tensor. This is done in the next step, where we show that Eq. (6.60) picks up four additional Wannier transformation matrices $T_{\mathbf{n}\alpha}$ proving that the weighted expression (6.27) of the target polarizability (containing the diagonal of only four T -matrices) does not follow from the Kubo formula (6.30).

Step Two: Fourier Transformation

In the second step, the Fourier transformation is performed to reciprocal space. The general prescription for this procedure is described in Ref. 108 and given by:

$$\chi_{\mathbf{q}}^d(\mathbf{g}, \mathbf{g}', i\nu) = \int d\mathbf{r} \int d\mathbf{r}' e^{i(\mathbf{g}+\mathbf{q})\mathbf{r}} \chi^d(\mathbf{r}, \mathbf{r}', i\nu) e^{-i(\mathbf{g}'+\mathbf{q})\mathbf{r}'}. \quad (6.61)$$

Decomposing the Wannier functions into Bloch functions and using $\mathbf{n}_1 = (n_1, \mathbf{k}_1)$ as in Eq. (6.37) we obtain

$$\begin{aligned} \chi_{\mathbf{q}}^d(\mathbf{g}, \mathbf{g}', i\nu) &= \frac{1}{N_{\mathbf{k}}^2} \sum_{nn'\mathbf{k}\mathbf{k}'} \frac{1}{N_{\mathbf{k}}^4} \sum_{\mathbf{n}_1 \mathbf{n}_2 \mathbf{n}_3 \mathbf{n}_4} \sum_{\alpha\beta\gamma\delta \in \mathbb{D}} y(\nu, \xi_{\mathbf{a}\mathbf{i}}) \\ & T_{\alpha n}^{*(\mathbf{k})} T_{\alpha n_1}^{(\mathbf{k}_1)} \langle \phi_{\mathbf{n}_1} | e^{i(\mathbf{g}+\mathbf{q})\mathbf{r}} | \phi_{\mathbf{n}_2} \rangle T_{\beta n_2}^{*(\mathbf{k}_2)} T_{\beta m}^{(\mathbf{k}')} \\ & T_{\gamma m}^{*(\mathbf{k}')} T_{\gamma n_3}^{(\mathbf{k}_3)} \langle \phi_{\mathbf{n}_3} | e^{-i(\mathbf{g}'+\mathbf{q})\mathbf{r}'} | \phi_{\mathbf{n}_4} \rangle T_{\delta n_4}^{*(\mathbf{k}_4)} T_{\delta n}^{(\mathbf{k})} \\ & \sum_{\mathbf{R}_{\alpha}} e^{i\mathbf{R}_{\alpha}(\mathbf{k}_1-\mathbf{k})} \sum_{\mathbf{R}_{\beta}} e^{-i\mathbf{R}_{\beta}(\mathbf{k}_2-\mathbf{k}')} \sum_{\mathbf{R}_{\gamma}} e^{i\mathbf{R}_{\gamma}(\mathbf{k}_3-\mathbf{k}')} \sum_{\mathbf{R}_{\delta}} e^{-i\mathbf{R}_{\delta}(\mathbf{k}_4-\mathbf{k})} \end{aligned} \quad (6.62)$$

¹ To see this, first one decomposes the factor $(\xi_{\mathbf{a}\mathbf{i}} + i\nu)^{-1}$ into a symmetric and antisymmetric tensor in \mathbf{a}, \mathbf{i} . That is

$$\frac{1}{\xi_{\mathbf{a}\mathbf{i}} + i\nu} = \underbrace{\frac{\xi_{\mathbf{a}\mathbf{i}}}{\xi_{\mathbf{a}\mathbf{i}}^2 + \nu^2}}_{\frac{1}{2}y(\nu, \xi_{\mathbf{a}\mathbf{i}})} - i \frac{\nu}{\xi_{\mathbf{a}\mathbf{i}}^2 + \nu^2}.$$

In the next step, one uses the fact that both, the factor $(f_{\mathbf{i}} - f_{\mathbf{a}})$ as well as the first term on the r.h.s. are odd tensors in \mathbf{i}, \mathbf{a} and therefore are non-zero, whereas the second term is an even tensor in \mathbf{i}, \mathbf{a} and vanishes.

6.1 Constrained Random Phase Approximation

The sum over lattice vectors \mathbf{R} can be carried out using the simple identity[108]

$$\sum_{\mathbf{R}} e^{i\mathbf{k}\mathbf{R}} = \sum_{\mathbf{g}} \delta_{\mathbf{k}\mathbf{g}}. \quad (6.63)$$

and restricts the k-vectors

$$\mathbf{k}_1 = \mathbf{k} + \mathbf{g}_1, \quad \mathbf{k}_2 = \mathbf{k}' + \mathbf{g}_2, \quad \mathbf{k}_3 = \mathbf{k}' + \mathbf{g}_3, \quad \mathbf{k}_4 = \mathbf{k} + \mathbf{g}_4, \quad (6.64)$$

where $\mathbf{g}_1 \cdots \mathbf{g}_4$ are reciprocal lattice vectors. Furthermore, the periodicity condition[139]

$$T_{n\alpha}^{(\mathbf{k})} = T_{n\alpha}^{(\mathbf{k}+\mathbf{g})} \quad (6.65)$$

allows to carry out the sum over lattice sites $\alpha \cdots \delta$ resulting in four projectors defined in Eq. (6.31). Hence, the sum over reciprocal lattice vectors $\mathbf{g}_1, \cdots, \mathbf{g}_4$ yields four times the same contribution, namely

$$\chi_{\mathbf{q}}^d(\mathbf{g}, \mathbf{g}', i\nu) = \frac{1}{N_{\mathbf{k}}^2} \sum_{nn'\mathbf{k}\mathbf{k}'} y(\nu, \xi_{a\mathbf{i}}) \langle \bar{\phi}_{\mathbf{i}} | e^{i(\mathbf{g}+\mathbf{q})\mathbf{r}} | \bar{\phi}_{\mathbf{a}} \rangle \langle \bar{\phi}_{\mathbf{a}} | e^{-i(\mathbf{g}'+\mathbf{q})\mathbf{r}'} | \bar{\phi}_{\mathbf{i}} \rangle, \quad (6.66)$$

where the definition of the correlated Bloch functions (6.32) have been used with the short hands $\mathbf{i} = (n, \mathbf{k})$ and $\mathbf{a} = (n', \mathbf{k}')$. Pointing out, that the matrix elements on the r.h.s. of Eq. (6.66) are invariant under the transformations $\mathbf{r} \rightarrow \mathbf{r} + \mathbf{R}$ and $\mathbf{r}' \rightarrow \mathbf{r}' - \mathbf{R}$ reveals the restriction on the primed k-point

$$\mathbf{k}' = \mathbf{k} + \mathbf{q}. \quad (6.67)$$

This removes an additional factor $N_{\mathbf{k}}^{-1}$ and we obtain the main result of this section

$$\chi_{\mathbf{q}}^d(\mathbf{g}, \mathbf{g}', i\nu) = \frac{1}{N_{\mathbf{k}}} \sum_{nn'\mathbf{k}} y(\nu, \xi_{a\mathbf{i}}) \langle \bar{\phi}_{\mathbf{i}} | e^{i(\mathbf{g}+\mathbf{q})\mathbf{r}} | \bar{\phi}_{\mathbf{a}} \rangle \langle \bar{\phi}_{\mathbf{a}} | e^{-i(\mathbf{g}'+\mathbf{q})\mathbf{r}'} | \bar{\phi}_{\mathbf{i}} \rangle, \quad (6.68)$$

with $\mathbf{i} = (n, \mathbf{k})$ representing the occupied and $\mathbf{a} = (n', \mathbf{k} + \mathbf{q})$ the unoccupied indices.

If the composite band consists only of target states, *i.e.* the target space \mathbb{D} forms an isolated set of Bloch bands, the projectors (6.31) become diagonal and expression (6.68) reduces to the constrained Adler and Wisner form (6.24). The weighted expression of Şaşıoğlu *et al.* (respectively and Shih and coworkers) Eq. (6.27) follows only from the replacement

$$|\bar{\phi}_{n\mathbf{k}}\rangle \rightarrow \sqrt{P_{nn}^{(\mathbf{k})}} |\phi_{n\mathbf{k}}\rangle \quad (6.69)$$

in Eq. (6.68), which seems, to be an unjustifiable ad-hoc step.

6. MERGING *GW* WITH DMFT

6.1.3.1 Technical details

In this section we discuss technical details of our CRPA implementation. The derivation of Eq. (6.68) holds strictly for an isolated set of Bloch bands (composite Bloch band) that can be represented by the localized Wannier functions

$$|w_{\alpha\mathbf{k}}\rangle = \sum_n T_{\alpha n}^{(\mathbf{k})} |\phi_{n\mathbf{k}}\rangle. \quad (6.70)$$

For systems, where such a set of bands is absent (for instance the 3d transition metals series Sc-Ni), expression (6.68) is not uniquely defined. From the practical point of view, this is due to the ill-conditioned "inverse projection" of Eq. (4.90). However, we found that one can use the regularized projectors

$$\bar{P}_{nm}^{(\mathbf{k})} = \Theta_m^{(\mathbf{k})} P_{nm}^{(\mathbf{k})} \quad (6.71)$$

instead. Here the window function $\Theta_m^{(\mathbf{k})}$ is either 0 (for a null-vector) or 1 (for a rank-vector) and is obtained from the Jacobi diagonalization of the original projector $P_{nm}^{(\mathbf{k})}$. [92, 150]

To illustrate this regularization procedure, we consider the case where Bloch bands are projected onto Wannier states via the projector

$$T_{n\alpha}^{(\mathbf{k})} = \begin{pmatrix} \square & \square & \square & \square & \square & \square & \square \\ \blacksquare & \blacksquare & \blacksquare & \square & \square & \square & \square \\ \blacksquare & \blacksquare & \blacksquare & \square & \square & \square & \square \\ \blacksquare & \blacksquare & \blacksquare & \square & \square & \square & \square \\ \blacksquare & \blacksquare & \blacksquare & \square & \square & \square & \square \\ \square & \square & \square & \square & \square & \square & \square \\ \square & \square & \square & \square & \square & \square & \square \end{pmatrix},$$

with \blacksquare and \square indicating a non-zero and zero entry respectively. In this specific example the Bloch bands ϕ_2, \dots, ϕ_5 are projected onto the Wannier states w_1, w_2 and w_3 . The corresponding correlated projector $P_{nm}^{(\mathbf{k})}$ assumes the form

$$P_{nm}^{(\mathbf{k})} = \begin{pmatrix} \square & \square & \square & \square & \square & \square & \square \\ \square & \blacksquare & \blacksquare & \blacksquare & \blacksquare & \square & \square \\ \square & \blacksquare & \blacksquare & \blacksquare & \blacksquare & \square & \square \\ \square & \blacksquare & \blacksquare & \blacksquare & \blacksquare & \square & \square \\ \square & \blacksquare & \blacksquare & \blacksquare & \blacksquare & \square & \square \\ \square & \square & \square & \square & \square & \square & \square \\ \square & \square & \square & \square & \square & \square & \square \end{pmatrix}$$

6.1 Constrained Random Phase Approximation

and the resulting $(N - N_{\mathbb{D}}) \times (N - N_{\mathbb{D}})$ non-zero sub-block (here $N - N_{\mathbb{D}} = 4$) has rank $N_{\mathbb{D}}$. For instance, if the Jacobi diagonalization of $P_{nm}^{(\mathbf{k})}$ yields $diag(1, 1, 0, 1)$ for this sub-block, the regularized projector $\bar{P}_{nm}^{(\mathbf{k})}$ is

$$\bar{P}_{nm}^{(\mathbf{k})} = \Theta_m^{(\mathbf{k})} P_{nm}^{(\mathbf{k})} = \begin{pmatrix} \square & \square & \square & \square & \square & \square & \square \\ \square & \blacksquare & \blacksquare & \square & \blacksquare & \square & \square \\ \square & \blacksquare & \blacksquare & \square & \blacksquare & \square & \square \\ \square & \blacksquare & \blacksquare & \square & \blacksquare & \square & \square \\ \square & \blacksquare & \blacksquare & \square & \blacksquare & \square & \square \\ \square & \square & \square & \square & \square & \square & \square \\ \square & \square & \square & \square & \square & \square & \square \end{pmatrix}$$

and has ultimately the same number of rows and columns as $T_{nm}^{(\mathbf{k})}$.

Once the correlated polarizability (6.68) is determined, we subtract it from the full polarizability (3.41), yielding the effective polarizability χ^r . In the next step the screening equation (6.21) is solved for the effective kernel $\mathcal{U}_{\mathbf{g}\mathbf{g}'}(\mathbf{q}, i\nu)$ for every \mathbf{k} -point \mathbf{q} in the irreducible wedge of the Brillouin zone. In the final step the interaction matrix is evaluated via

$$U_{\alpha\beta\gamma\delta} = \frac{1}{N_{\mathbf{k}}^2} \sum_{\mathbf{q}\mathbf{k}} \sum_{\mathbf{g}\mathbf{g}'} \mathcal{U}_{\mathbf{g}\mathbf{g}'}(\mathbf{q}, 0) \langle w_{\alpha\mathbf{k}} | e^{i(\mathbf{q}+\mathbf{g})\mathbf{r}} | w_{\delta\mathbf{k}+\mathbf{q}} \rangle \langle w_{\beta\mathbf{k}+\mathbf{q}} | e^{-i(\mathbf{q}+\mathbf{g}')\mathbf{r}'} | w_{\gamma\mathbf{k}} \rangle, \quad (6.72)$$

with the mixed basis representations (6.70).

We emphasize that our approach, *i.e.* the correlated polarizability (6.68) and effectively the matrix elements (6.72), differ from the disentanglement method of Miyake and coworkers, since in contrast to Ref. 145 we do not change the original band structure.

6.1.4 Computational details

We have considered the high temperature superconductor La_2CuO_4 and the 3d transition metal series Sc up to Ni. The lattice constants for the latter are obtained by minimizing the PBE density functional[106] and are summarized in Tab. 6.1. For the cuprate the lattice constant $a = 3.86 \text{ \AA}$ and a ratio of $c/a = 3.41$ for the bct unit cell was used with the positions given in Tab. 6.2. Convergence of the effective interaction matrix (6.72) w.r.t. the plane wave basis set is reached using the same method as described in Ref. 151. First, the effective matrix elements (6.72) are determined using a rather low energy cutoff $\underline{E}_{\text{cut}}$ for the CRPA polarizability χ^r on a plane wave grid. This result is corrected by the difference of the bare Coulomb interaction $V_{\alpha\beta\gamma\delta}$ obtained with the

6. MERGING *GW* WITH DMFT

Table 6.1: Used structures for the transition metal (TM) series. Lattice constants are given in Å and obtained from PBE.

Sc	Ti	V	Cr	Mn	Fe	Co	Ni
fcc	fcc	bcc	bcc	bcc	bcc	fcc	fcc
4.64	4.13	2.99	2.85	2.78	2.77	3.47	3.52

Table 6.2: Atomic positions in La_2CuO_4 in direct coordinates

Atom	Position		
	x	y	z
La	0.64	0.64	0.00
La	0.36	0.36	0.00
Cu	0.00	0.00	0.00
O	0.00	0.50	0.50
O	0.50	0.00	0.50
O	0.19	0.19	0.00
O	0.81	0.81	0.00

6.1 Constrained Random Phase Approximation

same cutoff on the same grid and $V_{\alpha\beta\gamma\delta}$ obtained using the exact all-electron method described in Ref. 96 with a higher cutoff \bar{E}_{cut} . This is justified, since the high energy contributions to the polarizability χ^r vanish and the screening becomes ineffective for large \mathbf{g} vectors.[151]

In all calculations we included 128 bands and plane wave contributions up to a cutoff of $\underline{E}_{\text{cut}} = 400$ eV in the calculation of the CRPA polarizability. For the high cutoff \bar{E}_{cut} 700 eV and for the PAW basis set a cutoff of 500 eV was chosen. In order to obtain a well-converged groundstate, a dense k-point grid of $16 \times 16 \times 16$ points was used in combination with the tetrahedron method of Blöchl *et al.*[152] with a smearing factor of $\sigma = 0.2$ eV⁻¹.

6.1.5 Wannier basis

The quality of the Wannier basis is a crucial point for all CRPA methods. Therefore, we discuss here in detail, how the localized basis is obtained.

We start with the superconductor La₂CuO₄, which possesses an isolated composite band of 17 Bloch bands. These states correspond to the 12 p-states centered at the four oxygen atoms and the five d-states centered at the copper atom in the unit cell. We, therefore, transform these bands to 17 Wannier states and call this the *dp* basis in the following. The quality of the Wannier transformation is investigated by diagonalizing the corresponding Wannier Hamiltonian and comparing with the original PBE band structure. The comparison is given in Fig. 6.1 and shows that the match is perfect already at a rather coarse k-point mesh of $8 \times 8 \times 8$ points. We have used this k-point setting for both, the Wannier transformation as well as the CRPA calculations.

In contrast to the cuprate, the 3d transition metals do not possess an isolated set of bands. However, a one to one correspondence between six Wannier states and six bands around the Fermi level, five narrow bands (mainly of d-character) and a crossing s-like band, can be achieved. Thereby the location of the s-state was chosen at the reciprocal coordinates (0.25, 0.25, 0.25) for the fcc and at (0.5, 0.5, 0.5) for the bcc unit cells, whereas the d-states are centered at the TM. We call this basis set the *ds* basis in the following and show in Fig. 6.2 (a) a comparison between the original PBE bands of Ni and the eigenvalues of the Hamiltonian in the *ds* basis. One clearly sees that the *ds* basis reproduces most symmetry lines accurately, but has difficulties to represent the symmetry points *W* and *K* of the s-state. This is due to the fact, that these

6. MERGING GW WITH DMFT

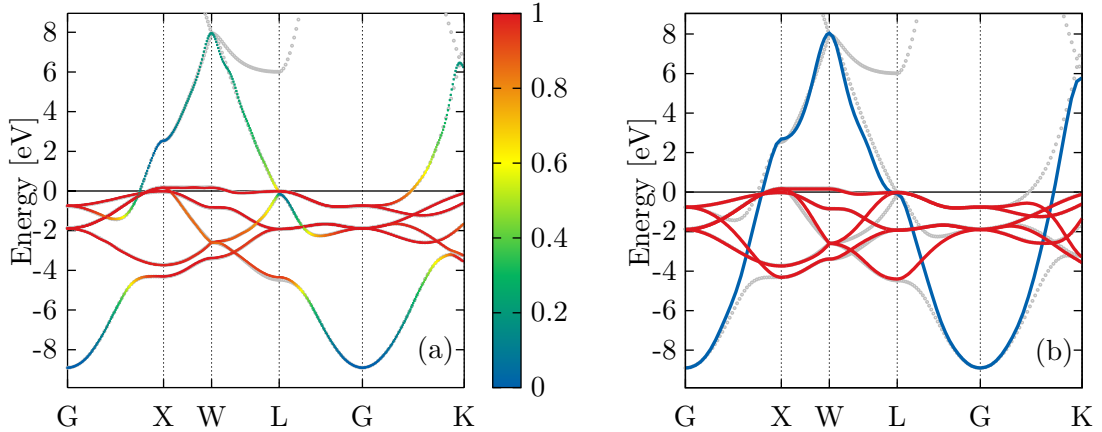


Figure 6.2: Bands of fcc Ni with d-character resolution obtained from Wannier90. Red bands indicate strong d-character, blue bands indicate strong s-character. (a) d-character resolution in ds basis. (b) Comparison of disentangled system (red and blue bands) with original system (gray bands) in d basis.

Table 6.3: Used energy windows in [eV] for the construction of the d basis in the 3d series. The Fermi level is set to 0 eV.

	Sc	Ti	V	Cr	Mn	Fe	Co	Ni
E_{min}	-3.0	-4.0	-4.5	-4.5	-6.0	-6.0	-6.5	-7.5
E_{max}	+5.0	+5.0	+5.5	+5.5	+5.0	+5.0	+4.0	+3.5

points are crossing points with higher energy states and since the Wannier basis is lacking this information, the eigenvalues of the Wannier Hamiltonian start to oscillate. Consequently, the representability of the ds basis is never perfect, as it is in the case of the aforementioned dp basis for La_2CuO_4 . To compensate this defect, we have decided to use a very dense $16 \times 16 \times 16$ k-point grid for the Wannier projection.

In addition to the ds basis, we considered a third basis set. The d basis contains only five d-states and is obtained as a projection of the same six Bloch bands using the energy windows given in Tab. 6.3 for the method of Souza.[143] For Ni we show in Fig. 6.2 (b) the eigenvalues of the Hamiltonian in this basis (red bands). The same figure shows, in addition, the original PBE bands and the disentangled s-band (blue band), which was obtained by applying the method of Miyake *et al.*[147]

Last but not least, we have compared the spatial spread of the two basis sets, given in Fig.6.3. It can be seen that the inclusion of the s-state tends to yield more localized

6.1 Constrained Random Phase Approximation

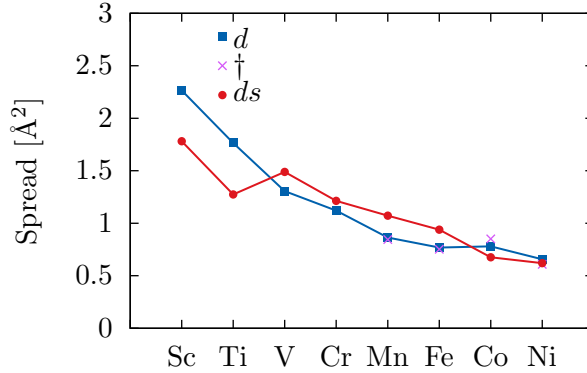


Figure 6.3: Average spread of Wannier d-functions of the TM series in the d (squares) and ds (points) basis. For comparison data of Ref. 153 (†) is given for the d basis.

(delocalized) Wannier functions in the fcc (bcc) unit cells. The general decreasing spread towards the right in the series is evident and expected.

6.1.6 Transition metals

In the following subsection, we discuss our results for the bare \bar{V} , fully screened \bar{W} and effective interaction averages U , defined in Eqs. (6.17), (6.18) and (6.14) for the transition metal series Sc-Ni. For the CRPA calculations we have considered three distinct models, summarized in Tab. 6.4. Model (i) corresponds to the disentanglement method of Ref. 147, model (ii) is the the weighting method in the ds basis of Refs. 145 and 146, whereas model (iii) is the CRPA approach derived in section 6.1.3.

Table 6.4: Used models.

model	basis	applied to	χ^d
(i)	d	TMs	Eq.(6.24)
(ii)	ds/dp	TMs/La ₂ CuO ₄	Eq.(6.27)
(iii)	ds/dp	TMs/La ₂ CuO ₄	Eq.(6.68)

6.1.6.1 Bare Coulomb interaction

As a starting point of our investigation we have evaluated the bare Hubbard-Kanamori interaction \bar{V} for both basis sets d and ds . For the latter we have averaged only over the d-states of the TMs. The results in the d basis are shown in Fig. 6.4 (a) (red points)

6. MERGING GW WITH DMFT

together with published values. We see good agreement with Shih *et al.*¹ and for the early transition metals Sc, Ti, and V with an increasing discrepancy for the later TMs, reaching the largest difference of 2.76 eV for Ni. This can be related to the second energy window used in Ref. 154 yielding ultimately a different basis than in the present work. If the same Wannier settings are chosen (compare to Ref. 153) one obtains almost identical interactions.

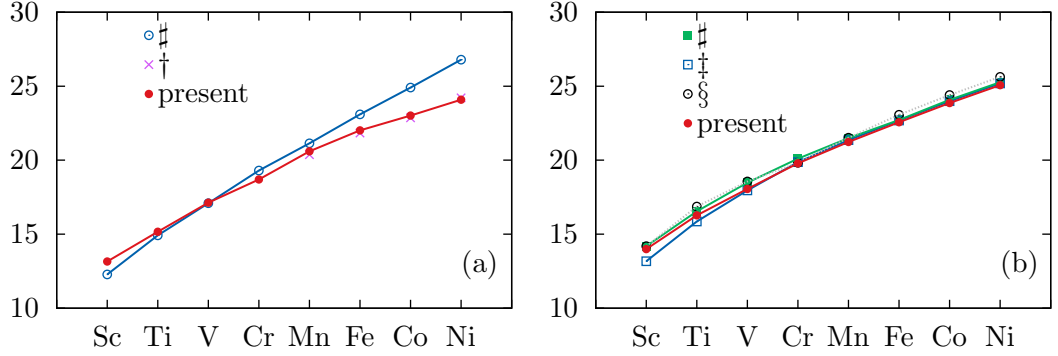


Figure 6.4: Bare Coulomb repulsion V in [eV] of 3d TMs series in d (a) and ds basis (b). For comparison Ref.[#]146, Ref.[†]153, Ref.[§]145 and Ref.[‡]155 are given

The inclusion of the s -state in the localized basis set (basis ds) tends to yield more localized d -states in the fcc unit cells. The consequence is that the bare interaction in the ds basis is larger than in the d basis, as can be seen in Fig. 6.4 (b), for Sc, Ti, Co and Ni. Despite the fact, that the spread of the d -states in the ds basis is slightly larger (see Fig. 6.3), the bare interaction is still slightly larger in the ds basis than in the minimal basis set. For instance the difference to the d basis for bcc Cr is around 1.7 eV. Hence, we conclude that the presence of the additional s -state compensates the larger spread in the ds basis. Compared to literature, we obtain excellent agreement with Şaşıoğlu *et al.*[145, 155] and Shih *et al.*[154].

6.1.6.2 Fully screened RPA interaction

Next, we investigated the fully screened interaction \bar{W} on the random phase approximation level in both basis sets d and ds . In contrast to the ds basis, the minimal d basis allows for two different calculations.[147] On the one side, the original PBE eigensystem [gray bands in Fig. 6.2 (b)] can be used for the determination of the RPA polarizability

¹See Ref. 146 and references therein.

6.1 Constrained Random Phase Approximation

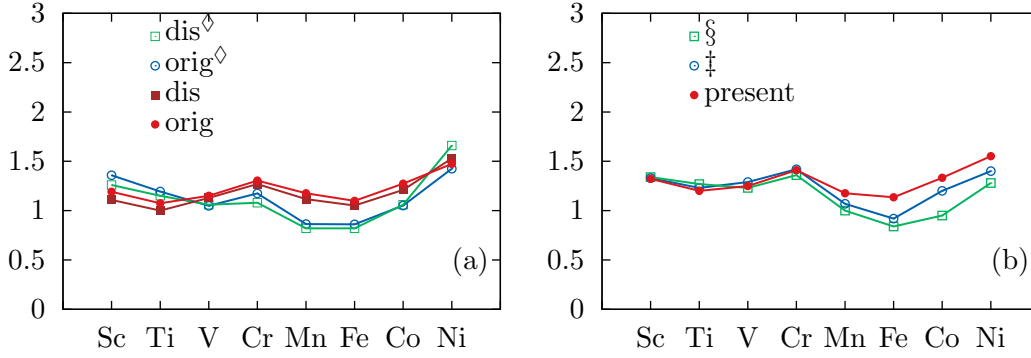


Figure 6.5: (a) On-site fully screened d-Coulomb repulsion measured in [eV] in d basis of disentangled (squares) and original Kohn-Sham system (circles). (b) Full RPA interaction of original system in ds basis. For comparison Ref.[◇] 147, Ref.[§] 145 and Ref.[‡] 155 are shown.

in Eq. (6.19). On the other side, the latter can be computed using the disentangled system [blue and red bands in 6.2 (b)]. In both cases the resulting interaction kernel $W_{\mathbf{GG}'}(\mathbf{q}, \omega)$ is evaluated in the d basis [red bands in Fig. 6.2 (b)].

The results for the TMs with the original Kohn-Sham system are given by the red points in Fig. 6.5 (a), whereas the filled squares show \bar{W} obtained from disentanglement. Comparing the latter with the red points in Fig. 6.5 (a) shows that the disentanglement effect can be safely disregarded. The same figure shows, in addition, previously published data of Ref. 147 (circles and empty squares). All in all, the agreement is good, except for Mn and Fe, where we obtain considerably larger interactions. Most probably, as discussed below, this can be related to the pseudo potentials, even though we used slightly different energy windows in our calculations (see previous section).

The fully screened interaction in the ds basis is shown in Fig. 6.5 (b) (filled circles). Comparing to the minimal d basis, the interactions are again slightly larger due to the stronger localization of the d-states [compare dots in Fig. 6.5 (a) and (b)]. The same figure shows in addition published data of Şaşıoğlu *et al.* in 2011 (empty squares) and 2013 (empty circles) respectively.[145, 155] Here we observe excellent agreement for early metals up to bcc Cr with small deviations starting at bcc Mn and increasing towards Ni. We mainly make the used pseudo potentials responsible for the discrepancies to the literature.

6. MERGING GW WITH DMFT

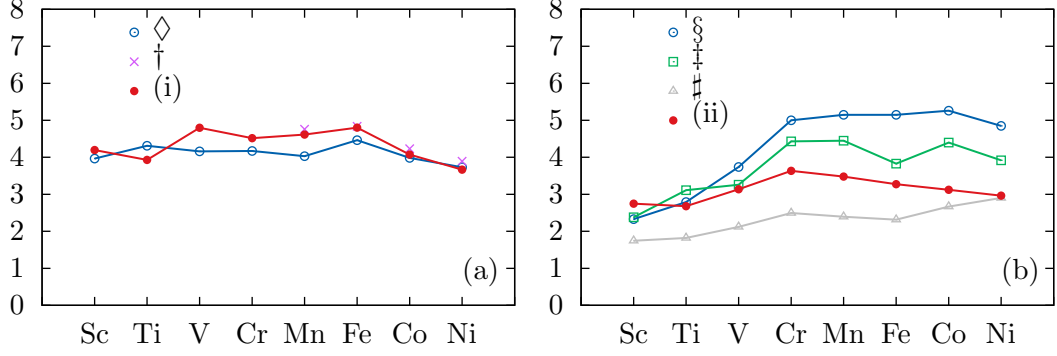


Figure 6.6: On-site effective d-Coulomb repulsion U in [eV] for different models. (a) model (i), disentanglement method in basis d . (b) model (ii), weighted CRPA method in ds basis. For comparison Ref.[◇] 147 Ref.[†]153, Ref.[‡]155 Ref.[§]145 and Ref.[#]146 are shown.

6.1.6.3 Effective Coulomb interaction

In this section we compare our CRPA approach with the conventionally applied models (i) and (ii), *i.e.* the disentanglement and weighted method Eq. (6.27), respectively.

We start with a comparison of our results of model (i) and (ii) with the literature. The results for the effectively screened interaction U obtained from the disentanglement method in the d basis is shown in Fig. 6.6 (a). Comparing Ref. 147 (circles) with our results (red points) shows good agreement for the complete TM series, whereas recent calculations, done by Sakuma and Aryasetiawan,[153] show almost a perfect match. It is gratifying that two distinct code packages can agree on the same interactions for the same method.

The results for the effective interaction of the weighted method, model (ii) are given in Fig. 6.6 (b) (red dots) and are in reasonable agreement with Ref. 155 for early TMs and with Ref. 154 for late TMs. All in all our results lie somewhere in between those of Şaşıoğlu *et al.*[145] and Shih *et al.*[146] However, the scatter in the literature is huge compared to model (i), especially for Cr, Mn and Fe. Even worse, our results tend to decrease as one moves from Cr to Ni, whereas the opposite behavior is obtained by Şaşıoğlu *et al.*[145, 155] and Shih *et al.*[146]

There may be various reasons for this, most probably, the used pseudo potentials should be made responsible for these discrepancies. In summary, we may say that the disentanglement method is numerically more robust than the weighting approach, as can be seen from Fig. 6.6 (a) and (b).

6.1 Constrained Random Phase Approximation

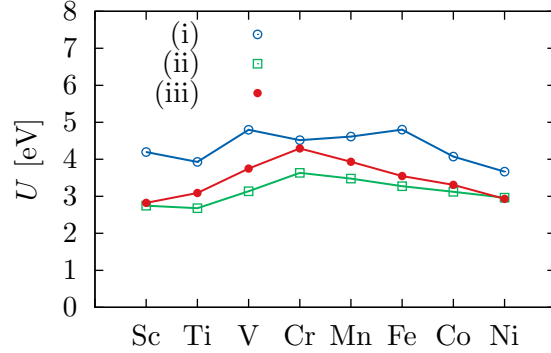


Figure 6.7: Comparison of present CRPA approach, model (iii) (red points), with disentangling (i) and weighted method (ii).

We complete this subsection with the discussion of results obtained with our approach, *i.e.* model (iii). A comparison with model (i) and (ii) is given in Fig. 6.7. First, we observe that the overall trend of model (ii) (squares) and (iii) (points) is similar and differs from model (i) (circles). This might be related to the disentanglement used in model (i). Second, comparing model (ii) with (iii) one sees that our approach yields in general larger interactions than (ii). This comes from the fact, that Eq. (6.68) removes more screening effects than the weighted formula (6.27), since also off-diagonal terms of the projectors (6.31) are taken into account in the correlated polarizability. The resulting effective polarizability is smaller, the corresponding screening is less effective and shifts the effective interaction U of model (iii) towards the values of model (i). However, the shift is not constant and varies from system to system. In general, we observe a smaller shift for the fcc than for the bcc structures.

Last but not least we have investigated the low frequency dependence of model (i)-(iii) for fcc Ni and bcc Cr. The frequency regime shown in Fig. 6.8 might be of interest for frequency dependent DMFT calculations. The solid red line represents model (iii), the dashed green curve model (ii) and the dashed blue curve stands for model (i). One observes a rather flat low frequency behavior for model (i) in Ni and Cr. However, model (ii) and (iii) show more structure. Whereas the difference between the weighted and our CRPA approach is negligible for fcc Ni, the difference in bcc Cr is clearly visible around 3 eV and approaches the analytically continued data of Şaşıoğlu *et al.* for higher frequencies. This implies that the conventionally chosen static approximation (6.12) of the CRPA might be problematic and needs to be further investigated.

6. MERGING *GW* WITH DMFT

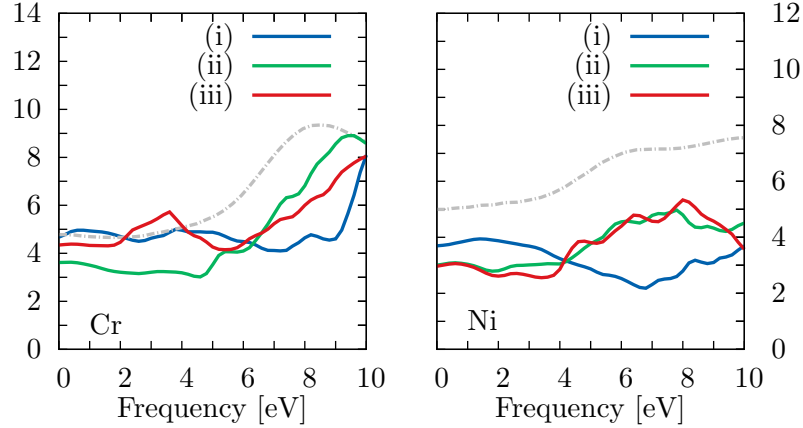


Figure 6.8: Frequency dependence of effectively screened interaction for fcc Ni and bcc Cr in model (i) (blue), model (ii) (green) and model (iii) (solid line). The gray line shows analytically continued data of model (ii) published in Ref. 155.

6.1.7 La_2CuO_4

La_2CuO_4 is the prototype of a high temperature superconductor and has been heavily studied in the condensed-matter community since the 1980s. In the following, we want to sketch only the most important aspects of this compound, which are necessary for the computation of the effective interaction in the one-band and five-band Hubbard model. The interested reader is referred to literature.[156, 157, 158, 159]

PBE yields the band structure given in Fig. 6.1. The single band crossing the Fermi surface makes this compound interesting for single-band DMFT studies. This band is often referred to as the $d_{x^2-y^2}$ state of Cu, however, Fig. 6.1 shows that it is strongly entangled with the surrounding oxygen p-states. Therefore the dp basis mentioned in section 6.1.5 is a good choice to study the interactions of this compound.

As for the TM series, we first determined the bare and fully screened interactions \bar{V} and \bar{W} . The complete interaction matrices $V_{\alpha\alpha\beta\beta}$, $V_{\alpha\beta\alpha\beta}$, $W_{\alpha\alpha\beta\beta}$ and $W_{\alpha\beta\alpha\beta}$ of the d-submanifold are given in the appendix E. It can be seen that the $d_{x^2-y^2}$ - $d_{x^2-y^2}$ matrix element has the largest value, 28.7 eV for the bare and 2.6 eV for the fully screened interaction.

Next we have considered the effective interaction of the one-band model. Here only the intra $d_{x^2-y^2}$ - $d_{x^2-y^2}$ screening effects are removed. Using the CRPA method developed in this paper we obtain an effective interaction of $U = 3.0$. This is only 0.1 eV larger

6.1 Constrained Random Phase Approximation

than in the weighting approach of model (ii) and both models are in reasonable agreement with the chosen U in recent one-band DMFT studies of this compound.[160, 161]

If, however, the complete d-manifold is considered as target space in the CRPA the difference between the weighting and our model becomes evident. For model (ii) we obtain an averaged interaction of $U = 3.7$, whereas model (iii) yields $U = 5.7$ eV. Recent multi-orbital LDA+DMFT calculations used interaction parameters between 4 and 10 eV.[162] The complete Hubbard matrices $U_{\alpha\alpha\beta\beta}$ and $U_{\alpha\beta\alpha\beta}$ of model (iii) are given in Tab. 6.5.

Table 6.5: Effective Hubbard interaction matrices $U_{\alpha\alpha\beta\beta}$ and $U_{\alpha\beta\alpha\beta}$ for La_2CuO_4 obtained with model (iii).

	d_{xy}	d_{xz}	d_{yz}	$d_{x^2-y^2}$	d_{z^2}	d_{xy}	d_{xz}	d_{yz}	$d_{x^2-y^2}$	d_{z^2}
d_{xy}	5.8	4.4	4.4	3.5	3.5	5.4	0.7	0.7	1.1	1.1
d_{zy}	4.4	5.7	3.9	3.7	3.7	0.7	5.3	0.9	1.0	0.9
d_{yz}	4.4	3.9	5.7	3.7	3.7	0.7	0.9	5.3	1.0	0.9
$d_{x^2-y^2}$	3.5	3.7	3.7	5.6	4.4	1.1	1.0	1.0	5.2	0.6
d_{z^2}	3.5	3.7	3.7	4.4	5.5	1.1	0.9	0.9	0.6	5.1

6. MERGING GW WITH DMFT

6.2 Unscreening Method for Isolated Target States

Large parts of the following section have been published in Ref. 151.

In this section we consider the special case, where the correlated subspace \mathbb{D} is restricted to the target states located the impurity cell $\mathbf{R} = 0$. This means that only local excitations are neglected in the RPA screening process. We shall see in moment that this approach is applicable only for isolated target bands, where a minimal Wannier basis can be found. The method relies on the general recipe given already in Eq. (6.2) and requires the knowledge of both, the on-site fully screened interaction $W_{\alpha\beta\gamma\delta}$ as well as the independent particle polarizability $\chi_{\alpha\beta\gamma\delta}^0$ in the Wannier basis at $\mathbf{R} = 0$. One can say that the effective matrix elements $U_{\alpha\beta\gamma\delta}$ are obtained from *unscreening* the fully screened interaction using the impurity polarization.

Eq. (6.2) can be rewritten into the common Dyson form

$$W^{\alpha\beta\gamma\delta} = U^{\alpha\beta\gamma\delta} + U^{\alpha\rho\tau\delta} \chi_{\rho\mu\nu\tau}^0 W^{\mu\beta\gamma\nu}. \quad (6.73)$$

In the previous sections we have determined the on-site fully screened interaction matrix $W_{\alpha\beta\gamma\delta}$. What remains, to solve the equation above for the matrix elements $U_{\alpha\beta\gamma\delta}$, is to determine the correlated polarizability tensor $\chi_{\alpha\beta\gamma\delta}^0$. Fortunately, this follows trivially from Hanke's expression, derived in (6.59), by renaming $\delta \rightarrow \gamma, \beta \rightarrow \delta, \gamma \rightarrow \beta$ and restricting the lattice vectors $\mathbf{R}_\alpha - \mathbf{R}_\delta$ to the impurity cell $\mathbf{R} = \mathbf{0}$. One then obtains

$$\chi_0^{\alpha\beta\gamma\delta}(i\nu) = \frac{1}{N_{\mathbf{k}}^2} \sum_{\mathbf{ia}} y(\nu, \xi_{\mathbf{a}\mathbf{i}}) T_{\mathbf{i}}^{*\alpha} T_{\mathbf{a}}^\beta T_{\mathbf{a}}^{*\gamma} T_{\mathbf{i}}^\delta, \quad (6.74)$$

with $\mathbf{i} = (n\mathbf{k})$ denoting the occupied and $\mathbf{a} = (n'\mathbf{k} + \mathbf{q})$ the unoccupied Bloch index.

We introduce the composite indices $\{(\alpha, \delta), (\beta, \gamma), (\rho, \tau), (\mu, \nu)\}$ to represent the corresponding matrix elements in Eq. (6.73) by conventional matrices $\mathbf{U}, \boldsymbol{\chi}^0, \mathbf{W}$. This allows us to rewrite the equation into the computationally convenient matrix form

$$\mathbf{U} = \mathbf{W} \cdot (\mathbf{1} + \boldsymbol{\chi}^0 \cdot \mathbf{W})^{-1}. \quad (6.75)$$

However, a closer look to Eq. (6.73) reveals a problem if the target space is smaller than the space spanned by the Wannier states, like for instance for the systems investigated in the previous section. In this case the correct unscreening equation is

$$W^{\alpha\beta\gamma\delta} = U^{\alpha\beta\gamma\delta} + \sum_{\rho\mu\nu\tau \in \mathbb{D}} U^{\alpha\rho\tau\delta} \chi_{\rho\mu\nu\tau}^0 W^{\mu\beta\gamma\nu} \quad (6.76)$$

6.2 Unscreening Method for Isolated Target States

and is ill-defined, because the corresponding matrix equation (6.75) contains matrices of different dimensions, see Ref. 163 for a similar discussion. To our knowledge there is no unambiguous regularization scheme for such equations, so that the unscreening method described above is ultimately restricted to a small class of materials. One example for such a system is SrVO₃ and is discussed in section 6.2.2.

6.2.1 Implementation Details

We have implemented this method into VASP using the same technique as in section 6.1.3.1, with one noteworthy difference. We impose an energy cutoff of 1000 eV⁻¹ on the polarizability tensor χ^0 to be consistent with metallic screening, $W_{\mathbf{q}\rightarrow\mathbf{0}}(\mathbf{0}, \mathbf{0}, 0) \rightarrow 0$. We found that this approach improves remarkably the stability of the unscreening method.

6.2.2 Application to SrVO₃

We have compared the unscreening method with the CRPA approach, derived in section (6.1.3) for the test bet material SrVO₃. This material is a d^1 metal and one of the most benchmarked systems within LDA+DMFT.[83] We have considered the the ideal perovskite structure, shown in Fig. 6.9 with a lattice constant of $a = 3.78$ Å. The perovskite is characterized by Sr atoms located between octahedral crystal fields (red octahedra) build by six oxygen atoms with a V atom (not visible) in the center. The octahedral crystal field splits the five-fold energetically degenerate atomic d -states of V into two subgroups, the t_{2g} - and e_g -states consisting of three, respectively two states with same energy. More precisely, the e_g -group contains the d_{z^2} - and $d_{x^2-y^2}$ -states and lies higher in energy than the t_{2g} -group consisting of the d_{xy} -, d_{xz} - and d_{yz} -state. This becomes evident by considering the band structure of the system shown in Fig. 6.9, where the two blue bands above Fermi level (at $\mu = 0$ eV) are mainly of e_g character and the the three bands crossing the Fermi surface are the t_{2g} -states.

These properties have two advantages. First, considering the t_{2g} -states as target space for DMFT is computationally convenient, due to the presence of only three correlated states. Second, the t_{2g} manifold is topologically separated from the remaining Fock space and forms a composite Bloch band.[138] We, therefore, are able to compare the unscreening method, presented above, with the CRPA approach of section 6.1.3.

6. MERGING *GW* WITH DMFT

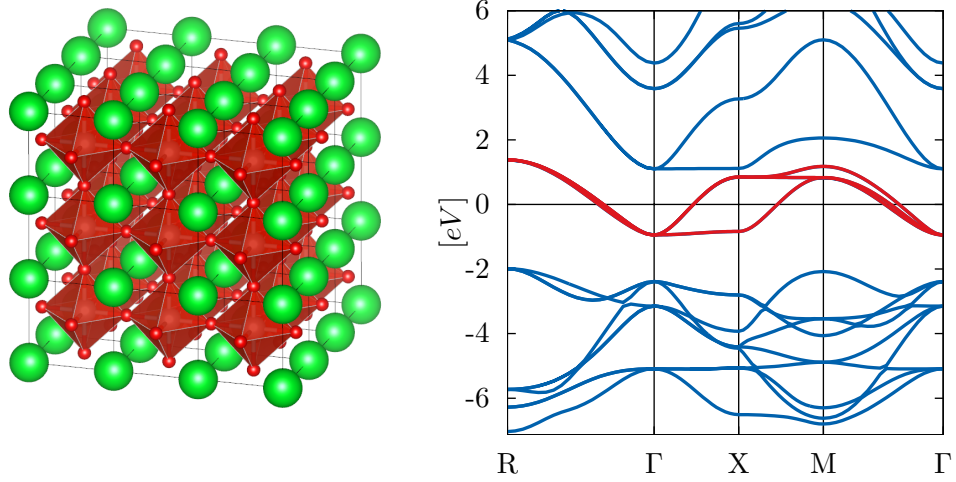


Figure 6.9: Left: Crystal structure of SrVO₃. Sr atoms (green) are located between the oxygen crystal fields indicated by red octahedra with a V atom in the center. Right: Band structure of SrVO₃. The three t_{2g} -states of V cross the chemical potential chosen at $\mu = 0$ eV.

6.2.3 Comparison with CRPA

We have chosen maximally localized Wannier states as basis for our calculations. [140] These states were obtained from the `Wannier90` library by excluding all, except the three t_{2g} -bands of V, in the projection.[142] The plane wave cutoff energies for the orbitals and the CRPA-polarizability have been set to 414 eV and 350 eV respectively. Extrapolation to a high energy cutoff of 500 eV was performed as described in section 6.1.4 and a Methfessel-Paxton smearing function was chosen for the Fermi occupancies with $\sigma = 0.1$. [164]

Due to the ideal perovskite structure any interaction matrix of SrVO₃, including the effective matrix $U_{\alpha\beta\gamma\delta}$ are determined by the three Hubbard-Kanamori parameters (6.14)-(6.16). They are given in Tab. 6.6 for the unscreening U and the CRPA method, denoted by U^{CRPA} . The same table shows, in addition, the Hubbard-Kanamori parameter for the bare Coulomb and fully screened interaction. The bare Coulomb interactions (~ 16 eV) are largely screened by the high-energy bands to give $U^{\text{CRPA}} \sim 3$ eV. In the present case of SrVO₃, the unscreened U turns out to have a value similar to U^{CRPA} .

It can be shown that the unscreened U and U' depend strongly on the filling of the system, which is mainly due to an oscillatory antiscreening effect induced by non-local

6.2 Unscreening Method for Isolated Target States

Table 6.6: On-site bare (\mathbf{V}), fully screened RPA (\mathbf{W}), constrained RPA U^{CRPA} and unscreening interaction (U).

	\mathbf{V}	\mathbf{W}	U^{CRPA}	U
U	16.0	1.12	3.36	3.46
U'	14.8	0.30	2.35	2.47
J	0.55	0.39	0.49	0.47

polarizations. This effect is absent in the CRPA method, because here on-, as well as off-center terms are removed completely in screening and consequently the screening oscillations are 'flatten out'. The small difference of 0.1 eV between U and U^{CRPA} is just a consequence of an accidental cancellation of the antiscreening by the non-local polarizations with the screening by the long-range interaction. More details about this effect can be found in Ref. 151.

However, we found that apart from the limited applicability of the unscreening method, the additional antiscreening effect can cause serious issues for other systems. This effect is not present for the method presented in previous section and it seems that CRPA is much more reliable than the unscreening scheme. We, therefore, suggest to apply the CRPA approach whenever possible to determine effective interactions for model Hamiltonians.

6. MERGING *GW* WITH DMFT

6.3 Quasi Particle *GW*+DMFT

In this section we apply the qp*GW*+DMFT algorithm to the test bed material SrVO₃. In addition, a comparison with conventional LDA+DMFT calculations are given.

The following subsection were published in Ref. 165.

6.3.1 Comparing qp*GW*+DMFT and LDA+DMFT for SrVO₃

The starting point of our calculation is the *GW* implementation within VASP. Specifically, we first performed Kohn-Sham density functional theory calculations within the settings mentioned in section 6.2.2 to obtain one-electron orbitals $\phi_{n\mathbf{k}}$ and one-electron energies $\epsilon_{n\mathbf{k}}$. The position of the *GW* quasi particle peaks $\tilde{\epsilon}_{n\mathbf{k}}$ were calculated by solving the linearized Eq. (4.65) for the diagonal

$$\tilde{\epsilon}_{n\mathbf{k}} = \epsilon_{n\mathbf{k}} + Z_{n\mathbf{k}} \text{Re} \left[\langle \phi_{n\mathbf{k}} | \hat{T} + \hat{\varphi} + \hat{V}_h + \hat{\Sigma}(\mathbf{k}, \epsilon_{n\mathbf{k}}) | \phi_{n\mathbf{k}} \rangle - \epsilon_{n\mathbf{k}} \right], \quad (6.77)$$

where $\hat{\Sigma}$ is the G_0W_0 self-energy and $Z_{n\mathbf{k}}$ the renormalization factor

$$Z_{n\mathbf{k}} = \frac{1}{1 - \text{Re} \langle \phi_{n\mathbf{k}} | \left. \frac{\partial \hat{\Sigma}(\mathbf{k}, \omega)}{\partial \omega} \right|_{\omega=\epsilon_{n\mathbf{k}}} | \phi_{n\mathbf{k}} \rangle}. \quad (6.78)$$

The original Kohn-Sham orbitals are maintained at this step and expressed in the projector augmented wave basis. Using Wannier90 these orbitals are projected onto the minimal t_{2g} Wannier basis, presented in section 6.2.2. To construct an effective low-energy Hamiltonian for the vanadium t_{2g} orbitals, we follow Faleev, van Schilfhaarde, and Kotani and approximate the frequency dependent G_0W_0 self-energy by an hermitian operator

$$\Sigma_{nm,\mathbf{k}} = \frac{1}{2} \langle \phi_{n\mathbf{k}} | \hat{\Sigma}^\dagger(\epsilon_{n\mathbf{k}}) + \hat{\Sigma}(\epsilon_{n\mathbf{k}}) | \phi_{m\mathbf{k}} \rangle. \quad (6.79)$$

This qp approximation is commonly used in *GW* calculations, in particular for self-consistent calculations, since fully frequency dependent calculations are computationally very demanding, see section 4.2.1 for more details.

In practice, for the present calculations, we have applied the slightly more involved procedure to derive an hermitian approximation outlined in Ref. 65, although this yields essentially an almost identical hermitian operator $\Sigma_{nm\mathbf{k}}$. Furthermore, the off-diagonal components are found to be negligibly small, and henceforth disregarded. The final hermitian and \mathbf{k} -point dependent operator is transformed to the Wannier basis and

6.3 Quasi Particle GW +DMFT

passed on to the DMFT code, where it is used to construct the \mathbf{k} -dependent self-energy by adding the local DMFT self-energy.

This qp GW +DMFT procedure allows us to maintain the structure and outline of the common DFT+DMFT scheme and can be easily adopted in any DMFT code. Instead of the LDA one-electron matrix elements, the qp GW ones are passed to the DMFT. This procedure neglects lifetime broadening and any frequency dependence of the GW self-energy beyond its linear part. Subtracting the local part of this qp GW hermitian operator (to avoid a double counting) does not yield a constant shift for the degenerate t_{2g} orbitals, see for instance Tomczak *et al.*[166]. However, due to an implementation error, the calculations have been performed, such that the removal of the local self-energy terms results in a constant shift of the G_0W_0 energies. Our approach is, therefore, similar to LDA+DMFT, but with renormalized band structure. Let us also note that hitherto we did not perform self-consistency on the GW part.

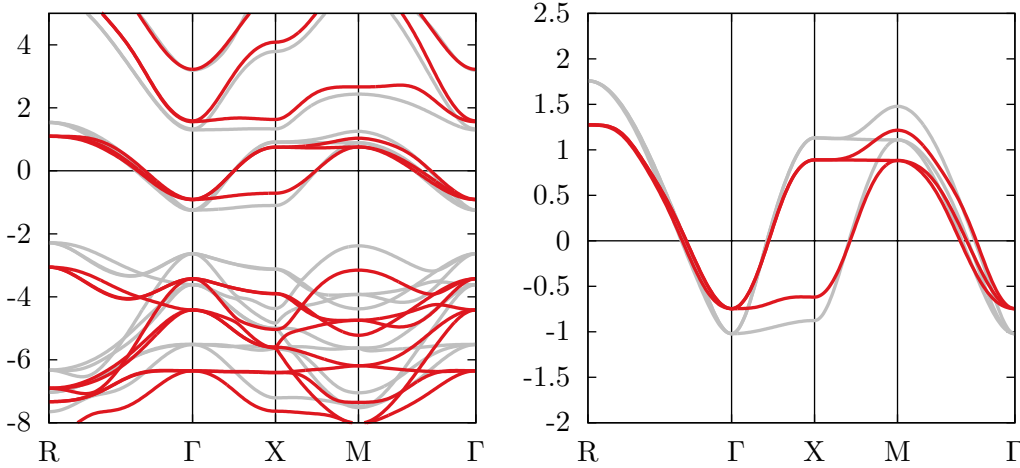


Figure 6.10: (Color online) Left panel: G_0W_0 quasi particle bands (red) in comparison to LDA (gray). The Fermi level sets our zero of energy and is marked as a line. Right panel: Wannier projected t_{2g} band structure from G_0W_0 (red) and LDA (gray). The t_{2g} target bands bandwidth is reduced by ~ 0.7 eV in GW .

Figure 6.10 shows the obtained G_0W_0 band structure, which for the t_{2g} vanadium target bands is about 0.7 eV narrower than for the LDA. The oxygen p band (below -2 eV) is shifted downwards by 0.5 eV compared to the LDA, whereas the vanadium e_g bands (located about 1.5 eV above the Fermi level) are slightly shifted upwards by 0.2 eV. In the LDA, the top most vanadium t_{2g} band at the M point is slightly above the

6. MERGING *GW* WITH DMFT

lowest e_g band at the Γ point, whereas the G_0W_0 correction opens a gap between the t_{2g} and e_g states.

Within this Wannier basis, we use an interaction value of $U^{nl} = 3.4$ eV, as obtained from the unscreening method described in section 6.2. It can be expected, that the CRPA interaction of $U^{\text{CRPA}} = 3.3$ eV will yield similar results, however, this might not be the case for other materials and doping levels. We carefully compare $qpGW$ +DMFT with LDA+DMFT calculations and experiment. In both cases, we use (frequency-independent) interaction. The Kanamori interaction parameters as derived from the locally unscreened RPA are listed in Tab. 6.6 and are almost identical to the CRPA. In constrained LDA (CLDA), on the other hand, somewhat larger interaction parameters were obtained and are employed by us for the corresponding calculations $U^{\text{CLDA}} = 5.05$ eV, $U^{\text{CLDA}} = 3.55$ eV and $J^{\text{CLDA}} = 0.75$ eV.¹[167]

For the subsequent DMFT calculation we employ the Würzburg-Wien `w2dynamics` code,[168] based on the hybridization-expansion variant [169] of the continuous-time quantum Monte Carlo (CT-QMC) method.[170] This algorithm is particularly fast since it employs additional quantum numbers for a rotationally invariant Kanamori interaction.[171] The maximum entropy method is employed for the analytic continuation of the imaginary time and (Matsubara) frequency CT-QMC data to real frequencies, see Ref. 172 for more details.

All our calculations are without self-consistency, which is to some extent justified for SrVO_3 . Since the three t_{2g} bands of SrVO_3 are degenerate, DMFT does not change the charge density of the low-energy t_{2g} manifold and hence self-consistency effects are expected to be small for LDA+DMFT. This is, in principle, different for $qpGW$ +DMFT. Here the frequency dependence of the DMFT self-energy might yield some feedback already for a simplified Faliev, van Schilfgaarde and Kotani quasi particle self-consistency.[173, 174] Finally, we also test the \mathcal{Z}_B -factor renormalized GW bandwidth with $\mathcal{Z}_B = 0.7$ obtained in Ref. 175 for mimicking the frequency dependence of the CRPA interaction.

¹Note that CLDA tends to overestimate the Hund's exchange, see Ref. 83 so that in subsequent LDA+DMFT calculations smaller values of have been employed. For the system SrVO_3 this smaller value of mainly influences the upper Hubbard band.

6.3.2 Results

For analyzing the differences between $qpGW+DMFT$ and $LDA+DMFT$ we analyze and compare five different calculations in the following:

- (1) $LDA+DMFT@U'^{cLDA}$ (conventional $LDA+DMFT$ calculation with the $CLDA$ interaction $U'^{cLDA} = 3.55$ eV).
- (2) $LDA+DMFT@U'^{nl}$ ($LDA+DMFT$ calculation but with the locally unscreened RPA interaction $U'^{nl} = 2.49$ eV).
- (3) $qpGW+DMFT@U'^{nl}$ ($qpGW+DMFT$ calculation with $U'^{nl} = 2.49$ eV).
- (4) $qpGW+DMFT@U'^{cLDA}$ ($qpGW+DMFT$ calculation with $U'^{cLDA} = 3.55$ eV).
- (5) $qpGW+DMFT@U'^{nl}, \mathcal{Z}_B = 0.7$ (as 3 but with a Bose renormalization factor \mathcal{Z}_B).

Let us first turn to the imaginary part of the local self-energy which is shown as a function of (Matsubara) frequency in Fig. 6.11. The self-energy yields a first impression of how strong the electronic correlations are in the various calculations. The $LDA+DMFT@U'^{nl}$ self-energy is the least correlated one, somewhat less correlated than $LDA+DMFT@U'^{cLDA}$ due to the smaller locally unscreened Coulomb interaction ($U'^{nl} = 2.49 < 3.55$ eV = U'^{cLDA}). For the same reason also the $qpGW+DMFT@U'^{nl}$ self-energy is less correlated than that of a $qpGW+DMFT@U'^{cLDA}$ calculation.

If we compare $LDA+DMFT$ and $qpGW+DMFT$ on the other hand, the $LDA+DMFT$ self-energy is less correlated than the $qpGW+DMFT$ one, if the Coulomb interaction is kept the same. This is due to the 0.7 eV smaller GW t_{2g} bandwidth in comparison to LDA . This observation also reflects in the $DMFT$ quasi particle renormalization factor Z , which were obtained from a forth-order fit to the lowest for Matsubara frequencies, see Tab. 6.7. Also there is an additional GW renormalization factor reducing the bandwidth in comparison to LDA .

However, the effect of the smaller GW bandwidth partially compensates with the smaller U'^{nl} interaction strength. Altogether this yields rather similar self-energies of the standard approaches: $LDA+DMFT@U'^{cLDA}$ and $qpGW+DMFT@U'^{nl}$, see lower panel of Fig. 6.12. This also reflects in very similar renormalization factors in Table 6.7,

6. MERGING GW WITH DMFT

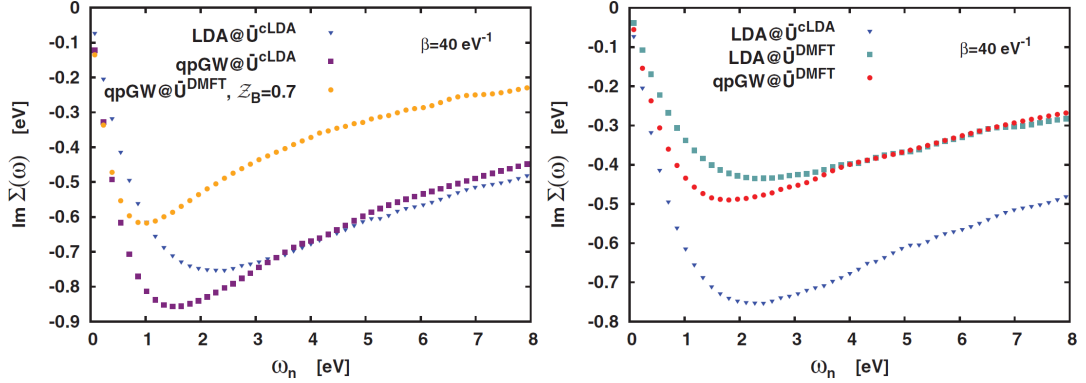


Figure 6.11: Comparison of the imaginary part of the DMFT t_{2g} self-energies Σ vs (Matsubara) frequency ω for SrVO₃ at inverse temperature $\beta = 40 \text{ eV}^{-1}$ as computed in five different ways: employing qpGW and LDA Wannier bands, the locally unscreened RPA interaction $U'^{nl} = 2.49 \text{ eV}$ and the CLDA $U'^{CLDA} = 3.55 \text{ eV}$, as well as the $Z_B = 0.7$ renormalization.[175].

$Z = 0.51$ vs. $Z = 0.57$, which both agree well with experimental estimates of $0.5 - 0.6$.¹ [167, 176]

Since one important difference is the strength of the interaction, it is worthwhile recalling that U'^{nl} is defined as the local interaction strength at low frequencies. While this value is almost constant within the range of the t_{2g} bandwidth, it approaches the bare Coulomb interaction at larger energies, exceeding 10 eV. It has been recently argued and shown in model calculations, see Ref. 175, that the stronger frequency dependence of the screened Coulomb interaction at high energies is of relevance and can be mimicked by a Z_B renormalization of the GW bandwidth. The latter has been determined as $Z_B = 0.7$ for SrVO₃. We have tried to take this into account in the qpGW+DMFT@ $U'^{nl}, Z_B = 0.7$ calculation. Due to the additional bandwidth renormalization, this calculation is very different from all others and yields the largest quasi particle renormalization, *i.e.* $Z = 0.36$ is smallest.

This too small quasi particle weight can be understood as follows: The Z_B factor mimics the frequency dependence of CRPA screened Coulomb interaction, which is much

¹Note that due to the presence of kinks there are actually two such renormalization factors: A Fermi liquid for the renormalization at the lowest energies and a second for higher energies. The latter also corresponds to the overall weight of the central peak. With the energy resolution in Fig. 6.12 being limited by the discrete Matsubara frequencies the of Table 6.7 still rather corresponds to as do the experimental values of Refs. 167 and 176.

6.3 Quasi Particle $GW+DMFT$

Table 6.7: DMFT quasi particle renormalization factors Z from the five different calculations at inverse temperature $\beta = 40 \text{ eV}^{-1}$. Also shown are the pairwise double occupations within the same orbital d_{intra} and between different orbitals with the same $d_{\text{inter}}^{\uparrow\uparrow}$ and opposite spin $d_{\text{inter}}^{\uparrow\downarrow}$. The 'standard' $\text{LDA+DMFT}@U'^{CLDA}$ and $\text{qpGW+DMFT}@U'^{nl}$ calculations are similarly correlated and agree well with experiment. Using the CLDA interaction U'^{CLDA} for qpGW+DMFT or the locally unscreened RPA U'^{nl} for LDA+DMFT yields a too strongly and too weakly correlated solution in comparison to experiment, respectively. Note that qpGW+DMFT becomes even more strongly correlated if the Bose renormalization factor is included.

Scheme	Z	d_{intra}	$d_{\text{inter}}^{\uparrow\uparrow}$	$d_{\text{inter}}^{\uparrow\downarrow}$
$\text{LDA+DMFT}@U'^{CLDA}$	0.51	0.004	0.013	0.009
$\text{LDA+DMFT}@U'^{nl}$	0.67	0.007	0.016	0.013
$\text{qpGW+DMFT}@U'^{nl}$	0.57	0.005	0.014	0.010
$\text{qpGW+DMFT}@U'^{CLDA}$	0.39	0.003	0.010	0.007
$\text{qpGW+DMFT}@U'^{nl}, \mathcal{Z}_B = 0.7$	0.36	0.003	0.009	0.006
Experiment	$\sim 0.5 - 0.6$			

larger at high frequencies. In a fully frequency dependent GW calculation, this is properly matched by a correspondingly large GW self-energy at large frequencies. However, within the quasi particle treatment of the GW self-energy (which represents a linear approximation to its frequency dependence, see section 4.2.1) such high frequency contributions of the GW self-energy are not included. As our results show, in this case, it is hence more consistent not to include the frequency dependence for the Coulomb interaction only, which the \mathcal{Z}_B factor emulates.

Next, we compare the k-integrated spectrum in Fig. 6.13. At low frequency we find the same trends as for the self-energy results: the $\text{qpGW+DMFT}@U'^{nl}$ and LDA+DMFT at U'^{nl} and U'^{CLDA} , respectively, yield a rather similar spectrum. In particular, the quasi particle peak has a similar weight and shape. However, a difference is found at larger frequencies: The $\text{qpGW+DMFT}@U'^{nl}$ Hubbard bands are closer to the Fermi level in comparison to LDA+DMFT (see Sec. 6.3.3). If we perform $\text{qpGW+DMFT}@U'^{nl}$ and LDA+DMFT at the 'wrong' interaction strength (*i.e.*, U'^{CLDA} and U'^{nl} , respectively), we obtain a noticeably stronger and weaker correlated solution, respectively. This trend is also reflected in the double occupations presented in Table 6.7. Finally, as in the case

6. MERGING GW WITH DMFT

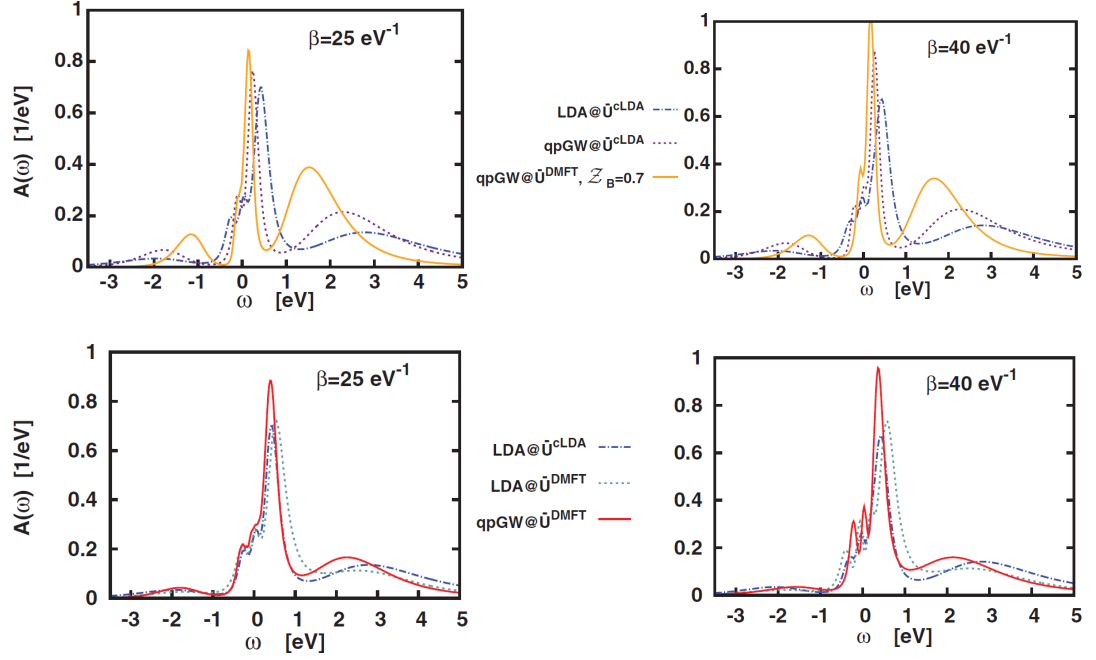


Figure 6.12: Spectral function for SrVO_3 (t_{2g} orbitals only) computed in five different ways as in Fig. 6.11. At lower temperatures the central peak gets only slightly sharper and higher, although the temperature effects from $\beta = 25$ to 40 eV^{-1} are small.

of the self-energy, the $\text{qpGW}+\text{DMFT}@U'^{nl}$, $Z_B = 0.7$ solution is much more strongly correlated, with Hubbard side bands at much lower energies.

6.3.3 Comparison to Photoemission Spectroscopy

An obvious question is whether $\text{LDA}+\text{DMFT}$ or $\text{qpGW}+\text{DMFT}$ yields 'better' results. This question is difficult to answer and for the time being we resort to a comparison with experimental photoemission spectroscopy (PES).[167] However, one should be well aware of the limitations of such a comparison. On the theory side, the involved approximations common to the calculations, as, *e.g.*, neglecting non-local correlations beyond the DMFT and GW level, or further effects, such as the electron-phonon coupling or the photoemission matrix elements, might bias the theoretical result in one way or the other. On the experimental side, care is in place, as well, although the PES results have considerably improved in the last years due to better photon sources. Furthermore, in Ref. 167 an oxygen p background has been subtracted, which by a construction removes

6.3 Quasi Particle $GW+DMFT$

all spectral weight below the region identified as the lower Hubbard band.

Figure 6.13 compares the proposed $LDA+DMFT$ and $qpGW+DMFT$ (with and without Bose renormalization) with PES experiment. To this end, the theoretical results have been multiplied with the Fermi function at the experimental temperature of 20 K and broadened by the experimental resolution of 0.1 eV. The height of the PES spectrum has been fixed so that its integral yields 1, *i.e.*, accommodates one t_{2g} electron, as in theory.

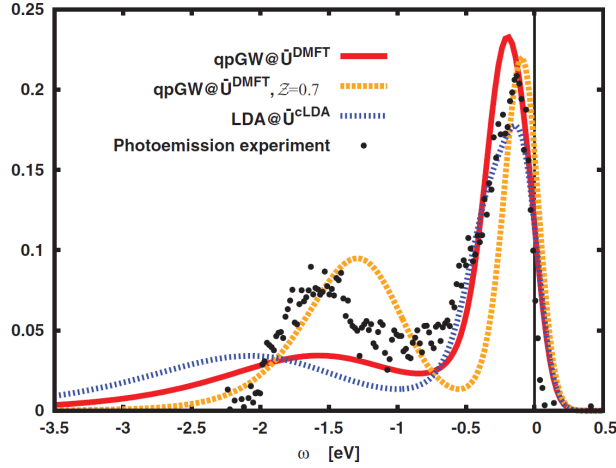


Figure 6.13: Comparison of $LDA+DMFT@U'^{cLDA}$, $qpGW+DMFT@U'^{nl}$ (without and with Bose renormalization $Z_B = 0.7$), and experiment. The position of the lower Hubbard band is better reproduced in $qpGW+DMFT$, whereas the central peak is similar in $LDA+DMFT$ and $qpGW+DMFT$. The Bose renormalization $qpGW+DMFT$ differs considerably (photoemission spectra reproduced from Ref. 167).

The $qpGW+DMFT@U'^{nl}$ and $LDA+DMFT@U'^{cLDA}$ have a quite similar quasi particle peak, which also well agrees with experiment, as it was already indicated by the quasi particle renormalization factor. A noteworthy difference is the position of the lower Hubbard band which is at -2 eV for $LDA+DMFT@U'^{cLDA}$ and ~ -1.6 eV for $qpGW+DMFT@U'^{nl}$. The latter is in agreement with experiment and a result of the reduced GW bandwidth. Let us note that the sharpness and height of the lower Hubbard band very much depends on the maximum entropy method, which tends to overestimate the broadening of the high-energy spectral features. Hence, only the position and weight is a reliable result of the calculation.

6. MERGING GW WITH DMFT

As we have already seen, the Bose-factor renormalized $qpGW+DMFT@U'^{nl}$, $Z_B = 0.7$ calculation is distinct from both $qpGW+DMFT@U'^{nl}$ and $LDA+DMFT@U'^{cLDA}$. It is also different from experiment with a much more narrow quasi particle peak and a lower Hubbard band much closer to the Fermi level. A similar difference between static U on the one side and frequency dependent U was reported in Ref. 177. A difference of this magnitude is hence to be expected. Recently we became aware of Ref. 178, in which Tomczak *et al.* report a $qpGW+DMFT$ calculation with the full frequency dependence of the CRPA interaction for $SrVO_3$ obtaining good agreement with experiment as well.

Conclusion

The aim of this thesis was to develop algorithms and approximate techniques to solve the electronic problem of condensed matter. In general, there are two possible approaches to solve a system of interacting electrons.

On the one hand, there are the mean-field methods such as Hartree-Fock and density functional theory, which are summarized in chapter 1. Both approaches allow for an accurate determination of the groundstate energy of N interacting electrons with a rather low computational cost, provided the groundstate wavefunction of the system is described well by one Slater determinant (1.6). However, often this is an inaccurate approximation and one has to either include additional Slater determinants, see Eq. (1.19) or use more advanced density functionals to solve the Kohn-Sham equations (1.33).

In this thesis we used a different route to the electronic structure problem based on the second quantization formalism of QFT and diagrammatic perturbation theory. For this purpose we have introduced the necessary framework in the chapters 2 and 3. We have discussed three different approaches including the RPA, GW approximation and DMFT. While the former, RPA, yields a post-mean-field estimate for the correlation energy of the interacting system [see section 3.3], GW and DMFT provide access to spectral properties of the materials in terms of interacting electron and effectively screened photon propagator functions [see chapter 4 and 4.5.1].

We have seen that GW and RPA are strongly related with each other, since both approximations restrict the polarizability of the system to the independent particle bubble of Eq. (3.25) resulting in the well-known GW diagram of the self-energy (4.27). To be able to compute RPA correlation energies of large systems we have implemented a

7. CONCLUSION

low scaling RPA algorithm in VASP, which is based on the discovery of dual non-uniform imaginary time and frequency grids for the polarizability [see chapter 3.3]. Using this algorithm we have calculated the RPA energy of Si for supercells of up to 256 atoms and obtained defect formation energies in excellent agreement with recent DMC calculations. This shows that RPA and GW describes accurately weakly correlated systems, where delocalized correlation effects are dominating.

In contrast, DMFT provides access to the full, but local self-energy diagrams of a system by mapping the many-body Hamiltonian to an auxiliary impurity problem [see section 4.5.1]. We have seen that the mapping to the impurity model is exact only in infinite dimensions, but gives an excellent description of the local correlation effects of partially filled narrow bands. However, the solution of the impurity problem is typically found using quantum Monte Carlo methods making DMFT calculations ultimately very expensive, so that one effectively has to downfold the full many-body Hamiltonian onto a small low energy model. To describe realistic systems this downfolded model Hamiltonian has to include non-local correlation effects as well. In section 4.5.1 we have shown how commonly non-local correlation effects are incorporated in the DMFT approach using LDA. We have seen that every LDA+DMFT scheme suffers necessarily from the double counting problem, due to the fact that DFT is not a diagrammatic theory.

In contrast to the commonly used LDA+DMFT scheme, both theories, GW and DMFT, can be formulated in a diagrammatic language [see 4.2.1 and 4.5.1], so that the double counting problem of LDA+DMFT can be avoided. For this purpose we elaborated on the combination of the GW approximation with DMFT by introducing the PI formalism in section 4.3 and integrating out all, but local degrees of freedom using the cavity method in section 4.5. This results in the general Dyson equations (4.127) for the propagator and the effective interaction (4.128) and shows that formally, in a true GW +DMFT framework, both propagators must be determined self-consistently [see GW +DMFT algorithm in chapter 6].

This requires a true first-principles downfolding method of the full many-body Hamiltonian on a low energy model including the *ab initio* computation of the effective interaction of the model. To find such a prescription we have investigated the constrained CRPA in detail in section 6.1, where screening effects within the DMFT target space are neglected. We have shown that the CRPA approach is well-defined only in the case of isolated target states, such as the t_{2g} states of V in SrVO₃, with ambiguities

appearing for entangled target bands. For entangled target states, there are two different CRPA approaches known, both suffering from deficiencies and not derivable from first-principles [see 6.1.1]. To obtain a well-defined CRPA prescription we have used the Kubo-Nakano formula (6.30) for the correlated subspace and derived an expression for the target polarizability obtaining a similar expression to the Adler and Wiser formula [see Eq. (6.68)]. We have applied our CRPA method to the 3d TMs series Sc-Ni, where these functions are absent, obtaining effective interactions lying in between the two known CRPA approaches [see Fig. 6.7]. Similar results have been obtained for the superconductor La_2CuO_4 and shown in section 6.1.7.

In section 6.3, we have presented a simple GW +DMFT algorithm based on the qp approximation of the GW self-energy [see section 4.2.1] and applied our qp GW +DMFT scheme to the test material SrVO_3 . Using our qp GW +DMFT approach, which can be seen as an LDA+DMFT scheme where G_0W_0 quasi-particle energies replace the KS energies, we have obtained excellent agreement for the spectral function with experimental data measured using PES [see Fig. 6.13]. We have seen that our qp GW +DMFT method outperforms conventional LDA+DMFT calculations, that clearly underestimate the lower Hubbard band.

These results show that combining GW with DMFT is a promising route to go and to investigate in future. Here, additional questions about the correct treatment of the double counting terms in a qp or fully frequency dependent GW picture are raised, side by side with the question how to include the effective potential in the self-consistency GW +DMFT cycle. This will be investigated in future work.

7. CONCLUSION

Appendices

Appendix A

From QED to the Many-Body Problem

In this appendix the many-body Hamiltonian of QFT from the QED Lagrangian is derived. For this purpose, the Einstein summation convention is employed and the Minkowski metric $\eta_{\mu\nu}$ with signature $(+ - - -)$ is used, where Latin indices $i = 1, 2, 3$ indicate space indices and Greek indices $\mu = 0, \dots, 3$ arbitrary indices with $\mu = 0$ representing the time index. Within this notation the QED Lagrangian in units of $\hbar = 1 = c$ reads (see for instance Bjorken and Drell[25])

$$\mathcal{L} = \bar{\Psi} (i\gamma_\mu \partial^\mu - m - q\gamma_\mu V_{\text{ext}}^\mu) \Psi + q\bar{\Psi}\gamma_\mu \Psi A^\mu - \frac{1}{16\pi} F_{\mu\nu} F^{\mu\nu}, \quad (\text{A.1})$$

where $F_{\mu\nu}$ is the electromagnetic field tensor. Here, γ^μ is the four-vector of the 4×4 -matrices

$$\gamma^0 = \begin{pmatrix} 1 & 0 \\ 0 & -1 \end{pmatrix}, \quad \gamma^i = \begin{pmatrix} 0 & \sigma^i \\ -\sigma^i & 0 \end{pmatrix}, \quad (\text{A.2})$$

with σ^i representing the Pauli spin matrices. This implies that the field spinor Ψ is a vector with four entries, see Ref. 24.

We are interested primarily in the conserved energy of the Lagrangian (A.1), i.e. a scalar that is invariant under time shifts. This is obtained by Noether's theorem, which tells us that the energy-momentum density tensor[60]

$$\mathcal{T}^{\mu\nu} = \partial^\nu A_\alpha \frac{\partial \mathcal{L}}{\partial(\partial_\mu A_\alpha)} + \partial^\nu \Psi \frac{\partial \mathcal{L}}{\partial(\partial_\mu \Psi)} - \eta^{\mu\nu} \mathcal{L}, \quad (\text{A.3})$$

obeys the four conservation laws

$$\partial_\mu \mathcal{T}^{\mu\nu} = 0. \quad (\text{A.4})$$

A. FROM QED TO THE MANY-BODY PROBLEM

Integrating this expression over the full space, and using the divergence theorem of Gauss

$$\int d^3\mathbf{r}\partial_i\mathcal{T}^{i\nu} = 0, \quad (\text{A.5})$$

one finds for $\nu = 0$ that

$$\partial_0 \int d^3\mathbf{r}\mathcal{T}^{00} = 0. \quad (\text{A.6})$$

This is the conservation law for the energy and one therefore associates the \mathcal{T}^{00} with the Hamiltonian density \mathcal{H} . The latter is obtained from Eq. (A.3)

$$\mathcal{H} = \underbrace{\frac{\partial\mathcal{L}}{\partial\partial_0 A_\alpha}}_{=\Pi^\mu} \partial^0 A_\alpha + \underbrace{\frac{\partial\mathcal{L}}{\partial\partial_0\Psi}}_{=\Pi} \partial^0\Psi - \mathcal{L} \quad (\text{A.7})$$

and yields, when integrated, the Hamilton function¹

$$H(t) = \int d^3\mathbf{r}\mathcal{H}. \quad (\text{A.8})$$

Now, one looks for an explicit expression of the Hamilton function $H(t)$.

For the Lagrangian of Eq. (A.1), the conjugate field momenta of the Dirac Π and Maxwell field Π^μ are

$$\Pi = i\bar{\Psi}\gamma^0 = i\Psi^\dagger \quad (\text{A.9})$$

$$\Pi^\mu = \frac{1}{4\pi} (0, -F^{0i}) = \frac{1}{4\pi} (0, E^i) \quad (\text{A.10})$$

Where the definition of the electric field

$$F^{0i} = \partial^0 A^i - \partial^i A^0 = -E^i \quad (\text{A.11})$$

in the last step of Eq. (A.10) was used. Combining these momenta with the result for the kinetic Maxwell term

$$F_{\mu\nu}F^{\mu\nu} = (B^i B_i - E^i E_i) \quad (\text{A.12})$$

and the electron four-current $j^\mu = \bar{\Psi}\gamma^\mu\Psi$ one obtains the Hamiltonian density

$$\mathcal{H} = \Psi^\dagger (i\alpha^i\partial_i + m) \Psi + qj^\mu V_\mu^{\text{ext}} - \frac{1}{8\pi} (B^i B_i + E^i E_i) + \frac{1}{4\pi} E^i \partial_i A_0 - qj^\mu A_\mu. \quad (\text{A.13})$$

Here the Dirac matrices $\alpha^i = \gamma^0\gamma^i$ have been used. From the density (A.13) and the Hamiltonian equation of motion

$$\frac{\partial\Psi}{\partial t} = \frac{\partial\mathcal{H}}{\partial\Pi}, \quad (\text{A.14})$$

¹We emphasize that Eq. (A.7) is the Legendre transformation of the Lagrangian (A.1).

follows the Dirac equation in the Hamilton form[25]

$$i\frac{\partial\Psi}{\partial t} = [i\alpha^i\partial_i + m + q\gamma^\mu(V_\mu^{\text{ext}} - A_\mu)]\Psi. \quad (\text{A.15})$$

So far no specific gauge condition on the electromagnetic field or any reference frame was assumed. For our considerations it is advantageous to choose the rest frame of the nuclei as the reference frame. Assuming fixed locations of the nuclei in space, this implies that the external potential can be written as

$$V_{\text{ext}}^\mu = (\varphi, 0, 0, 0). \quad (\text{A.16})$$

Customary gauges are the Lorentz gauge $\partial_\mu A^\mu = 0$ and the Coulomb (or radiation) gauge condition

$$\partial_i A^i = 0. \quad (\text{A.17})$$

The former is suitable for maintaining co-variance, whereas the latter is useful if the radiating part of the electromagnetic field should be separated, see Ref. 59 for more details. Electromagnetic radiation will not be considered in this thesis, since in most cases it can be neglected for condensed matter. Therefore Eq. (A.17) is chosen as gauge condition for the electromagnetic field in the following.

To achieve this, the co-variance notation is dropped in the forthcoming and one concentrates on the last two terms of the Hamiltonian density (A.13). It is convenient to split the electric field \vec{E} into its normal

$$\vec{E}_\perp = -\frac{\partial\vec{A}}{\partial t} \quad (\text{A.18})$$

and parallel components[179]

$$\vec{E}_\parallel = -\vec{\nabla}\phi. \quad (\text{A.19})$$

Integrating the density \mathcal{H} one obtains for the last three terms of the Hamilton function $H(t)$ (A.13)

$$\begin{aligned} \frac{1}{8\pi} \int d^3\mathbf{r} (\vec{B}^2 + \vec{E}_\perp^2) &+ \frac{1}{4\pi} \int d^3\mathbf{r} \vec{E}_\perp \cdot \vec{E}_\parallel + \frac{1}{8\pi} \int d^3\mathbf{r} \vec{E}_\parallel^2 \\ &+ \frac{1}{4\pi} \int d^3\mathbf{r} \vec{E} \cdot \vec{\nabla}\phi - q \int d^3\mathbf{r} \rho\phi + q \int d^3\mathbf{r} \vec{j} \cdot \vec{A}, \end{aligned} \quad (\text{A.20})$$

where $j^\mu = (\rho, \vec{j})$ was used.

A. FROM QED TO THE MANY-BODY PROBLEM

The second term vanishes, which follows from partial integration and the fact that $\vec{\nabla} \cdot \vec{E}_\perp = 0$ holds within the Coulomb gauge. Partial integration of the fourth term with additional usage of the Maxwell equation

$$\vec{\nabla} \cdot \vec{E} = 4\pi q\rho \quad (\text{A.21})$$

cancels term five. Furthermore, the third contribution in (A.20) can be rewritten into

$$\frac{1}{8\pi} \int d^3\mathbf{r} \vec{E}_\parallel^2 = \frac{1}{8\pi} \underbrace{\int d^3\mathbf{r} \vec{\nabla} \cdot (\phi \vec{\nabla} \phi)}_{=0} - \frac{1}{8\pi} \int d^3\mathbf{r} \phi \underbrace{\Delta \phi}_{-4\pi q\rho} \quad (\text{A.22})$$

by using the Maxwell equation in the Coulomb gauge

$$-\Delta \phi = 4\pi q\rho. \quad (\text{A.23})$$

The general solution of this equation is the well-known Poisson integral

$$\rho(\mathbf{r}, t) = q \int d^3\mathbf{r}' \frac{\rho(\mathbf{r}', t)}{|\mathbf{r} - \mathbf{r}'|} \quad (\text{A.24})$$

and can be inserted into the last term of Eq. (A.22) as well as into Eq. (A.20). Collecting all terms of the Hamiltonian (A.13) and using $\rho = \Psi^\dagger \Psi$ yields finally

$$\begin{aligned} H(t) &= \int d^3\mathbf{r} \Psi^\dagger \left(\vec{\alpha} \cdot \vec{\nabla} + m + q\beta\varphi \right) \Psi \\ &+ \frac{e^2}{2} \int d^3\mathbf{r} d^3\mathbf{r}' \frac{\Psi^\dagger(\mathbf{r}, t) \Psi(\mathbf{r}, t) \Psi^\dagger(\mathbf{r}', t) \Psi(\mathbf{r}', t)}{|\mathbf{r} - \mathbf{r}'|} \\ &+ \frac{1}{8\pi} \int d^3\mathbf{r} \left[\left(\vec{\nabla} \times \vec{A} \right)^2 + \left(\frac{\partial \vec{A}}{\partial t} \right)^2 + q\vec{j} \cdot \vec{A} \right] \end{aligned} \quad (\text{A.25})$$

In the second line of this expression the instantaneous Coulomb interaction of two charge distributions ρ at different positions appears. The third term describes the energy of the electromagnetic field and explains how an electron current interacts with the magnetic field.

Finding solutions of the corresponding field equations for the Hamiltonian (A.25) is not feasible for any but the simplest systems.[180] So, before one continues with the quantization of the field theory, it is time to make three assumption.

Firstly, we are mostly interested in the physics of condensed matter and the interactions of bound valence electrons in solid matter. For this purpose a static external potential $\varphi(\mathbf{r}, t) = \varphi(\mathbf{r})$ is an sufficiently accurate approximation for our considerations.

Secondly, electrostatic systems, where the electronic current \vec{j} is small compared to the Coulomb interaction between the charges ρ are considered only. Hence the last term in (A.25) is neglected.

Lastly, valence electrons have typically small energies compared to its rest mass m , so that the non-relativistic limit of the first term in Eq. (A.25) is appropriate. For this purpose, we reintroduced the constants \hbar and c and consider the corresponding Dirac equation of the first term in Eq. (A.25), which reads

$$i\hbar\frac{\partial\Psi}{\partial t} = \left[c\vec{\alpha} \cdot \left(\underbrace{-i\hbar\vec{\nabla}}_{=\vec{p}} - \frac{q}{c}\vec{A} \right) + \beta mc^2 + q\beta\varphi \right] \Psi. \quad (\text{A.26})$$

Following Bjorken and Drell[25], one inserts the two-component ansatz $\Psi = e^{-i\frac{mc^2}{\hbar}t}(\psi, \chi)$ for the Dirac spinor Ψ into Eq. (A.26) and obtains

$$i\hbar\frac{\partial}{\partial t} \begin{pmatrix} \psi \\ \chi \end{pmatrix} = c\vec{\sigma} \cdot \vec{\pi} \begin{pmatrix} \chi \\ \psi \end{pmatrix} - 2mc^2 \begin{pmatrix} 0 \\ \chi \end{pmatrix} + q\varphi \begin{pmatrix} \psi \\ \chi \end{pmatrix}, \quad \vec{\pi} = \vec{p} - \frac{q}{c}\vec{A}. \quad (\text{A.27})$$

In the next step, small energies and field interactions of the positron

$$i\hbar\frac{\partial\chi}{\partial t} \approx 0 \approx q\varphi\chi \quad (\text{A.28})$$

are assumed and the identity¹

$$(\vec{\sigma} \cdot \vec{\pi})^2 = \vec{\pi} \cdot \vec{\pi} - \frac{q\hbar}{c}\vec{\sigma} \cdot \vec{B} \quad (\text{A.29})$$

is used to derive the Pauli equation for the following Schrödinger field spinor

$$i\hbar\frac{\partial\psi}{\partial t} = \left[\frac{1}{2m}(\vec{\pi} \cdot \vec{\pi})^2 - \frac{q\hbar}{2mc}\vec{\sigma} \cdot \vec{B} + q\varphi \right] \psi. \quad (\text{A.30})$$

This equation can be further simplified for constant and weak magnetic fields \vec{B}_0 with corresponding vector potential $\vec{A} = \frac{1}{2}\vec{B}_0 \times \vec{r}$ to end up with the Schrödinger equation

$$i\hbar\frac{\partial\psi}{\partial t} = \left[\frac{1}{2m}\vec{p}^2 - \frac{q\hbar}{2mc}(\vec{L} + 2\vec{S}) \cdot \vec{B}_0 + q\varphi \right] \psi. \quad (\text{A.31})$$

Here the second term on the r.h.s. contains the angular momentum $\vec{L} = \vec{r} \times \vec{p}$ and spin operator $\vec{S} = \hbar/2\vec{\sigma}$ and can be safely disregarded for the systems considered in this thesis, *i.e.* by performing the limit $c \rightarrow \infty$. Then Eq. (A.31) assumes the form of the non-interacting Schrödinger equation with the Hamiltonian given in Eq. (2.2).

¹This follows from the commutation relations of the Pauli spin matrices $[\sigma^i, \sigma^j] = 2i\varepsilon^{ij}_k \sigma^k$, see Ref. 25 for more details.

A. FROM QED TO THE MANY-BODY PROBLEM

Appendix B

Non-Interacting Lehman Amplitudes

In this appendix the Lehman amplitudes

$$A_{<(>)}^{(*)\pm}(\mathbf{r}) = \left\langle \Psi_{\nu}^{(N\pm 1)} \left| \hat{\psi}_{<(>)}^{\dagger}(\mathbf{r}) \right| \Psi_0^{(N)} \right\rangle \quad (\text{B.1})$$

appearing in the expression of the lesser part of the non-interacting propagator (2.49) are evaluated. We focus our attention on the special case

$$A_{<}^{*-}(\mathbf{r}) = \left\langle \Psi_{\nu}^{(N-1)} \left| \hat{\psi}_{<}^{\dagger}(\mathbf{r}) \right| \Psi_0^{(N)} \right\rangle, \quad (\text{B.2})$$

since, as one shall see in a moment, the result can be generalized easily to all amplitudes of the form (B.1).

In the first step, the completeness relation

$$1 = \int d\mathbf{r}_2 \cdots d\mathbf{r}_N |\mathbf{r}_2 \cdots \mathbf{r}_N\rangle \langle \mathbf{r}_2 \cdots \mathbf{r}_N| \quad (\text{B.3})$$

is inserted into Eq. (B.2) and Eq. 2.25 is used to obtain

$$\begin{aligned} A_{<}^{*-}(\mathbf{r}) &= \left\langle \Psi_{\nu}^{(N-1)} \left| \hat{\psi}_{<}^{\dagger}(\mathbf{r}) \times 1 \right| \Psi_0^{(N)} \right\rangle \\ &= \sqrt{N} \int d\mathbf{r}_2 \cdots d\mathbf{r}_N \Psi_{\nu}^{*(N-1)}(\mathbf{r}_2, \cdots, \mathbf{r}_N) \Psi_0^{(N)}(\mathbf{r}, \mathbf{r}_2, \cdots, \mathbf{r}_N). \end{aligned} \quad (\text{B.4})$$

Next, the explicit form of the Slater determinants (1.6) is used to derive

$$A_{<}^{*-}(\mathbf{r}) = \sqrt{N} [\varepsilon_{(\nu)}]^{\alpha_2 \cdots \alpha_N} [\varepsilon_{(0)}]^{i_1 \cdots i_N} \phi_{i_1}(\mathbf{r}) \langle \phi_{\alpha_2} | \phi_{i_2} \rangle \cdots \langle \phi_{\alpha_N} | \phi_{i_N} \rangle, \quad (\text{B.5})$$

B. NON-INTERACTING LEHMAN AMPLITUDES

where the indices $\alpha_2, \dots, \alpha_N$ and i_1, \dots, i_N are restricted to the sets

$$\alpha_2, \dots, \alpha_N \in I_\nu^{(N-1)} \quad \text{and} \quad i_2, \dots, i_N \in I_0^{(N)}. \quad (\text{B.6})$$

The orthogonality of the Bloch functions (1.10) implies that Eq. (B.5) reduces to

$$A_{<}^{*-1}(\mathbf{r}) = \sqrt{N} [\varepsilon(\nu)]^{\alpha_2 \dots \alpha_N} [\varepsilon(0)]^{i_1}_{\alpha_2 \dots \alpha_N} \phi_{i_1}(\mathbf{r}). \quad (\text{B.7})$$

The contraction of the Levi-Civita tensors can be determined by writing explicitly

$$[\varepsilon(0)]^{i_1}_{\alpha_2 \dots \alpha_N} = \sum_{j \in I_0^{(N)}} \delta_j^{i_1} [\varepsilon(0)]^j_{\alpha_2 \dots \alpha_N} \quad (\text{B.8})$$

and using the saturated contraction formula (see Ref. 47)

$$[\varepsilon(\nu)]^{\alpha_1 \dots \alpha_N} [\varepsilon(\nu)]_{\alpha_1 \dots \alpha_N} = N! \quad (\text{B.9})$$

for each term in (B.8). This results in

$$[\varepsilon(\nu)]^{\alpha_2 \dots \alpha_N} [\varepsilon(0)]^{i_1}_{\alpha_2 \dots \alpha_N} = \frac{(-1)^{1+|i_1|}}{\sqrt{N}} \delta_\nu^{i_1}, \quad i_1 \in I_0^{(N)}, \nu \in I_0^{(N)} \setminus \{i_1\}, \quad (\text{B.10})$$

where $|i_1|$ denotes the position of the index i_1 in the set $I_0^{(N)}$. The restriction on the indices in combination with Eq. (B.7) shows that

$$A_{<}^{*-}(\mathbf{r}) = (-1)^{1+|\nu|} \phi_\nu(\mathbf{r}) \Theta(-\epsilon_\nu), \quad \nu \in I_0^{(N)} \cap I_\nu^{(N-1)} \quad (\text{B.11})$$

This result is generalized straightforwardly to other matrix elements (B.1), such as

$$A_{>}^{*+}(\mathbf{r}) = \left\langle \Psi_\nu^{(N+1)} \left| \hat{\psi}_{>}(\mathbf{r}) \right| \Psi_0^{(N)} \right\rangle^* = (-1)^{1+|\nu|} \phi_\nu^*(\mathbf{r}) \Theta(\epsilon_\nu), \quad \nu \in I_0^{(N)} \cap I_\nu^{(N+1)} \quad (\text{B.12})$$

A last remark is in place here. The factor $(-1)^{1+|\nu|}$ always drops out in the Lehman representation of the Green's function (2.49), because only absolute values of the amplitudes (B.1) contribute.

Appendix C

Functional Integral Identities

The Gaussian integral formula

$$\int_{-\infty}^{\infty} \frac{dp}{2\pi} e^{-\lambda p^2} = \frac{1}{\sqrt{2\pi\lambda}}, \quad \lambda \in \mathbb{R} \quad (\text{C.1})$$

can be generalized to

$$\int_{-\infty}^{\infty} \frac{d^n \mathbf{p}}{(2\pi)^n} e^{-\frac{1}{2} \mathbf{p} \cdot \mathbf{V} \cdot \mathbf{p} + \mathbf{j} \cdot \mathbf{p}} = \frac{e^{\frac{1}{2} \mathbf{j} \cdot \mathbf{V}^{-1} \cdot \mathbf{j}}}{\sqrt{|\mathbf{V}|} (2\pi)^n}, \quad \mathbf{j} \in \mathbb{R}^n \quad (\text{C.2})$$

where \mathbf{V} is a real matrix with non-zero determinant $|\mathbf{V}|$ of dimension $n \times n$. Similarly, one has for complex variables[47]

$$\int \frac{d^n \mathbf{z}^*}{(2\pi i)^{\frac{n}{2}}} \frac{d^n \mathbf{z}}{(2\pi i)^{\frac{n}{2}}} e^{-\mathbf{z}^* \cdot \mathbf{H} \cdot \mathbf{z} + \mathbf{j}^* \cdot \mathbf{z} + \mathbf{z}^* \cdot \mathbf{j}} = \frac{e^{\mathbf{j}^* \cdot \mathbf{H} \cdot \mathbf{j}}}{|\mathbf{H}|}, \quad (\text{C.3})$$

where \mathbf{H} is a non-singular hermitian matrix of dimension $n \times n$.

C.1 Grassmann Algebra

Grassman numbers are defined by

$$\psi_1 \psi_2 = -\psi_2 \psi_1, \quad (\text{C.4})$$

so that

$$\psi^2 = 0. \quad (\text{C.5})$$

C. FUNCTIONAL INTEGRAL IDENTITIES

Due to this property the power series of an analytic functions f in ψ contains only two terms

$$f(\psi) = f(0) + f'(0)\psi, \quad (\text{C.6})$$

respectively four terms for a function in ψ and ψ^*

$$A(\psi^*, \psi) = A(0, 0) + \partial_1 A(0, \psi)\psi^* + \partial_2 A(\psi^*, 0)\psi + \partial_1 \partial_2 A(0, 0)\psi^*\psi^*. \quad (\text{C.7})$$

Here one defines the derivative as

$$\frac{\partial}{\partial \psi^*} (\psi^* \psi) = \psi \quad (\text{C.8})$$

implying that following identities hold

$$\frac{\partial}{\partial \psi} (\psi^* \psi) = -\frac{\partial}{\partial \psi} (\psi \psi^*) = -\psi^* \quad (\text{C.9})$$

$$\frac{\partial^2}{\partial \psi^2} = -\frac{\partial^2}{\partial \psi^2} = 0. \quad (\text{C.10})$$

The integration is defined as the inverse of the derivative as

$$\int d\psi \psi = 1, \quad \int d\psi = 0, \quad (\text{C.11})$$

which yields for Eqs. (C.6) and (C.7)

$$\int d\psi f(\psi) = f'(0), \quad \int d\psi A(\psi^*, \psi) = \partial_2 A - \partial_1 \partial_2 \psi^*. \quad (\text{C.12})$$

Gaussian integrals of Grassman variables are evaluated trivially by

$$\int d\psi^* d\psi e^{-\psi^* \lambda \psi} = \int d\psi^* d\psi (1 - \psi^* \lambda \psi) = \lambda \quad (\text{C.13})$$

and the generalization of this result to vectors yields[39, 47]

$$\int d\psi^* d\psi e^{-\psi^* \cdot \mathbf{H} \cdot \psi + \mathbf{j}^* \cdot \psi + \psi \cdot \mathbf{j}} = |\mathbf{H}| e^{\mathbf{j} \cdot \mathbf{H}^{-1} \cdot \mathbf{j}}, \quad (\text{C.14})$$

where \mathbf{R} is a matrix with determinant $|\mathbf{R}|$ and \mathbf{j}, \mathbf{j}^* arbitrary Grassmann vectors.

C.2 Hubbard-Strotonovich Transformation

Replacing $\mathbf{j} \rightarrow \pm i\boldsymbol{\rho}$, $\mathbf{V} \rightarrow \mathbf{V}^{-1}$ and writing ϕ instead of p in Eq. (C.2) yields the useful identity

$$e^{-\frac{1}{2}\boldsymbol{\rho}\cdot\mathbf{V}\cdot\boldsymbol{\rho}} = \frac{1}{\sqrt{|\mathbf{V}|}(2\pi)^n} \int_{-\infty}^{\infty} d^n\phi e^{-\frac{1}{2}\phi\cdot\mathbf{V}^{-1}\cdot\phi \pm i\boldsymbol{\rho}\cdot\phi}, \quad \boldsymbol{\rho} \in \mathbb{R}^n \quad (\text{C.15})$$

where $\boldsymbol{\rho} = (\rho_1, \dots, \rho_n)$ is an n dimensional vector. This identity is known as Hubbard-Strotonovich transformation[76] and allows to decouple the Coulomb interaction term in partition functions by means of introducing additional degrees of freedom, described by ϕ .

C. FUNCTIONAL INTEGRAL IDENTITIES

Appendix D

Analytic Continuation of Spectral Functions

In section 2.4.1, we have seen that the retarded propagator (2.69) and the Feynman propagator (2.68) of the non-interacting system are only different branches of a more general function f . Looking at the Lehman representation (4.59), it becomes evident that the analyticity holds true for the interacting case as well.[35] That is, the interacting Feynman and retarded propagators $G(\mathbf{r}', \mathbf{r}, \omega)$, $G_r(\mathbf{r}', \mathbf{r}, \omega)$ correspond to specific branches of a more general function $F(\mathbf{r}', \mathbf{r}, z)$.

Consequently, by analytic continuation of the Feynman or retarded propagator to complex frequencies z one obtains all branches of the function $F(\mathbf{r}', \mathbf{r}, z)$, where the branch cut of the function F is located at $z \in \mathbb{R}$. This is insofar of interest, because only the retarded Green's function G_r is measurable. More precisely, the spectral density function \mathcal{A}_r of the retarded propagator G_r , defined implicitly by the Hilbert transform

$$G_r(\mathbf{r}', \mathbf{r}, z) = \int \frac{d\omega'}{\pi} \frac{\mathcal{A}_r(\mathbf{r}', \mathbf{r}, \omega')}{z - \omega' - i\eta}, \quad z \in \mathbb{C}, \eta \rightarrow 0 \quad (\text{D.1})$$

can be measured only for real frequencies ω' , *e.g.* using the angle resolved photoemission spectroscopy (ARPES) method, see Refs. 181, 182 for more details about the measuring principle.

In contrast DMFT or the GWA provides access to the time-ordered propagator G only. A comparison of theoretical with experimental data is, therefore, only possible for real frequencies. This is problematic if DMFT (or GW) calculations are performed on the imaginary frequency line yielding $\{G(i\omega_n)\}_{n=1}^{N_\omega}$ for a finite set of imaginary frequency (or

D. ANALYTIC CONTINUATION OF SPECTRAL FUNCTIONS

time) points. The reason for this is, that mathematically the extraction of the spectral density function $\mathcal{A}_r(\omega)$ on the real frequency axis from a finite set of points $\{G(i\omega_n)\}_{n=1}^{N_\omega}$ can be formulated as the inversion of a Laplace transform.[183] The latter is known to be an ill-posed problem, implying that the reconstruction of the spectral density function cannot be done unambiguously for the complete real frequency line.

Fortunately, in the neighborhood of the chemical potential $z = \mu$ (which in our case is chosen to be 0) the spectral density function can be recast sufficiently accurate with various methods. At this point, the interested reader is referred to the literature, *e.g.* Refs. 172, 183, 184, 185.

Appendix E

Interaction Matrices for La_2CuO_4 and the 3d TM series

This appendix list additional effective interactions for the TM series Sc-Ni and the superconductor La_2CuO_4 .

Table E.1: Bare, fully and effectively screened exchange interaction J in [eV] for transition metals in model (iii).

Sc	Ti	V	Cr	Mn	Fe	Co	Ni
0.5	0.6	0.6	0.7	0.7	0.8	0.8	0.8
0.3	0.4	0.4	0.4	0.5	0.5	0.5	0.6
0.4	0.4	0.6	0.6	0.6	0.6	0.7	0.7

E. INTERACTION MATRICES FOR La_2CuO_4 AND THE 3D TM SERIES

Table E.2: Bare interaction matrices $V_{\alpha\alpha\beta\beta}$ and $V_{\alpha\beta\alpha\beta}$ in La_2CuO_4 .

	d_{xy}	d_{xz}	d_{yz}	$d_{x^2-y^2}$	d_{z^2}	d_{xy}	d_{xz}	d_{yz}	$d_{x^2-y^2}$	d_{z^2}
d_{xy}	27.1	25.7	25.7	25.5	24.9	27.1	0.7	0.7	1.2	1.1
d_{zy}	25.7	27.0	25.0	25.8	25.2	0.7	27.0	1.0	1.0	1.0
d_{yz}	25.7	25.0	27.0	25.8	25.2	0.7	1.0	27.0	1.0	1.0
$d_{x^2-y^2}$	25.5	25.8	25.8	28.7	27.0	1.2	1.0	1.0	28.7	0.6
d_{z^2}	24.9	25.2	25.2	27.0	27.5	1.1	1.0	1.0	0.6	27.5

Table E.3: Fully screened interaction matrices $W_{\alpha\alpha\beta\beta}$ and $W_{\alpha\beta\alpha\beta}$ in La_2CuO_4 .

	d_{xy}	d_{xz}	d_{yz}	$d_{x^2-y^2}$	d_{z^2}	d_{xy}	d_{xz}	d_{yz}	$d_{x^2-y^2}$	d_{z^2}
d_{xy}	3.8	2.4	2.4	1.1	1.3	3.8	0.7	0.7	0.9	1.1
d_{zy}	2.4	3.5	1.8	1.3	1.4	0.7	3.5	0.9	0.9	0.9
d_{yz}	2.4	1.8	3.5	1.3	1.4	0.7	0.9	3.5	0.9	0.9
$d_{x^2-y^2}$	1.1	1.3	1.3	2.6	1.7	0.9	0.9	0.9	2.6	0.5
d_{z^2}	1.3	1.4	1.4	1.7	2.9	1.1	0.9	0.9	0.5	2.9

List of Figures

2.1	Complex frequency plane for $f(z)$ defined in (2.66) with branch cut (dashed line). Blue line: Feynman contour \mathcal{C}_F for the complex frequency plane. Red line: Contour for the retarded propagator (2.67). Contours are closed for negative (positive) times and occupied (unoccupied) energies $\epsilon_\mu < 0$ in upper (lower) half-plane.	28
2.2	Complex contour for the Wick rotation from real time t to imaginary time τ	35
2.3	Typical imaginary time-dependence of the non-interacting propagator G^0 illustrating the anti-periodicity property (2.114). Here a two-state model with one occupied state with energy $\epsilon_1 = -1.5$ eV and an unoccupied state with energy $\epsilon_2 = 2.3$ eV for a inverse temperature of $\beta = 10$ eV ⁻¹ is shown.	38
3.1	Labeled diagram for the interaction matrix element $G_\alpha^0 G_\beta^0 V^{\alpha\beta\gamma\delta} G_\gamma^0 G_\delta^0$	47
3.2	Hartree (right) and Fock diagram (left).	48
3.3	Ladder (left) and bubble (right) contraction as labeled diagrams.	48
3.4	Disconnected unlabeled diagrams in second order. The symmetry factors (from left to right) are 8, 4 and 8.	49
3.5	Second order irreducible, connected diagrams. With symmetry factors 4, 4, 2, 2, 1 (from left to right).	49

LIST OF FIGURES

3.6	Illustration of the symmetry factor of diagram A . Diagram B is obtained from A using Eq. (3.23) for the upper interaction line, whereas diagram C follows from B using the same identity for the lower one and diagram D is obtained from C after exchanging $\tau_1 \leftrightarrow \tau_2$. Only diagram A and D belong to the same equivalence class with symmetry factor $S_\gamma = 2$, because they are topologically the same directed graph.	50
3.7	Random Phase Approximation for the grand canonical potential.	52
3.8	Typical imaginary time-dependence of the independent-particle polarizability χ^0 illustrating the periodic property (3.28). Here a two-state model with one occupied state with energy $\epsilon_1 = -1.5$ eV and an unoccupied state with energy $\epsilon_2 = 2.3$ eV for a inverse temperature of $\beta = 10$ eV $^{-1}$ is shown.	54
4.1	Second order contributions to the interacting Feynman propagator.	59
4.2	Hedin scheme for the self-consistent solution of Eqs. (4.45)-(4.50).	69
5.1	Calculation scheme for the RPA correlation energy E_c^{RPA} adopted in this paper. The first and third step is a spatial FFT described in Sec. 5.3. The second step is the contraction of two Green's functions in the space-time domain (GG) giving the independent-particle polarizability χ (see Sec. 5.4). The CT in the fourth step is described in Sec. 5.2.3. The ACFDT is formulated in Eq. (3.37).	90
5.2	Least square error surface $\mathcal{E}(\gamma^0, \nu^0, \xi, \xi')$ measured in [eV $^{-1}$] for $\epsilon_{\min} = 1$, $\epsilon_{\max} = 10$ and $n = 3$. The largest errors are located along the diagonal $\xi = \xi'$	96
5.3	(a) Cosine transformation (CT) error $\min \ \eta^c\ _2$ as a function of the frequency ν for a MM time grid $\{\tau_i^*\}_{i=1}^N$ with transition energy ratio $R = 100$ and 5 grid points. (b) transformation error in the time domain $\min \ \hat{\eta}^c\ _2$ for the corresponding MM frequency grid. The error is minimal at the MM points ν_k^* in (a) and τ_i^* in (b) (red dots).	100
5.4	Minimax error functions for the time $\hat{\eta}$ (blue line) and frequency η (red line) domain for $R_7 = 28387$ and $n = 7$. Both functions decay strictly for $\xi > R_7$	101
5.5	Convergence of direct MP2 energy $E_c^{(2)}$ for the LS and MM quadratures for ZnO.	102

LIST OF FIGURES

5.6	Minimax (blue line) and least square error (red line) functions for $R = 500$ and $n = 7$ in the time (a) and frequency domain (b). For small ξ (dominating terms in χ and $\hat{\chi}$) the least square solution is more accurate.	103
5.7	Convergence of RPA correlation energy E_c^{RPA} for ZnO and Si w.r.t. the number of grid points n for the LS (red line) and MM (blue line) quadratures. If polarizabilities are determined by cosine transformations (CT) from the time to the frequency axis, larger errors are obtained (purple and green line).	104
5.8	Convergence of RPA correlation energy E_c^{RPA} for Al and Nb w.r.t. the number of grid points n for the LS (red line) and MM (blue line) quadratures. If polarizabilities are determined by cosine transformations (CT) from the time to the frequency axis similar errors are obtained (purple and green line).	106
5.9	Illustration of relation between reciprocal cell C^* (dark gray cell), k-point grid \mathcal{K}_c^* (red dots in dark gray square) and reciprocal supercell S^* (small light gray square) for a two dimensional cubic cell with $S = (2 \times 2)C$. The vector \mathbf{g} is a reciprocal lattice vector of C^* and \mathbf{G} is a reciprocal lattice vector of S^* . The set of all reciprocal lattice vectors \mathcal{L}_c^* is represented by big dots and is a subset of \mathcal{L}_s^* , the set of all reciprocal superlattice vectors (small and big dots). The k-point \mathbf{k} coincides with the reciprocal superlattice vector \mathbf{G}' and every vector $\mathbf{k} + \mathbf{g}$ can be represented by a reciprocal superlattice vector \mathbf{G} .	110
5.10	Symmetry of the Green's function matrix in real space $G(\mathbf{R}, \mathbf{R}')$ for a $S = (2 \times 2)C$ supercell with the irreducible stripe $G(\mathbf{r}, \mathbf{R}')$ (thick rectangle). Due to Eq. (5.40) the blocks below the diagonal are complex conjugated.	113
5.11	Computational time for 64, 128 and 216 atoms as a function of the number of k-points (in the full Brillouin zone). The total (wall clock) time is shown for 64, 128 and 224 cores. The computational demand increases linearly in the number of k-points and cubically in the number of atoms. The deviation from linearity is related to the need to double the number of cores for $3 \times 3 \times 3$ k-points (64 atoms) and $2 \times 2 \times 2$ k-points (128 atoms), and the non perfect scaling with the number of cores. The corresponding reported compute time has been doubled.	119

LIST OF FIGURES

6.1	Composite band of La_2CuO_4 consisting of 17 Bloch bands. Red bands indicate strong copper d-character, blue bands indicate strong oxygen p-character. The plot was obtained using the <code>Wannier90</code> library[142]	141
6.2	Bands of fcc Ni with d-character resolution obtained from <code>Wannier90</code> . Red bands indicate strong d-character, blue bands indicate strong s-character. (a) d-character resolution in ds basis. (b) Comparison of disentangled system (red and blue bands) with original system (gray bands) in d basis.	150
6.3	Average spread of Wannier d-functions of the TM series in the d (squares) and ds (points) basis. For comparison data of Ref. 153 (†) is given for the d basis.	151
6.4	Bare Coulomb repulsion V in [eV] of 3d TMs series in d (a) and ds basis (b). For comparison Ref.#146, Ref.†153, Ref.§145 and Ref.‡155 are given	152
6.5	(a) On-site fully screened d-Coulomb repulsion measured in [eV] in d basis of disentangled (squares) and original Kohn-Sham system (circles). (b) Full RPA interaction of original system in ds basis. For comparison Ref.◇147, Ref.§145 and Ref.‡155 are shown.	153
6.6	On-site effective d-Coulomb repulsion U in [eV] for different models. (a) model (i), disentanglement method in basis d . (b) model (ii), weighted CRPA method in ds basis. For comparison Ref.◇147 Ref.†153, Ref.‡155 Ref.§145 and Ref.#146 are shown.	154
6.7	Comparison of present CRPA approach, model (iii) (red points), with disentangling (i) and weighted method (ii).	155
6.8	Frequency dependence of effectively screened interaction for fcc Ni and bcc Cr in model (i) (blue), model (ii) (green) and model (iii) (solid line). The gray line shows analytically continued data of model (ii) published in Ref. 155.	156
6.9	Left: Crystal structure of SrVO_3 . Sr atoms (green) are located between the oxygen crystal fields indicated by red octahedra with a V atom in the center. Right: Band structure of SrVO_3 . The three t_{2g} -states of V cross the chemical potential chosen at $\mu = 0$ eV.	160

LIST OF FIGURES

6.10 (Color online) Left panel: G_0W_0 quasi particle bands (red) in comparison to LDA (gray). The Fermi level sets our zero of energy and is marked as a line. Right panel: Wannier projected t_{2g} band structure from G_0W_0 (red) and LDA (gray). The t_{2g} target bands bandwidth is reduced by ~ 0.7 eV in GW	163
6.11 Comparison of the imaginary part of the DMFT t_{2g} self-energies Σ vs (Matsubara) frequency ω for SrVO_3 at inverse temperature $\beta = 40$ eV ¹ as computed in five different ways: employing qp GW and LDA Wannier bands, the locally unscreened RPA interaction $U'^{nl} = 2.49$ eV and the CLDA $U'^{CLDA} = 3.55$ eV, as well as the $\mathcal{Z}_B = 0.7$ renormalization.[175].	166
6.12 Spectral function for SrVO_3 (t_{2g} orbitals only) computed in five different ways as in Fig. 6.11. At lower temperatures the central peak gets only slightly sharper and higher, although the temperature effects from $\beta = 25$ to 40 eV ⁻¹ are small.	168
6.13 Comparison of LDA+DMFT@ U'^{CLDA} , qp GW +DMFT@ U'^{nl} (without and with Bose renormalization $\mathcal{Z}_B = 0.7$), and experiment. The position of the lower Hubbard band is better reproduced in qp GW +DMFT, whereas the central peak is similar in LDA+DMFT and qp GW +DMFT. The Bose renormalization qp GW +DMFT differs considerably (photoemission spectra reproduced from Ref. 167).	169

LIST OF FIGURES

List of Tables

5.1	Timings in minutes for an RPA calculation for different bulk Si bcc cells. The calculations are done for the Γ point only and the number of cores is increased with system size. Since one of the computational steps scales only quadratically with system size, the total scaling is better than cubic.	121
5.2	The second, third and fourth columns report the difference between RPA and PBE formation energies for different defect configurations, k-points and supercells, with the k-point set indicated in the first row (all values in eV). The second row in each set reports the k-point convergence of the PBE formation energies. The columns PBE and RPA report the final converged formation energies. The RPA value was calculated by adding the most accurate corrections to the k-point converged PBE values. The range separated rsRPA values are from Ref. 121, and the values for HSE+vdW are from Ref. 120.	123
6.1	Used structures for the TM series. Lattice constants are given in \AA and obtained from PBE.	148
6.2	Atomic positions in La_2CuO_4 in direct coordinates	148
6.3	Used energy windows in [eV] for the construction of the d basis in the 3d series. The Fermi level is set to 0 eV.	150
6.4	Used models.	151
6.5	Effective Hubbard interaction matrices $U_{\alpha\alpha\beta\beta}$ and $U_{\alpha\beta\alpha\beta}$ for La_2CuO_4 obtained with model (iii).	157
6.6	On-site bare (\mathbf{V}), fully screened RPA (\mathbf{W}), constrained RPA \mathbf{U}^{CRPA} and unscreening interaction (\mathbf{U}).	161

LIST OF TABLES

6.7 DMFT quasi particle renormalization factors Z from the five different calculations at inverse temperature $\beta = 40 \text{ eV}^{-1}$. Also shown are the pairwise double occupations within the same orbital d_{intra} and between different orbitals with the same $d_{\text{inter}}^{\uparrow\uparrow}$ and opposite spin $d_{\text{inter}}^{\uparrow\downarrow}$. The 'standard' LDA+DMFT@ U'^{CLDA} and qpGW+DMFT@ U'^{nl} calculations are similarly correlated and agree well with experiment. Using the CLDA interaction U'^{CLDA} for qpGW+DMFT or the locally unscreened RPA U'^{nl} for LDA+DMFT yields a too strongly and too weakly correlated solution in comparison to experiment, respectively. Note that qpGW+DMFT becomes even more strongly correlated if the Bose renormalization factor is included. 167

E.1 Bare, fully and effectively screened exchange interaction J in [eV] for transition metals in model (iii). 191

E.2 Bare interaction matrices $V_{\alpha\alpha\beta\beta}$ and $V_{\alpha\beta\alpha\beta}$ in La_2CuO_4 192

E.3 Fully screened interaction matrices $W_{\alpha\alpha\beta\beta}$ and $W_{\alpha\beta\alpha\beta}$ in La_2CuO_4 192

References

- [1] J. C. SLATER. **The Theory of Complex Spectra.** *Phys. Rev.*, **34**:1293–1322, 1929. 5
- [2] C.B. LANG AND N. PUCKER. *Mathematische Methoden in der Physik.* Spektrum Akademischer Verlag, 2005. 5
- [3] P. LÖWDIN. **On the NonOrthogonality Problem Connected with the Use of Atomic Wave Functions in the Theory of Molecules and Crystals.** *J. Chem. Phys.*, **18**:365–375, 1950. 6
- [4] J. KOHANOFF. *Electronic structure calculations for solids and molecules.* Cambridge University Press, 2006. 6, 12, 14, 16
- [5] A. SZABO AND N.S. OSTLUND. *Modern Quantum Chemistry: Introduction to Advanced Electronic Structure Theory.* Dover Publications, 1996. 8
- [6] P. HOHENBERG AND W. KOHN. **Inhomogeneous electron gas.** *Phys. Rev.*, **136**:B864–B871, 1964. 8
- [7] R.M. MARTIN. *Electronic Structure: Basic Theory and Practical Methods.* Cambridge University Press, 2004. 8, 16, 109
- [8] W. KOHN AND L.J. SHAM. **Self-consistent equations including exchange and correlation effects.** *Phys. Rev.*, **140**:A1133–A1138, 1965. 11, 12
- [9] A. GÖRLING. **Density-functional theory for excited states.** *Phys. Rev. A*, **54**:3912–3915, 1996. 12
- [10] R. G. PARR AND R. G. P. W. YANG. *Density-Functional Theory of Atoms and Molecules.* Oxford University Press, USA, 1989. 13, 14
- [11] P. A. M. DIRAC. **Note on Exchange Phenomena in the Thomas Atom.** *Mathematical Proceedings of the Cambridge Philosophical Society*, **26**:376–385, 1930. 13
- [12] M. GELL-MANN AND K. A. BRUECKNER. **Correlation Energy of an Electron Gas at High Density.** *Phys. Rev.*, **106**:364–368, 1957. 13, 52, 135
- [13] F. SEITZ AND D. TURNBULL. *Solid State Physics.* Academic Press, New York, 1955. 13
- [14] E. WIGNER. **Effects of the electron interaction on the energy levels of electrons.** *Trans. Faraday Soc.*, **34**:678–685, 1938. 13
- [15] W. J. CARR. **Energy, Specific Heat, and Magnetic Properties of the Low-Density Electron Gas.** *Phys. Rev.*, **122**:1437–1446, 1961. 13
- [16] P. NOZIÈRES AND D. PINES. **Correlation Energy of a Free Electron Gas.** *Phys. Rev.*, **111**:442–454, 1958. 13, 135
- [17] D. M. CEPERLEY AND B. J. ALDER. **Ground State of the Electron Gas by a Stochastic Method.** *Phys. Rev. Lett.*, **45**:566–569, 1980. 14
- [18] S. H. VOSKO, L. WILK, AND M. NUSAIR. **Accurate spin-dependent electron liquid correlation energies for local spin density calculations: a critical analysis.** *Canadian Journal of Physics*, **58**:1200–1211, 1980. 14
- [19] J. P. PERDEW, K. BURKE, AND M. ERNZERHOF. **Generalized Gradient Approximation Made Simple.** *Phys. Rev. Lett.*, **77**:3865–3868, 1996. 15, 105, 117
- [20] J. P. PERDEW, A. RUZSINSZKY, G. I. CSONKA, O. A. VYDROV, G. E. SCUSERIA, L. A. CONSTANTIN, X. ZHOU, AND K. BURKE. **Restoring the Density-Gradient Expansion for Exchange in Solids and Surfaces.** *Phys. Rev. Lett.*, **100**:136406, 2008. 15
- [21] D. HANNEKE, S. FOGWELL, AND G. GABRIELSE. **New Measurement of the Electron Magnetic Moment and the Fine Structure Constant.** *Phys. Rev. Lett.*, **100**:120801, 2008. 17
- [22] D. PINES. *The many-body problem: a lecture note and reprint volume.* Frontiers in physics. W. A. Benjamin, 1962. 17
- [23] L. PARKER AND D. TOMS. *Quantum Field Theory in Curved Spacetime: Quantized Fields and Gravity.* Cambridge Monographs on Mathematical Physics. Cambridge University Press, 2009. 19, 20
- [24] M. E. PESKIN AND D. V. SCHROEDER. *An Introduction to Quantum Field Theory.* Advanced book classics. Addison-Wesley Publishing Company, 1995. 19, 67, 177
- [25] J. D. BJORKEN AND S. D. DRELL. *Relativistic quantum mechanics.* International series in pure and applied physics. McGraw-Hill, 1964. 19, 177, 179, 181
- [26] O. KLEIN. **Die Reflexion von Elektronen an einem Potentialsprung nach der relativistischen Dynamik von Dirac.** *Zeitschrift für Physik*, **53**:157–165, 1929. 19
- [27] M. REED AND B. SIMON. *Methods of Modern Mathematical Physics: Functional analysis.* Number Bd. 1 in Methods of Modern Mathematical Physics. Academic Press, 1980. 20
- [28] W. PAULI. **The Connection Between Spin and Statistics.** *Phys. Rev.*, **58**:716–722, 1940. 21
- [29] K. FREDENHAGEN. *Quantum field theory.* Lecture Notes, 2009. 21
- [30] N. D. BIRRELL AND P. C. W. DAVIES. *Quantum Fields in Curved Space.* Cambridge Monographs on Mathematical Physics. Cambridge University Press, 1984. 23, 36
- [31] A. SALAM. **The Field Theory of Superconductivity.** *Progress of Theoretical Physics*, **9**:550–554, 1953. 23, 24

REFERENCES

- [32] J. HUBBARD. **The Description of Collective Motions in Terms of Many-Body Perturbation Theory.** *Proceedings of the Royal Society of London A: Mathematical, Physical and Engineering Sciences*, **240**:539–560, 1957. 24, 48, 62
- [33] R. D. MATTUCK. *A Guide to Feynman Diagrams in the Many-body Problem.* Dover Books on Physics Series. Dover Publications, 1976. 24, 52, 59, 60, 61, 62, 105
- [34] A. L. FETTER AND J. D. WALECKA. *Quantum Theory of Many-particle Systems.* Dover Books on Physics. Dover Publications, 2003. 24, 30, 31, 32, 33, 45, 46, 50, 59, 60, 62, 63, 66, 67, 140
- [35] V. M. GALITSKII AND A. B. MIGDAL. **Application of Quantum Field Theory methods to the Many Body Problem.** *J. Exptl. Theoret. Phys. (U.S.S.R.)*, **34**:139–150, 1958. 25, 70, 189
- [36] C. M. DEWITT AND B. S. DEWITT. *Dynamical theory of groups and fields.* Documents on modern physics. Gordon and Breach, 1965. 26, 27
- [37] V. MUKHANOV AND S. WINITZKI. *Introduction to Quantum Effects in Gravity.* Cambridge University Press, 2007. 26
- [38] A. D. POLYANIN AND A. V. MANZHROV. *Handbook of Integral Equations: Second Edition.* Handbooks of mathematical equations. CRC Press, 2012. 31, 32
- [39] J. W. NEGELE AND H. ORLAND. *Quantum Many-particle Systems.* Advanced Books Classics. Westview Press, 2008. 31, 40, 48, 50, 51, 52, 58, 73, 74, 75, 78, 186
- [40] M. GELL-MANN AND F. LOW. **Bound States in Quantum Field Theory.** *Phys. Rev.*, **84**:350–354, 1951. 32, 33
- [41] L. G. MOLINARI. **Another proof of Gell-Mann and Lows theorem.** *Journal of Mathematical Physics*, **48**:052113, 2007. 33
- [42] C. BROUDER, G. STOLTZ, AND G. PANATI. **Adiabatic approximation, Gell-Mann and Low theorem, and degeneracies: A pedagogical example.** *Phys. Rev. A*, **78**:042102, 2008. 33
- [43] G. WICK. **Properties of Bethe-Salpeter Wave Functions.** *Phys. Rev.*, **96**:1124–1134, 1954. 35
- [44] G. STEFANUCCI AND R. VAN LEEUWEN. *Nonequilibrium Many-Body Theory of Quantum Systems: A Modern Introduction.* Cambridge University Press, 2013. 36, 40, 57, 66
- [45] H. BRUUS AND K. FLENSBERG. *Many-Body Quantum Theory in Condensed Matter Physics: An Introduction.* OUP Oxford, 2004. 36, 37, 39
- [46] A. A. ABRIKOSOV, L. P. GORKOV, AND I. E. DZIALOSHINSKI. *Methods of Quantum Field Theory in Statistical Physics.* Dover Books on Physics Series. Dover Publications, 1975. 39, 40, 45, 46, 50
- [47] R. A. BERILMANN. *Anomalies in Quantum Field Theory.* Clarendon Press, 2000. 40, 74, 75, 142, 184, 185, 186
- [48] R. FEYNMAN. **The Theory of Positrons.** *Phys. Rev.*, **76**:749–759, 1949. 47
- [49] J. GOLDSTONE. **Derivation of the Brueckner Many-Body Theory.** *Proceedings of the Royal Society of London A: Mathematical, Physical and Engineering Sciences*, **239**:267–279, 1957. 50
- [50] D. C. LANGRETH AND J. P. PERDEW. **Exchange-correlation energy of a metallic surface: Wave-vector analysis.** *Phys. Rev. B*, **15**:2884–2901, 1977. 55
- [51] S. ADLER. **Quantum Theory of the Dielectric Constant in Real Solids.** *Phys. Rev.*, **126**:413–420, 1962. 55
- [52] N. WISER. **Dielectric Constant with Local Field Effects Included.** *Phys. Rev.*, **129**:62–69, 1963. 55
- [53] H. N. ROJAS, R. W. GODBY, AND R. J. NEEDS. **Space-Time Method for Ab Initio Calculations of Self-Energies and Dielectric Response Functions of Solids.** *Phys. Rev. Lett.*, **74**:1827–1830, 1995. 55, 72, 114
- [54] D. FOERSTER, P. KOVAL, AND D. SANCHEZ-PORTAL. **An $O(N^3)$ implementation of Hedin’s GW approximation for molecules.** *J. Chem. Phys.*, **135**:074105, 2011. 55
- [55] J. E. MOUSSA. **Cubic-scaling algorithm and self-consistent field for the random-phase approximation with second-order screened exchange.** *J. Chem. Phys.*, **140**:014107, 2014. 55
- [56] L. HEDIN. **New Method for Calculating the One-Particle Green’s Function with Application to the Electron-Gas Problem.** *Phys. Rev.*, **139**:A796–A823, 1965. 57, 60, 62, 63, 64, 65, 66, 68, 69
- [57] R. STARKE AND G. KRESSE. **Self-consistent Green function equations and the hierarchy of approximations for the four-point propagator.** *Phys. Rev. B*, **85**:075119, 2012. 57, 67
- [58] F. J. DYSON. **The S Matrix in Quantum Electrodynamics.** *Phys. Rev.*, **75**:1736–1755, 1949. 59, 61
- [59] V. B. BERESTETSKII, L. P. PITAEVSKII, AND E. M. LIFSHITZ. *Quantum Electrodynamics.* Number 4 in Course of Theoretical Physics. Elsevier Science, 2012. 61, 179
- [60] F. SCHECK. *Quantisierte Felder. Von den Symmetrien zur Quantenelektrodynamik.* Number 4 in Theoretische Physik. Springer London, Limited, 2007. 61, 177
- [61] E. E. SALPETER AND H. A. BETHE. **A Relativistic Equation for Bound-State Problems.** *Phys. Rev.*, **84**:1232–1242, 1951. 66
- [62] G. ONIDA, L. REINING, AND A. RUBIO. **Electronic excitations: density-functional versus many-body Green’s-function approaches.** *Rev. Mod. Phys.*, **74**:601–659, 2002. 67, 68, 69
- [63] F. J. DYSON. **The Radiation Theories of Tomonaga, Schwinger, and Feynman.** *Phys. Rev.*, **75**:486–502, 1949. 67
- [64] M. S. HYBERTSEN AND S. G. LOUIE. **Electron correlation in semiconductors and insulators: Band gaps and quasiparticle energies.** *Phys. Rev. B*, **34**:5390–5413, 1986. 68, 70, 71

REFERENCES

- [65] M. SHISHKIN, M. MARSMAN, AND G. KRESSE. **Accurate Quasiparticle Spectra from Self-Consistent GW Calculations with Vertex Corrections.** *Phys. Rev. Lett.*, **99**:246403, 2007. 69, 162
- [66] F. ARYASETIAWAN AND O. GUNNARSSON. **The GW method.** *Reports on Progress in Physics*, **61**:237, 1998. 69
- [67] O. PULCI, G. ONIDA, R. DEL SOLE, AND L. REINING. **Ab Initio Calculation of Self-Energy Effects on Optical Properties of GaAs(110).** *Phys. Rev. Lett.*, **81**:5374–5377, 1998. 69, 71, 72
- [68] M. STRANGE, C. ROSTGAARD, H. HÄKINEN, AND K. S. THYGESEN. **Self-consistent GW calculations of electronic transport in thiol- and amine-linked molecular junctions.** *Phys. Rev. B*, **83**:115108, 2011. 69, 71, 72
- [69] L. STEINBECK, A. RUBIO, L. REINING, M. TORRENT, I. D. WHITE, AND R. W. GODBY. **Enhancements to the GW space-time method.** *Computer Physics Communications*, **125**:105 – 118, 2000. 72, 90, 111, 114, 116
- [70] X. REN, P. RINKE, V. BLUM, J. WIEFERINK, A. TKATCHENKO, A. SANFILIPPO, K. REUTER, AND M. SCHEFFLER. **Resolution-of-identity approach to Hartree-Fock, hybrid density functionals, RPA, MP2 and GW with numeric atom-centered orbital basis functions.** *New J. Phys.*, **14**:053020, 2012. 72
- [71] J. SCHWINGER. *Selected Papers on Quantum Electrodynamics.* Dover Publications, 1958. 73
- [72] R. P. FEYNMAN. **Space-Time Approach to Non-Relativistic Quantum Mechanics.** *Rev. Mod. Phys.*, **20**:367–387, 1948. 73
- [73] T. AYRAL, S. BIERMANN, AND P. WERNER. **Screening and nonlocal correlations in the extended Hubbard model from self-consistent combined GW and dynamical mean field theory.** *Phys. Rev. B*, **87**:125149, 2013. 77, 82, 83, 85
- [74] A. GEORGES, G. KOTLIAR, W. KRAUTH, AND M. J. ROZENBERG. **Dynamical mean-field theory of strongly correlated fermion systems and the limit of infinite dimensions.** *Rev. Mod. Phys.*, **68**:13–125, 1996. 77, 81, 85
- [75] W. KOHN. **Construction of Wannier Functions and Applications to Energy Bands.** *Phys. Rev. B*, **7**:4388–4398, 1973. 77, 136
- [76] J. HUBBARD. **Calculation of Partition Functions.** *Phys. Rev. Lett.*, **3**:77–78, 1959. 79, 187
- [77] J. HUBBARD. **Electron Correlations in Narrow Energy Bands.** *Royal Society of London Proceedings Series A*, **276**:238–257, 1963. 83
- [78] H. TASAKI. **The Hubbard model - an introduction and selected rigorous results.** *Journal of Physics: Condensed Matter*, **10**(20):4353, 1998. 83
- [79] N. ANDREI. **Diagonalization of the Kondo Hamiltonian.** *Phys. Rev. Lett.*, **45**:379–382, 1980. 84
- [80] H. BETHE. **Zur Theorie der Metalle.** *Zeitschrift für Physik*, **71**:205–226, 1931. 84
- [81] W. METZNER AND D. VOLLHARDT. **Correlated Lattice Fermions in $d = \infty$ Dimensions.** *Phys. Rev. Lett.*, **62**:324–327, 1989. 84, 85
- [82] E. PAVARINI, E. KOCH, D. VOLLHARDT, AND A. LICHTENSTEIN. *DMFT at 25: Infinite Dimensions.* Modeling and Simulation. Forschungszentrum Jülich Zentralbibliothek, Verlag, 2014. 84
- [83] K. HELD. **Electronic structure calculations using dynamical mean field theory.** *Advances in Physics*, **56**:829–926, 2008. 86, 159, 164
- [84] E. PAVARINI, E. KOCH, D. VOLLHARDT, AND A. LICHTENSTEIN. *The LDA+DMFT approach to strongly correlated materials.* Forschungszentrum, Zentralbibliothek, 2011. 86
- [85] K. HELD, I. A. NEKRASOV, G. KELLER, V. EYERT, N. BLÜMER, A. K. McMAHAN, R. T. SCALETTAR, T. PRUSCHKE, V. I. ANISIMOV, AND D. VOLLHARDT. **Realistic investigations of correlated electron systems with LDA + DMFT.** *Physica Status Solidi (b)*, **243**:2599–2631, 2006. 86
- [86] M. KAROLAK, G. ULM, T. WEHLING, V. MAZURENKO, A. POTERYAEV, AND A. LICHTENSTEIN. **Double counting in LDA+DMFT - The example of NiO.** *Journal of Electron Spectroscopy and Related Phenomena*, **181**:11 – 15, 2010. 86
- [87] S. BIERMANN, F. ARYASETIAWAN, AND A. GEORGES. **First-Principles Approach to the Electronic Structure of Strongly Correlated Systems: Combining the GW Approximation and Dynamical Mean-Field Theory.** *Phys. Rev. Lett.*, **90**:086402, 2003. 86, 131
- [88] M. KALTAK, J. KLIMEŠ, AND G. KRESSE. **Low Scaling Algorithms for the Random Phase Approximation: Imaginary Time and Laplace Transformations.** *Journal of Chemical Theory and Computation*, **10**:2498–2507, 2014. 89, 90, 104
- [89] M. KALTAK, J. KLIMEŠ, AND G. KRESSE. **Cubic scaling algorithm for the random phase approximation: Self-interstitials and vacancies in Si.** *Phys. Rev. B*, **90**:054115, 2014. 89, 109
- [90] J. HARL AND G. KRESSE. **Cohesive energy curves for noble gas solids calculated by adiabatic connection fluctuation-dissipation theory.** *Phys. Rev. B*, **77**:045136, 2008. 89, 102, 116, 118, 121
- [91] M. HÄSER AND J. ALMLÖF. **Laplace transform techniques in MøllerPlesset perturbation theory.** *J. Chem. Phys.*, **96**:489–494, 1992. 91, 93, 94
- [92] W. H. PRESS, S. A. TEUKOLSKY, W. T. VETTERLING, AND B. P. FLANNERY. *Numerical Recipes 3rd Edition: The Art of Scientific Computing.* Cambridge University Press, 2007. 92, 98, 146
- [93] G. GOLUB AND V. PEREYRA. **Separable nonlinear least squares: the variable projection method and its applications.** *Inverse Problems*, **19**:R1, 2003. 92, 100
- [94] D. BRAESS. *Nonlinear Approximation Theory.* Springer Series in Computational Mathematics. Springer, 2011. 92

REFERENCES

- [95] E. I. A. REMEZ. *General computational methods of Chebyshev approximation: The problems with linear real parameters*. U. S. Atomic Energy Commission, Division of Technical Information, 1962. 92
- [96] M. MARSMAN, A. GRÜNEIS, J. PAIER, AND G. KRESSE. **Second-order Møller-Plesset perturbation theory applied to extended systems. I. Within the projector-augmented-wave formalism using a plane wave basis set**. *J. Chem. Phys.*, **130**:184103, 2009. 93, 94, 149
- [97] H. ESHUIS, J. YARKONY, AND F. FURCHE. **Fast computation of molecular random phase approximation correlation energies using resolution of the identity and imaginary frequency integration**. *J. Chem. Phys.*, **132**:234114, 2010. 93
- [98] C. MÖLLER AND M. S. PLESSET. **Note on an Approximation Treatment for Many-Electron Systems**. *Phys. Rev.*, **46**:618–622, 1934. 94
- [99] A. K. WILSON AND J. ALMLÖF. **Møller-Plesset correlation energies in a localized orbital basis using a Laplace transform technique**. *Theoretica chimica acta*, **95**:49–62, 1997. 95
- [100] D. BRAESS AND W. HACKBUSCH. **Approximation of $1/x$ by exponential sums in $[1, \infty)$** . *IMA Journal of Numerical Analysis*, **25**:685–697, 2005. 97, 101
- [101] D. KATS, D. USVYAT, S. LOIBL, T. MERZ, AND M. SCHÜTZ. **Comment on "Minimax approximation for the decomposition of energy denominators in Laplace-transformed MøllerPlesset perturbation theories"**. *J. Chem. Phys.*, **130**:127101, 2009. 97
- [102] A. DUTT AND V. ROKHLIN. **Fast Fourier Transforms for Nonequispaced Data**. *SIAM Journal on Scientific Computing*, **14**:1368–1393, 1993. 97
- [103] G. KRESSE AND J. HAFNER. **Ab initio molecular dynamics for liquid metals**. *Phys. Rev. B*, **47**:558–561, 1993. 100
- [104] G. KRESSE AND D. JOUBERT. **From ultrasoft pseudopotentials to the projector augmented-wave method**. *Phys. Rev. B*, **59**:1758–1775, 1999. 100, 114, 115, 117
- [105] **VARPRO**. <http://jblevins.org/mirror/amiller/>. Alan Miller's Fortran Software. 100
- [106] J. P. PERDEW, M. ERNZERHOF, AND K. BURKE. **Rationale for mixing exact exchange with density functional approximations**. *J. Chem. Phys.*, **105**:9982–9985, 1996. 105, 147
- [107] C. KITTEL. *Introduction to Solid State Physics*. Wiley, 2004. 109
- [108] G. CZYCHOLL. *Theoretische Festkörperphysik: Von Den Klassischen Modellen Zu Modernen Forschungsthemen*. Springer, 2004. 109, 144, 145
- [109] P. E. BLÖCHL. **Projector augmented-wave method**. *Phys. Rev. B*, **50**:17953–17979, 1994. 114, 117
- [110] M. SHISHKIN AND G. KRESSE. **Implementation and performance of the frequency-dependent GW method within the PAW framework**. *Phys. Rev. B*, **74**:035101, 2006. 114
- [111] M. GAJDOŠ, K. HUMMER, G. KRESSE, J. FURTHMÜLLER, AND F. BECHSTEDT. **Linear optical properties in the projector-augmented wave methodology**. *Phys. Rev. B*, **73**:045112, 2006. 115
- [112] B. XIAO, J. SUN, A. RUZSINSZKY, J. FENG, AND J. P. PERDEW. **Structural phase transitions in Si and SiO crystals via the random phase approximation**. *Phys. Rev. B*, **86**:094109, 2012. 118, 119
- [113] E. R. BATISTA, J. HEYD, R. G. HENNIG, B. P. UBERUAGA, R. L. MARTIN, G. E. SCUSERIA, C. J. UMRIGAR, AND J. W. WILKINS. **Comparison of screened hybrid density functional theory to diffusion Monte Carlo in calculations of total energies of silicon phases and defects**. *Phys. Rev. B*, **74**:121102, 2006. 118, 124
- [114] D. ALFÈ, M. J. GILLAN, M. D. TOWLER, AND R. J. NEEDS. **Diamond and β -tin structures of Si studied with quantum Monte Carlo calculations**. *Phys. Rev. B*, **70**:214102, 2004. 118, 119
- [115] R. G. HENNIG, A. WADEHRA, K. P. DRIVER, W. D. PARKER, C. J. UMRIGAR, AND J. W. WILKINS. **Phase transformation in Si from semiconducting diamond to metallic β phase in QMC and DFT under hydrostatic and anisotropic stress**. *Phys. Rev. B*, **82**:014101, 2010. 118
- [116] J. HARL, L. SCHIMKA, AND G. KRESSE. **Assessing the quality of the random phase approximation for lattice constants and atomization energies of solids**. *Phys. Rev. B*, **81**:115126, 2010. 119
- [117] O. K. AL-MUSHADANI AND R. J. NEEDS. **Free-energy calculations of intrinsic point defects in silicon**. *Phys. Rev. B*, **68**:235205, 2003. 121
- [118] P. RINKE, A. JANOTTI, M. SCHEFFLER, AND C. G. VAN DE WALLE. **Defect Formation Energies without the Band-Gap Problem: Combining Density-Functional Theory and the GW Approach for the Silicon Self-Interstitial**. *Phys. Rev. Lett.*, **102**:026402, 2009. 121
- [119] F. CORSETTI AND A. A. MOSTOFI. **System-size convergence of point defect properties: The case of the silicon vacancy**. *Phys. Rev. B*, **84**:035209, 2011. 122, 124
- [120] W. GAO AND A. TKATCHENKO. **Electronic Structure and van der Waals Interactions in the Stability and Mobility of Point Defects in Semiconductors**. *Phys. Rev. Lett.*, **111**:045501, 2013. 122, 123, 125, 126, 199
- [121] F. BRUNEVAL. **Range-Separated Approach to the RPA Correlation Applied to the van der Waals Bond and to Diffusion of Defects**. *Phys. Rev. Lett.*, **108**:256403, 2012. 123, 126, 199
- [122] M. I. J. PROBERT AND M. C. PAYNE. **Improving the convergence of defect calculations in supercells: An ab initio study of the neutral silicon vacancy**. *Phys. Rev. B*, **67**:075204, 2003. 124

REFERENCES

- [123] W. D. PARKER, J. W. WILINS, AND R. G. HENNIG. **Accuracy of quantum Monte Carlo methods for point defects in solids.** *Phys. Status Solidi B*, **248**:267, 2011. 124
- [124] W.-K. LEUNG, R. J. NEEDS, G. RAJAGOPAL, S. ITOH, AND S. IHARA. **Calculations of Silicon Self-Interstitial Defects.** *Phys. Rev. Lett.*, **83**:2351–2354, 1999. 124
- [125] S. CHIESA, D. M. CEPERLEY, R. M. MARTIN, AND M. HOLZMANN. **Finite-Size Error in Many-Body Simulations with Long-Range Interactions.** *Phys. Rev. Lett.*, **97**:076404, 2006. 124
- [126] A. TKATCHENKO, R. A. DiSTASIO, R. CAR, AND M. SCHEFFLER. **Accurate and Efficient Method for Many-Body van der Waals Interactions.** *Phys. Rev. Lett.*, **108**:236402, 2012. 125
- [127] ANT URAL, P. B. GRIFFIN, AND J. D. PLUMMER. **Self-Diffusion in Silicon: Similarity between the Properties of Native Point Defects.** *Phys. Rev. Lett.*, **83**:3454–3457, 1999. 126
- [128] H. BRACHT, N. A. STOLWIJK, AND H. MEHRER. **Properties of intrinsic point defects in silicon determined by zinc diffusion experiments under nonequilibrium conditions.** *Phys. Rev. B*, **52**:16542–16560, 1995. 126
- [129] G. D. WATKINS. *ECS Proc.*, **99-1**:38, 1999. 126
- [130] D. CALISTE AND P. POCHE. **Vacancy-Assisted Diffusion in Silicon: A Three-Temperature-Regime Model.** *Phys. Rev. Lett.*, **97**:135901, 2006. 127
- [131] L. HUANG, T. AYRAL, S. BIERMANN, AND P. WERNER. **Extended dynamical mean-field study of the Hubbard model with long-range interactions.** *Phys. Rev. B*, **90**:195114, 2014. 131, 132
- [132] H. JIANG L. VAUGIER AND S. BIERMANN. **Hubbard U and Hund exchange J in transition metal oxides: Screening versus localization trends from constrained random phase approximation.** *Phys. Rev. B*, **86**:165105, 2012. 134
- [133] T. RIBIC, E. ASSMANN, A. TÓTH, AND K. HELD. **Cubic interaction parameters for t_{2g} Wannier orbitals.** *Phys. Rev. B*, **90**:165105, 2014. 134
- [134] D. BOHM AND D. PINES. **A Collective Description of Electron Interactions. I. Magnetic Interactions.** *Phys. Rev.*, **82**:625–634, 1951. 135
- [135] D. PINES AND D. BOHM. **A Collective Description of Electron Interactions: II. Collective vs Individual Particle Aspects of the Interactions.** *Phys. Rev.*, **85**:338–353, 1952. 135
- [136] D. BOHM AND D. PINES. **A Collective Description of Electron Interactions: III. Coulomb Interactions in a Degenerate Electron Gas.** *Phys. Rev.*, **92**:609–625, 1953. 135
- [137] F. ARYASETIAWAN, M. IMADA, A. GEORGES, G. KOTLIAR, S. BIERMANN, AND A. I. LICHTENSTEIN. **Frequency-dependent local interactions and low-energy effective models from electronic structure calculations.** *Phys. Rev. B*, **70**:195104, 2004. 135
- [138] C. BROUDER, G. PANATI, M. CALANDRA, C. MOURougANE, AND N. MARZARI. **Exponential Localization of Wannier Functions in Insulators.** *Phys. Rev. Lett.*, **98**:046402, 2007. 136, 137, 141, 159
- [139] N. MARZARI, A. A. MOSTOFI, J. R. YATES, I. SOUZA, AND D. VANDERBILT. **Maximally localized Wannier functions: Theory and applications.** *Rev. Mod. Phys.*, **84**:1419–1475, 2012. 136, 145
- [140] N. MARZARI AND D. VANDERBILT. **Maximally localized generalized Wannier functions for composite energy bands.** *Phys. Rev. B*, **56**:12847–12865, 1997. 136, 160
- [141] E. ŞAŞIOĞLU, A. SCHINDLMAYR, C. FRIEDRICH, F. FREIMUTH, AND S. BLÜGEL. **Wannier-function approach to spin excitations in solids.** *Phys. Rev. B*, **81**:054434, 2010. 136
- [142] A. A. MOSTOFI, J. R. YATES, Y.-S. LEE, I. SOUZA, D. VANDERBILT, AND MARZARI N. **wannier90: A tool for obtaining maximally-localised Wannier functions.** *Comp. Phys. Comm.*, **178**:685–699, 2008. 136, 141, 160, 196
- [143] I. SOUZA, N. MARZARI, AND D. VANDERBILT. **Maximally localized Wannier functions for entangled energy bands.** *Phys. Rev. B*, **65**:035109, 2001. 137, 150
- [144] T. MIYAKE AND F. ARYASETIAWAN. **Screened Coulomb interaction in the maximally localized Wannier basis.** *Phys. Rev. B*, **77**:085122, 2008. 137
- [145] E. ŞAŞIOĞLU, C. FRIEDRICH, AND S. BLÜGEL. **Effective Coulomb interaction in transition metals from constrained random-phase approximation.** *Phys. Rev. B*, **83**:121101, 2011. 137, 138, 147, 151, 152, 153, 154, 196
- [146] B.-C. SHIH, Y. ZHANG, W. ZHANG, AND P. ZHANG. **Screened Coulomb interaction of localized electrons in solids from first principles.** *Phys. Rev. B*, **85**:045132, 2012. 137, 138, 151, 152, 154, 196
- [147] T. MIYAKE, F. ARYASETIAWAN, AND M. IMADA. **Ab initio procedure for constructing effective models of correlated materials with entangled band structure.** *Phys. Rev. B*, **80**:155134, 2009. 137, 150, 151, 152, 153, 154, 196
- [148] W. R. HANKE. **Microscopic Theory of Dielectric Screening and Lattice Dynamics in the Wannier Representation. I. Theory.** *Phys. Rev. B*, **8**:4585–4590, 1973. 144
- [149] W. HANKE AND L. J. SHAM. **Many-particle effects in the optical spectrum of a semiconductor.** *Phys. Rev. B*, **21**:4656–4673, 1980. 144
- [150] J.-F. CARDOSO AND A. SOULOUMIAC. **Jacobi angles for simultaneous diagonalization.** *SIAM J. Mat. Anal. Appl.*, **17**:161–164, 1996. 146
- [151] Y. NOMURA, M. KALTAK, K. NAKAMURA, C. TARANTO, S. SAKAI, A. TOSCHI, R. ARITA, K. HELD, G. KRESSE, AND M. IMADA. **Effective on-site interaction for dynamical mean-field theory.** *Phys. Rev. B*, **86**:085117, 2012. 147, 149, 158, 161

REFERENCES

- [152] P. E. BLÖCHL, O. JEPSSEN, AND O. K. ANDERSEN. **Improved tetrahedron method for Brillouin-zone integrations.** *Phys. Rev. B*, **49**:16223–16233, 1994. 149
- [153] R. SAKUMA AND F. ARYASETIAWAN. **First-principles calculations of dynamical screened interactions for the transition metal oxides MO (Mn, Fe, Co, Ni).** *Phys. Rev. B*, **87**:165118, 2013. 151, 152, 154, 196
- [154] B.-C. SHIH, A. TESFAYE, X. YUAN, W. ZHANG, AND P. ZHANG. **Screened Coulomb interactions of localized electrons in transition metals and transition-metal oxides.** *Phys. Rev. B*, **86**:165124, 2012. 152, 154
- [155] E. ŞAŞIOĞLU, C. FRIEDRICH, AND S. BLÜGEL. **Strength of the Effective Coulomb Interaction at Metal and Insulator Surfaces.** *Phys. Rev. Lett.*, **109**:146401, 2012. 152, 153, 154, 156, 196
- [156] P. W. ANDERSON. **The Resonating Valence Bond State in La₂CuO₄ and Superconductivity.** *Science*, **235**:1196–1198, 1987. 156
- [157] M. S. HYBERTSEN, M. SCHLÜTER, AND N. E. CHRISTENSEN. **Calculation of Coulomb-interaction parameters for La₂CuO₄ using a constrained-density-functional approach.** *Phys. Rev. B*, **39**:9028–9041, 1989. 156
- [158] P. A. LEE, N. NAGAOSA, AND X.-G. WEN. **Doping a Mott insulator: Physics of high-temperature superconductivity.** *Rev. Mod. Phys.*, **78**:17–85, 2006. 156
- [159] D. N. BASOV AND T. TIMUSK. **Electrodynamics of high- T_c superconductors.** *Rev. Mod. Phys.*, **77**:721–779, 2005. 156
- [160] A. COMANAC, L. DE MEDICI, M. CAPONE, AND A. J. MILLIS. **Optical conductivity and the correlation strength of high-temperature copper-oxide superconductors.** *Nat. Phys.*, **4**:287, 2008. 157
- [161] A. TOSCHI, M. CAPONE, M. ORTOLANI, P. CALVANI, S. LUPI, AND C. CASTELLANI. **Temperature Dependence of the Optical Spectral Weight in the Cuprates: Role of Electron Correlations.** *Phys. Rev. Lett.*, **95**:097002, 2005. 157
- [162] X. WANG, M. J. HAN, L. DE MEDICI, H. PARK, C. A. MARIANETTI, AND A. J. MILLIS. **Covalency, double-counting, and the metal-insulator phase diagram in transition metal oxides.** *Phys. Rev. B*, **86**:195136, 2012. 157
- [163] L. X. BENEDICT. **Screening in the exchange term of the electron-hole interaction of the Bethe-Salpeter equation.** *Phys. Rev. B*, **66**:193105, 2002. 159
- [164] M. METHFESSEL AND A. T. PAXTON. **High-precision sampling for Brillouin-zone integration in metals.** *Phys. Rev. B*, **40**:3616–3621, 1989. 160
- [165] C. TARANTO, M. KALTAK, N. PARRAGH, G. SANGIOVANNI, G. KRESSE, A. TOSCHI, AND K. HELD. **Comparing quasiparticle GW+DMFT and LDA+DMFT for the test bed material SrVO₃.** *Phys. Rev. B*, **88**:165119, 2013. 162
- [166] J. M. TOMCZAK, M. CASULA, T. MIYAKE, AND S. BIERMANN. **Asymmetry in band widening and quasiparticle lifetimes in SrVO₃: Competition between screened exchange and local correlations from combined GW and dynamical mean-field theory GW + DMFT.** *Phys. Rev. B*, **90**:165138, 2014. 163
- [167] A. SEKIYAMA, H. FUJIWARA, S. IMADA, S. SUGA, H. EISAKI, S. I. UCHIDA, K. TAKEGAHARA, H. HARIMA, Y. SAITOH, I. A. NEKRASOV, G. KELLER, D. E. KONDAKOV, A. V. KOZHEVNIKOV, TH. PRUSCHKE, K. HELD, D. VOLLHARDT, AND V. I. ANISIMOV. **Mutual Experimental and Theoretical Validation of Bulk Photoemission Spectra of Sr_{1-x}Ca_xVO₃.** *Phys. Rev. Lett.*, **93**:156402, 2004. 164, 166, 168, 169, 197
- [168] P. WISSGOTT, J. KUNEŠ, A. TOSCHI, AND K. HELD. **Dipole matrix element approach versus Peierls approximation for optical conductivity.** *Phys. Rev. B*, **85**:205133, 2012. 164
- [169] P. WERNER, A. COMANAC, L. DE MEDICI, M. TROYER, AND A. J. MILLIS. **Continuous-Time Solver for Quantum Impurity Models.** *Phys. Rev. Lett.*, **97**:076405, 2006. 164
- [170] A. N. RUBTSOV AND A. I. LICHTENSTEIN. **Continuous-time quantum Monte Carlo method for fermions: Beyond auxiliary field framework.** *Journal of Experimental and Theoretical Physics Letters*, **80**:61–65, 2004. 164
- [171] N. PARRAGH, A. TOSCHI, K. HELD, AND G. SANGIOVANNI. **Conserved quantities of SU(2)-invariant interactions for correlated fermions and the advantages for quantum Monte Carlo simulations.** *Phys. Rev. B*, **86**:155158, 2012. 164
- [172] M. JARRELL AND J. E. GUBERNATIS. **Bayesian inference and the analytic continuation of imaginary-time quantum Monte Carlo data.** *Physics Reports*, **269**(3):133 – 195, 1996. 164, 190
- [173] S. V. FALEEV, M. VAN SCHILFGAARDE, AND T. KOTANI. **All-Electron Self-Consistent GW Approximation: Application to Si, MnO, and NiO.** *Phys. Rev. Lett.*, **93**:126406, 2004. 164
- [174] A. N. CHANTIS, M. VAN SCHILFGAARDE, AND T. KOTANI. **Ab Initio Prediction of Conduction Band Spin Splitting in Zinc Blende Semiconductors.** *Phys. Rev. Lett.*, **96**:086405, 2006. 164
- [175] M. CASULA, P. WERNER, L. VAUGIER, F. ARYASETIAWAN, T. MIYAKE, A. J. MILLIS, AND S. BIERMANN. **Low-Energy Models for Correlated Materials: Bandwidth Renormalization from Coulombic Screening.** *Phys. Rev. Lett.*, **109**:126408, 2012. 164, 166, 197
- [176] K. MAITI, U. MANJU, S. RAY, P. MAHADEVAN, I. H. INOUE, C. CARBONE, AND D. D. SARMA. **Understanding the bulk electronic structure of Ca_{1-x}Sr_xVO₃.** *Phys. Rev. B*, **73**:052508, 2006. 166
- [177] M. CASULA, A. RUBTSOV, AND S. BIERMANN. **Dynamical screening effects in correlated materials: Plasmon satellites and spectral weight transfers from a Green’s function ansatz to extended dynamical mean field theory.** *Phys. Rev. B*, **85**:035115, 2012. 170

REFERENCES

- [178] J. M. TOMCZAK, M. CASULA, T. MIYAKE, F. ARYASETIAWAN, AND S. BIERMANN. **Combined GW and dynamical mean-field theory: Dynamical screening effects in transition metal oxides.** *EPL (Europhysics Letters)*, **100**:67001, 2012. 170
- [179] J. D. JACKSON, C. WITTE, AND K. MULLER. *Klassische Elektrodynamik*. Bod Third Party Titles, 2006. 179
- [180] M. RUGGENTHALER, J. FLICK, C. PELLEGRINI, H. APPEL, I. V. TOKATLY, AND A. RUBIO. **Quantum-electrodynamical density-functional theory: Bridging quantum optics and electronic-structure theory.** *Phys. Rev. A*, **90**:012508, 2014. 180
- [181] Z.-X. SHEN AND D. S. DESSAU. **Electronic structure and photoemission studies of late transition-metal oxides Mott insulators and high-temperature superconductors.** *Physics Reports*, **253**(13):1 – 162, 1995. 189
- [182] A. DAMASCELLI, Z. HUSSAIN, AND Z.-X. SHEN. **Angle-resolved photoemission studies of the cuprate superconductors.** *Rev. Mod. Phys.*, **75**:473–541, 2003. 189
- [183] H. B. SCHÜTTLER AND D. J. SCALAPINO. **Monte Carlo studies of the dynamical response of quantum many-body systems.** *Phys. Rev. B*, **34**:4744–4756, 1986. 190
- [184] C. E. CREFFIELD, E. G. KLEPFISH, E. R. PIKE, AND SARBEN SARKAR. **Spectral Weight Function for the Half-Filled Hubbard Model: A Singular Value Decomposition Approach.** *Phys. Rev. Lett.*, **75**:517–520, 1995. 190
- [185] A. W. SANDVIK. **Stochastic method for analytic continuation of quantum Monte Carlo data.** *Phys. Rev. B*, **57**:10287–10290, 1998. 190

REFERENCES

Acronyms

ACFDT	adiabatic connection fluctuation dissipation theorem. 55, 89, 90, 104, 194
ARPES	angle resolved photoemission spectroscopy. 189
CI	configuration interaction. 8
CLDA	constrained LDA. 164–167, 197, 200
CPT	charge-parity-time inversion. 19
CRPA	constrained random phase approximation. 134, 135, 137, 138, 146, 147, 149, 151, 154–157, 159–161, 164, 166, 170, 172, 173, 196
CT	cosine transformation. 89, 90, 104, 194
CT-QMC	continuous-time quantum Monte Carlo. 164
DFT	density functional theory. 8, 16, 67, 71, 84, 86, 117, 122, 124, 125, 134, 163, 172
DMC	diffusion Monte Carlo. 118, 119, 124, 125, 127–129, 172
DMFT	dynamical mean field theory. 83, 85, 86, 131–136, 155–157, 159, 162–169, 171–173, 189, 197, 200
eDMFT	extended DMFT. 83, 132, 133
EXX	exact exchange. 117, 122, 125
FFT	fast fourier transformation. 90, 109, 112, 113, 116, 194
GGA	generalized gradient approximation. 12, 14, 16
GWA	<i>GW</i> approximation. 69, 70, 72, 84, 134, 189
HEG	homogenous electron gas. 13, 14, 52
HF	Hartree-Fock. 6, 7, 67, 84
HSE	Heyd-Scuseria-Ernzerhof. 123, 125, 126, 128, 199
KS	Kohn-Sham. 11, 12, 71, 86, 173

Acronyms

LDA	local density approximation. 12–16, 86, 131, 133, 157, 159, 162–164, 167–169, 172, 173, 197
LS	least square. 91, 99, 101–104, 106, 194, 195
LT-MP2	Laplace-transformed MP2. 91
MAD	median absolute deviation. 98, 99
MLWF	maximally localized Wannier function. 136
MM	Minimax. 92, 99, 100, 102–104, 106, 194, 195
MP2	second order Møller-Plesset. 91–94, 97, 100, 102, 103, 107, 194
PAW	projector augmented wave. 112, 114, 118, 127
PBE	Perdew-Burke-Ernzerhof. 14, 15, 105, 117, 118, 121–127, 147–150, 152, 156, 199
PES	photoemission spectroscopy. 168, 169, 173
PI	path integral. 73, 74, 76, 81, 172
QED	quantum electrodynamics. 17, 18, 47, 177
QFT	quantum field theory. 17, 19, 35, 40, 46, 73, 75, 171, 177
qp	quasi particle. 71, 133, 162, 164, 173
RPA	random phase approximation. 13, 52, 54, 55, 63, 65, 72, 89–93, 97, 100, 102–108, 112, 115–129, 135, 152, 153, 158, 171, 172, 194–196, 199
rsRPA	range separated RPA. 123, 126, 199
scGW	self-consistent <i>GW</i> . 71
TM	transition metal. 148, 149, 151–154, 156, 173, 191, 196, 199
vdW	van der Waals. 123, 125, 126, 128, 199
VJT	Jahn-Teller distorted vacancy. 122, 123

Glossary

$\hat{\phi}$	Coulomb potential of all nuclei. 4
\hat{V}_{ee}	Coulomb interaction between all electrons. 4
\hat{V}_x	Exchange potential. 6
\hat{V}_h	Hartree potential. 6, 71
\hat{T}	Kinetic energy of all electrons. 4
μ	Chemical potential, usually set to 0. 86, 159
q	Coupling constant or electronic charge. 29, 32
\mathcal{E}_{xc}	Exchange-correlation energy functional. 10, 12
$\varepsilon_{xc}^{\text{HEG}}$	Energy density of the exchange-correlation potential for the HEG. 13
r_s	Wigner-Seitz radius of HEG. 13, 52
Ω_μ	Energy eigenvalue of interacting system. 4
Ω_μ^{HF}	Hartree-Fock energy of the Hartree-Fock solution $ \Omega_\mu^{\text{HF}}\rangle$. 6
$E_\mu^{(N)}$	Non-interacting total energy of N electrons. 6
E_c^{RPA}	Correlation energy in the random phase approximation. 54, 55, 89, 90, 97, 102, 104–107, 116, 117, 194, 195
$\hat{\psi}(\mathbf{r})$	Electron-hole field operator, annihilates (creates) particles with positive (negative) energy. 21, 24, 139
$\hat{\psi}_>(\mathbf{r})$	Electron field operator, annihilates particles with positive energy. 24
$\hat{\psi}_<(\mathbf{r})$	Hole field operator, annihilates particles with negative energy. 24
$\hat{\psi}^\dagger(\mathbf{r})$	Electron-hole field operator, creates (annihilates) particles with positive (negative) energy. 24, 139
$\mathcal{W}[j, j^*]$	Generating functional of QFT. 40, 76
$Z(\beta)$	Total partition function of the interacting system. 39, 49, 58, 76, 79, 81
$Z_v(\beta)$	Interacting part of total partition function $Z(\beta)$. 39, 43
$Z_0(\beta)$	Partition function of non-interacting system. 36
Φ	Grand canonical potential. 40, 50, 52, 58
Φ_v	Interacting part of the grand canonical potential. 44

Glossary

Φ_c^{RPA}	Correlation part of grand potential in the random phase approximation. 54
β	Inverse temperature of the system. 34
x	Spacetime index $x = (\mathbf{r}, \tau)$. 51, 59, 61
τ	Imaginary time of the system, typically restricted to $0 \leq \tau \leq \beta$. 34
$ \Omega_\mu^{\text{HF}}\rangle$	Hartree-Fock solution of interacting electrons. 6
$ \Omega_\mu\rangle$	Eigenstate of interacting system. 4, 39
$ \Psi_\mu^{(N)}\rangle$	Slater determinant of N non-interacting electrons. 5, 20, 21, 39
$ 0\rangle$	Vacuum state, respectively the null vector of the Fock space \mathbb{F} . 20, 22, 23
ν_n	Bosonic Matsubara frequencies. 53
ω_n	Fermionic Matsubara frequencies. 39, 53, 86
Θ	Heaviside step function. 23, 31
f_β	Fermi occupancy function. 37
$\hat{\rho}$	Density operator of interacting system. 39
$\hat{\rho}_0$	Density operator of non-interacting system. 36
\hat{T}	Dyson time ordering operator. 31
\hat{H}	Hamiltonian of N interacting electrons. 4, 29, 30, 78, 83
\hat{H}_0	Non-interacting Hamiltonian for N electrons. 6, 29, 30
\hat{V}	Interacting part of the Hamiltonian for N electrons. 29–31, 44
$\hat{n}(\mathbf{r})$	Density operator at space point \mathbf{r} , respectively number operator in real-space representation. 140
$\delta\hat{n}(\mathbf{r})$	Density fluctuation operator at space point \mathbf{r} . 140
\hat{h}_l	One-electron Hamiltonian acting on electron at \mathbf{r}_l . 5
\hat{S}	Time-evolution operator. 30, 31
G	Interacting Feynman propagator. 40, 57–62, 65, 68–70, 76, 85, 86, 131, 132
G^0	Non-interacting Feynman propagator. 24–26, 28, 35–38, 45, 53, 58, 60, 61, 64, 70, 79, 83, 85, 89, 193
$G_{>}^0$	Greater non-interacting Green's function. 25, 26
$G_{<}^0$	Lesser non-interacting Green's function. 25
χ^d	Correlated part of independent particle polarizability describing screening with target space \mathbb{D} . 135, 136, 138, 141–145
χ^r	Effective independent particle polarizability of constrained random phase approximation. 135
χ^0	Independent particle polarizability. 52–55, 89, 135, 140, 194
χ	Irreducible polarizability. 62–66, 68, 83, 131, 135

W	Screened interaction in Schwinger-Dyson equations. 57, 61–63, 65, 68, 82, 131, 132, 135
Σ	Irreducible self-energy of interacting Feynman propagator. 59, 60, 65, 66, 68, 83, 85, 131
Γ	Irreducible vertex function. 57, 64–66, 68
S_{eff}	Effective action for local degrees of freedom. 77, 81, 82, 84
S	Full many-body action of the system. 79
S_v	Interacting part of the many-body action. 79
S_0	Non-interacting part of the many-body action. 79
\bar{V}	On-site bare Hubbard-Kanamori interaction. 135, 151, 156
\bar{W}	On-site fully RPA-screened Hubbard-Kanamori interaction. 135, 151–153, 156
U	Effective on-site Hubbard-Kanamori interaction. 133, 134, 151, 154–157, 164, 196
J	Effective Hund interaction. 134
\mathcal{U}	Retarded interaction of auxillary impurity model or bare impurity interaction. 82, 83, 85, 86, 131, 132, 134, 135
χ_{imp}	Irreducible polarizability (bosonic self-energy) of impurity model. 83, 132
G_{imp}	Fully dressed (fermionic) propagator of impurity model. 82, 85, 132
W_{imp}	Fully dressed interaction (bosonic propagator) of impurity model. 82
Σ_{imp}	Irreducible (fermionic) self-energy of impurity model. 83, 85, 132
\mathcal{G}	Weiss field of auxillary impurity model or non-interacting impurity propagator. 82–85, 131, 132
\mathbb{D}	Correlated subspace described by model Hamiltonian solved with DMFT. 134–138, 140, 141, 144, 145, 158
$N_{\mathbb{D}}$	Number of states in the correlated subspace \mathbb{D} . 134
N	System size, i.e. total number of electrons considered. 3, 4, 7, 8, 12, 20, 21, 23, 25, 55, 69, 70, 72, 89–91, 113, 142, 171
\mathbb{F}	Fock space of the many-body problem. 20, 76, 134, 142
$\wedge^N \mathbb{H}$	Antisymmetrized Hilbert space \mathbb{H} of N particles. 20
\mathbb{C}	Set of complex numbers. 7
$I_{\mu}^{(N)}$	Index set of N quantum numbers defining the μ^{th} non-interacting eigenstate $ \Psi_{\mu}^{(N)}\rangle$. 5, 21
\mathbb{Z}	Set of all integer numbers. 37–39, 53
\mathbb{N}	Set of natural numbers (positive integers). 20
\mathbb{R}	Set of real numbers. 8
$\mathcal{C}^{\infty}(\mathbb{R}^3)$	Set of all smooth functions defined on \mathbb{R}^3 . 8, 9
$[\varepsilon(\mu)]$	Levi-Civita tensor with indices are restricted to the index set $I_{\mu}^{(N)}$. 5, 6, 139

Glossary

\AA	Length unit Ånström, $1 [\text{\AA}] = 10^{-10} [\text{m}]$. 102
$\boldsymbol{\alpha}$	Bold greek indices indicate general Wannier indices $\boldsymbol{\alpha} = (\alpha, \mathbf{R}_\alpha)$. 77
α	Greek indices with indicate local indices $\alpha = (\alpha, \mathbf{0})$. 77
$\bar{\alpha}$	Greek indices with a bar indicate non-local indices $\bar{\alpha} = (\alpha, \mathbf{R}_\alpha \neq \mathbf{0})$. 77
$ w_\alpha\rangle$	General one-particle Wannier state with $\boldsymbol{\alpha} = (\alpha, \mathbf{R}_\alpha)$. 77
$T_{n\alpha}^{(\mathbf{k})}$	Unitary transformation matrix between Bloch and Wannier states. 77, 136, 145, 146

Zusammenfassung

Der erste Teil der vorliegenden Arbeit deckt grundlegende Literatur zum Thema Vielelektronensysteme in kondensierter Materie ab. Dies beinhaltet die zugehörige Schrödingergleichung sowie die beiden Näherungsverfahren Hartree-Fock- und Dichtefunktionaltheorie. Dieser Abschnitt sollte als eine kurze Einleitung zum Thema betrachtet werden, da der Hauptfokus der vorliegenden Arbeit auf quantenfeldtheoretischen Zugängen liegt. Aus diesem Grund wird in Kapitel 2 die Zweite Quantisierung des Schrödingerfeldes besprochen, um anschließend (in Kapitel 3) Feynman-Regeln für die Störungsreihe des Großkanonischen Potentials abzuleiten. Das Beschränken der Reihe auf sogenannte Ringdiagramme ergibt die bekannte Random-Phase-Approximation (RPA) des Großkanonischen Potentials bzw. die elektronische Korrelationsenergie am absoluten Nullpunkt.

Um die Vereinigung der GW - mit der Dynamischen Molekularfeldtheorie (DMFT) Näherung des Elektronenpropagators zu untersuchen, werden die Schwinger-Dyson-Gleichungen und das Konzept des Pfadintegrals in Kapitel 4 eingeführt. Die GW -Näherung wird über die Dysongleichung für den Elektronenpropagator hergeleitet indem die Selbstenergiebeiträge auf Ringdiagramme beschränkt werden. Im Gegensatz dazu erhält man die DMFT-Näherung durch das Ausintegrieren von nicht-lokalen Feldvariablen in der großkanonischen Zustandssumme im Grenzwert von unendlich vielen Dimensionen. Daraus folgt, dass die DMFT- eine akkuratere Bestimmung aller lokalen Selbstenergiediagramme des Elektronenpropagators als die GW -Approximation erlaubt. Anschließend wird der Wechselwirkungsterm des Hamiltonoperators mit einer Hubbard-Stratonovich-Transformation entkoppelt, um zu zeigen, dass eine konsistente Kombination von GW - und DMFT-

Glossary

Näherung nur dann möglich ist, wenn sowohl die fermionische als auch die bosonische Dysongleichung selbst-konsistent gelöst wird.

Der zweite Teil der vorliegenden Arbeit beinhaltet zwei Kapitel die aus einer Kollektion von kürzlich publizierten Arbeiten bestehen. Darin werden methodologische Entwicklungen für das Ausführen von praktischen $GW+DMFT$ -Rechnungen vorgestellt beginnend mit einem effizienten RPA-Algorithmus in Kapitel 5. Dieser Algorithmus basiert auf optimierten imaginären Zeit- und Frequenzgittern für die Møller-Plesset-Störungstheorie und erlaubt eine genaue Bestimmung der RPA-Korrelationsenergie mit einem Rechenaufwand, der kubisch mit der Systemgröße skaliert. Die Algorithmuseffizienz wird durch das Berechnen der Defektformationsenergien von Si mit Superzellen von bis zu 256 Atomen demonstriert. Da die GW -Näherung mit der RPA eng verwandt ist, kann der präsentierte RPA-Algorithmus als der erste Schritt zu einem effizienten GW -Algorithmus betrachtet werden.

In Kapitel 6 wird ein vereinfachter $GW+DMFT$ -Zugang vorgestellt. Das beinhaltet die Ableitung einer beschränkten RPA-Methode (CRPA), die auf der Kubo-Formel für die Dichte-Dichte-Antwortfunktion basiert. Die so hergeleitete CRPA erlaubt die Berechnung der effektiven Wechselwirkung in korrelierten Unterraum, der durch die DMFT akkurat beschrieben wird. Um die Spektralfunktion von $SrVO_3$ zu berechnen, wird im letzten Teil die Quasi-Teilchen- GW - in Kombination mit der DMFT-Näherung verwendet. Es wird gezeigt, dass das Resultat zu einer guten Übereinstimmung mit dem Experiment führt.

Abstract

Part one of the present thesis covers basic textbook knowledge about the many-body problem of condensed matter physics introduced in chapter 1 by means of Hartree-Fock and density functional theory. The main part of this work, however, is focused on quantum field theory methods to solve the many-body problem. For this purpose the second quantization technique for the many-body Hamiltonian is used to derive Feynman rules for the perturbation expansion of the grand canonical potential in terms of Feynman diagrams. Restricting the series to ring diagrams the random phase approximation (RPA) of the grand potential, respectively the correlation energy at zero-temperature is obtained.

To investigate the combination of the GW and dynamical mean field theory (DMFT) approximation of the electron propagator, the Schwinger-Dyson equations as well as the path integral formalism of condensed matter physics are introduced. The GW approximation is explained using the Dyson equation for the electron propagator and showing that it is obtained by restricting the self-energy to RPA bubble diagrams. In contrast we derive the DMFT approximation of the propagator by integrating out all non-local field variables and using the infinite dimensional limit. This reveals, that DMFT allows for an accurate determination of all local self-energy diagrams of the electron propagator.

To merge GW with DMFT, we decouple the interaction term of the Hamiltonian using a Hubbard-Stratonovich transformation to show that a consistent $GW+DMFT$ approach is possible only if the Dyson equation for the fermionic as well as for the bosonic propagator is solved self-consistently. The latter includes the effective, purely local interaction between DMFT target states and

has to be determined from first principles by downfolding the full many-body Hamiltonian onto a small localized basis set.

Part two of this thesis is covered by chapter 5 and 6 and consists of a collection of recently published papers, presenting methodological developments to carry out practical GW +DMFT calculations from first principles. Emphasis is put on a low scaling RPA algorithm, presented in chapter 5. This algorithm is based on optimized imaginary time and frequency grids for Møller-Plesset perturbation theory and allows for an accurate determination of the RPA correlation energy with a computational effort scaling cubically with the system size. The performance of the algorithm is demonstrated by computing RPA defect formation energies for Si using supercells with up to 256 atoms. Due to the strong relation of the GW with the random phase approximation, the presented RPA algorithm should be seen as a first step towards the improvement and acceleration of quasi particle (qp) GW calculations.

In chapter 6 a simplified qp GW +DMFT algorithm is presented and applied to SrVO₃. This includes a derivation of a constrained RPA (CRPA) scheme based on the Kubo formula of the density-density response function, which is used to determine effective interaction parameter for DMFT Hamiltonians from first principles. In contrast to conventionally applied CRPA methods, our approach does not change the original band structure and follows from basic principles without additional ad-hoc steps. In the next step the quasi particle GW approximation is combined with DMFT to a qp GW +DMFT scheme and the algorithm is applied to SrVO₃ finding good agreement with experimentally measured data.

Acknowledgements

First of all, I thank my family, my parents Mevla and Juso, who have always supported my studies, as well as my sisters Azra and Edina and my girlfriend's parents Imi and Hansi.

Special thanks I owe Georg Kresse, who did an impressive job as my supervisor by introducing me into the many-body problem and computational material physics. I always enjoyed the time with him discussing new ideas and perspectives in front of a whiteboard or computer.

Likewise, the working atmosphere in the group was always friendly and professional. This is definitely due to my cooperative group members Jiri Klimes, Leif-Eric Hintzsche, Andreas Grüneis, Doris Vogtenhuber, Cesare Franchini, Tobias Sander, Felix Hummel, Kerstin Hummer, Gerald Jordan, Emanuele Maggio, Menno Bokdam, Lubomir Benko, Laurids Schimka, Ronald Starke, Michael Pörtl, Doris Hecht-Aichholzer and Katharina Simma. It was a pleasure discussing physics and other topics with them. Especially, I would like to thank Martijn Marsman, who always had time for me and helped me a lot to understand the source code of VASP.

Last but most important, I thank Tamara, the love of my life, for her unconditional support in all circumstances. Without you this work would not have been possible.

Publications and Presentations

1. M. KALTAK, M. MARSMAN AND G. KRESSE. **Constrained Random Phase Approximation: Effective Interactions from First Principles.** *In preparation.*
2. J. KLIMEŠ, M. KALTAK, E. MAGGIO AND G. KRESSE. **Singles correlation energy contributions in solids.** *submitted to Journal of Chemical Physics*, 2015.
3. M. KALTAK, J. KLIMEŠ AND G. KRESSE. **Cubic scaling algorithm for the random phase approximation: Self-interstitials and vacancies in Si.** *Phys. Rev. B*, **90**:054115, 2014.
4. J. KLIMEŠ, M. KALTAK AND G. KRESSE. **Predictive GW calculations using plane waves and pseudopotentials.** *Phys. Rev. B*, **90**:075125, 2014.
5. M. SETVIN, C. FRANCHINI, X. HAO, M. SCHMID, A. JANOTTI, M. KALTAK, C. G. VAN DE WALLE, G. KRESSE AND U. DIEBOLD. **Direct View at Excess Electrons in TiO₂ Rutile and Anatase.** *Phys. Rev. Lett.*, **113**:086402, 2014.
6. M. KALTAK, J. KLIMEŠ AND G. KRESSE. **Low Scaling Algorithms for the Random Phase Approximation: Imaginary Time and Laplace Transformations.** *Journal of Chemical Theory and Computation*, **10**:2498–2507, 2014.
7. C. TARANTO, M. KALTAK, N. PARRAGH, G. SANGIOVANNI, G. KRESSE, A. TOSCHI, AND K. HELD. **Comparing quasiparticle GW+DMFT and LDA+DMFT for the test bed material SrVO₃.** *Phys. Rev. B*, **88**:165119, 2013.
8. Y. NOMURA, M. KALTAK, K. NAKAMURA, C. TARANTO, S. SAKAI, A. TOSCHI, R. ARITA, K. HELD, G. KRESSE, AND M. IMADA. **Effective on-site interaction for dynamical mean-field theory.** *Phys. Rev. B*, **86**:085117, 2012.

Mag. Merzuk Kaltak

MAIL | merzuk.kaltak@univie.ac.at

Education

02/2011 - PRESENT	<p>Doctoral Program in Physics, University of Vienna, Faculty of Physics and Center for Computational Materials Science Thesis title: "Merging <i>GW</i> with DMFT" Adviser: Prof. Georg Kresse</p> <ul style="list-style-type: none">• Optimized integral quadratures for RPA and <i>GW</i> calculations.• Low scaling algorithms for the random phase and <i>GW</i> approximation.• Interaction parameters for DMFT.• Realistic approach to combine <i>GW</i> and DMFT.
09/2004 - 01/2011	<p>Master Program in Physics University of Vienna, Faculty of Physics, Gravitational Physics</p> <p>Graduation (Master of Science) with highest distinction Thesis title: "Particle creation via tunneling effect" Adviser: Prof. Helmut Rumpf</p> <ul style="list-style-type: none">• Investigation of Quantum Field Theory in rotating reference frames.• Particle creation as tunneling effect in accelerated reference frames.
01/2004 - 09/2004	<p>Basic Military Service Khevenhüller Kaserne, Klagenfurt, Austria</p>
06/2004	<p>High school graduation Alpen-Adria-Gymnasium, Völkermarkt</p>